



January 2019

# Fine Scale Characterization Of Organic Matter Using Analytical Methods: Raman And NMR Spectroscopies

Seyedalireza Khatibi

Follow this and additional works at: <https://commons.und.edu/theses>

## Recommended Citation

Khatibi, Seyedalireza, "Fine Scale Characterization Of Organic Matter Using Analytical Methods: Raman And NMR Spectroscopies" (2019). *Theses and Dissertations*. 2566.  
<https://commons.und.edu/theses/2566>

This Dissertation is brought to you for free and open access by the Theses, Dissertations, and Senior Projects at UND Scholarly Commons. It has been accepted for inclusion in Theses and Dissertations by an authorized administrator of UND Scholarly Commons. For more information, please contact [zeinebyousif@library.und.edu](mailto:zeinebyousif@library.und.edu).

Fine scale characterization of organic matter using analytical methods:  
Raman and NMR spectroscopies

by

**Seyedalireza Khatibi**

Bachelor of Science in Petroleum Engineering, Amirkabir University of Technology, Iran, 2007

Master of Science in Petroleum Engineering, Amirkabir University of Technology, Iran, 2013

A Dissertation

Submitted to the Graduate Faculty

of the

University of North Dakota

in fulfillment of the requirements

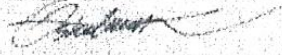
for the degree of

Doctor of Philosophy

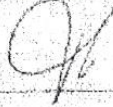
Grand Forks, North Dakota

August  
2019

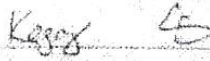
This dissertation, submitted by Seyedalireza Khatibi in partial fulfillment of the requirements for the Degree of Doctor of Philosophy from the University of North Dakota, has been read by the Faculty Advisory Committee under whom the work has been done and is hereby approved.



Dr. Mehdi Ostadhassan



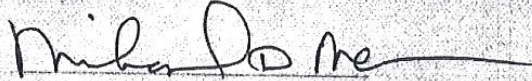
Dr. Vamagh Rasouli



Dr. Kegan Ling



Mr. David Tuschel



Dr. Michael Mann

This dissertation is being submitted by the appointed advisory committee as having met all of the requirements of the School of Graduate Studies at the University of North Dakota and is hereby approved.



Erin Nelson

Interim Dean of the School of Graduate Studies

7/19/19

Date

## PERMISSION

Title            Fine scale characterization of organic matter using analytical methods: Raman  
and NMR spectroscopies

Department    Petroleum engineering

Degree         Doctor of Philosophy

In presenting this dissertation in partial fulfillment of the requirements for a graduate degree from the University of North Dakota, I agree that the library of this University shall make it freely available for inspection. I further agree that permission for extensive copying for scholarly purposes may be granted by the professor who supervised my dissertation work. It is understood that any copying or publication or other use of this dissertation or part thereof for financial gain shall not be allowed without my written permission. It is also understood that due recognition shall be given to me and to the University of North Dakota in any scholarly use which may be made of any material in my dissertation.

Seyedalireza Khatibi

7/10/2019

## Contents

Chapter 1 Introduction .....	1
Chapter 2 Raman Spectroscopy to Study Thermal Maturity and Elastic Modulus of Kerogen .....	3
2-1 Introduction .....	4
2-2 Geological Setting .....	6
2-3 Samples and experiments .....	9
2-3-1 Raman spectroscopy .....	13
2-4 Results and discussion .....	23
2-5 Conclusion.....	36
2-6 References .....	37
Chapter 3 Evaluating Molecular Evolution of Kerogen by Raman Spectroscopy: Correlation with Optical Microscopy and Rock-Eval Pyrolysis .....	53
3-1 Introduction .....	54
3-2 Geological Setting .....	55
3-3 Sample preparation and experiments .....	56
3-4 Results and discussion .....	63
3-4.1 Raman signals on pure kerogen .....	63
3-4.2 Raman spectroscopy for evaluating production potential of OM .....	65

3-5	Conclusions .....	72
3-6	References .....	73
Chapter 4 Understanding Organic Matter Heterogeneity and Maturation Rate by Raman Spectroscopy.		79
4-1	Introduction .....	80
4-2	Samples and methods .....	82
4-2.1	Hydrous pyrolysis.....	85
4-2.2	Raman Spectroscopy .....	86
4-3	Results and discussion .....	91
4-3.1	Heterogeneity .....	99
4-4	Conclusion.....	110
4-5	Acknowledgment.....	111
4-6	Reference.....	111
Chapter 5 CNMR Relaxometry a New Approach to Detect Geochemical Properties of Organic Matter in Tight Shales.....		119
5-1	Introduction .....	120
5-2	Geological setting of the studied area.....	121
5-3	Analytical methods.....	121
5-3.1	Reflectance measurements.....	121

5-3.2	Rock-Eval Pyrolysis .....	122
5-3.3	NMR relaxometry.....	122
5-4	Results and discussion.....	125
5-4.1	Rock-Eval Pyrolysis and Organic Petrography.....	125
5-4.2	NMR 2-D mapping.....	127
5-4.3	Correlations between NMR and Pyrolysis.....	131
5-5	Conclusions .....	139
5-6	References .....	140
Chapter 6	Conclusions and recommendations.....	145

## List of figures

Figure 2-1-1 Young's modulus of shale vs. TOC for: (left) the Woodford Shale formation, (right) the Woodford, Barnett, Haynesville and Eagle Ford Shale formations (Sources: From Aoudia et al. (2010) and Kumar et al. (2012), respectively).....	4
Figure 2-2-1 Map of the Bakken Formation located in the United States portion of the Williston Basin. (Source: modified Liu et al. (2017)).....	7
Figure 2-2-2 Stratigraphic column representing the Bakken Formation and the associated lithology with the Upper, Middle, and Lower Members of the Bakken Formation. (Source: Modified from Kuhn et al. (2010)).....	8
Figure 2-3-1 Wells used in the study distributed throughout the Bakken Formation, Williston Basin, ND. ....	10
Figure 2-3-2 (A) to (F) Photo of core samples of Well No.1 to 6, respectively. (G) to (L) corresponding sample chips for Raman measurements.....	11
Figure 2-3-3 Rock-Eval results showing Kerogen type based on HI vs. $T_{max}$ (up) and S2 vs. TOC (down). As seen, samples are mainly Type II Kerogen. ....	12
Figure 2-3-4 Raman spectra (intensity versus raman shift) for all samples with five time measurements on five spots. ....	17
Figure 2-3-5 (A) Hydrogen-rich low-reflecting bitumen (L-Bit) viewed under white reflected light. (B) The same view under UV light (fluorescence). Note the dull-yellow fluorescing of L-Bit. ....	17

Figure 2-3-6 Sample of Well No. 2: (top) before and (down) after processing by Labspec 6. Baseline subtraction method was used to have a better spectrum for determining band position. Polynomial baseline defined is shown in red, which was subtracted to yield a background free spectrum. .... 18

Figure 2-3-7 (top) Mean of five time measurements of Raman spectra of each sample, (bottom) the same data, but spectra are overlaid in one plot for better comparison of band positions. .... 20

Figure 2-3-8 Visual kerogen assessment on whole-rock sample was performed and the mineral percentage based on visual analysis are approximated for Well No. 4 (top) and Well No. 6 (down). .... 21

Figure 2-3-9 Young’s modulus of some sedimentary rock forming minerals. As it can be seen, kerogen is the least stiff constituent. .... 22

Figure 2-4-1 (left) D band changes with depth, (middle) G band changes with depth, (right) band separation changes with depth. As seen, D band shows decrease, G band no trends, and band separation shows an increase with increasing depth. .... 23

Figure 2-4-2 (A) %Ro versus D band; (B) %Ro versus G band; (C) Band separation versus %Ro for 12 different data sets. There is a nonlinear relationship between Band separation and %Ro. Data are extracted from Spötl et al. (1998), Kelemen and Fang (2001), Sauerer et al. (2017) and results of this study; (D)  $T_{max}$  versus band separation for three different fields. Data are extracted from Sauerer et al. (2017) and results of this study. As seen, by increasing band separation,  $T_{max}$  is also increasing. It verifies Raman as a tool to predict thermal maturities in terms of vitrinite reflectance and Tmax from Rock-Eval. .... 26

Figure 2-4-3 Transmission electronic microscopy (TEM) image of three samples with different maturities. (Left) 7.5 % VRo, (middle) 5.19 % VRo, (right) 2.8 % VRo. Changes in the molecular structure of kerogen at different maturity levels is visible. (Source: From Quirico et. al., 2005). .... 27

Figure 2-4-4 (A) Young’s modulus versus band separation with linear correlation with  $R^2=71\%$ ; (B) Young’s modulus versus band separation with non-linear correlation with  $R^2=87\%$ . As seen, non-linear correlation matches better with data which might be related to non-linear correlation between %Ro and band separation..... 28

Figure 2-4-5 Band separation versus maturity with general thermal maturity map overlaid. Considering %Ro=3 as the late dry gas window, band separation of kerogen can vary from 210-255  $\text{cm}^{-1}$ . Samples are the same as Figure 13(C)..... 29

Figure 2-4-6 Non-linear correlation between band separation and Young’s modulus, with 95% confidence interval of regression and error profile. Predicted value for Well No.3 is shown in green dot. .... 30

Figure 2-4-7 Created plastic zone around the wellbore. .... 33

Figure 2-4-8 Changes of bottomhole pressure during hydraulic fracturing over simulation time steps.... 34

Figure 2-4-9 Injected fluid volume versus averaged fracture aperture in fracture extension test. .... 35

Figure 2-4-10 Total mechanical work which should be done to enlarge the fracture aperture. .... 35

Figure 3-2-1 (top) Wells in this study are overlaid on Bakken Formation map, (bottom) Stratigraphic column of the Bakken Formation and the lithology of Members (Source: modified from (Khatibi et al., 2017a)). .... 56

Figure 3-3-1 (A) to (D) Core samples of Well A to D, (E) to (H) corresponding sample chips, (I) extracted kerogen..... 58

Figure 3-3-2 (A) Blocky grain of primary bitumen (Bit), (B) Same as (A) but Pyrite (P) is also visible, (C) Low-reflecting bitumen (L-Bit), (D) Granular inertinite (Grnl Int) having a morphology that resembles a zooclast, Pyrite (P) is also visible. No reliable grain of primary vitrinite can be seen..... 59

Figure 3-3-3 HI vs. Tmax as pseudo-Van Krevelen diagram for kerogen typing..... 60

Figure 3-3-4 (top) Isolated kerogen of Well D, (bottom) the same sample under a scanning transmission electron microscope (STEM). ..... 61

Figure 3-3-5 (top) Raman spectra for in-situ samples, and (bottom) corresponding isolated kerogen samples. Note the lower background noise in samples, specifically Well A. .... 63

Figure 3-3-6 (left) (L-Bit) Hydrogen-rich Solid bitumen under reflected (white) light. (right) The same view under fluorescence. .... 63

Figure 3-4-1 Band separation versus two common maturity indicators: (left) %Ro and (right) Tmax for different fields. Data are extracted from (Spötl et al., 1998; Kelemen and Fang, 2001; Sauerer et al., 2017). Blue circles are data from this study and red ones are from the literature. .... 66

Figure 3-4-2 PI vs. Tmax for samples in the study. Such graph helps to understand conversion level of organic matter. .... 67

Figure 3-4-3 FTIR of Well A (red) and Well D (green) as lowest and highest mature samples in this study. Note Aliphatic C-H, C-H<sub>2</sub> and CH<sub>3</sub> decrease, Aromatic C=C and C-H (either 2 neighboring or 4 neighboring) increase. (Band assignments for the infrared spectra were based on literature (Painter et al., 1981; Solomon et al., 1988; Chen et al., 1998; Painter et al., 2012; Chen et al., 2015; Craddock et al., 2015). .... 68

Figure 3-4-4 Image of isolated kerogen for Well D with two different scales of: (left) 0.5  $\mu\text{m}$  and (right) 10 nm captured by STEM. The image on the right shows imperfect stacked aromatic layer in the sample. By increasing maturity, aromatics stack and make larger clusters. .... 69

Figure 3-4-5 (left) Correlation of S<sub>2</sub> with G band from Raman spectrum of four samples in this study. (right) The same plot using data from other sources (red circles) including samples in this study (blue

circles) and (Cheshire et al., 2017; Sauerer et al., 2017) with 87% R<sup>2</sup>. Note the negative correlation which corresponds to less potential of production by increasing aromaticity. .... 70

Figure 3-4-6 (left) Correlation of HI from Rock-Eval with G band position of four samples in this study. (right) The same plot using data from other sources (red circles) (Sauerer et al., 2017; Cheshire et al., 2017; Craddock et al., 2017) including samples in this study (blue circles) with R<sup>2</sup> 75%. HI for data from other sources were calculated based on the definition, as they did not report HI directly. Note the negative correlation which corresponds to less hydrogen content of organic matter by increasing aromaticity. .... 70

Figure 3-4-7 (left) Correlation of S<sub>1</sub> with D band of four samples in this study. (right) The same plot using data from other sources (red circles) (Cheshire et al., 2017; Sauerer et al., 2017; Craddock et al., 2018) including samples in this study (blue circles) with 71% R<sup>2</sup>. .... 71

Figure 3-4-8 Correlation between PI from Rock-Eval and PI based on definition using Raman signals. Data from other sources (red circles) (Sauerer et al., 2017; Cheshire et al., 2017; Craddock et al., 2017) including samples in this study (blue circles) with 78% R<sup>2</sup>. PI data from other sources were calculated based on the definition, as they did not report PI directly. .... 71

Figure 4-2-1 (A) and (B) location of the Bakken formation and the wells used in this study for sampling; (C) and (D) Solid bitumen in samples of Well 1 and Well 5, respectively, (E) occurrence of dispersed organic matter in the form of inertinite in Well 4. The red square in the middle of each image is a scale of 5 μm of each side. .... 85

Figure 4-2-2 (A) area selected for Raman spectroscopy, a complete spectrum is acquired at every pixel of the area of interest (1000 spectra are acquired which can all be processed with the same processing steps), (B) a point selected on solid bitumen, (C) and its corresponding Raman spectrum. .... 88

Figure 4-2-3 Raman signals before (A) and after (B) baseline correction for Well 2 as a naturally matured sample. .... 88

Figure 4-2-4 (A) schematic of binning; (B) single spectrum; (C) binning factor of 4; (D) binning factor of 8; (E) binning factor of 20. Note the increase in signal to noise ratio and correspondingly losing spectral features by increasing binning factor..... 89

Figure 4-2-5 Schematic of band peaking procedure using 5 peaks (D, G, D2, D3 and D4) and the experimental Raman spectrum (black). By adding more peaks, the reconstructed spectrum is more similar to experimental results and the  $\chi^2$  value is reduced..... 90

Figure 4-3-1 SBRo and Tmax (as maturity indicators) vs. band separation along with 95% confidence interval of regression and residual error profile for each sample set. The 95% confidence interval defines a range of values that the population mean is covered with 95% of certainty. Note the consistent increase of band separation with increasing thermal maturity. Trendlines for HP and naturally matured samples along with their corresponding correlation coefficients are shown on each plot. Orange represents naturally matured samples and blue represents HP samples..... 93

Figure 4-3-2 (top) %SBRo vs. TOC; (middle) %SBRo vs. S2; (bottom) %SBRo vs. HI along with 95% confidence interval of regression and residual error profile. For each parameter plotted vs. %SBRo, trends are different for artificially and naturally matured samples. Orange represents naturally matured and blue represents HP samples..... 97

Figure 4-3-3 Observed relationship between VRo% and Tmax for natural samples (modified after Epistalié et al., 1985; Dembicki, 2016; Abarghani et al., 2018). It should be noted that measurements were based on %SBRo and were converted to vitrinite reflectance %VRo using the Jacob (1989) equation. Hydrrous pyrolysis results (red circles) do not exactly follow the natural trend limits with dark blue curves. Light

orange circles are naturally matured samples in this study, and black circles are naturally matured Bakken data extracted from Abarghani et al. (2018). ..... 98

Figure 4-3-4 Hydrogen index vs. Tmax for kerogen typing. As seen all samples including naturally and artificially matured are approximately in type II kerogen (modified after Tyson, 1995). ..... 99

Figure 4-3-5 sample HP1 with 0.32 %SBRo: (top) Showing spots selected for averaging Raman signals (each green circle has about 3.6  $\mu\text{m}^2$  area); (middle) Raman spectra of corresponding spots; (bottom) Histogram of D and G bands position along with the statistical information of Avg.: average, SD: standard deviation, CI+: upper bound of confidence interval and CI-: lower bound of confidence interval. Bin sizes were defined based on Deviant (2011), range of data divided by number of bins. .... 102

Figure 4-3-6 Sample HP6 with 0.95 %SBRo: (top) Showing spots selected for averaging Raman signals; (middle) Raman spectra of corresponding spots; (bottom) Histogram of D and G bands position along with the statistical information of Avg.: average, SD: standard deviation, CI+: upper bound of confidence interval and CI-: lower bound of confidence interval. Bin sizes were defined based on what is discussed by Deviant (2011), range of data divided by number of bins. .... 104

Figure 4-3-7 Sample HP8 with 1.29 %SBRo: (top) Showing spots selected for averaging Raman signals; (middle) Raman spectra of corresponding spots; (bottom) Histogram of D and G bands position along with the statistical information of Avg.: average, SD: standard deviation, CI+: upper bound of confidence interval and CI-: lower bound of confidence interval. Bin sizes were defined based on what is discussed by Deviant (2011), range of data divided by number of bins. .... 106

Figure 4-3-8 Raman map of a bitumen corresponding to Figure 4-3-5 to Figure 4-3-7 (HP 1, HP6 and HP8, respectively). Note the changes of band separation indicating changes of chemical composition of the solid

bitumen. As seen, variation of band separation is reducing by increasing maturity. Please note bar graphs next to color scales shows the frequency of each band separation. .... 108

Figure 4-3-9 Results of classical least square fitting procedure for three samples of HP 1, HP6 and HP8. A reference spectrum in the middle of the window is selected and similarity of each spectrum to the reference spectrum is shown. Higher values in the legend show higher dissimilarity..... 109

Figure 5-3-1 General map of T1-T2 map (modified after Fleury et al. (2016), Romero-Sarmiento et al. (2017), Washburn and Birdwell (2013), Mehana and El-monier (2016))..... 124

Figure 5-4-1 HI vs. Tmax is showing the type of kerogen in the six samples of this study..... 126

Figure 5-4-2 (A) Micrinite (Mic) showing granular texture (Ro=0.54%), 5438 ft; (B) Bitumen (Bit) with Ro of 0.50%, 8325 ft; (C) Bitumen (Bit) with Ro of 0.80%, 10437 ft; (D) Alginite (Alg) having greenish-yellow fluorescence, 5438 ft; (E) A large oil-prone Tasmanites alginite (Alg) exhibiting golden-yellow fluorescence color, 8325 ft; (F) Alginite (Alg) showing golden-yellow fluorescence, 8325 ft. Scale bar is 10 micrometers. Excitation is at 465 nm; combined dichroic and barrier filter have a cut at 515 nm. Total magnification of photos A-C is 500X and the total magnification of photos D-F is 250X..... 127

Figure 5-4-3 (a-f) T1-T2 maps for Well 1 to Well 6. Regions (1) to (5) and their corresponding amplitudes (NMR Hydrogen fraction (mg/g)) are shown on each map. A cut-off of T2=0.05 ms derived from Well 1 and Well 5, was applied to Well 4 to separate Regions (3) and (4). 1-D distributions of relaxation times for each map are also shown at the top and left side (blue is incremental, and red is cumulative), which represent the intensity projection of the map on each axis. Signal amplitudes are expressed in a unit of milligram hydrogen per gram rock sample (mg H/g rock). It should be mentioned that the blue curve is incremental, and the red curve is cumulative. .... 131

Figure 5-4-4 T1/T2 ratio of Region 3 from the NMR T1-T2 map vs. VRo (equivalent). The trend shows the T1/T2 ratio increases with thermal maturity. The power function relationship has a correlation coefficient (R2) value of 0.99 including all samples. .... 132

Figure 5-4-5 Hydrogen volume of Region 3 in the NMR T1-T2 map vs. VRo (equivalent) from Petrography. The correlation coefficient of samples excluding two immature ones is 0.98. .... 133

Figure 5-4-6 Hydrogen volume (mg H/g rock) of Region 3 in the NMR T1-T2 map vs. HI from Rock-Eval. The linear relationship with correlation coefficient 0.90 excluding Well 1. .... 134

Figure 5-4-7 Hydrogen volume (mg H/g rock) of Region 3 in the NMR T1-T2 map vs. S1 from Rock-Eval. The linear relationship with correlation coefficient 0.96 excluding Well 1. .... 135

Figure 5-4-8 Hydrogen Volume of Region 3 in the NMR T1-T2 map vs. S2 HC volume from Rock-Eval, with correlation coefficient 0.97 excluding Well 1. .... 135

Figure 5-4-9 Hydrogen volume (mg H/g rock) of Region 3 in the NMR T1-T2 map vs. S1 from Rock-Eval. Squares are the corresponding Sh0 from MHR method. .... 137

## List of tables

Table 2-3-1 Properties of six samples used in this study from the Upper and Lower Bakken.....	10
Table 2-3-2 Bands position of each well. ....	20
Table 2-3-3 Measured Young's modulus for in-situ kerogens in this study (* Well No. 3 lacks Young's modulus measurement).....	22
Table 2-4-1 Properties assigned to the modeled Formation.....	32
Table 3-3-1 Properties of four samples in this study. ....	59
Table 3-4-1 Raman signals for shale and isolated kerogen samples for all wells. Mean and standard deviation (st. dev.) for each band for all available measurements are provided. Note the lower standard deviation in kerogen samples. ....	64
Table 4-2-1 Geochemical properties of two sets of Bakken samples: artificially matured by HP and naturally matured. Note the systematic changes in Tmax, TOC, S2, HI, and PI with increasing maturity in both naturally and artificially matured samples.....	84
Table 4-2-2 Major D and G bands shifts for both artificially and naturally matured samples in this study derived from the average spectrum across the ROI. ....	90
Table 4-3-1 Standard deviation (SD) and Coefficient of variation (CV) of band separations for HP 1, HP6 and HP8 for the entire area of interest. As see, by increasing maturity, the measures of variability are decreasing. CV is useful for calculating the relative magnitude of the standard deviation when few data are available for different datasets.....	108
Table 5-4-1 Rock-Eval data for the six samples using the Basic/Bulk-Rock method.....	125
Table 5-4-2 Amplitude of the NMR signal of regions 1 to 5 and T1/T2 ratios.....	131

Table 5-4-3 Data for the two immature samples processed using the MHR method..... 136

Table 5-4-4 XRD data of Wells 1-5 showing wt% of different minerals. .... 138

## ACKNOWLEDGMENTS

I wish to express my sincere appreciation to the members of my advisory Committee for their guidance and support during my time in the doctoral program at the University of North Dakota.

I am so thankful and grateful to the University of North Dakota and the College of Engineering and Mines, which gave me the opportunity, the financial support, and material means to do this thesis.

I would like to express my gratitude to my supervisor, Dr. Mehdi Ostadhassan, who offered me the chance to pursue this PhD degree and for his precious instructions and valuable guidance. I would also want to thank Dr. Vamegh Rasouli, Dr. Kegan Ling, David Tuschel who honored me for being members of my committee.

I would like to give my great thanks to my parents and my wife who supported me patiently from long distance.

*To my parents who gave me life,*

*To Azadeh who changed my life.*

## Abstract

In order to assess a source rock for economical exploitation purposes, many parameters should be considered. Regarding the geochemical aspects, the most important ones are amount of organic matter (OM) and its quality. Quality refers to thermal maturity level and the nature of the OM from which it was formed that affect the ability of oil and gas generation. Vitrinite reflectance and programmed pyrolysis such as Rock-Eval (RE) are common methods for such analysis. However, vitrinite is not always present in sediments and RE is providing bulk properties. Moreover, the increase in exploration and production of unconventional reservoirs and their complexity has led to the employment of new methods for resource-play assessment, such as Raman spectroscopy and nuclear magnetic resonance (NMR).

In the present dissertation, two mentioned analytical methods of Raman spectroscopy and Hydrogen NMR were utilized for fine scale studying of organic matter and individual macerals to show the potential of such methods in thermal maturity level detection, prediction of elastic properties, structural evolution, and heterogeneity of organic matter.

## Chapter 1 Introduction

Shale reservoirs with organic-rich intervals are often characterized by high quantities of kerogen, solid bitumen and also moveable hydrocarbons, which can be extracted through stimulation methods. Although organic matter (OM) is the main component of the hydrocarbon generation, in most cases, our understanding of OM is limited to its thermal maturity level. While organic matter acts as the storage unit by developing nanoscale pores which hold generated hydrocarbons. Moreover, as it is not as stiff as inorganic minerals, its presence can have a significant impact on the initiation and propagation of fractures in organic-rich formations that should undergo hydraulic fracturing. Therefore, our knowledge about OM will help us with characterization of geochemical, petrophysical and geomechanical properties of organic matter to understanding mechanisms related to generation and migration of hydrocarbons, especially in self-sourced unconventional reservoirs.

In this dissertation, we are going to focus on studying OM using analytical methods such as Raman spectroscopy which enable us to examine OM at fine scale. Our samples are retrieved from Bakken Formation as one of the most important source rocks in the Williston Basin, ND, USA. However, we believe the methodologies used in the research are applicable to other formations as well.

Dissertation includes 7 chapters. Chapter 2 is about a new application of Raman spectroscopy in predicting thermal maturity and elastic modulus of kerogen by using the idea that OM structures and its properties are related to its maturity level. Chapter 3 is the application of previous chapter in hydraulic fracturing to show the effect of OM in such operation. Chapter 4 is shown that Raman spectroscopy by detecting structural information of OM, could reflect thermal maturity parameters that were derived from programmed pyrolysis as one of the most important and common bulk analyzers methods of OM. In chapter 5, the importance of detecting heterogeneity of OM using Raman spectroscopy is discussed. Chapter 6 debates a new application of high frequency H NMR for detecting geochemical properties of organic matter in tight shales. In the final chapter a conclusion and recommendations for further studies are mentioned.

Publications including journal papers and conference proceedings based on this study are listed below:

- Khatibi, Seyedalireza, Mehdi Ostadhassan, David Tuschel, Thomas Gentzis, Bailey Bubach, and Humberto Carvajal-Ortiz. "Raman spectroscopy to study thermal maturity and elastic modulus of kerogen." *International Journal of Coal Geology* 185 (2018): 103-118.
- Khatibi, Seyedalireza, Mehdi Ostadhassan, and Azadeh Aghajanjpour. "Raman spectroscopy: an analytical tool for evaluating organic matter." *Journal of Oil, Gas and Petrochemical Sciences* 1, no. 1 (2018): 28-33.
- Khatibi, Seyedalireza, Azadeh Aghajanjpour, Mehdi Ostadhassan, Ebrahim Ghanbari, Ehsan Amirian, and Rehanali Mohammed. "Evaluating the impact of mechanical properties of kerogen on hydraulic fracturing of organic rich formations." In *SPE Canada Unconventional Resources Conference*. Society of Petroleum Engineers, 2018.
- Khatibi, Seyedalireza, Mehdi Ostadhassan, David Tuschel, Thomas Gentzis, and Humberto Carvajal-Ortiz. "Evaluating molecular evolution of kerogen by raman spectroscopy: correlation with optical microscopy and Rock-Eval pyrolysis." *Energies* 11, no. 6 (2018): 1406.
- Khatibi, Seyedalireza, Mehdi Ostadhassan, and Azadeh Aghajanjpour. "Geomechanical and Geochemical Characterization of Organic Matter by Raman Spectroscopy." In *52nd US Rock Mechanics/Geomechanics Symposium*. American Rock Mechanics Association, 2018.
- Khatibi, Seyedalireza, Mehdi Ostadhassan, Z. Harry Xie, Thomas Gentzis, Bailey Bubach, Zheng Gan, and Humberto Carvajal-Ortiz. "NMR relaxometry a new approach to detect geochemical properties of organic matter in tight shales." *Fuel* 235 (2019): 167-177.
- Khatibi, Seyedalireza, Mehdi Ostadhassan, Paul Hackley, David Tuschel, Arash Abarghani, and Bailey Bubach. "Understanding organic matter heterogeneity and maturation rate by Raman spectroscopy." *International Journal of Coal Geology* (2019).

## **Chapter 2 Raman Spectroscopy to Study Thermal Maturity and Elastic Modulus of Kerogen**

A paper published in the **International Journal of Coal geology**

Seyedalireza Khatibi, Mehdi Ostadhassan, David Tuschel, Thomas Gentzis, Bailey Bubach, Humberto Carvajal-Ortiz

### **Abstract**

Although organic-rich oil-producing mudrocks have been studied extensively during the last decade, kerogen, as one the main constituents, is not thoroughly understood. The unknowns about kerogen elevate when it comes to its modulus of elasticity. Since kerogen is not as stiff as inorganic minerals, its presence can have a significant impact on the initiation and propagation of fractures in kerogen-rich formations that should undergo stimulation.

This study proposes an approach to estimate modulus of elasticity of kerogen with different thermal maturities using Raman spectroscopy. Various shale samples from the upper and lower members of the Bakken Formation were picked from several wells within the Williston Basin in North Dakota, USA. These samples were analyzed using Rock-Eval (RE) pyrolysis and vitrinite reflectance (%Ro) for thermal maturity. In addition, Raman spectroscopic measurements were made on samples and followed by PeakForce AFM for Young's modulus estimation of the organic matter. First, the Raman responses were correlated with the thermal maturity and then, a correlation was established to show the potential relationship between elastic modulus of organic matter and its Raman response based on the maturity levels.

**Keywords:** Kerogen, Raman spectroscopy, PeakForce AFM, Elastic modulus

## 2-1 Introduction

Organic matter, predominantly kerogen that has formed from the burial and preservation of living organisms, is interspersed within the mineral matrix (Hutton et al., 1994). Shale reservoirs with organic-rich intervals are often characterized by high quantities of kerogen, solid bitumen and also moveable hydrocarbons, which can be extracted through hydraulic fracturing and other stimulation methods.

Interest in the experimental and theoretical investigation of the mechanical properties of shale reservoirs has grown significantly in recent years due to the dependence of fracturing models on mechanical properties. Aoudia et al. (2010) and Kumar et al. (2012) presented how increasing total organic carbon (TOC) is correlated with a decrease in Young's modulus of shale, Figure 2-1-1. Hu et al. (2015) concluded that shales with higher TOC have lower fracture pressure gradients. This implies that organic matter such as kerogen has a non-negligible effect on the overall rock mechanical response (Dietrich, 2015). Thus, considering matrix mechanical properties along with an accurate knowledge of the TOC content, maturity, and mechanical properties of kerogen becomes important for a successful stimulation project.

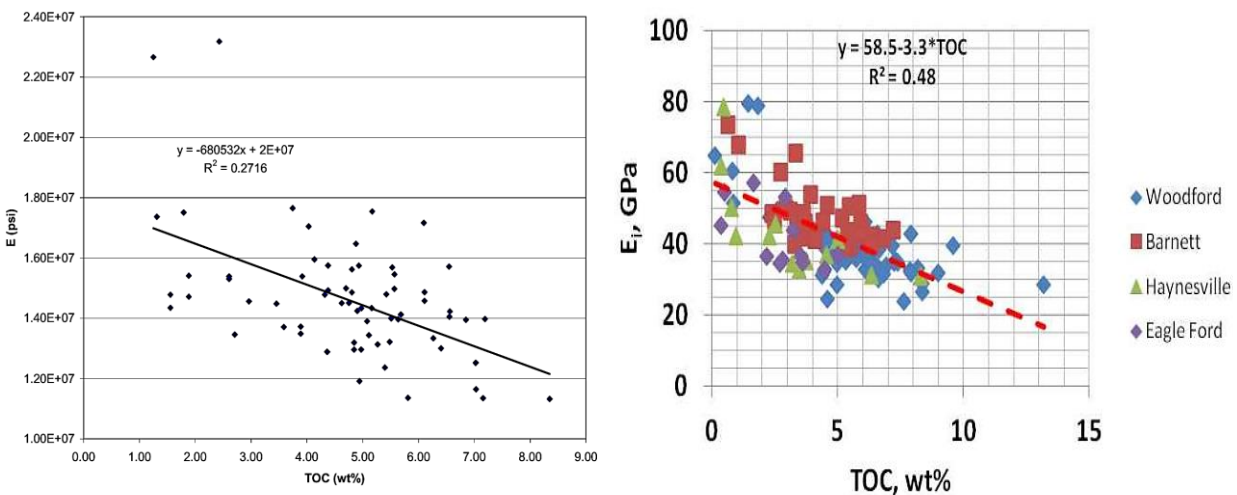


Figure 2-1-1 Young's modulus of shale vs. TOC for: (left) the Woodford Shale formation, (right) the Woodford, Barnett, Haynesville and Eagle Ford Shale formations (Sources: From Aoudia et al. (2010) and Kumar et al. (2012), respectively).

TOC can be obtained from the Rock-Eval (RE) or LECO tests (Espitalie´ et al., 1985; Peters, 1986). Vitrinite reflectance (%VRO) is considered as one of the most reliable methods to obtain

thermal maturity (Diessel et al., 1978). However, vitrinite reflectance can be challenging when samples contain very little or no primary vitrinite (Hackley et al., 2015; Sauerer et al., 2017).

In addition to RE and vitrinite reflectance, Raman spectroscopy can also provide us with valuable information regarding kerogen properties. Wopenka and Pasteris (1993) used laser Raman microprobe for characterizing the structural state of carbonaceous materials such as kerogen and coals (Zhao and Wagner, 2004). Kelemen and Fang (2001) studied kerogen and coals from various sources and established a correlation between Raman spectroscopy and maturity. Tuschel (2013) discussed the use of Raman spectroscopy for characterizing oil shales and showed the contribution of other materials such as calcite in the Raman spectrum. Other researchers have successfully used Raman spectroscopy as a powerful non-destructive tool to quantitatively evaluate thermal maturity of organic matter (Beyssac et al., 2002; Quirico et al., 2005; Lahfid et al., 2010; Guedes et al., 2012; Hinrichs et al., 2014; Wilkins et al., 2014; Zhou et al., 2014; Lünsdorf, 2016; Mumm and Inan, 2016; Ferralis et al., 2016). During thermal maturation, organic matter experiences an increase in aromaticity and a reduction in H, O, N and S content (Tissot and Welte, 1984). Such processes result in a more ordered-structure kerogen (Tyson, 1995; Waples, 1981), which allows Raman spectroscopy to detect different levels of maturation, reflecting these structural changes.

There has been a significant amount of research regarding the thermal maturity of kerogen, whereas its mechanical properties have not well studied (Manjunath and Nair, 2015). The reason for the minimal studies on mechanical properties of kerogen is mostly due to the lack of advanced equipment. Generally, to acquire mechanical properties of a sample in the lab, unconfined compressive strength (UCS) or tri-axial tests are performed on inch-sized cylindrical cores (Shukla et al., 2013, Alexeyev et al., 2017; Aghajanpour et al., 2017). While, kerogen is dispersed within the matrix, isolating a location that contains solely kerogen would be challenging. Thus, high-resolution equipment to study small volumes is required (Zhao et al., 2002; Ulm et al., 2007; Sweers et al., 2011; Schon et al., 2011; Trtik et al., 2012; Ghanbari et al., 2015; Babaei et al., 2015; Babaei et al., 2017; Manjunath and Nair, 2017). Nanoindentation is a testing technique to indirectly determine mechanical properties of materials at the micro- and nano-scales. Researchers in petroleum engineering have applied the nanoindentation method to study shale properties (Kumar et al., 2012; Mason et al., 2014; Pal-Bathija et al., 2008; Liu and Ostadhassan, 2017). These studies have been mostly focused on the minerals and not the kerogen. A few studies investigated

mechanical properties of kerogen with more advanced analytical equipment. Eliyahu et al. (2014) acquired atomic force microscopy (AFM) to examine mechanical properties of organic matter. Li et al. (2017) also used PeakForce AFM and measured the nanomechanical properties of kerogen with high precision.

In this study, first, Raman spectroscopy was used to detect the Raman spectrum of kerogen. Then, the mapping mode of AFM described by Li et al. (2017) was utilized to determine the Young's modulus of the organic particles within our samples. In the next step, a new approach was proposed to understand how the mechanical properties of kerogen in terms of Young's modulus could be reflected on the Raman spectra. It should be noted that the samples are also analyzed for thermal maturity to make this relationship more meaningful. This preliminary study will improve our understanding about the kerogen mechanical properties and will provide a fast, inexpensive and non-destructive method to estimate its modulus of elasticity.

## **2-2 Geological Setting**

For this study, samples were chosen from the upper and lower members of the Bakken Formation and analyzed with Raman, Rock-Eval, vitrinite reflectance and AFM PeakForce. The Bakken Formation is an organic rich shale, mudstone and sandstone that was deposited during the Late Devonian and Early Mississippian Periods. It is located in the Williston Basin, which is an elliptical shaped depression located in the western portion of North Dakota, northeastern region of Montana and extends into parts of Saskatchewan and Manitoba (Figure 2-2-1) (Smith and Bustin, 2000).

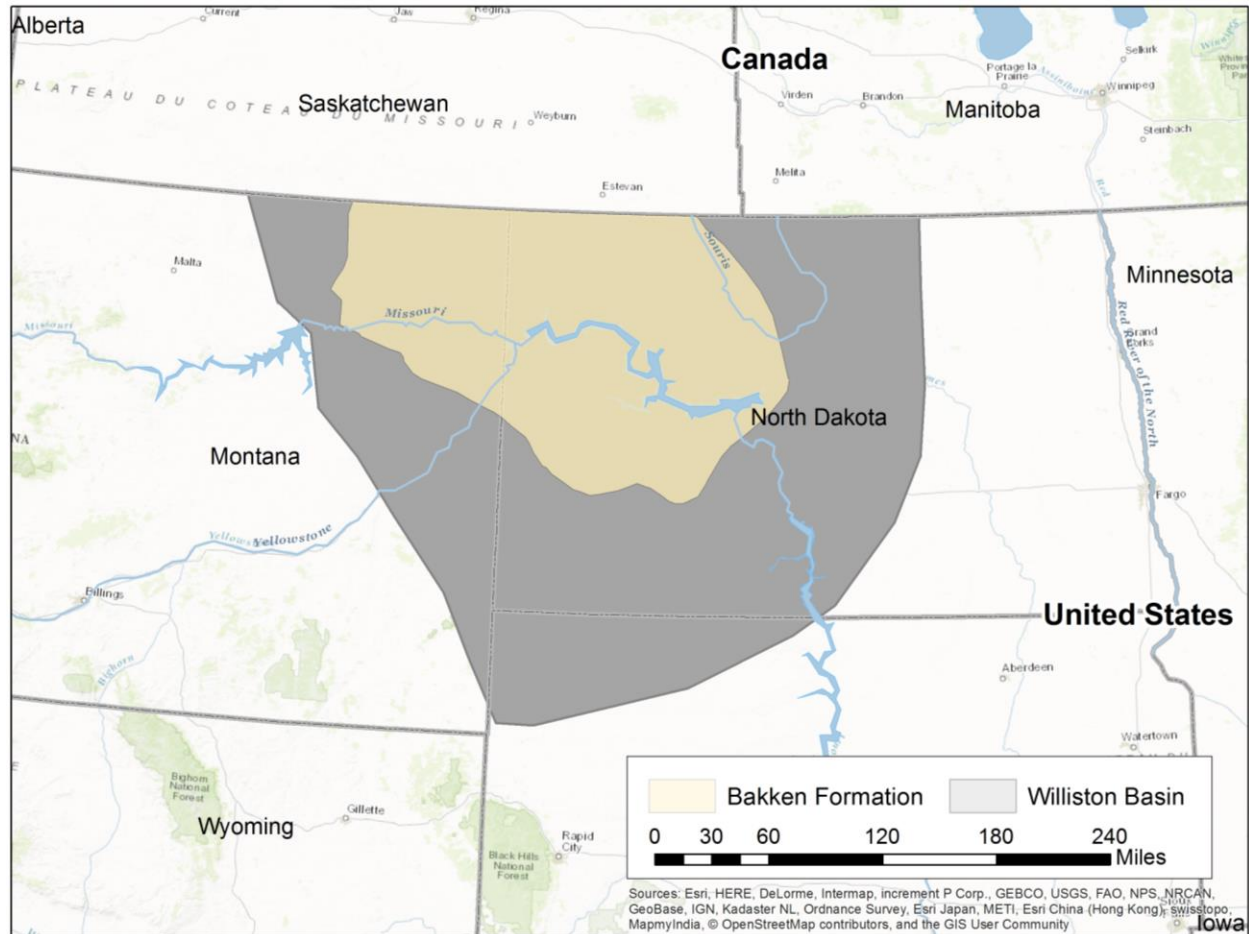


Figure 2-2-1 Map of the Bakken Formation located in the United States portion of the Williston Basin. (Source: modified Liu et al. (2017)).

The Bakken Formation is divided into three members, the Upper, Middle and Lower Bakken (Figure 2-2-2). The upper and lower members are organic rich shales that were classified by Smith and Bustin (1995) as the same lithofacies. The lower member is composed of a finely laminated black mudstone. The black color of the shale is due to the presence of organic matter in the rock, which can vary depending on the ratio of clay, silt, and carbonate in the rock (LeFever et al., 1991). Illite is the primary clay present and there is an abundance of authigenic pyrite (Smith and Bustin, 1995). The pyrite is present as lenses or nodules and it can also be found distributed throughout the shale members, occasionally filling in the fractures of the rock. The upper shale has a similar lithology to the lower shale, and varies in the amount of organic matter, as well as being more fossiliferous (LeFever et al., 1991).

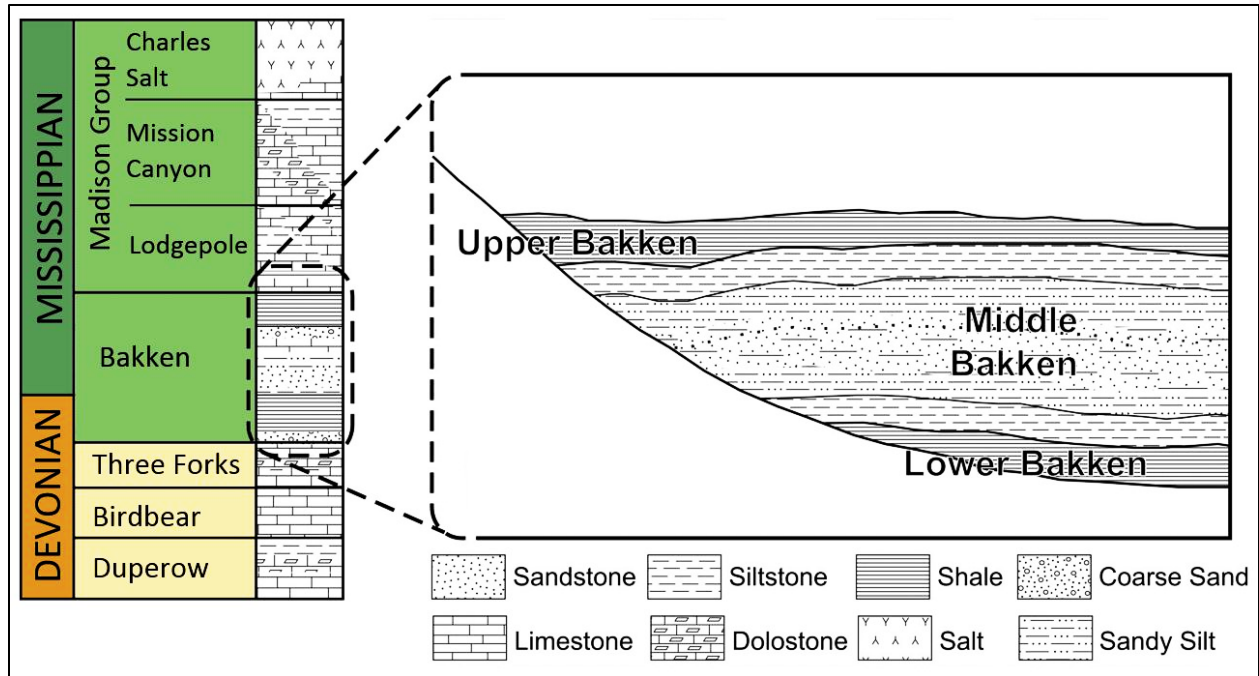


Figure 2-2-2 Stratigraphic column representing the Bakken Formation and the associated lithology with the Upper, Middle, and Lower Members of the Bakken Formation. (Source: Modified from Kuhn et al. (2010)).

The lower and upper members contain Type-I and Type-II organic matter that originated mostly from marine algae. The TOC has a maximum of 30% and 20% in the upper and lower members, respectively (Smith and Bustin, 1995). The organic matter is disseminated evenly throughout the lower member whereas the upper member has a higher amount of TOC.

The Middle Bakken overlies the Lower Bakken and is composed primarily of siltstones and sandstone. Smith and Bustin (1995) classified it as eight different lithofacies, and three different sub-units at a larger scale. The three sub-units are termed A, B, and C, with ascending depth respectively. The basal A sub-unit and upper C sub-unit are composed primarily of siltstone, with the middle sub-unit B having a composition of mud- and sandstone. The formation is massive and well sorted, due to bioturbation (LeFever et al., 1991). The Middle Bakken has much less TOC than upper and lower formations and is primarily targeted as a reservoir rock (Smith and Bustin, 1995).

Deposition of the formation began during the Upper Kaskaskia Sequence, during the Late Devonian Period. The Bakken Formation is recognized as the basal unit of the Upper Kaskaskia and is distinguishable by its black color, as well as a sharp erosional contact with underlying Three Forks Formation. This unconformity is due to the rapid transgression that occurred at the start of

the Upper Kaskaskia Sequence, leading to the deep marine depositional environment of the Lower Member of the Bakken Formation (Gerhard et al., 1990). The upper and lower shales were deposited in similar environments, which was conducive to an anaerobic environment that would preserve the organic matter. This occurred due to the depth of the water (>200 m) being so large, that the point of deposition was below storm wave base, creating a stratified water column. The stagnant bottom water conditions lead to an anoxic environment containing a high concentration of hydrogen sulfide (Smith and Bustin, 1995). The Middle Bakken was deposited in three different episodes that range from offshore for sub-unit A, fair weather wave base and the zone of breaking waves for sub-unit B, and between storm and fair-weather wave base for sub-unit C (Smith and Bustin, 1995).

### 2-3 Samples and experiments

The samples were retrieved from six different wells varying in depth and maturities. Figure 2-3-1 Figure 2-3-2, indicate well locations and the samples that were used for the experiments. Vitrinite maturity (%VRo) and Rock-Eval (RE) Pyrolysis measurements were carried out on the samples. RE is one of the most common methods for evaluating origin and thermal properties of kerogen by heating the samples in the absence of oxygen (Espitalie´ et al., 1985; Peters, 1986; Cheshire et al., 2017). Using the parameters that were generated from the RE analysis, kerogen production potential can be identified. Rock-Eval analysis of the samples revealed that the kerogen is mainly Type II, either immature or in the oil window as shown in Figure 2-3-3. TOC values vary from 13.26 wt% to 24.71 wt%, and %VRo maturity from 0.38 to 0.94. Table 2-3-1 shows a summary of organic matter properties. For vitrinite reflectance (%VRo) analysis, the whole-rock samples were crushed to 20 mesh (850um) particles, mixed with the epoxy resin and hardener (ratio of 2:1) and left to harden under vacuum conditions for 24 hours (Gorbanenko and Ligouis, 2014; Hackley et al., 2015). The samples were polished to ensure the surface is scratch and relief free by using Buehler EcoMet/ AutoMet 250 automated polishing equipment. A Carl Zeiss Axio Imager A2m microscope, equipped with a white light source and a UV light to analyze the random reflectance in oil (%VRo) and qualitative fluorescence, was used for reflectance measurements and visual kerogen analysis.

Approximately 60-70 mg per sample were used for Rock-Eval pyrolysis. The instrument is Rock-Eval 6 analyzer, commercialized by Vinci Technologies in France. The pyrolysis method was the Default method, in which the sample is placed in the chamber and heated at 300°C isothermally for 3 minutes before the temperature is increased to 650°C at a rate of 25°C/min. The detailed Rock-Eval pyrolysis procedure and the parameters obtained from this analysis are outlined in Behar et al. (2001).

Table 2-3-1 Properties of six samples used in this study from the Upper and Lower Bakken.

WELL NO.	SAMPLE DEPTH (FT)	TOC (WT%)	RO (%)	S1	S2	HI	OI	T <sub>MAX</sub> (°C)
1	5438	24.71	0.38	7.97	128.71	520.88	8.42	419
2	8326	16.27	0.54	8.27	90.69	557.41	2.15	428
3	9886	15.76	0.59	9.27	83.7	531.09	0.51	432
4	10555	13.26	0.86	0.31	33.01	260.1	0.94	449
5	10725.5	9.04	0.94	6.13	13.94	154.2	1.22	450
6	11199	16.36	0.92	0.71	28.05	171.45	1.58	452

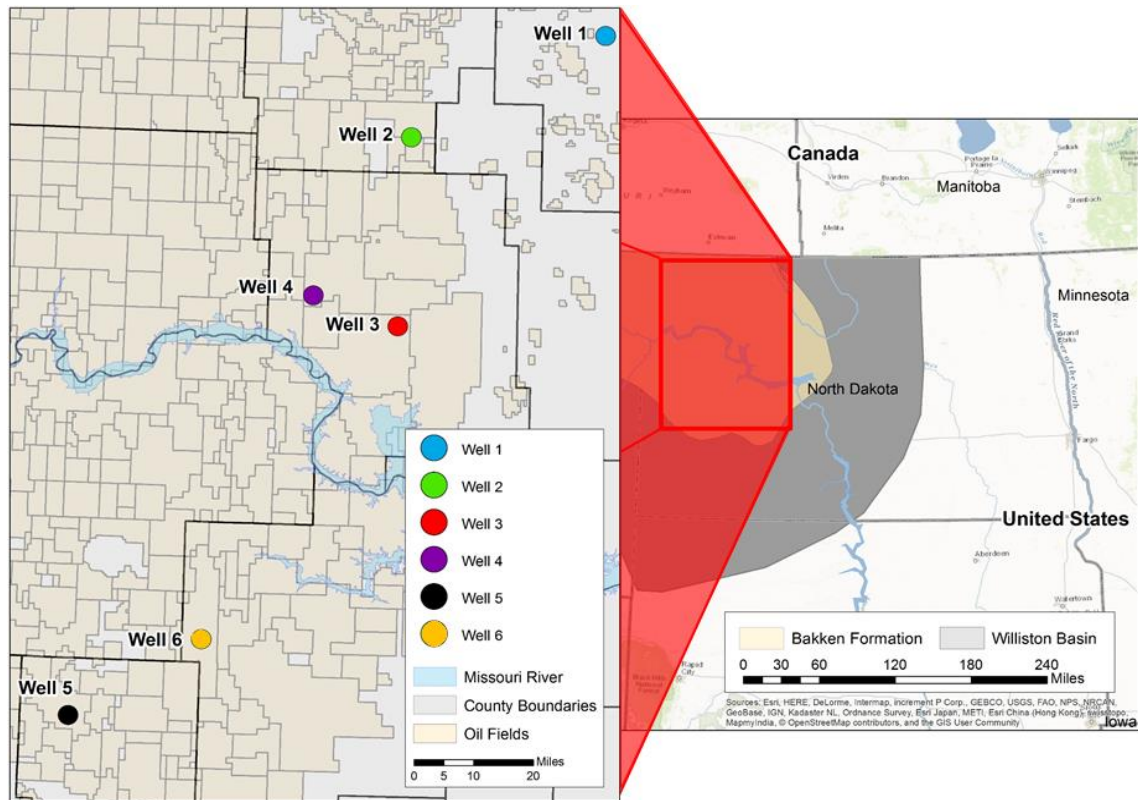


Figure 2-3-1 Wells used in the study distributed throughout the Bakken Formation, Williston Basin, ND.

Chapter 2



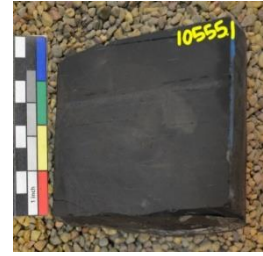
(A)



(B)



(C)



(D)



(E)



(F)



(G)



(H)



(I)



(J)



(K)



(L)

Figure 2-3-2 (A) to (F) Photo of core samples of Well No.1 to 6, respectively. (G) to (L) corresponding sample chips for Raman measurements.

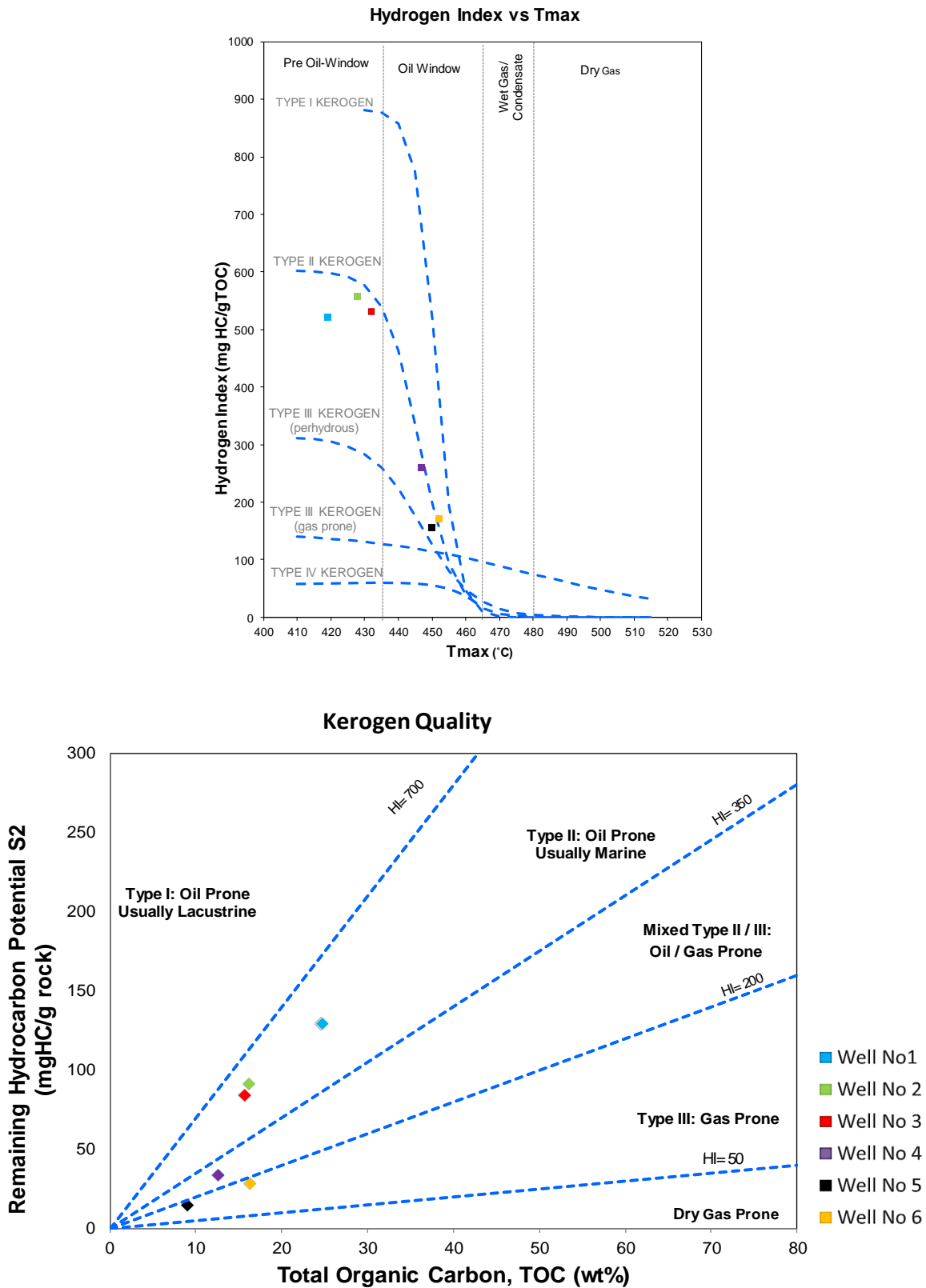


Figure 2-3-3 Rock-Eval results showing Kerogen type based on HI vs. T<sub>max</sub> (up) and S<sub>2</sub> vs. TOC (down). As seen, samples are mainly Type II Kerogen.

### 2-3-1 Raman spectroscopy

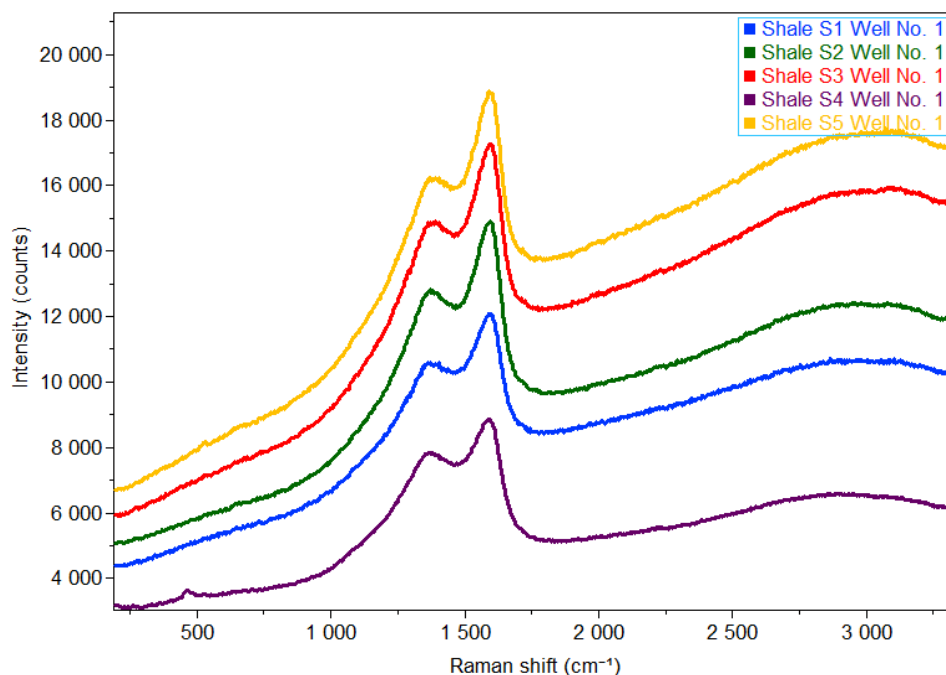
Raman scattering as a function of the molecular vibrations and symmetries of chemical bonds is a method to study carbon atoms. The first step in producing a Raman spectrum is to illuminate the sample with a monochromatic light source (Tuinstra and Koenig, 1970). This illumination causes a Raman shift, since photons (particles of light) exchange part of their energy with molecular vibrations in the material (Wang et al., 1990; Reich and Christian, 2004). The change in energy depends on the frequency of vibration of the molecule(s). Studies have been conducted to assess the structure of carbonaceous material by utilizing Raman spectroscopy (Ferrari and Robertson, 2000; Reich and Thomsen, 2004; Keown et al., 2007; Ammar et al., 2015).

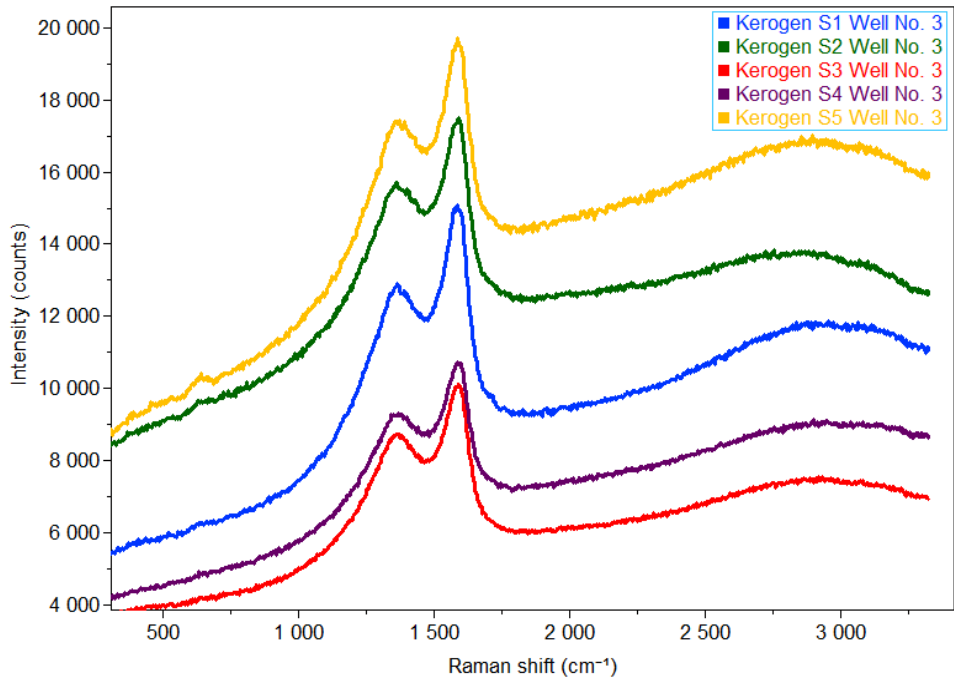
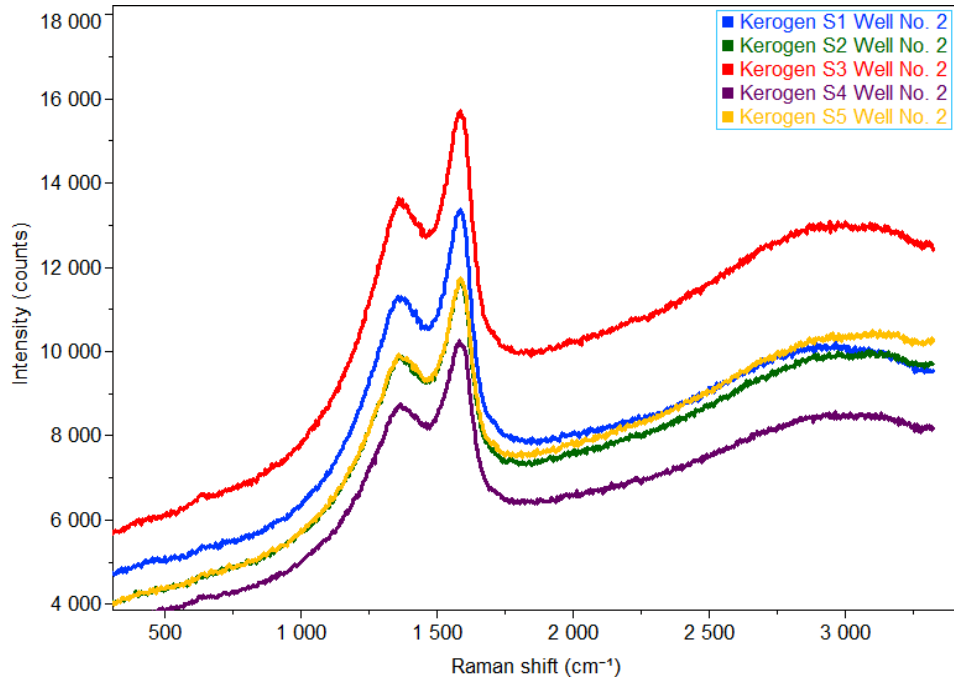
The Raman spectrum of kerogen consists of two main peaks known as G and D bands (Cesare and Maineri, 1999; Marshall et al., 2010; Tuschel, 2013). The G band refers to graphite, which appears at approximately  $1600\text{ cm}^{-1}$  with a sharp peak. The origin of the G band is due to the inplane  $E_{2g2}$  vibrational modes of the carbon atoms in aromatic ring structures ( $sp^2$  carbon) exhibiting  $D_{6h}^4$  symmetry (Sauerer et al., 2017). The D band refers to a disorder in the atoms which appears around  $1350\text{ cm}^{-1}$  as a narrow peak which is a result from the Raman-active  $A_{1g}$  symmetry associated with lattice defects and discontinuities of the  $sp^2$  carbon network (Sauerer et al., 2017). During the process of maturity, kerogen endures aromaticity and tends to be more ordered which finally results in the disappearance of the disorder band. For poorly organized carbonaceous material, additional bands appear around  $1150$ ,  $1350$ ,  $1500$  and  $1620\text{ cm}^{-1}$ . The significance and appearance of the minor bands is not well understood and strongly debated (Beysac et al., 2003). In this study, major bands are only considered.

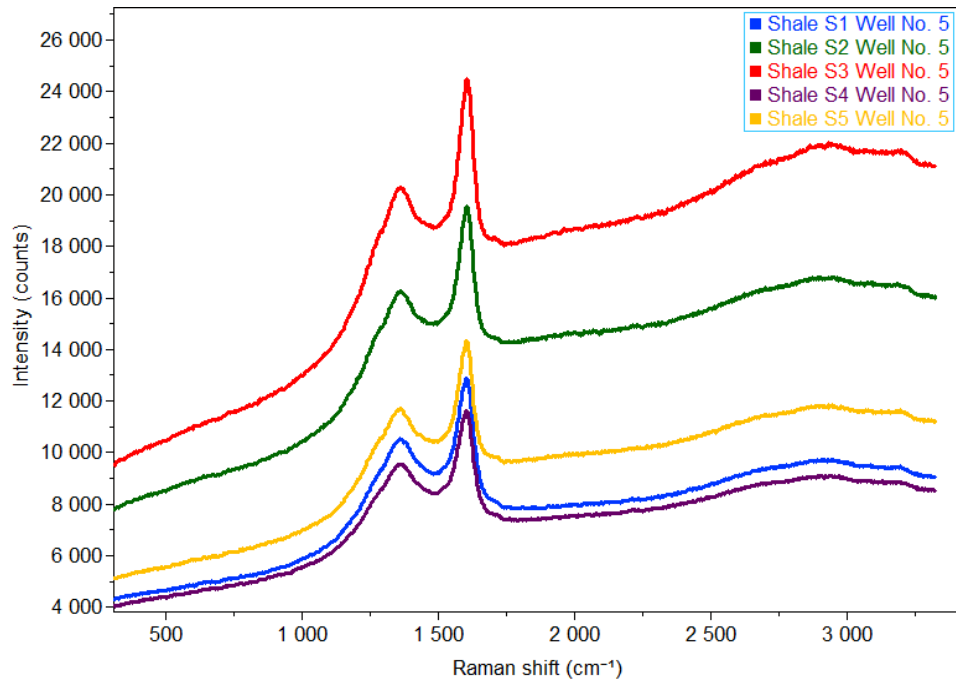
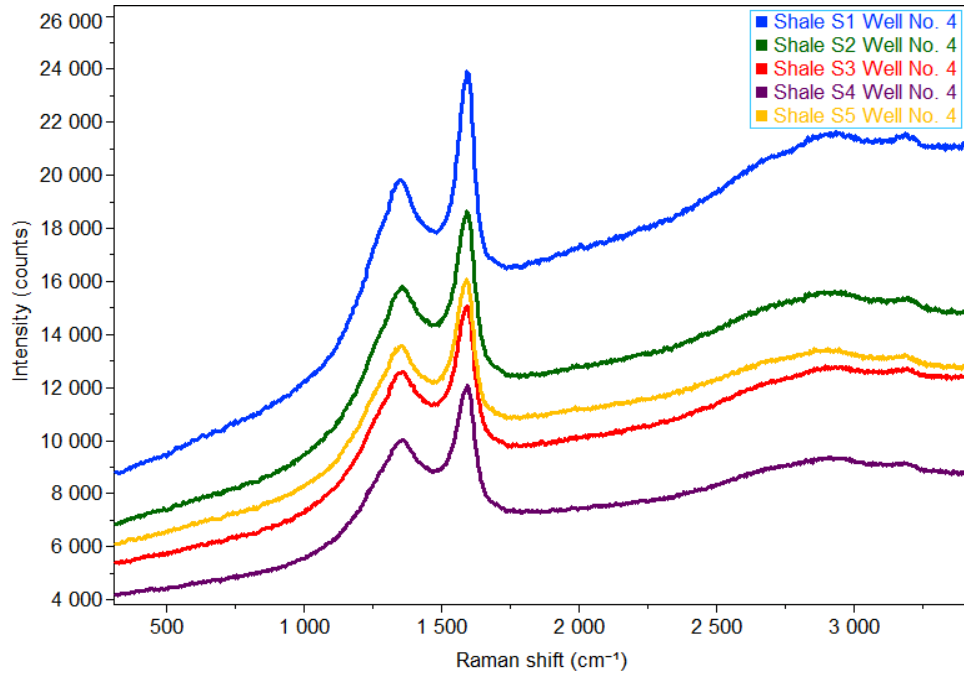
Raman spectra for all samples in this study were acquired by focusing the laser beam on the surface of the samples where organic matter is detected with  $532\text{ nm}$  excitation. The instrument was equipped with an  $50X$  long working distance optical microscope to easily locate the spot that Raman signals are going to be acquired. Scan range of the instrument was  $100\text{ }\mu\text{m} \times 100\text{ }\mu\text{m}$  with step size of  $1\text{ }\mu\text{m}$  with the focal volume of around  $3\text{ }\mu\text{m}^3$ . The high spatial resolution of the equipment enabled us to capture the Raman response of the organic matter with good accuracy. There is not any specific sample preparation such as polishing surfaces necessary. Grinding and polishing has shown to affect the lattice at the surface by creating additional defects, which causes Raman spectrum not to reflect the pristine sample signal (Lünsdorf, 2016).

Representative spectra for samples were obtained by acquiring spectrum from five locations on the surface of the samples, Figure 2-3-4. The fluorescence background noise interferes with Raman signals, specifically with weaker signals (Kelemen and Fang, 2001). The background noise might be due to disordered organic matter, solid bitumen, residual mineral matter, diffuse presence of hydrogen, high sulfur content or generally low thermally mature samples (low mature samples are rich in N, S and O) (Tissot and Welte, 1984). Figure 2-3-5 shows hydrogen-rich low-reflecting solid bitumen under white reflected and UV light (fluorescent). Note the dull yellow fluoresce of the solid bitumen in Figure 2-3-5, which can interfere with signals.

Producing a clear Raman spectrum from some samples was more challenging, such as Well No. 2 in which fluorescence background noise masked the Raman spectrum. In this case, a baseline subtraction processing method should be used to attenuate the noise, Figure 2-3-6. This method allows the high background spectrum to be subtracted from the main spectrum and yields distinguishable bands. To do so, a curve was fitted mathematically through the baseline points on the background noise spectrum (red curve in Figure 2-3-6) and then was subtracted from the main spectrum. Using this mathematical approach provides a flat zero baseline spectrum in order to pick band positions in a more straightforward manner. Mean of spectra for each sample was considered as final spectrum, Figure 2-3-7. Corresponding G and D bands characteristics are summarized in Table 2-3-2.







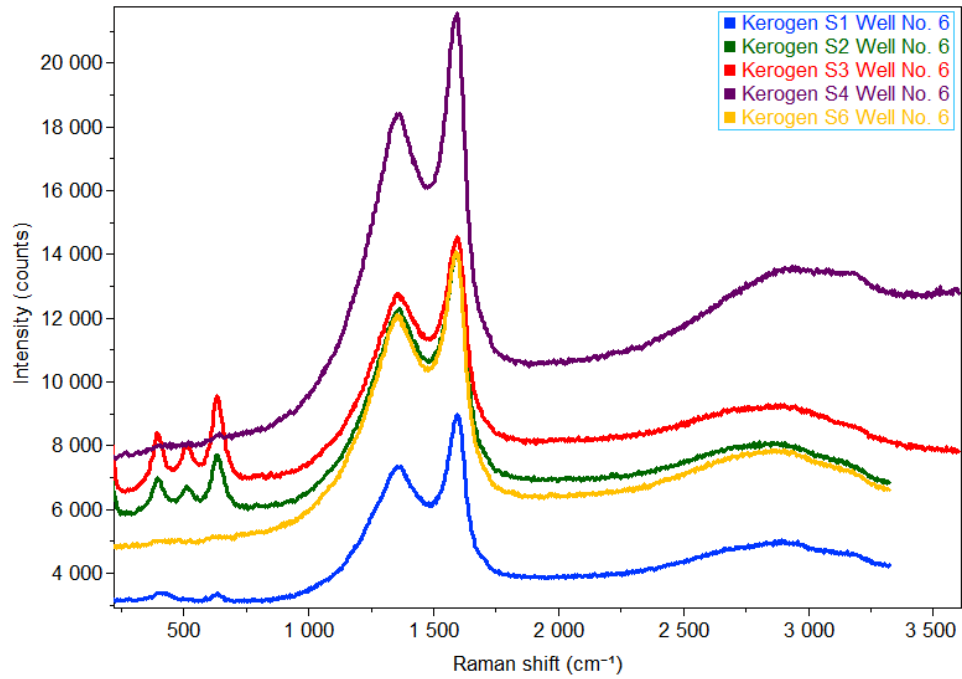


Figure 2-3-4 Raman spectra (intensity versus raman shift) for all samples with five time measurements on five spots.

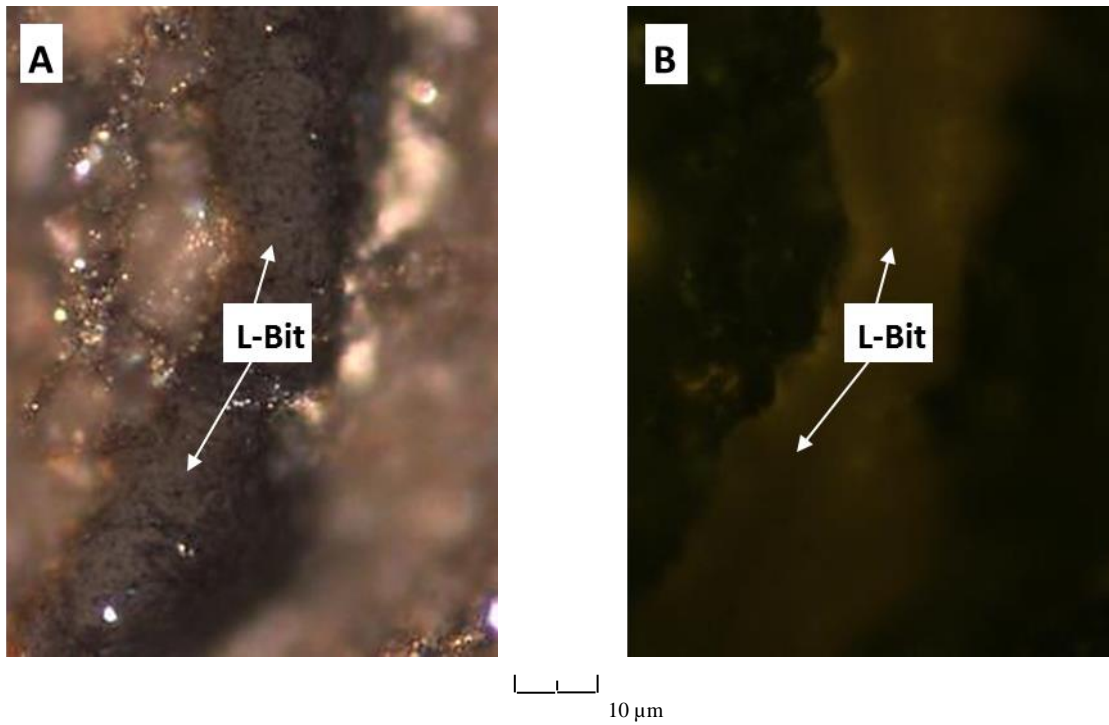


Figure 2-3-5 (A) Hydrogen-rich low-reflecting bitumen (L-Bit) viewed under white reflected light. (B) The same view under UV light (fluorescence). Note the dull-yellow fluorescing of L-Bit.

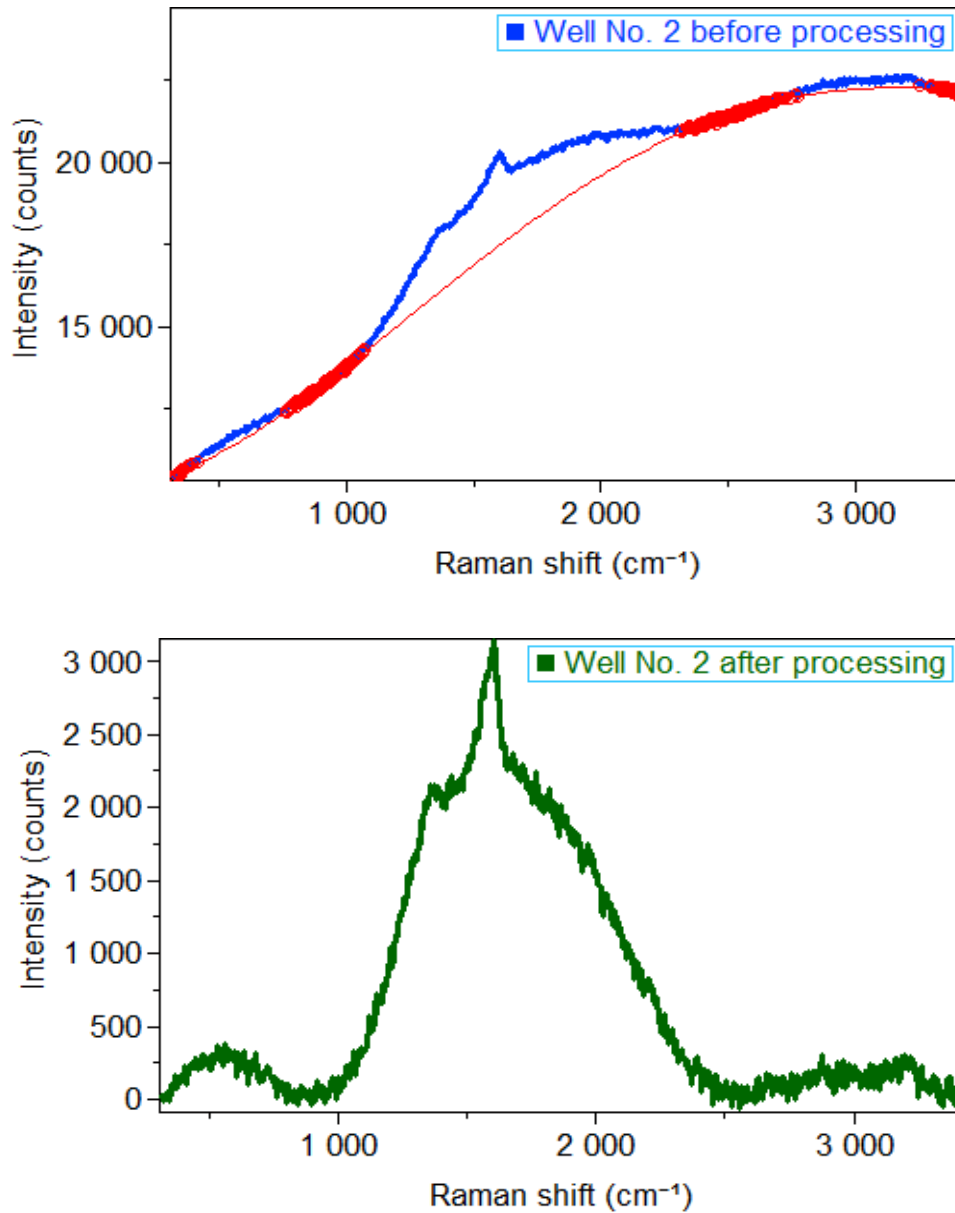


Figure 2-3-6 Sample of Well No. 2: (top) before and (down) after processing by Labspec 6. Baseline subtraction method was used to have a better spectrum for determining band position. Polynomial baseline defined is shown in red, which was subtracted to yield a background free spectrum.

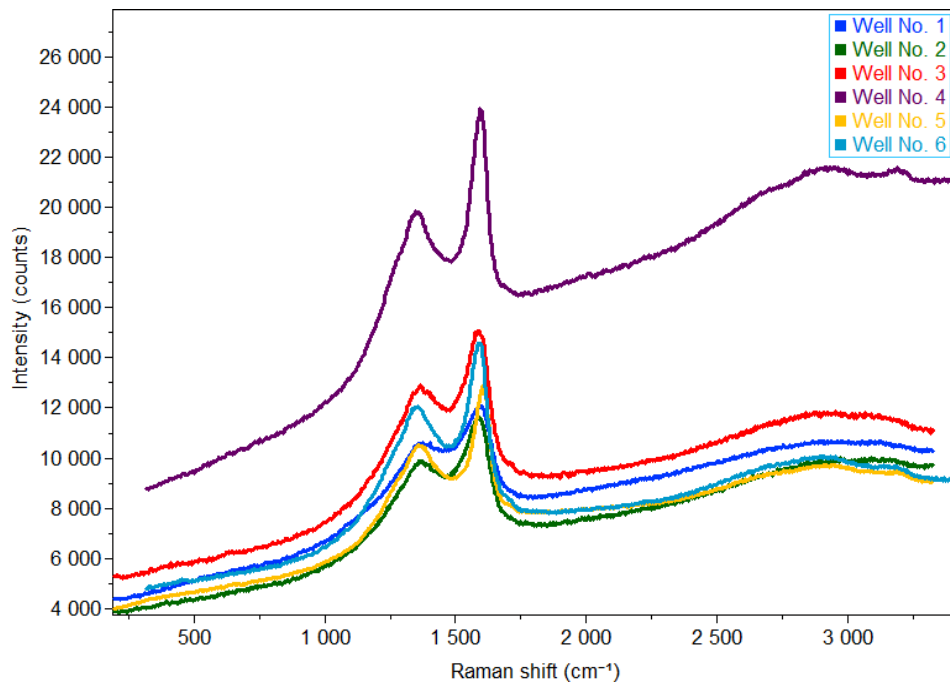
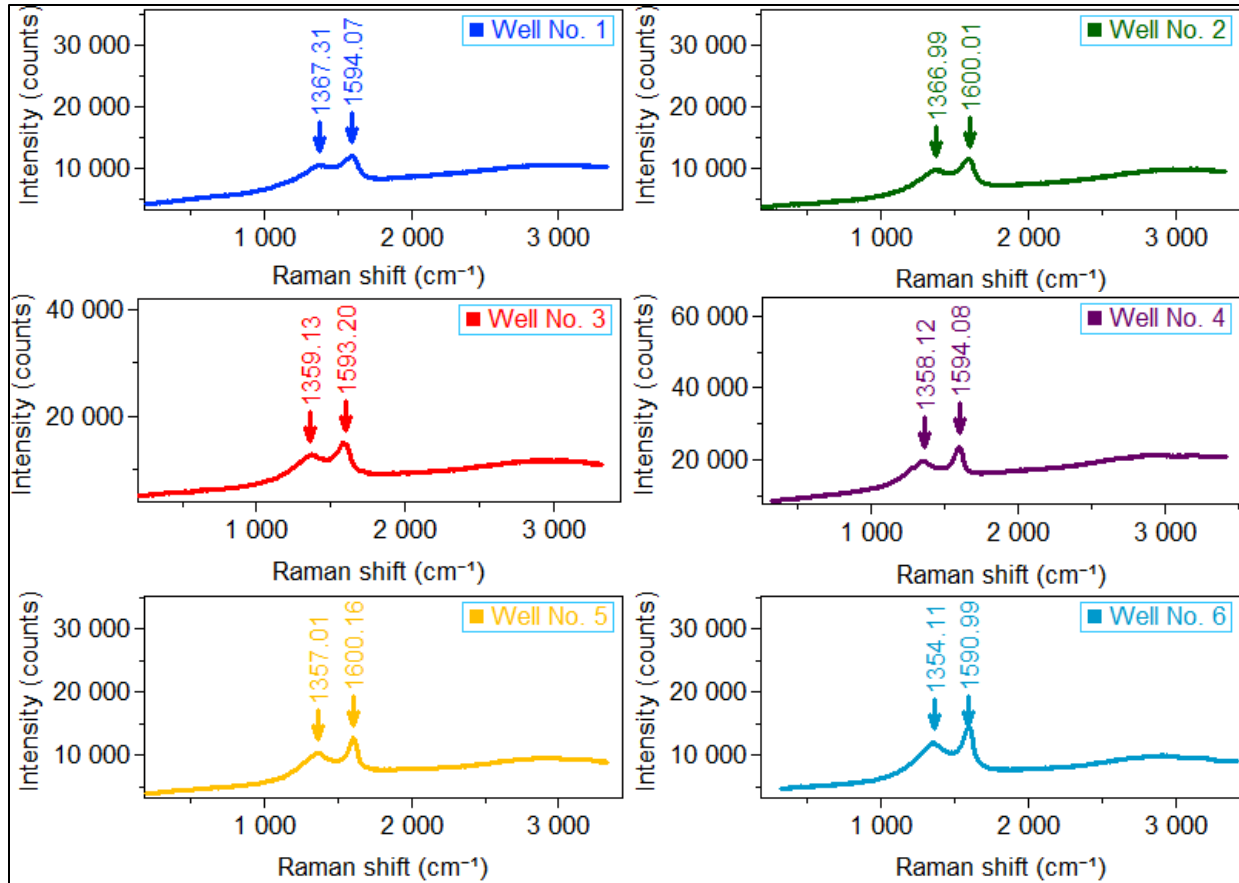


Figure 2-3-7 (top) Mean of five time measurements of Raman spectra of each sample, (bottom) the same data, but spectra are overlaid in one plot for better comparison of band positions.

Table 2-3-2 Bands position of each well.

WELL NO.	D BAND (CM <sup>-1</sup> )	G BAND (CM <sup>-1</sup> )	G-D (CM <sup>-1</sup> )
1	1367.44	1594.09	226.65
2	1367.03	1600.02	232.99
3	1359.21	1593.25	234.04
4	1357.96	1594.03	236.07
5	1356.98	1600.30	243.32
6	1354.01	1590.96	236.95

### 2-3-1 Mechanical Properties

Mechanical properties of the majority of minerals that can be found in mudrocks have been studied, whereas organic matter properties are not well understood or investigated fully. This is mostly due to the restrictions in available equipment that are capable of measuring the moduli of organic matter. VKA (Visual Kerogen Assessment) of samples revealed the existence of various types of minerals along with the organic matter within the matrix, as seen in Figure 2-3-8 from Well No. 4 and 6. It is found that clays followed by siliceous minerals and organic matter constitute the main portion of the sample weight. By comparing Young's modulus of kerogen, reported by Mavko et al. (2009), Kumar et al. (2012) and Eliyahu et al. (2014), with other inorganic parts that exist in mudrocks, it can be inferred that kerogen is the least stiff constituent component, Figure 2-3-9.

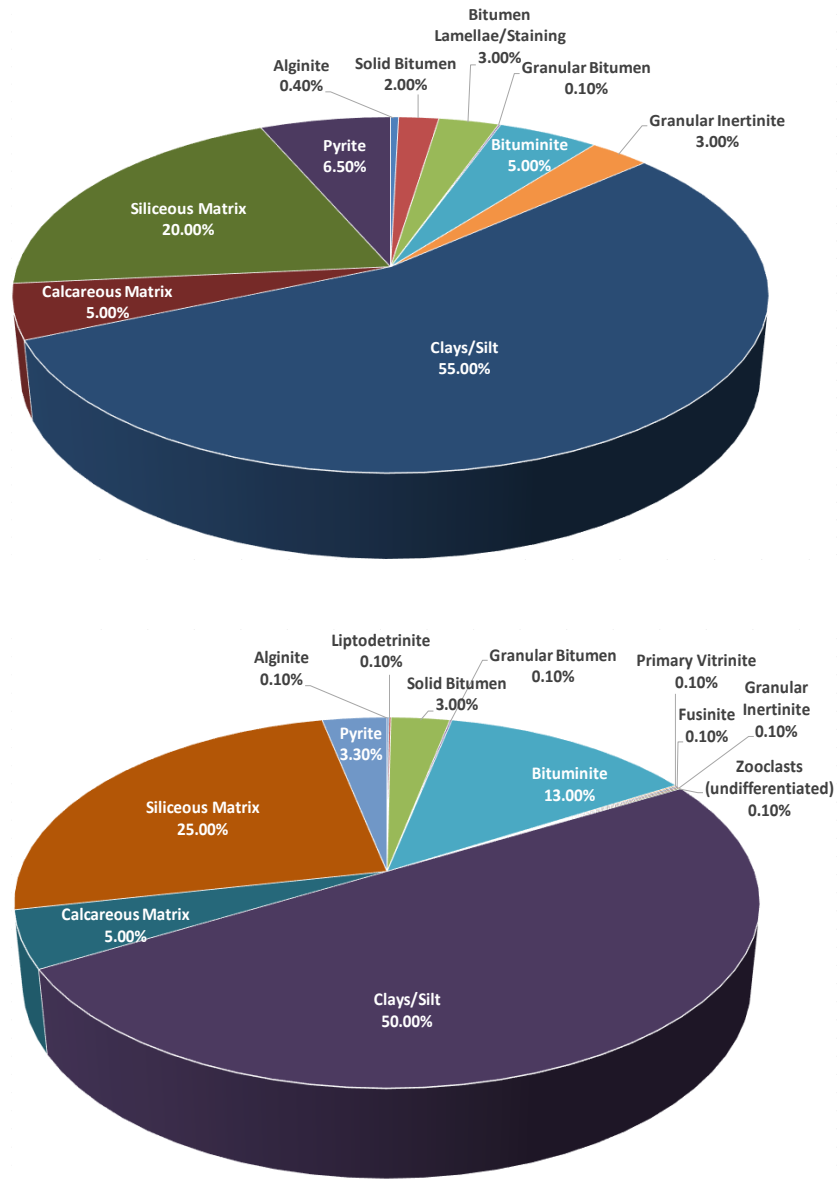


Figure 2-3-8 Visual kerogen assessment on whole-rock sample was performed and the mineral percentage based on visual analysis are approximated for Well No. 4 (top) and Well No. 6 (down).

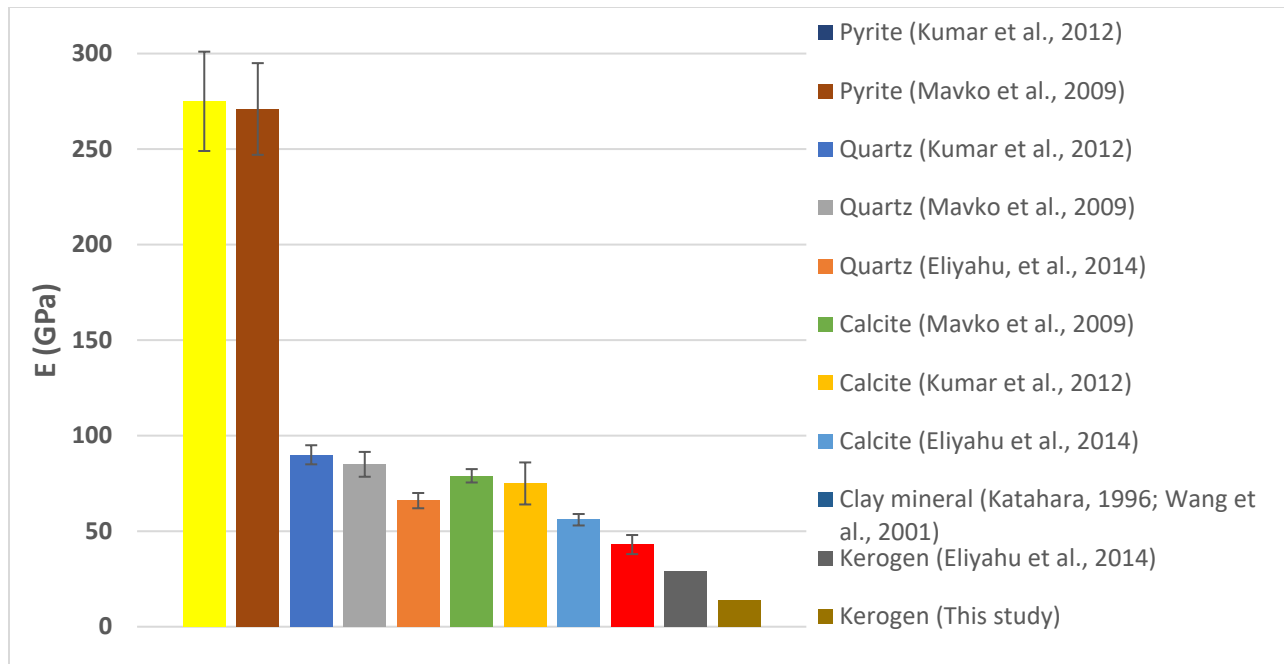


Figure 2-3-9 Young's modulus of some sedimentary rock forming minerals. As it can be seen, kerogen is the least stiff constituent.

Most of the attempts for studying in situ mechanical properties of shale have been made by nanoindentation (Zeszotarski et al., 2004; Ulm and Abousleiman, 2006; Bobko and Ulm, 2008; Ahmadov et al., 2008; Kumar et al., 2012; Shukla, 2013; Zargari et al., 2013). Nanoindentation mostly measures the micron- scale properties rather than true nano-scale ones. In this study, elastic modulus of organic matter was measured by the PeakForce Quantitative Nano-mechanical Mapping (QNM) mode of AFM. PeakForce QNM visualizes, identifies, and maps the elastic properties for every component separately in nanoscale. In this mode of AFM, the tip of the probe is pushed towards the surface of the sample until the PeakForce set point is reached (Li et al., 2017). Then it is withdrawn at the maximum adhesion point. While the probe scanning the surface of the sample, the deflection of the cantilever is measured. The deflection produces a Force-Distance curve which elastic modulus of matter can be calculated from. The details of the measurement technique can be found in the manuscript by Li et al. (2017). The measured Young's modulus for in-situ kerogen for our samples are reported in Table 2-3-3.

Table 2-3-3 Measured Young's modulus for in-situ kerogens in this study (\* Well No. 3 lacks Young's modulus measurement).

WELL NO.	E (GPa)
1	2.5
2	4
3	*

4	4.2
5	16
6	5.35

## 2-4 Results and discussion

### 2-4-1 Raman for Young's modulus prediction

Raman response shows that a trend exists between the depth of the samples and band position (Schito et al., 2017). Figure 2-4-1 shows a decrease of D band positions with depth, from 1367  $\text{cm}^{-1}$  to 1354  $\text{cm}^{-1}$ , while there is no definitive relationship for G band positions with depth, which varies between 1591  $\text{cm}^{-1}$  and 1600  $\text{cm}^{-1}$ . Consequently, band separation depicts an increase with depth from 226  $\text{cm}^{-1}$  to 243  $\text{cm}^{-1}$ . Such trends are attributed to an increase in thermal maturity versus depth. As discussed earlier, previous Raman studies have documented systematic changes in band positions and separation in the Raman spectra for carbonaceous materials as a function of thermal maturity.

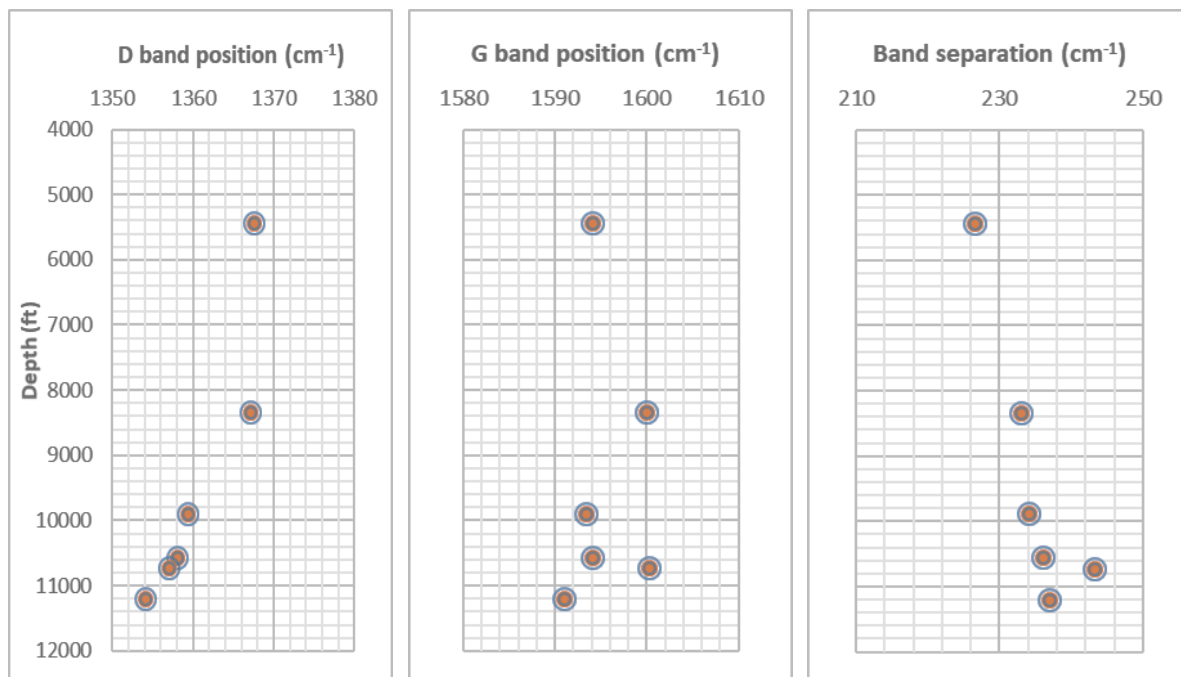
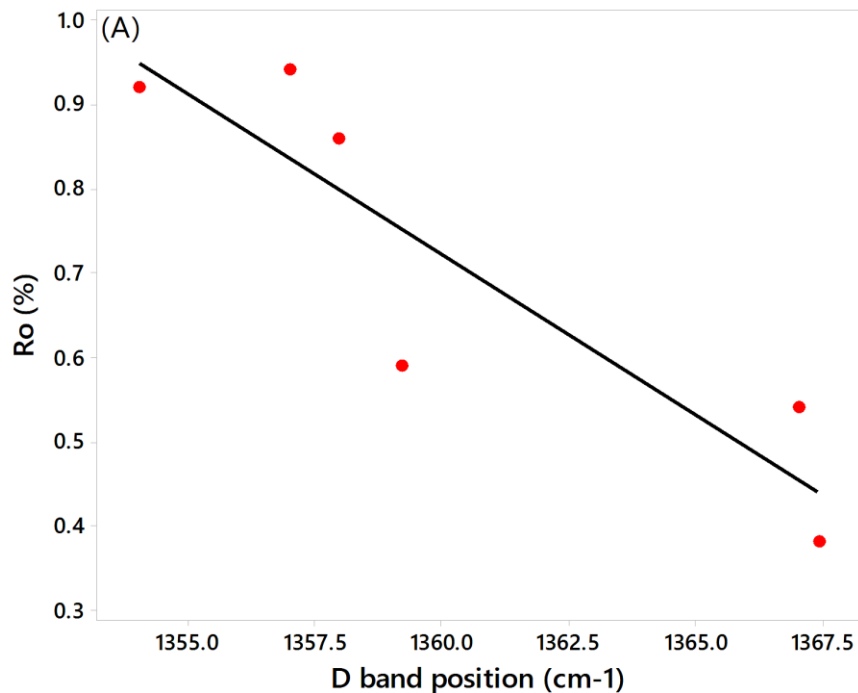
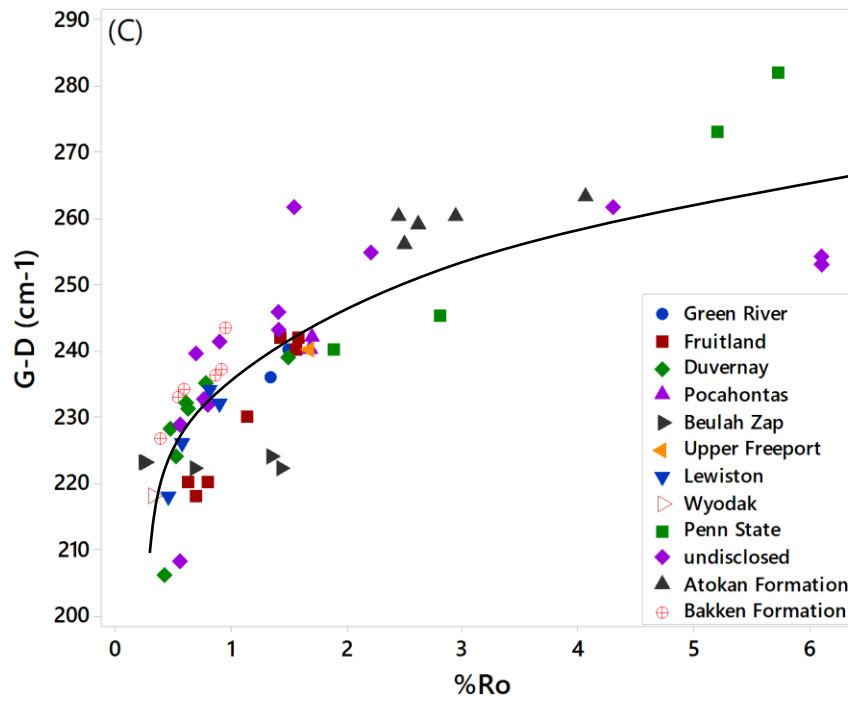
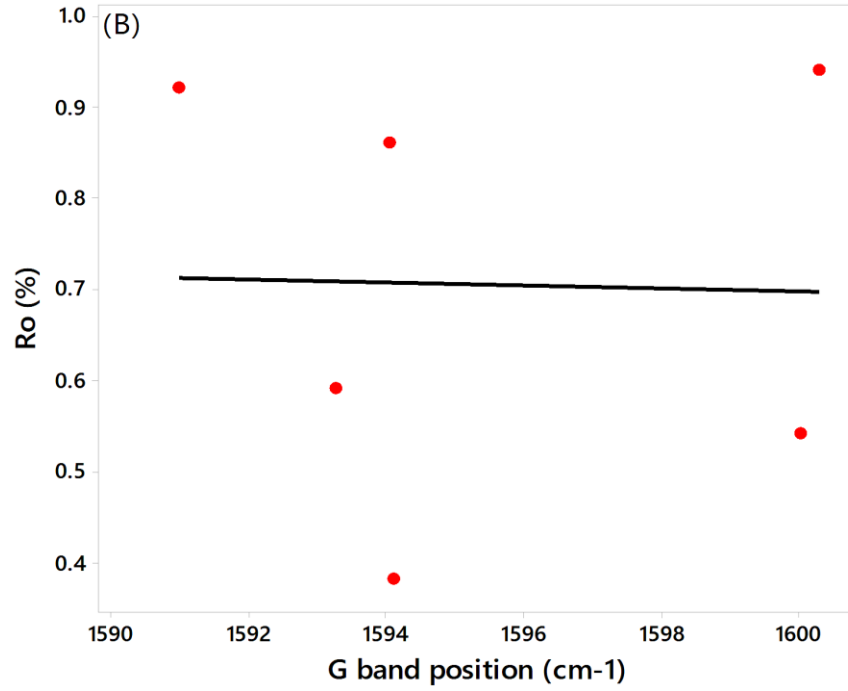


Figure 2-4-1 (left) D band changes with depth, (middle) G band changes with depth, (right) band separation changes with depth. As seen, D band shows decrease, G band no trends, and band separation shows an increase with increasing depth.

It was found that in response to an increase of thermal maturity, a shift in the position of the D band towards lower wavelength would take place, Figure 2-4-2(A). This shift is attributed to the

increase of larger aromatic clusters and more ordered-structure kerogen (Schito et al., 2017). We were not able to distinguish a similar trend for G band position, Figure 2-4-2(B). Such observations are in agreement with those made in earlier studies (Ferrari and Robertson, 2000; Quirico et al., 2005; Guedes et al., 2010). Statistical analysis shows that a logarithmic relationship ( $R^2=74\%$ ) exists between the band separation and %VRo for 11 different data sets including the one from the Bakken from this study, Figure 2-4-2(C). The increase of the band separation with maturity can be referred to the shift in the D band position towards lower wavenumbers without any systematic change in the G band position. At initial stages of maturation, band separation increases with a higher intensity while this rapid growth tapers off over higher maturities. The same trend was found in coal where metamorphism concurrent to maturity at catagenesis happens faster than the metagenesis stage (for both fresh and laboratory matured coal observed by Kelemen and Fang, 2001). Moreover, Raman response can be also related to  $T_{max}$ , which is a thermal maturity index, Figure 2-4-2(D).





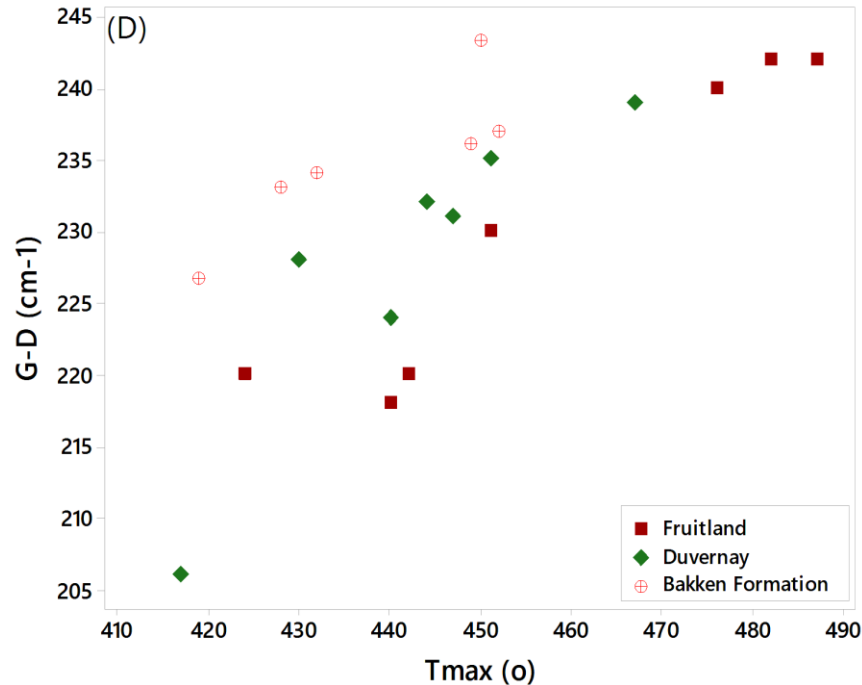
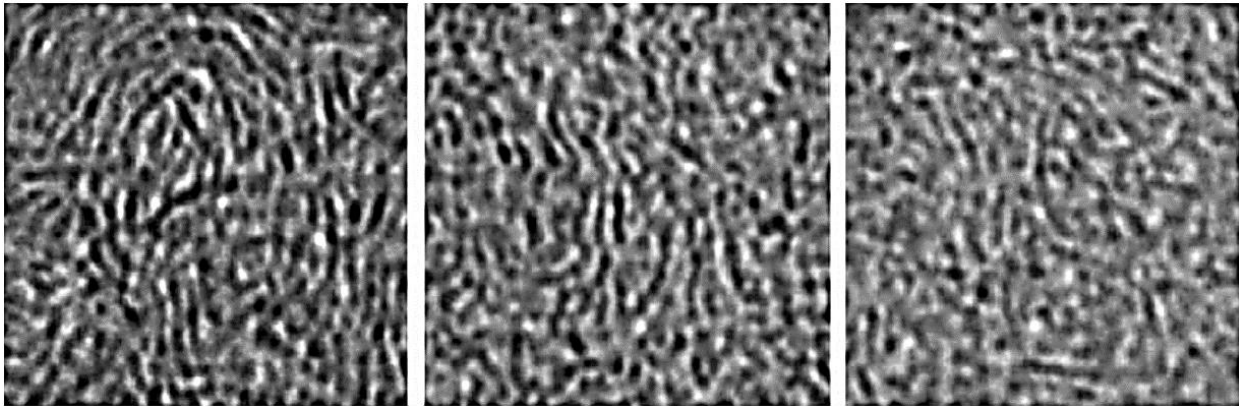


Figure 2-4-2 (A) %Ro versus D band; (B) %Ro versus G band; (C) Band separation versus %Ro for 12 different data sets. There is a nonlinear relationship between Band separation and %Ro. Data are extracted from Spötl et al. (1998), Kelemen and Fang (2001), Sauerer et al. (2017) and results of this study; (D)  $T_{max}$  versus band separation for three different fields. Data are extracted from Sauerer et al. (2017) and results of this study. As seen, by increasing band separation,  $T_{max}$  is also increasing. It verifies Raman as a tool to predict thermal maturities in terms of vitrinite reflectance and  $T_{max}$  from Rock-Eval.

It is believed that in immature source rock samples, the organic matter appears to surround other minerals, becoming a load-bearing part of the rock framework. However, as the maturity increases, kerogen becomes more isolated among other grains (Zargari et al., 2011; Dietrich, 2015) and its Young's modulus increases. Few studies have been able to confirm this interpretation by direct measurement (Emmanuel et al., 2016; Li et al., 2017). In general, comparing %VRo with the measured Young's modulus for the samples in this study, it can be deduced when maturity increases from 0.38% to 0.94% of %Ro, Young's modulus of corresponding samples increases from 2.5 GPa to 16 GPa. This phenomenon can be discussed from a molecular point of view. When maturity happens, kerogen loses heteroatoms (N, S, and O) and its aliphatic carbons (hydrogen-rich groups). The residue is a hydrogen-poor structure molecule, which is dominated by aromatic carbons. During the process of maturation, which increases with burial depth, pore-walls rupture. This sequence promotes the mechanical reorientation and alignment of the aromatic units, thus will facilitate the reduction of defects. This is due to diffusion, elimination of bonding vacancies and annealing of aromatic sheets to triperiodic graphite (Bustin et al., 1995). Therefore, from the

early stages of maturation, the macromolecule arrangements transform gradually from the chaotic and mixed layers to a more ordered arrangement (Pan et al., 2013).

The previously mentioned interpretation is also consistent with observations by Quirico et. al (2005). They analyzed a few samples by high-resolution transmission electronic microscope (TEM), Figure 2-4-3. TEM showed, in the samples with lower maturity, layers are stacked together in groups of two or three with length not more than 1 nm. While, in the more mature samples, not only the number of stacked layers slightly increases but also the length of distorted layers reaches 4 nm (Quirico et al., 2005). Consequently, an increase in thermal maturity leads to a significant change in the molecular structure of kerogen (Emmanuel et al., 2016). This change can easily become apparent in Raman response. Considering the relationship that exists between maturity and Raman spectra and also the alliance between maturity with Young's modulus, Raman data can be used as an indirect method to study the mechanical properties of organic matter with high accuracy.



*Figure 2-4-3 Transmission electronic microscopy (TEM) image of three samples with different maturities. (Left) 7.5 %VRo, (middle) 5.19 %VRo, (right) 2.8 %VRo. Changes in the molecular structure of kerogen at different maturity levels is visible. (Source: From Quirico et. al., 2005).*

Figure 2-4-4 shows Young's modulus versus Raman responses for different samples. It can be seen that the band separation can be fitted to Young's modulus better with a nonlinear correlation, Figure 2-4-2 (B), compared to linear one, Figure 2-4-2 (A). This might be pertinent to the nonlinear correlation between %Ro and the band separation as shown in Figure 2-4-2 (C).

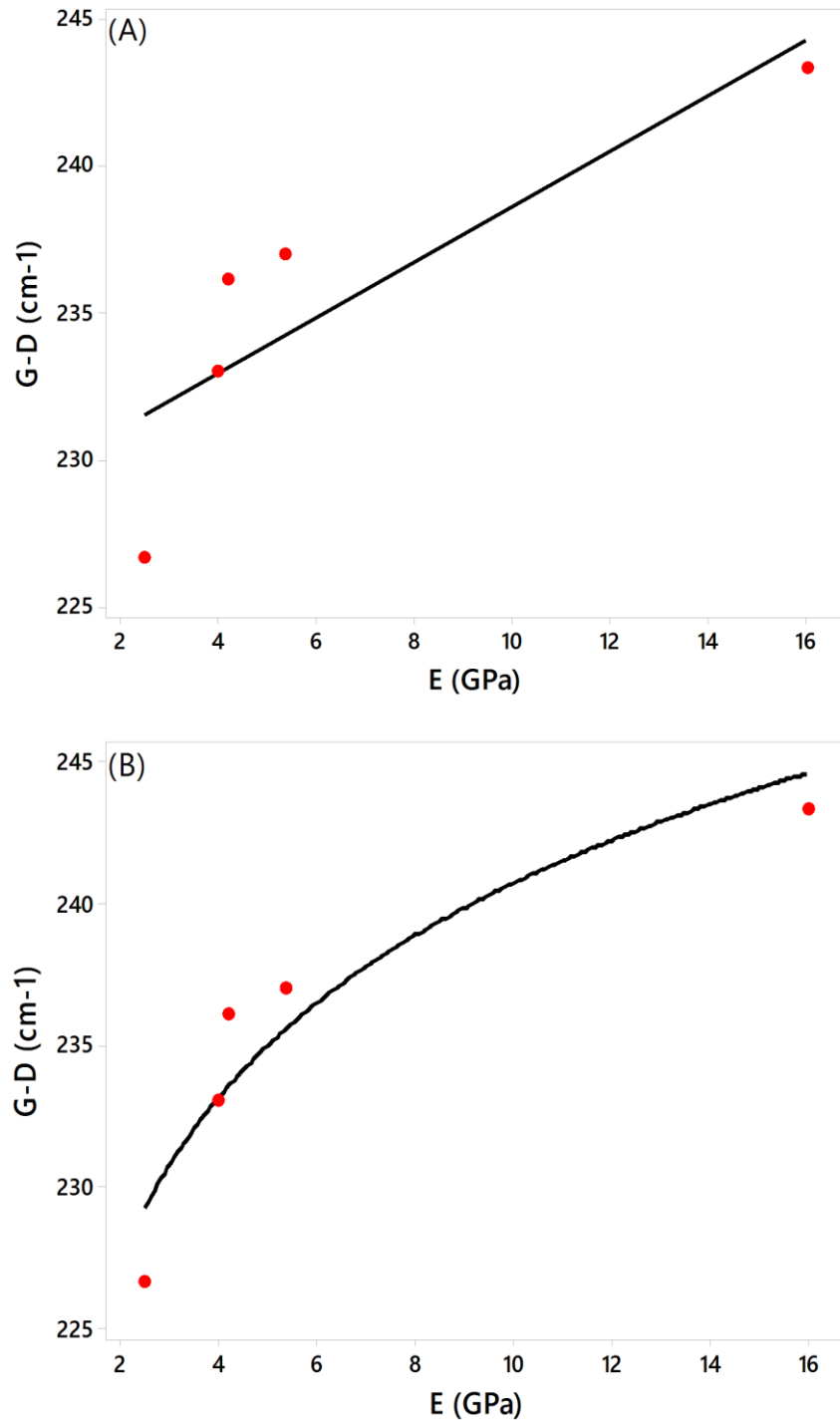


Figure 2-4-4 (A) Young's modulus versus band separation with linear correlation with  $R^2=71\%$ ; (B) Young's modulus versus band separation with non-linear correlation with  $R^2=87\%$ . As seen, non-linear correlation matches better with data which might be related to non-linear correlation between %Ro and band separation.

When %Ro varies from 0.3-3 (initial stages of maturation to late dry gas window), band separation varies approximately between  $210\text{ cm}^{-1}$  to  $255\text{ cm}^{-1}$ , respectively, Figure 2-4-5. Based on non-linear correlation in Figure 2-4-4 (B), Young's modulus (E) can be estimated from 0.32 GPa to 40 GPa.

This is in line with previous results by Eliyahu et al. (2015) who predicted E in the range of 0-25 GPa for maturities up to %Ro=2.1, and Kumar et al. (2012), that presented E of 15-16 GPa for higher maturity and 6-9 GPa for lower maturity samples in their study. Moreover, considering maturity of 2.1 (based on Eliyahu et al., 2015), Figure 2-4-5 assigns corresponding band separation as almost 250  $\text{cm}^{-1}$ . Fitted curve through the data from this study in Figure 2-4-6 and extrapolated to higher values, predicts Young's modulus of around 25 GPa which is in line with what Eliyahu et al., (2015) measured.

Moreover, considering Table 2-3-3, the sample taken from Well No. 3 lacks Young's modulus measurement, whereas, Raman spectroscopy and maturity information are available. Having a band separation of 234  $\text{cm}^{-1}$ , and using curve in Figure 2-4-6, Young's modulus of 4.11 GPa can be predicted for this sample. Considering %Ro of 0.59 for the sample, it should exhibit Young's modulus between the values that were measured for Well No. 2 and Well No. 4 (4 GPa and 4.2 GPa, respectively). Predicted E value for Well No. 3 is represented with a green dot in Figure 2-4-6 and shows the accuracy of method.

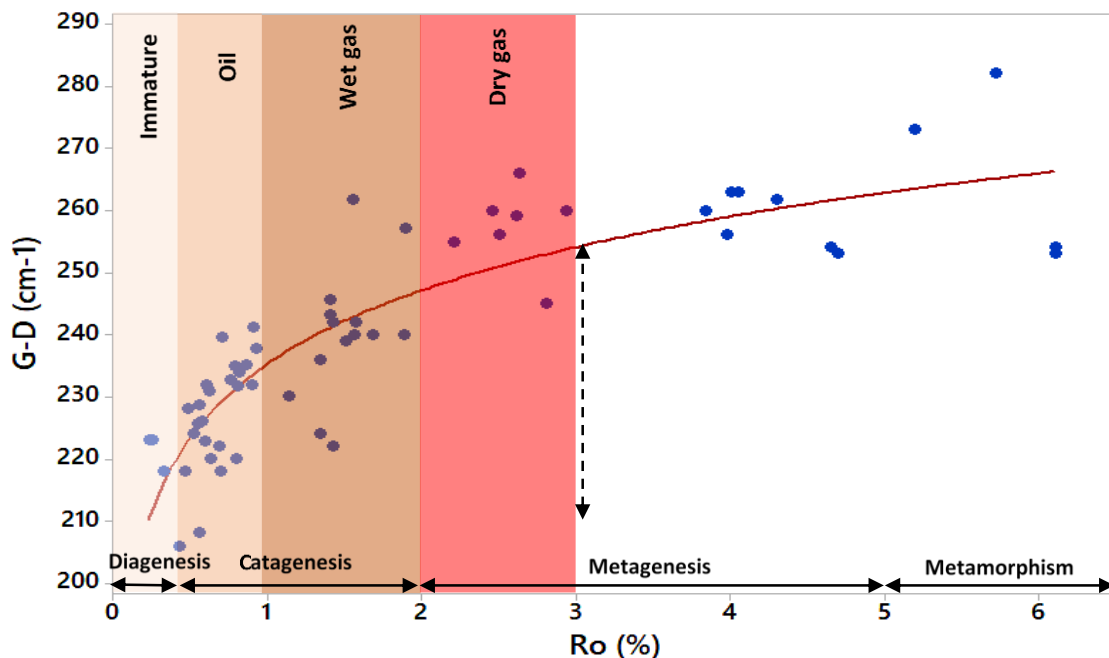


Figure 2-4-5 Band separation versus maturity with general thermal maturity map overlaid. Considering %Ro=3 as the late dry gas window, band separation of kerogen can vary from 210-255  $\text{cm}^{-1}$ . Samples are the same as Figure 13(C).

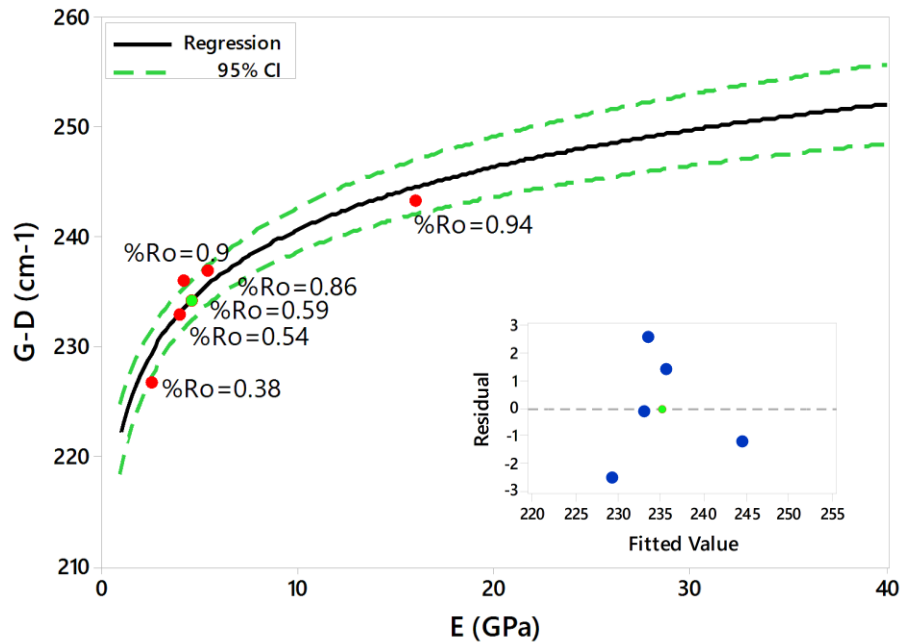


Figure 2-4-6 Non-linear correlation between band separation and Young's modulus, with 95% confidence interval of regression and error profile. Predicted value for Well No.3 is shown in green dot.

The proposed method is a fast and non-destructive way to understand kerogen's modulus of elasticity by using Raman spectroscopy and considering its thermal maturity. High resolution for the laser focal volume of the Raman equipment allows for the analysis of small volumes of dispersed organic material with good precision. Furthermore, the minimal and rapid sample preparation for Raman spectroscopy enables us to evaluate both maturity and elastic properties of samples at the wellsite for real-time measurements. In future studies, the mechanical properties of more samples with higher thermal maturities is suggested.

## 2-4-2 Numerical simulation

In this section, the method in the previous section will be used to see the impact of the OM on hydraulic fracturing. In order to create hydraulic fractures in a target formation, injection of a compressible fluid should be done with an injection rate of  $Q_{Inj}$ . The accumulation of the injected fluid in the bottom of the well leads bottomhole pressure to be increased as time proceeds. The following Equations 1 and 2 represent the bottomhole injection rate ( $Q_{BH}$ ) and pressure increase ( $\Delta P_{BH}$ ), respectively.

$$Q_{BH} = Q_{Inj} \left( 1 - \frac{P_{BH} - P_{Atm}}{K_f} \right) \quad (1)$$

$$\Delta P_{BH} = \frac{K_f * Q_{BH}}{Q_{BH} + V_{Well} + V_{Frac}} \quad (2)$$

where  $K_f$ ,  $P_{Atm}$  and  $P_{BH}$  are fluid bulk modulus, atmospheric pressure (14.7 psi) and bottomhole pressure.  $V_{Well}$  is the volume of fluid stored in the well which can be obtained through multiplying cross-section area of the wellbore by length of the well;  $V_{Frac}$  is representative of the volume of the fracture which can be estimated by Equation 3.

$$V_{Frac} = F_A * F_L * h \quad (3)$$

In this equation,  $F_A$  is the averaged aperture of fracture,  $F_L$  is the length of fracture and  $h$  is the length of the injected well section.

Fractures initiate in the target formation when wellbore fluid pressure exceeds fracture initiation pressure. The orientation of created fractures is generally perpendicular to the minimum principal stress. On the other hand, if the injection pressure is unloaded from the rock by removing the fluid from the wellbore, the created fractures will be returning to the initial situation and finally will be closed. Thus, proposing proppant to the hydraulic fracturing fluid is a must to retain the fracture open or to diminish the rate of fracture blocking. The total work amount required by fracturing fluid to enlarge the well and to open the fractures can be calculated by Equation 4.

$$W = \sum_{i=1}^N (2\pi r h * P_{BH} * \Delta r + P_{Frac} * F_L * h * \Delta F_A) \quad (4)$$

where  $N$  is the number of the calculation iterations;  $\Delta r$  and  $\Delta a$  are the amount of change in wellbore radius and fracture aperture during one step, respectively. It should be noted that both the hydraulic fracture geometry and wellbore radius ( $r$ ) will alter as bottomhole pressure changes. Therefore,  $P_{BH}$  should be updated after each iteration as shown in Equation 5.

$$P_{BH}^{j+1} = P_{BH}^j - K_f \frac{V_{well}^{j+1} + V_{Frac}^{j+1} - V_{well}^j - V_{Frac}^j}{V_{well}^j + V_{Frac}^j} \quad (5)$$

Where indices  $j + 1$  and  $j$  are the number of new and old values after one iteration. The updated values are then substituted in Equations 1 and 2 for starting the next calculation iteration.

In this paper, the numerical simulation calculation procedure was implemented by FISH function in Flac 3D software presented by ITASCA. First, a model of the reservoir was created in the

software and its size extended to be almost 60 times of the well radius (5 inch) in order to suppress the artifacts generated due to the end effects of the model. Moreover, grids get smaller as they get closer to the wellbore to increase the accuracy of calculation around the wellbore. Considering the symmetry of the geometry and loading condition only one-quarter of the model was considered for computations which also reduces the run time. Then the quarter portion was copied in a way to make a full model.

In the next step, the mechanical properties of the reservoir rock which presented in Table 2-4-1, were assigned to the created model. These properties were assumed as an average value of corresponding data Bakken formation acquired from logs and lab experiments. It should be noted, due to low permeability of shale formations, the rock was considered impermeable during the simulation process. Negligible communication between fracturing fluid and the fluid existed inside the rock pores was another assumption during the hydraulic fracturing. Table 2-4-1 represents the elastic and mechanical properties of the modeled formation as well as pore pressure and principal stresses exerted on the rock. All properties present the average values measured from top to bottom of the Bakken formation. The Young modulus presented here for the kerogen was obtained from AFM experiment performed on the organic matter.

*Table 2-4-1 Properties assigned to the modeled Formation*

Bulk density (g/cc)	<b>2.6</b>
Shear modulus (GPa)	<b>8.5</b>
Bulk modulus (GPa)	<b>15</b>
Young's modulus of rock (GPa)	<b>20</b>
Tensile strength of rock (MPa)	<b>17.5</b>
Young's modulus of kerogen (GPa)	<b>9</b>
Vertical stress (psi)	<b>9200</b>
Minimum horizontal stress (psi)	<b>8000</b>
Pore pressure (psi)	<b>5500</b>

After the model was built, it was run and solved to reach the initial equilibrium. Then two different scenarios were conducted to demonstrate how organic matter can affect the hydraulic fracturing operation by running two models with and without organic matter. In the next section, these two scenarios were presented in detail and the results were compared.

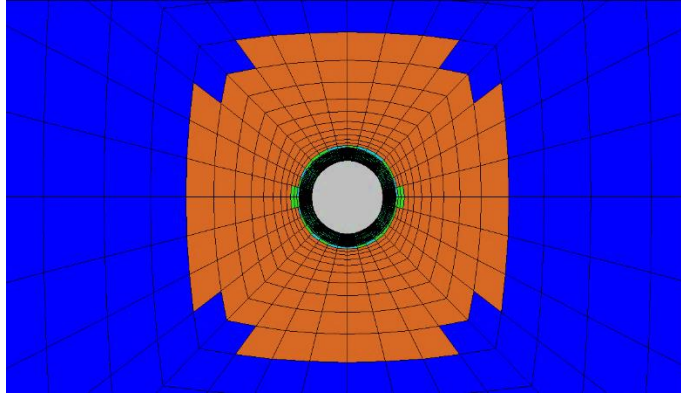


*Figure 2-4-7 Created plastic zone around the wellbore.*

To increase production through created hydraulic fractures, they need to be maintained open by placing proppant into the fractures. Thus, the fracture aperture should be bigger than the average size of the proppant particles, 0.04 inch; although fracture opening shifts to small values (micro inch) towards the tip of the fracture. Fracture can also extend in order of hundreds of meters after initiation.

Since kerogen exhibits strain-softening response under loading condition, shale formation containing high content of kerogen demonstrates higher tensile strength. In addition, tensile strength of kerogen rich shale decreases slightly after fracture initiation near the wellbore in comparison with the case of shale formation without kerogen which shows rapid decline towards zero after fracture opening.

To investigate the effect of kerogen existed in shale formation on fracture opening process, two different cases were considered and introduced to simulation. The former which simulates shale formation without organic matter, the tensile strength of the rock in the fracturing segment was assigned to 5 MPa and this property falls immediately to zero after the fracture originates. The latter which demonstrates kerogen rich shale, the tensile strength of kerogen obtained from the literature (Abousleiman et al. 2007; Ortega et al., 2007; Hull et al., 2015) was entered into simulation procedure. It should be noted that in the literature kerogen merely tested and a value over 130 Mpa was reported for tensile strength. Considering a volume fraction of 1:4 for organic matter to matrix for Bakken Formation, approximately an initial tensile strength value of 33 Mpa was considered for the bulk sample.

Through simulation process, bottomhole pressure, volume of injected fluid, fracture opening, and total fluid mechanical work as long as fracture width were recorded. Figure 2-4-8 illustrates the changes of bottomhole pressure with time implemented on the aforementioned two cases until the 0.04 inch fracture aperture was obtained by fluid injection. In the case of kerogen rich shale, which the model has higher fracture strength due to the presence of organic matter, fluid with higher bottomhole pressure should be injected to originate the fracture. On the contrary, in another scenario, bottomhole pressure is required to be maintained slightly higher than minimum horizontal stress during the procedure of opening the hydraulic fractures. As can be seen in Figure 2-4-8, after initiation of the fracture, bottomhole pressure starts decreasing over time due to continuous decay of tensile strength of the minerals placed in sides of the fracture.

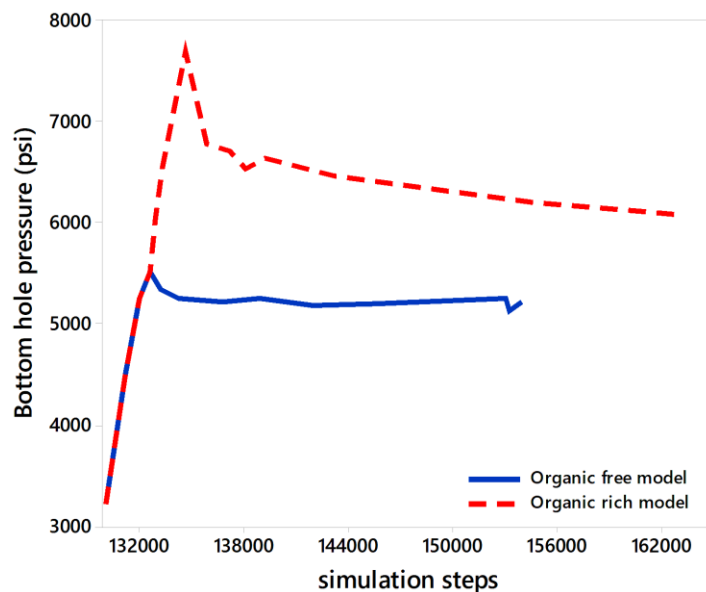


Figure 2-4-8 Changes of bottomhole pressure during hydraulic fracturing over simulation time steps.

Figure 2-4-9 illustrates the required volume of fluid which should be injected to initiate a fracture with 100 ft length and up to 0.04 inch average aperture. With comparison between curves of the two different cases shown in Figure 2-4-9, organic rich model needs more fluid to be injected until the desired fracture will be initiated. The strain-softening response of kerogen detected by AFM and nanoindentation tests in the literature can answer the difference in the required volume of injected fluid in the fracturing process.

Figure 2-4-10 also shows the total required mechanical work done by injected fluid to enlarge the wellbore wall and fracture aperture up to 0.04 inch. As Figure 2-4-10 shows, the works which

should be done for opening the fracture in kerogen rich shale is almost two times of the one in the case of kerogen free model.

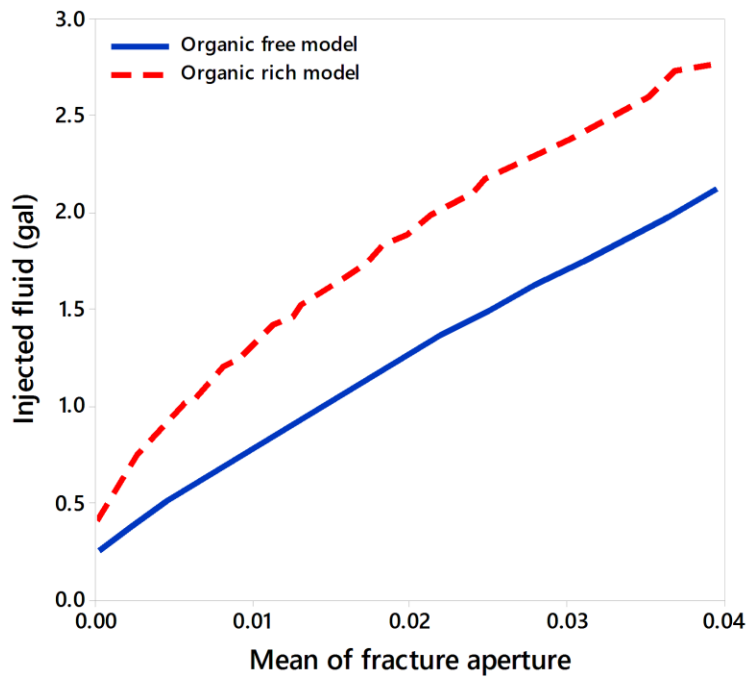


Figure 2-4-9 Injected fluid volume versus averaged fracture aperture in fracture extension test.

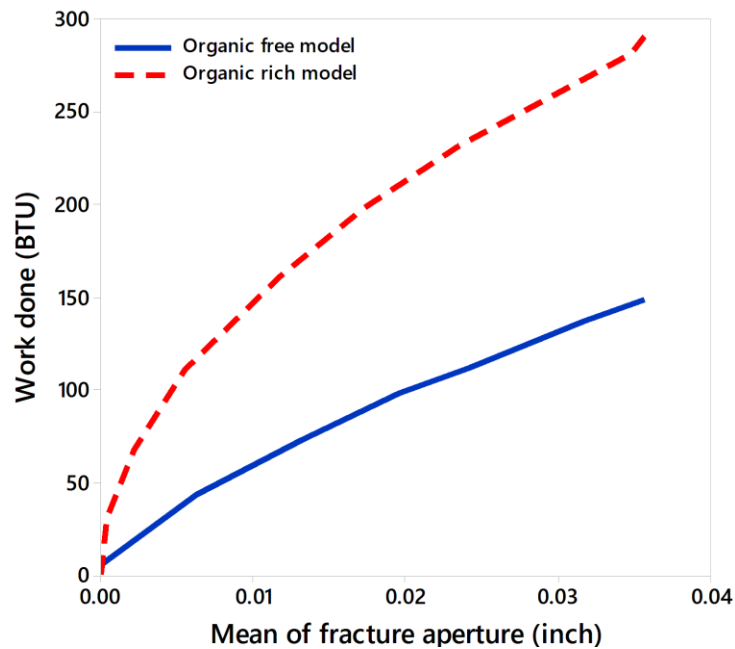


Figure 2-4-10 Total mechanical work which should be done to enlarge the fracture aperture.

## 2-5 Conclusion

Results from this study shows:

- Raman spectroscopy has the potential to understand Young's modulus of organic matter.
- Organic matter is the least stiff constitute of mud rock
- Due to strengthening effect of kerogen, higher bottomhole pressure is required to open the fracture in kerogen rich shales.
- The strain-softening response of kerogen under loading condition implies that in the kerogen rich shale the tensile strength along the fracture does not decrease as much as in the kerogen free shale.
- In the case with kerogen, bottomhole pressure starts decreasing over time due to continuous decay of tensile strength of the minerals placed in sides of the fracture.
- In order to induce the same size of fracture in organic rich shale, more fluid is required to be injected compared to organic free case. Accordingly, total mechanical work is also more in case with kerogen.

In this study, we examined samples taken from the Upper and Lower members of the Bakken Formation from six different wells drilled in Williston Basin, ND. Rock-Eval 6 pyrolysis and optical microscopy analysis showed the presence of oil-prone Type II marine kerogen. Solid bitumen reflectance was used to determine the level of thermal maturity, which varied from immature to peak oil window. Raman spectroscopy was employed, as a potential indirect method, to predict the maturity and Young's modulus of the organic matter. Based on the results, the following conclusions were made:

- Raman spectroscopy, which is based on molecular vibrations, was able to detect molecular alterations in the organic matter as it undergoes changes in thermal maturity. Therefore, thermal maturity of the samples can be related to their Raman spectra.
- As maturity increases, major Raman signals start to separate from one another. This separation occurs between the G and D bands. The G band does not move significantly while the D band shifts towards lower wavelengths. From this observation, it is concluded that this specific Raman response directly correlates not only to the geochemical characteristics of the organic matter but also to the maturity of each sample.

- As thermal maturity increases, mechanical properties (e.g., elastic modulus) of organic matter alter. This alteration in elastic properties is due to macromolecular arrangements, transforming gradually from chaotic and mixed-layered to a better-ordered molecular structure.
- Comparing samples of different maturity levels to their corresponding predicted Young's moduli from Raman spectroscopy, it was observed that Young's modulus increases as maturity increases.
- Young's modulus was correlated to band separation by considering through a nonlinear relationship that takes into account the thermal maturity of the samples. However, we were not able to develop a robust connection between individual G and D band wavelengths with Young's modulus.
- Raman spectroscopy was able to estimate the Young's modulus of organic matter. It showed 0.32 GPa in the initial stages of maturation to 40 GPa in the late dry gas window.

## 2-6 References

Abousleiman, Younane N., Minh Ha Tran, Son Hoang, Christopher P. Bobko, Alberto Ortega, and Franz-Joseph Ulm. "Geomechanics field and laboratory characterization of the Woodford Shale: The next gas play." In SPE Annual Technical Conference and Exhibition. Society of Petroleum Engineers, 2007.

Aghajanpour, A., Fallahzadeh, S.H., Khatibi, S., Hossain, M.M., Kadkhodaie, A., 2017. Full waveform acoustic data as an aid in reducing uncertainty of mud window design in the absence of leak-off test. *Journal of Natural Gas Science and Engineering* 45, 786-796.

Ahmadov, R., Vanorio, T., Mavko, G., 2008. Confocal Laser Scanning and Atomic-Force Microscopy in Estimation of Elastic Properties of Organic-Rich Rocks, Bazhenov Formation, Russia, AGU Fall Meeting Abstracts.

Alexeyev, A., Ostadhassan, M., Mohammed, R.A., Bubach, B., Khatibi, S., Li, C., Kong, L., 2017. Well Log Based Geomechanical and Petrophysical Analysis of the Bakken Formation.

Ammar, M., Galy, N., Rouzaud, J., Toulhoat, N., Vaudey, C., Simon, P., Moncoffre, N., 2015. Characterizing various types of defects in nuclear graphite using Raman scattering: Heat treatment, ion irradiation and polishing. *Carbon* 95, 364-373.

## Chapter 2

Aoudia, K., Miskimins, J.L., Harris, N.B., Mnich, C.A., 2010. Statistical analysis of the effects of mineralogy on rock mechanical properties of the Woodford Shale and the associated impacts for hydraulic fracture treatment design, 44th US Rock Mechanics Symposium and 5th US-Canada Rock Mechanics Symposium. American Rock Mechanics Association.

Babaei, A., Ghanbari, A., Vakili-Tahami, F., 2015. Size-Dependent Behavior of Functionally Graded Micro-Beams, Based on the Modified Couple Stress Theory. *Technology* 3, 364-372.

Babaei, A., Noorani, M.-R.S., Ghanbari, A., 2017. Temperature-dependent free vibration analysis of functionally graded micro-beams based on the modified couple stress theory. *Microsystem Technologies*, 1-12.

Behar, F., Beaumont, V., Penteadó, H.D.B., 2001. Rock-Eval 6 technology: performances and developments. *Oil & Gas Science and Technology* 56, 111-134.

Beysac, O., Goffé, B., Chopin, C., Rouzaud, J., 2002. Raman spectra of carbonaceous material in metasediments: a new geothermometer. *Journal of metamorphic Geology* 20, 859-871.

Beysac, O., Goffé, B., Petitet, J.-P., Froigneux, E., Moreau, M., Rouzaud, J.-N., 2003. On the characterization of disordered and heterogeneous carbonaceous materials by Raman spectroscopy. *Spectrochimica Acta Part A: Molecular and Biomolecular Spectroscopy* 59, 2267-2276.

Bobko, C., Ulm, F.-J., 2008. The nano-mechanical morphology of shale. *Mechanics of Materials* 40, 318-337.

Bustin, R., 1996. Mechanisms of graphite formation from kerogen: Experimental evidence, *Fuel and Energy Abstracts*. Elsevier, p. 187.

Cesare, B., Maineri, C., 1999. Fluid-present anatexis of metapelites at El Joyazo (SE Spain): constraints from Raman spectroscopy of graphite. *Contributions to Mineralogy and Petrology* 135, 41-52.

## Chapter 2

Cheshire, S., Craddock, P.R., Xu, G., Sauerer, B., Pomerantz, A.E., McCormick, D., Abdallah, W., 2017. Assessing thermal maturity beyond the reaches of vitrinite reflectance and Rock-Eval pyrolysis: A case study from the Silurian Qusaiba formation. *International Journal of Coal Geology* 180, 29-45.

Diessel, C., Brothers, R., Black, P., 1978. Coalification and graphitization in high-pressure schists in New Caledonia. *Contributions to Mineralogy and Petrology* 68, 63-78.

Dietrich, A.B., 2015. The impact of organic matter on geomechanical properties and elastic anisotropy in the Vaca Muerta Shale. Colorado School of Mines. Arthur Lakes Library.

Eliyahu, M., Emmanuel, S., Day-Stirrat, R.J., Macaulay, C.I., 2015. Mechanical properties of organic matter in shales mapped at the nanometer scale. *Marine and Petroleum Geology* 59, 294-304.

Emmanuel, S., Eliyahu, M., Day-Stirrat, R.J., Hofmann, R., Macaulay, C.I., 2016. Impact of thermal maturation on nano-scale elastic properties of organic matter in shales. *Marine and Petroleum Geology* 70, 175-184.

Espitalie, J., Deroo, G., Marquis, F., 1985. Rock-Eval pyrolysis and its applications. *Revue De L Institut Francais Du Petrole* 40, 563-579.

Ferralis, N., Matys, E.D., Knoll, A.H., Hallmann, C., Summons, R.E., 2016. Rapid, direct and non-destructive assessment of fossil organic matter via microRaman spectroscopy. *Carbon* 108, 440-449.

Ferrari, A.C., Robertson, J., 2000. Interpretation of Raman spectra of disordered and amorphous carbon. *Physical review B* 61, 14095.

Gerhard, L.C., Anderson, S.B., Fischer, D.W., 1990. Petroleum geology of the Williston Basin. Interior cratonic basins: AAPG Memoir 51, 507-559.

Ghanbari, A., Babaei, A., Vakili-Tahami, F., 2015. Free Vibration Analysis of Micro Beams Based on the Modified Couple Stress Theory, Using Approximate Methods. *Technology* 3, 136-143.

## Chapter 2

Guedes, A., Valentim, B., Prieto, A., Noronha, F., 2012. Raman spectroscopy of coal macerals and fluidized bed char morphotypes. *Fuel* 97, 443-449.

Guedes, A., Valentim, B., Prieto, A., Rodrigues, S., Noronha, F., 2010. Micro-Raman spectroscopy of collotelinite, fusinite and macrinite. *International Journal of Coal Geology* 83, 415-422.

Hackley, P.C., Araujo, C.V., Borrego, A.G., Bouzinos, A., Cardott, B.J., Cook, A.C., Eble, C., Flores, D., Gentzis, T., Gonçalves, P.A., 2015. Standardization of reflectance measurements in dispersed organic matter: Results of an exercise to improve interlaboratory agreement. *Marine and Petroleum Geology* 59, 22-34.

Hinrichs, R., Brown, M.T., Vasconcellos, M.A., Abrashev, M.V., Kalkreuth, W., 2014. Simple procedure for an estimation of the coal rank using micro-Raman spectroscopy. *International Journal of Coal Geology* 136, 52-58.

Hu, R., Vernik, L., Nayvelt, L., Dicman, A., 2015. Seismic inversion for organic richness and fracture gradient in unconventional reservoirs: Eagle Ford Shale, Texas. *The Leading Edge* 34, 80-84.

Hull, Katherine L., Younane N. Abousleiman, Yanhui Han, Ghaithan A. Al-Muntasheri, Peter Hosemann, S. Scott Parker, and Cameron B. Howard. "New insights on the mechanical characterization of Kerogen-Rich shale, KRS." In Abu Dhabi International Petroleum Exhibition and Conference. Society of Petroleum Engineers, 2015.

Hutton, A., Bharati, S., Robl, T., 1994. Chemical and petrographic classification of kerogen/macerals. *Energy & Fuels* 8, 1478-1488.

Katahara, K.W., 1996. Clay mineral elastic properties, SEG Technical Program Expanded Abstracts 1996. Society of Exploration Geophysicists, pp. 1691-1694.

Kelemen, S., Fang, H., 2001. Maturity trends in Raman spectra from kerogen and coal. *Energy & fuels* 15, 653-658.

## Chapter 2

Keown, D.M., Li, X., Hayashi, J.-i., Li, C.-Z., 2007. Characterization of the structural features of char from the pyrolysis of cane trash using Fourier Transform– Raman spectroscopy. *Energy & fuels* 21, 1816-1821.

Kuhn, P., Di Primio, R., Horsfield, B., 2010. Bulk composition and phase behaviour of petroleum sourced by the Bakken Formation of the Williston Basin, Geological Society, London, Petroleum Geology Conference series. Geological Society of London, pp. 1065-1077.

Kumar, V., Sondergeld, C.H., Rai, C.S., 2012. Nano to macro mechanical characterization of shale, SPE Annual Technical Conference and Exhibition. Society of Petroleum Engineers.

Lahfid, A., Beyssac, O., Deville, E., Negro, F., Chopin, C., Goffé, B., 2010. Evolution of the Raman spectrum of carbonaceous material in low-grade metasediments of the Glarus Alps (Switzerland). *Terra Nova* 22, 354-360.

LeFever, J.A., 1991. History of oil production from the Bakken Formation, North Dakota.

LeFever, J.A., Martiniuk, C.D., Dancsok, E.F., Mahnic, P.A., 1991. Petroleum potential of the middle member, Bakken Formation, Williston Basin. Williston Basin Symposium.

Li, C., Ostadhassan, M., Kong, L., 2017. Nanochemo-mechanical characterization of organic shale through AFM and EDS, SEG Technical Program Expanded Abstracts 2017. Society of Exploration Geophysicists, pp. 3837-3840.

Liu, K., Ostadhassan, M., 2017. Microstructural and geomechanical analysis of Bakken shale at nanoscale. *Journal of Petroleum Science and Engineering* 153, 133-144.

Liu, K., Ostadhassan, M., Gentzis, T., Carvajal-Ortiz, H., Bubach, B., 2017. Characterization of geochemical properties and microstructures of the Bakken Shale in North Dakota. *International Journal of Coal Geology*.

Lünsdorf, N.K., 2016. Raman spectroscopy of dispersed vitrinite—Methodical aspects and correlation with reflectance. *International Journal of Coal Geology* 153, 75-86.

## Chapter 2

Manjunath, G., Nair, R.R., 2015. Implications of the 3D micro scale coal characteristics along with Raman stress mapping of the scratch tracks. *International Journal of Coal Geology* 141, 13-22.

Manjunath, G., Nair, R.R., 2017. Microscale assessment of 3D geomechanical structural characterization of gondawana shales. *International Journal of Coal Geology* 181, 60-74.

Marshall, C.P., Edwards, H.G., Jehlicka, J., 2010. Understanding the application of Raman spectroscopy to the detection of traces of life. *Astrobiology* 10, 229-243.

Mason, J., Jordan, T., Carloni\*, J., Baker, S., Zehnder, A., 2014. Dependence of Micro-Mechanical Properties on Lithofacies: Indentation Experiments on Marcellus Shale, Unconventional Resources Technology Conference, Denver, Colorado, 25-27 August 2014. Society of Exploration Geophysicists, American Association of Petroleum Geologists, Society of Petroleum Engineers, pp. 1758-1770.

Matthews, M., Pimenta, M., Dresselhaus, G., Dresselhaus, M., Endo, M., 1999. Origin of dispersive effects of the Raman D band in carbon materials. *Physical Review B* 59, R6585.

Mavko, G., Mukerji, T., Dvorkin, J., 2009. *The rock physics handbook: Tools for seismic analysis of porous media*. Cambridge university press.

McNeil, D.H., Schulze, H.G., Matys, E., Bosak, T., 2015. Raman spectroscopic analysis of carbonaceous matter and silica in the test walls of recent and fossil agglutinated foraminifera. *AAPG Bulletin* 99, 1081-1097.

Mumm, A.S., İnan, S., 2016. Microscale organic maturity determination of graptolites using Raman spectroscopy. *International Journal of Coal Geology* 162, 96-107.

Oliver, W.C., Pharr, G.M., 1992. An improved technique for determining hardness and elastic modulus using load and displacement sensing indentation experiments. *Journal of materials research* 7, 1564-1583.

Ortega, J. Alberto, Franz-Josef Ulm, and Younane Abousleiman. "The effect of the nanogranular nature of shale on their poroelastic behavior." *Acta Geotechnica* 2, no. 3 (2007): 155-182.

## Chapter 2

Pal-Bathija, A., Prasad, M., Liang, H., Upmanyu, M., Lu, N., Batzle, M., 2008. Elastic properties of clay minerals, SEG Technical Program Expanded Abstracts 2008. Society of Exploration Geophysicists, pp. 1610-1614.

Pan, J., Meng, Z., Hou, Q., Ju, Y., Cao, Y., 2013. Coal strength and Young's modulus related to coal rank, compressional velocity and maceral composition. *Journal of Structural Geology* 54, 129-135.

Peters, K., 1986. Guidelines for evaluating petroleum source rock using programmed pyrolysis. *AAPG bulletin* 70, 318-329.

Pócsik, I., Hundhausen, M., Koós, M., Ley, L., 1998. Origin of the D peak in the Raman spectrum of microcrystalline graphite. *Journal of Non-Crystalline Solids* 227, 1083-1086.

Quirico, E., Rouzaud, J.-N., Bonal, L., Montagnac, G., 2005. Maturation grade of coals as revealed by Raman spectroscopy: Progress and problems. *Spectrochimica Acta Part A: Molecular and Biomolecular Spectroscopy* 61, 2368-2377.

Reich, S., Thomsen, C., 2004. Raman spectroscopy of graphite. *Philosophical Transactions of the Royal Society of London A: Mathematical, Physical and Engineering Sciences* 362, 2271-2288.

Sauerer, B., Craddock, P.R., AlJohani, M.D., Alsamadony, K.L., Abdallah, W., 2017. Fast and accurate shale maturity determination by Raman spectroscopy measurement with minimal sample preparation. *International Journal of Coal Geology* 173, 150-157.

Schito, A., Romano, C., Corrado, S., Grigo, D., Poe, B., 2017. Diagenetic thermal evolution of organic matter by Raman spectroscopy. *Organic Geochemistry* 106, 57-67.

Schön, P., Bagdi, K., Molnár, K., Markus, P., Pukánszky, B., Vancso, G.J., 2011. Quantitative mapping of elastic moduli at the nanoscale in phase separated polyurethanes by AFM. *European Polymer Journal* 47, 692-698.

## Chapter 2

Shukla, P., Kumar, V., Curtis, M., Sondergeld, C.H., Rai, C.S., 2013. Nanoindentation studies on shales, 47th US Rock Mechanics/Geomechanics Symposium. American Rock Mechanics Association.

Smith, M.G., Bustin, R.M., 1995. Sedimentology of the Late Devonian and Early Mississippian Bakken Formation, Williston Basin. Williston Basin Symposium.

Smith, M.G., Bustin, R.M., 2000. Late Devonian and Early Mississippian Bakken and Exshaw black shale source rocks, Western Canada Sedimentary Basin: a sequence stratigraphic interpretation. AAPG bulletin 84, 940-960.

Spötl, C., Houseknecht, D.W., Jaques, R.C., 1998. Kerogen maturation and incipient graphitization of hydrocarbon source rocks in the Arkoma Basin, Oklahoma and Arkansas: a combined petrographic and Raman spectrometric study. Organic Geochemistry 28, 535-542.

Stephoe, A., 2012. Petrofacies and depositional systems of the Bakken Formation in the Williston Basin, North Dakota. West Virginia University.

Sweers, K., Van Der Werf, K., Bennink, M., Subramaniam, V., 2011. Nanomechanical properties of  $\alpha$ -synuclein amyloid fibrils: a comparative study by nanoindentation, harmonic force microscopy, and Peakforce QNM. Nanoscale research letters 6, 270.

Tissot, B.P., Welte, D.H., 1984. Diagenesis, catagenesis and metagenesis of organic matter, Petroleum Formation and Occurrence. Springer, pp. 69-73.

Trtik, P., Kaufmann, J., Volz, U., 2012. On the use of peak-force tapping atomic force microscopy for quantification of the local elastic modulus in hardened cement paste. Cement and concrete research 42, 215-221.

Tuinstra, F., Koenig, J.L., 1970. Raman spectrum of graphite. The Journal of Chemical Physics 53, 1126-1130.

Tuschel, D., 2013. Raman spectroscopy of oil shale. Spectroscopy 28, 5.

## Chapter 2

Tyson, R.V., 1995. Abundance of organic matter in sediments: TOC, hydrodynamic equivalence, dilution and flux effects, *Sedimentary organic matter*. Springer, pp. 81-118.

Ulm, F.-J., Abousleiman, Y., 2006. The nanogranular nature of shale. *Acta Geotechnica* 1, 77-88.

Ulm, F.J., Vandamme, M., Bobko, C., Alberto Ortega, J., Tai, K., Ortiz, C., 2007. Statistical indentation techniques for hydrated nanocomposites: concrete, bone, and shale. *Journal of the American Ceramic Society* 90, 2677-2692.

Wang, Y., Alsmeyer, D.C., McCreery, R.L., 1990. Raman spectroscopy of carbon materials: structural basis of observed spectra. *Chemistry of Materials* 2, 557-563.

Wang, Z., Wang, H., Cates, M.E., 2001. Effective elastic properties of solid clays. *Geophysics* 66, 428-440.

Waples, D.W., 1981. *Organic geochemistry for exploration geologists*. Burgess Pub. Co.

Wilkins, R.W., Boudou, R., Sherwood, N., Xiao, X., 2014. Thermal maturity evaluation from inertinites by Raman spectroscopy: the 'RaMM' technique. *International Journal of Coal Geology* 128, 143-152.

Wopenka, B., Pasteris, J.D., 1993. Structural characterization of kerogens to granulite-facies graphite: applicability of Raman microprobe spectroscopy. *The American Mineralogist* 78, 533-557.

Zargari, S., Canter, K.L., Prasad, M., 2015. Porosity evolution in oil-prone source rocks. *Fuel* 153, 110-117.

Zargari, S., Prasad, M., Mba, K.C., Mattson, E., 2011. Organic maturity, hydrous pyrolysis, and elastic property in shales, Canadian Unconventional Resources Conference. Society of Petroleum Engineers.

Zeszotarski, J.C., Chromik, R.R., Vinci, R.P., Messmer, M.C., Michels, R., Larsen, J.W., 2004. Imaging and mechanical property measurements of kerogen via nanoindentation. *Geochimica et cosmochimica acta* 68, 4113-4119.

## Chapter 2

Zhao, Q., Frogley, M.D., Wagner, H.D., 2002. Direction-sensitive strain-mapping with carbon nanotube sensors. *Composites Science and Technology* 62, 147-150.

Zhao, Q., Wagner, H.D., 2004. Raman spectroscopy of carbon–nanotube–based composites. *Philosophical Transactions of the Royal Society of London A: Mathematical, Physical and Engineering Sciences* 362, 2407-2424.

Zhou, Q., Xiao, X., Pan, L., Tian, H., 2014. The relationship between micro-Raman spectral parameters and reflectance of solid bitumen. *International Journal of Coal Geology* 121, 19-25.

## **Chapter 3 Evaluating Molecular Evolution of Kerogen by Raman Spectroscopy: Correlation with Optical Microscopy and Rock-Eval Pyrolysis**

A paper published in the **Journal of Energies**.

Seyedalireza Khatibi, Mehdi Ostadhassan, David Tuschel, Thomas Gentzis,  
Humberto Carvajal-Ortiz

### **Abstract**

Vitrinite maturity and programmed pyrolysis are conventional methods to evaluate organic matter (OM) regarding its thermal maturity. While, they are exhaustive tasks with low resolution. Moreover, Vitrinite reflectance analysis can be difficult, if prepared samples have no primary vitrinite or dispersed widely. Raman spectroscopy is a nondestructive method that has been used in the last decade for maturity evaluation of organic matter by detecting structural transformations, however, it might suffer from fluorescence background in low mature samples. In this study, four samples of different maturities from both shale formations of Bakken (the upper and lower members) Formation were collected and analyzed with Rock-Eval (RE), and Raman spectroscopy. In the next step, portions of the same samples were then used for isolation of kerogen and analyzed by Raman spectroscopy. Results showed, Raman spectroscopy by detecting structural information of OM can reflect thermal maturity parameters derived from programmed pyrolysis. Moreover, isolating kerogen will reduce the background noise (fluorescence) in the samples dramatically and yields a better spectrum. The study showed that thermal properties of OM can be precise reflected in Raman signals.

**Keywords:** Unconventional reservoirs, Kerogen, Vitrinite maturity, Rock-Eval, Raman spectroscopy

### 3-1 Introduction

Organic matter usually known as kerogen, is derived from the animals, plants and micro-organisms burial and preservation within the rock matrix (Hutton et al., 1994). Organic-rich intervals are usually found in shale reservoirs including solid bitumen, kerogen and moveable hydrocarbons. Understanding kerogen properties regarding maturity has a key role in the development of unconventional resources. It is well understood that the quantities of hydrocarbon generation are a function of kerogen content and type in the formation and also its maturity (McCarthy et al., 2011), and then diffusion and permeability of the hydrocarbon in OM (Wang et al., 2017). Thermal maturity of kerogen is usually understood by the reflectance measurement of vitrinite. This method can be difficult, if samples have no primary vitrinite or it is dispersed widely in the sample (Hackley et al., 2015; Sauerer et al., 2017). The second method to evaluate the maturity of organic matter is programmed pyrolysis (Clementz et al., 1979; Larter and Douglas, 1980). The most widely used pyrolysis technique is Rock-Eval, in which a sample is subjected to a programmed heating from 300°C to 650°C in an inert gas atmosphere (Peters et al., 1986; Lafargue et al., 1998; Behar et al., 2001; Espitalie et al., 1985). The results are reported in various parameters characterizing the kerogen type, quality, and its potential to produce hydrocarbons. All of these properties reflect the molecular structure of kerogen and the chemical compounds that exist in organic matter.

Raman spectroscopy is a method that works based on molecular vibrations and can provide direct information about the organic matter's molecular compounds. During thermal maturation, aromaticity of kerogen structure increases and heteroatom content (N, O, S, and H) decreases (Tissot and Welte, 1984). This process results in a more-ordered molecular structure of kerogen (Waples, 1981; Tyson, 1995). Raman spectroscopy is shown to be a promising, rapid and non-destructive method for OM evaluation regarding its thermal maturity (Kelemen and Fang, 2001; Beyssac et al., 2002; Quirico et al., 2005; Lahfid et al., 2010; Guedes et al., 2012; Hinrichs et al., 2014; Wilkins et al., 2014; Zhou et al., 2014; Lünsdorf, 2016; Mumm and İnan, 2016; Ferralis et

al., 2016; Khatibi et al., 2018a) and also predicting elastic modulus (Young's modulus) (Khatibi et al., 2018b).

In this study, four samples from Bakken Formation in Williston Basin in North Dakota were collected. Then, Raman signals were related to the %VRo, and maturity parameters from Rock-Eval pyrolysis (Tmax, S1, S2, and production index). The conclusions are then confirmed with the Fourier Transform Infrared Spectroscopy (FTIR) spectrum of two samples with highest and lowest maturities to provide us with a better insight of molecular transformation of kerogen. In order to avoid the errors that may exist in the Raman spectrum when samples are mechanically polished or when carbonaceous minerals are present (Beysac et al., 2003; Lünsdorf et al., 2016; Sauerer et al., 2017) and fluorescent background, kerogen was isolated from mineral matrix. The Raman spectra of both the in-situ and pure kerogen were compared and the discrepancies in the data were presented.

It should be noted in this study for the first time we are proposing the process in which Raman signals can be correlated to Rock-Eval results. However due to lack of Raman and pyrolysis data necessary for a strong conclusion, to better support our hypothesis, additional data from published literature has been also utilized which reported their data for other purposes.

## 3-2 Geological Setting

The late Devonian-Early Mississippian Bakken Formation is one of the main source rocks of the Williston Basin (LeFever, 1991; Parapuram et al., 2018). The Williston Basin covers the southern portion of Canada (Manitoba and Saskatchewan) and the northern part of the United States (Montana and North Dakota), Figure 3-2-1. The Bakken Formation is underlain by the Three Forks Formation and overlain by the Lodgepole Formation. The Bakken as an organic rich formation consists upper and lower members serving as source rocks and middle member as the reservoir with low porosity and permeability. Thickness of the Bakken Formation is about 150 ft and has no surface outcrop. The Bakken Formation has high TOC (Total Organic Carbon) content, which ranges from 5 to 20 wt% with an average of 11.33 wt% across the basin (Webster, 1984; Smith and Bustin, 1995; Liu et al., 2018). Different literature showed that most abundant kerogen type in the Bakken Formation are types I and II (Sonnenberg and Pramudito, 2009; Jin and Sonnenberg, 2013; Gaswirth et al., 2013).

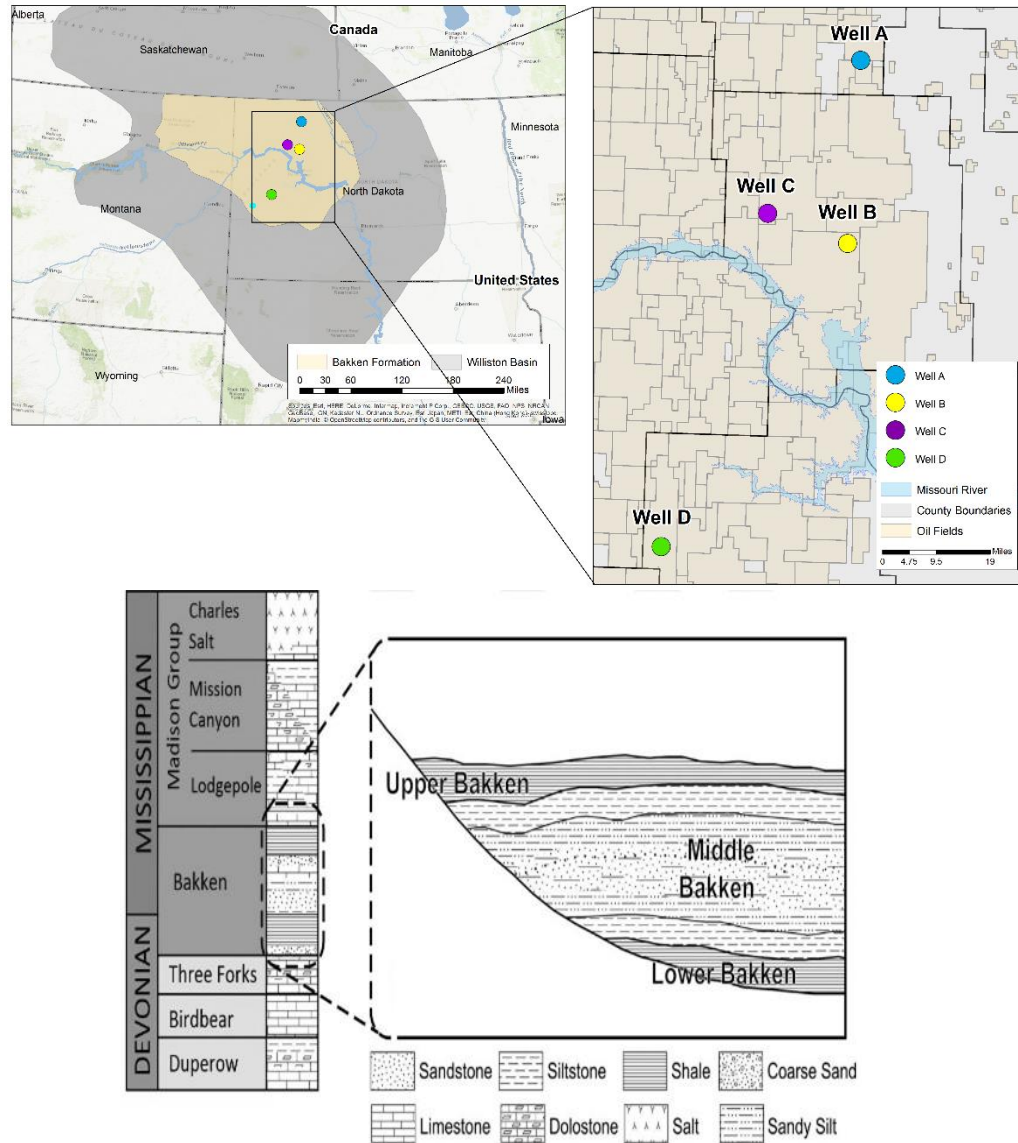


Figure 3-2-1 (top) Wells in this study are overlaid on Bakken Formation map, (bottom) Stratigraphic column of the Bakken Formation and the lithology of Members (Source: modified from (Khatibi et al., 2017a)).

### 3-3 Sample preparation and experiments

The samples are taken from four different Wells (A, B, C, and D) and vary in depth and maturity, core images are shown in Figure 3-3-1. Small pieces of samples were homogenized and divided into three parts to be used for Raman spectroscopy, vitrinite reflectance (% VRo) and Rock-Eval analysis. The same portions of the samples that were tested for Raman measurement were then gone through the kerogen isolation process by acid to separate the organic matter from mineral matrix.

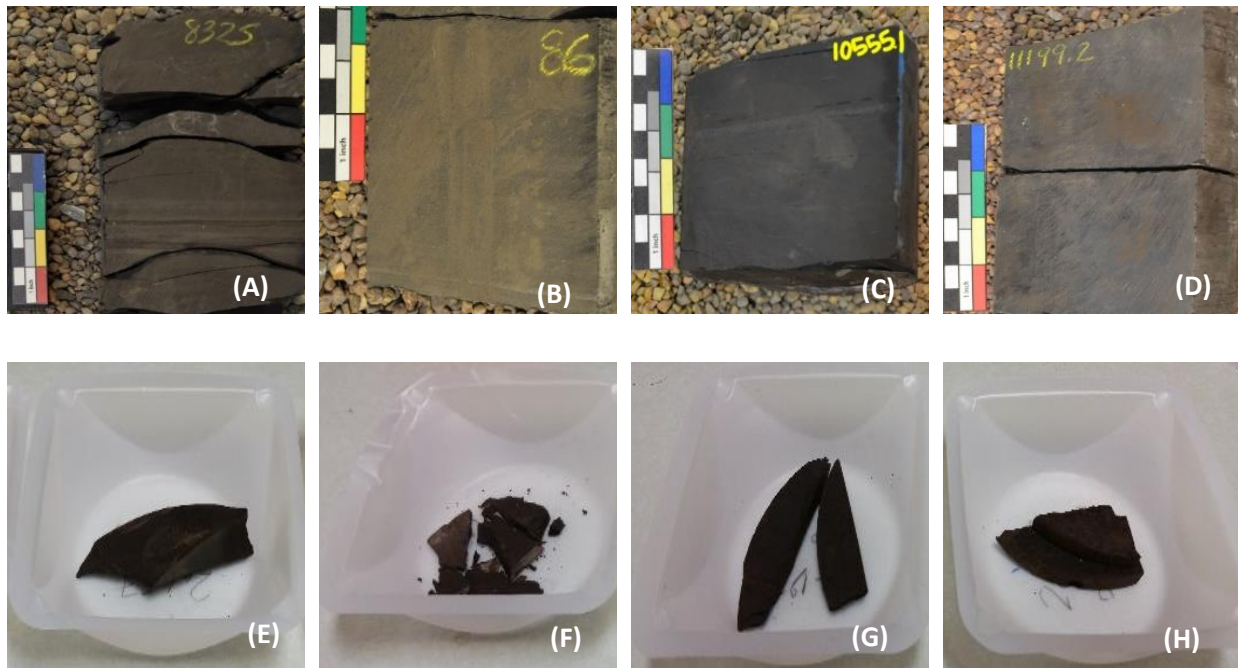
To evaluate the maturity of samples, they were crushed (850um), and hardened by mixing with the epoxy resin (Hackley et al., 2015). In the next step, to ensure the surfaces are scratch, samples were polished by polishing equipment. The random reflectance (%Ro) and qualitative fluorescence were then analyzed with a Carl Zeiss Axio imager A2m microscope. As primary vitrinite is absent in sedimentary formations older than the Devonian, the same as in four samples from Bakken formation (Figure 3-3-2), bitumen reflectance (%BRo) was used to obtain an equivalent vitrinite maturity (%VRo-eq) using the Jacob equation (Equation 1) (Jacob, 1989), which is one of numerous such equations available. In addition, VRo-eq was calculated by converting Tmax from Rock-Eval pyrolysis through Equation 2 (Jarvie et al., 2001). Equation 2 was used because it is derived from the Mississippian-age Barnett Shale in Texas, which contains type II marine kerogen, similar to that found in the Bakken Shale.

$$\%VRo = \%BRo * 0.618 + 0.4$$

(1)

$$\%VRo = 0.0180 * Tmax - 7.16$$

(2)



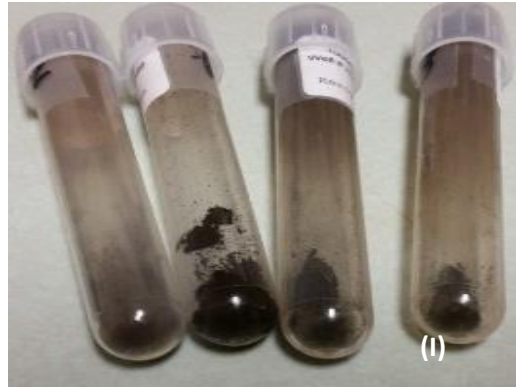
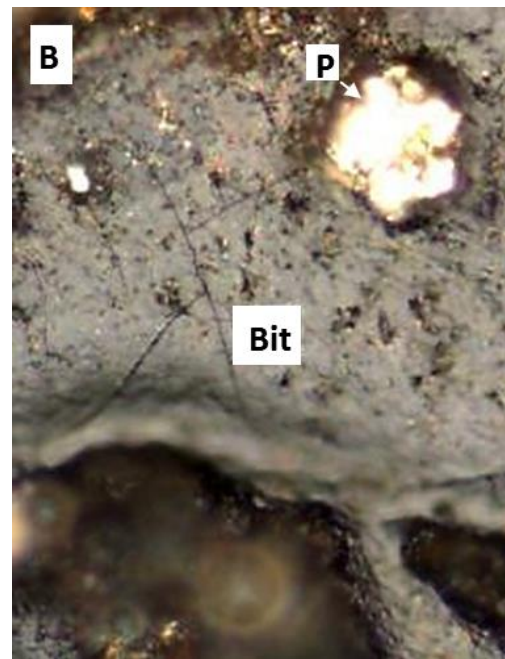
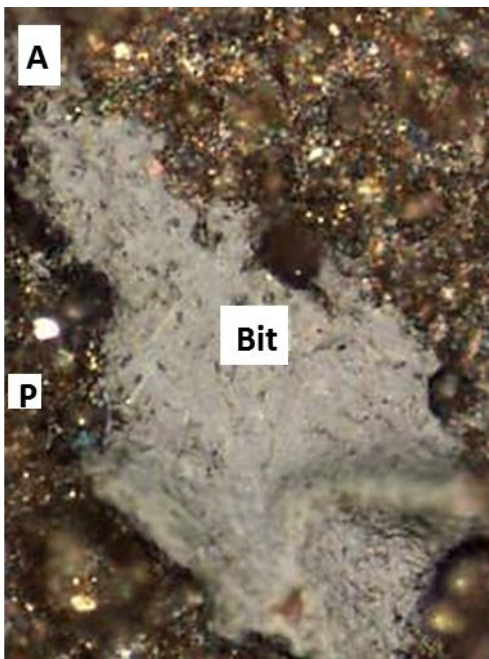


Figure 3-3-1 (A) to (D) Core samples of Well A to D, (E) to (H) corresponding sample chips, (I) extracted kerogen.



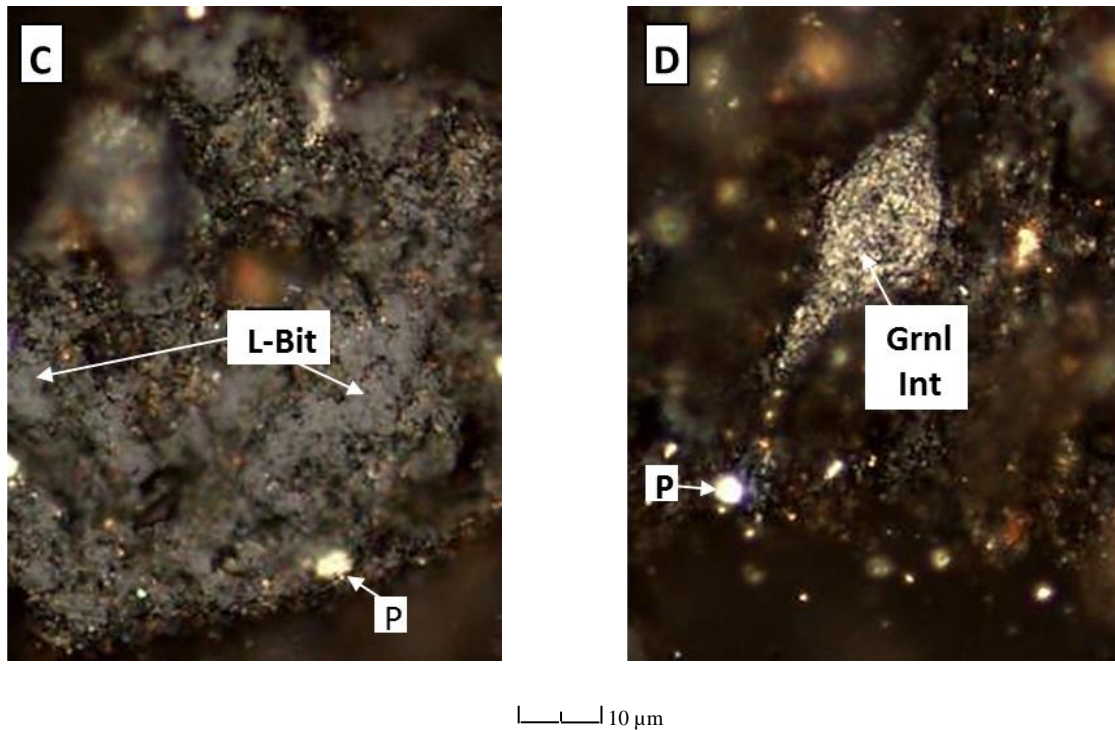


Figure 3-3-2 (A) Blocky grain of primary bitumen (Bit), (B) Same as (A) but Pyrite (P) is also visible, (C) Low-reflecting bitumen (L-Bit), (D) Granular inertinite (Grnl Int) having a morphology that resembles a zooclast, Pyrite (P) is also visible. No reliable grain of primary vitrinite can be seen.

In the next step, programmed Pyrolysis was performed on samples by Rock-Eval 6. Table 3-3-1 summarizes the properties derived from the Rock-Eval analysis of four samples. As in Figure 3-3-3 Type II is the main type of Kerogen of our samples, TOC values vary from 12.69 wt% to 16.36 wt%, and %VRo-eq maturity fluctuates from 0.53 to 0.99. S1 is the free hydrocarbons present in the rock, while S2 is the amount of hydrocarbon generated through pyrolysis and is used to derive hydrogen index (HI) (Behar et al., 2001; Ostadhassan et al., 2018). S3 is the CO<sub>2</sub> which will be released during pyrolysis and is in relationship to the oxygen in the kerogen structure which is used to derive oxygen index (OI) (Behar et al., 2001; Ostadhassan et al., 2018). Production index (PI) can also be a maturity indicator. More description of Rock-Eval pyrolysis can be found in (Espitalie et al., 1985).

Table 3-3-1 Properties of four samples in this study.

Well No.	Depth (ft)	TOC (wt%)	S1 (mg/g)	S2 (mg/g)	HI (S2x100/TOC)	PI (S1/(S1+S2))	%BRo	%VRo-eq
A	8,325	16.27	8.27	90.69	557.41	0.08	0.44	0.67
B	9,886	15.76	9.27	83.7	531.09	0.1	0.49	0.70
C	10,555	12.69	0.31	33.01	260.126	0.009	0.72	0.88

D	11,199	16.36	0.71	28.05	171.454	0.024	0.94	0.98
---	--------	-------	------	-------	---------	-------	------	------

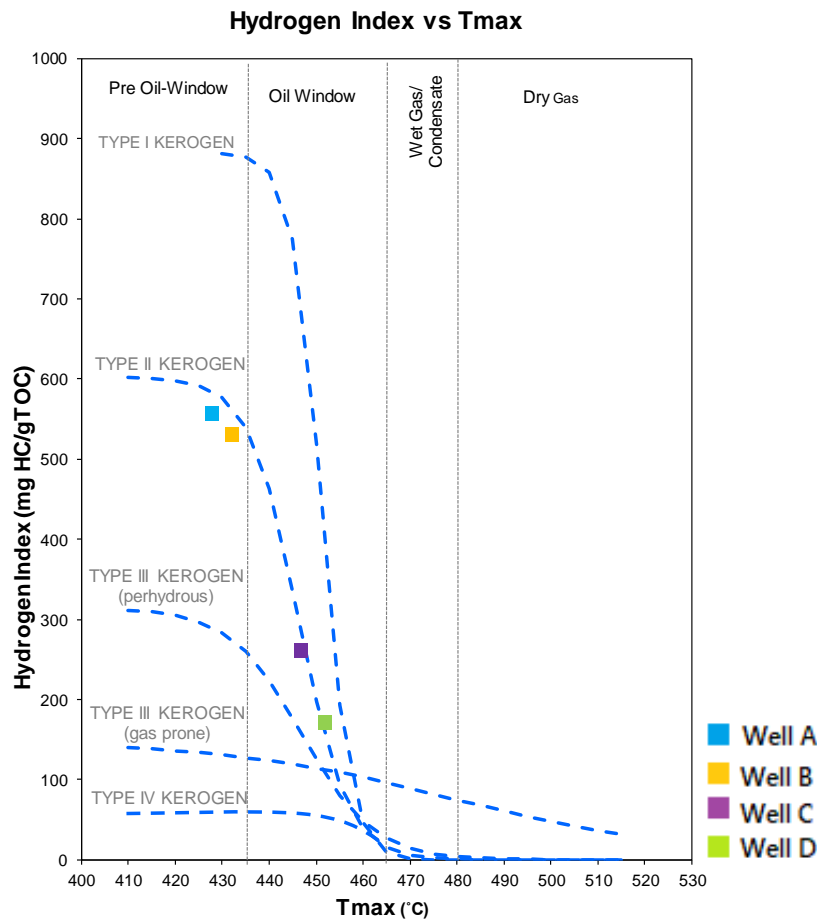


Figure 3-3-3 HI vs. Tmax as pseudo-Van Krevelen diagram for kerogen typing.

### 3-3.1 Isolation of Kerogen

Polishing rocks will create dislocation of constituent components within the samples which will affect their Raman response. Moreover, fluorescent background noise due to presences of Bitumen and sulfur in lower maturity samples masks the signal (Kelemen and Fang, 2001; Lünsdorf, 2016; Schito et al., 2017). In order to avoid these two issues, kerogen was isolated from the samples according to (Robl and Davis, 1993; Schimmelmann et al., 1999).

The process can be summarized as below:

- Pre-acid preparation of the samples: sample quality needs to be evaluated to ensure they are properly washed and brought to the appropriate mesh size (crushed if

necessary). Typical starting sample size is 20-30 grams of material depending on organic richness.

- The sample is then placed into concentrated 37% HCl (small increments should be added to prevent excessive foaming while timing is dependent on sample reaction).
- Samples are placed into concentrated 48% HF (HF is for digestion of remaining silicates).
- The samples are placed into concentrated HCl for the second time.
- Centrifugation: this is done essentially by taking a portion of the remnant of the sample and placing it into a centrifuge tube to create the kerogen slide. This process will separate the solid kerogen from remaining liquids, Figure 3-3-4.

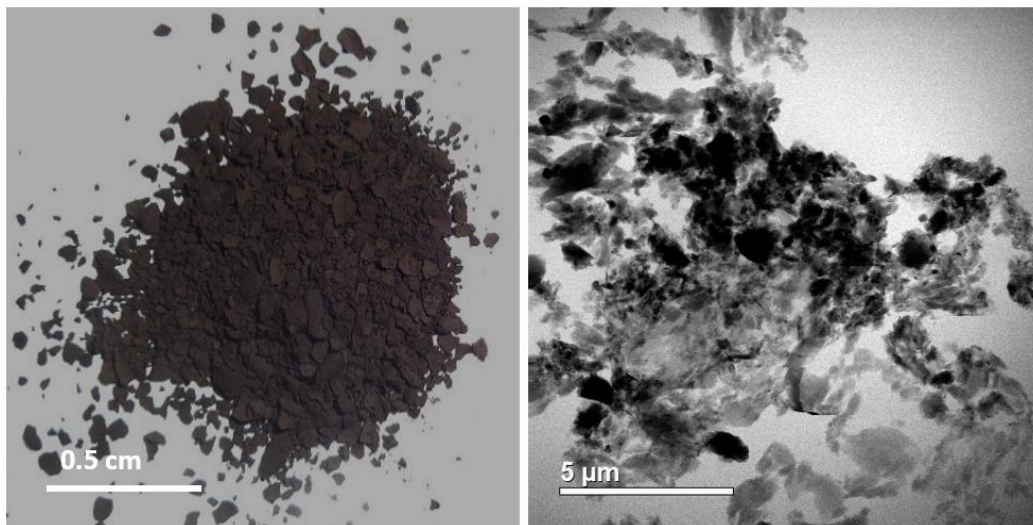


Figure 3-3-4 (top) Isolated kerogen of Well D, (bottom) the same sample under a scanning transmission electron microscope (STEM).

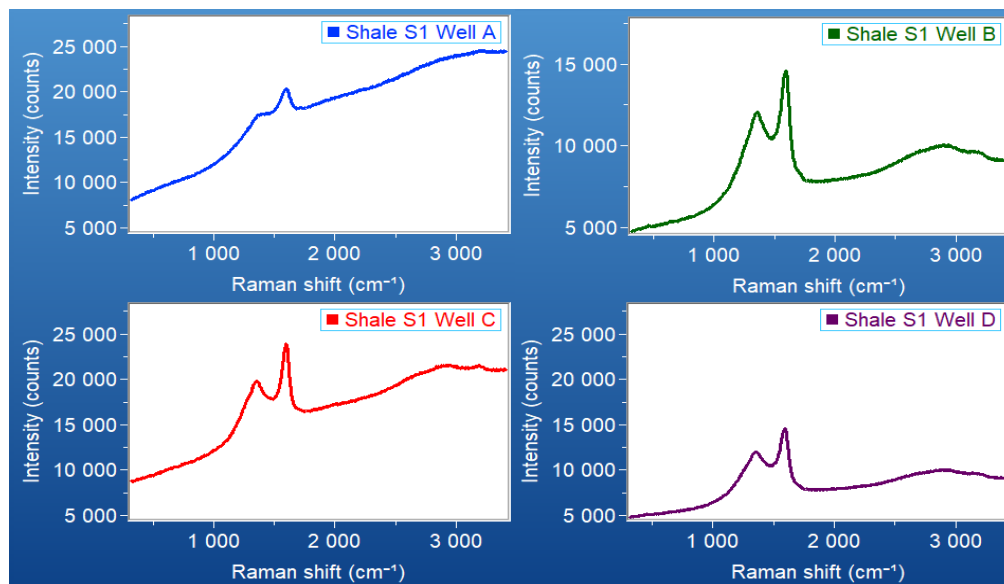
### 3-3.2 Raman spectroscopy

Inelastic scattering of monochromatic light in Raman spectroscopy, such as a laser beam, from the surface of the sample, interacts with molecular vibrations (Amer, 2009). The interaction causes exchange of energy in which the energy of laser photons will either shift up or down [44-46]. Based on the frequency of vibration of the molecule(s), change in energy varies which leads to unique spectral patterns for each molecule.

Kerogen depicts two main peaks in the spectrum known as G and D bands (Beysac et al., 2002; Cesare and Maineri, 1999; Marshall et al., 2010; Huang et al., 2010; Tuschel, 2013). The G band which refers to graphite appears around  $1600\text{ cm}^{-1}$  indicating well-ordered, graphite-like carbon

(Khatibi et al., 2018b). The D band appearing around  $1350\text{ cm}^{-1}$  depicts disorder in the atoms (Sauerer et al., 2017).

Raman spectra were acquired using  $532\text{ nm}$  excitation energy by focusing the laser beam on the surface of four samples (both in situ and extracted), Figure 3-3-5. It should be noted, Raman signals might interfere with fluorescence noise in generally low thermal maturity samples. Figure 2-3-5 shows solid bitumen under white reflected light and under UV light (fluorescent). Removing bitumen and sulfur content in the matrix by isolation of kerogen from the rest of the constituent components in the sample has led to attenuation of background noise. Note the change in the intensity and fluorescence of samples before and after extraction, in Figure 3-3-5.



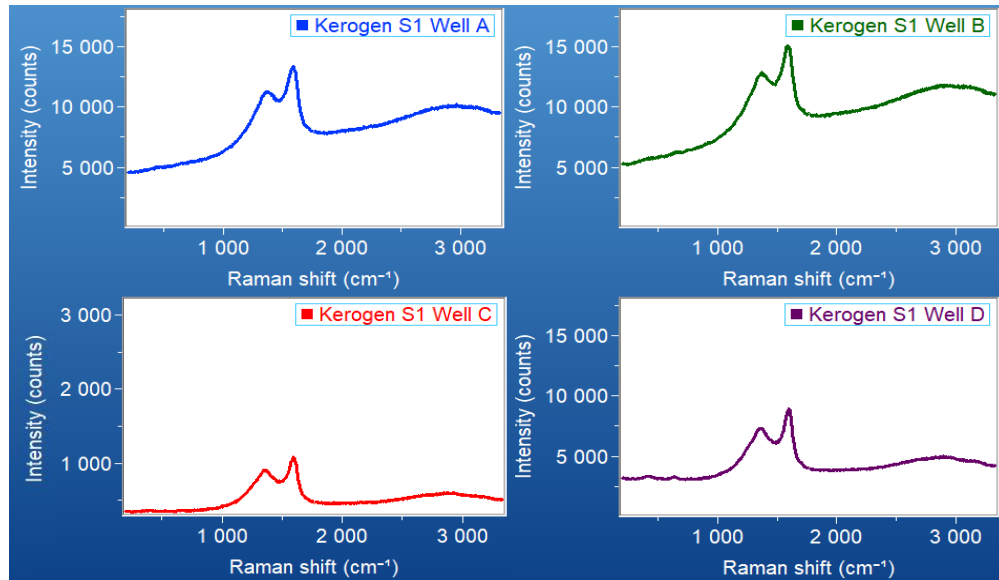


Figure 3-3-5 (top) Raman spectra for in-situ samples, and (bottom) corresponding isolated kerogen samples. Note the lower background noise in samples, specifically Well A.

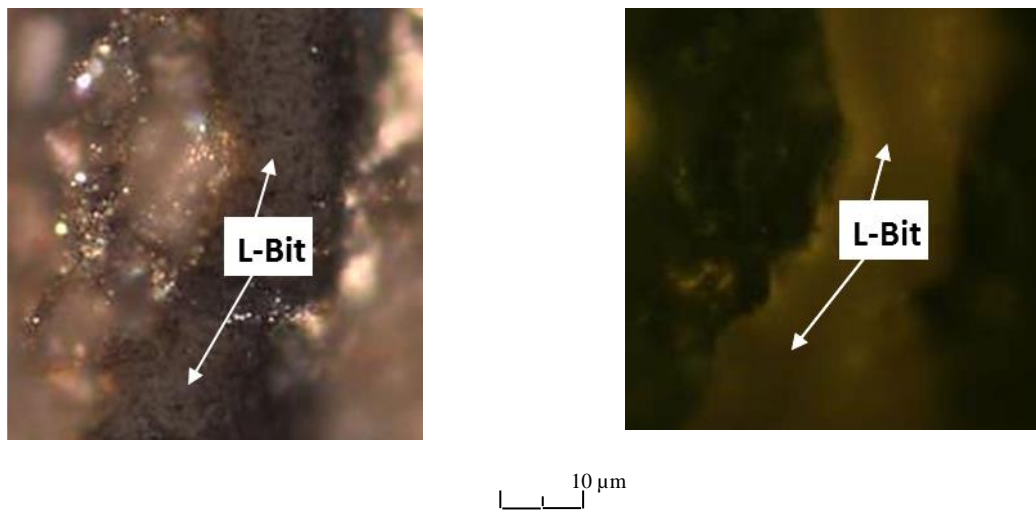


Figure 3-3-6 (left) (L-Bit) Hydrogen-rich Solid bitumen under reflected (white) light. (right) The same view under fluorescence.

## 3-4 Results and discussion

### 3-4.1 Raman signals on pure kerogen

As mentioned before, bitumen and sulfur content in mud rocks tend to express high fluorescent background noise in Raman spectrum. As shown in Figure 3-3-5, isolation of kerogen removes this issue by eliminating the effects of bitumen. Comparing spectra before and after kerogen

isolation in Figure 3-3-5 indicates high background fluorescent levels in in-situ samples which have been reduced, specifically for Well A with lower maturity.

Table 3-4-1 contains the details of the Raman spectroscopy data for both isolated and shale kerogen. It can be concluded from the table that standard deviations of D and G bands for isolated kerogen are less than the in-situ (non-isolated) samples. The higher deviation of D bands compared to G bands can be attributed to the fact that depending on the orientation of the crystallites to the exciting laser beam, spectral features of disordered sp<sup>2</sup> carbons (D band) may vary notably (Marshall et al., 2007).

Moreover, it has shown by (Lünsdorf et al., 2014) that polishing the samples to 0.05 µm roughness influences the Raman spectra. This originates from carbonaceous matters that are very sensitive to the polishing process, thus isolation will circumvent this problem. Furthermore, bitumen and sulfur content in mud rocks tend to express high fluorescent background noise in Raman spectrum. As shown in Figure 3-3-5, isolation also removes this issue by eliminating the effects of bitumen. Comparing spectra before and after kerogen isolation in Figure 3-3-5 indicates high background fluorescent levels in in-situ samples which have been reduced, specifically for Well A with lower maturity.

*Table 3-4-1 Raman signals for shale and isolated kerogen samples for all wells. Mean and standard deviation (st. dev.) for each band for all available measurements are provided. Note the lower standard deviation in kerogen samples.*

shale sample		kerogen sample		shale sample		kerogen sample	
D band	G band	D band	G band	D band	G band	D band	G band
1,368.8	1,591	1,356.1	1,587.7	1,364.3	1,587.7	1,368.2	1,587.8
1,357.2	1,589	1,364.3	1,581.4	1,361	1,590.8	1,361	1,590.5
1,366.9	1,593.3	1,356.8	1,587.7	1,364.3	1,590.8	1,364.3	1,590.8
1,362.7	1,582.5	1,359.6	1,583.4	1,367.5	1,584.5	1,366.5	1,587.5
1,367.9	1,593.5	1,361.9	1,587.7	1,370.2	1,587.7	1,366.3	1,587.7
<b>Mean</b>	<b>Mean</b>	<b>Mean</b>	<b>Mean</b>	<b>Mean</b>	<b>Mean</b>	<b>Mean</b>	<b>Mean</b>
1,364.7	1,589.9	1,359.7	1,585.6	1,365.4	1,588.3	1,365.2	1,588.9
<b>St. Dev.</b>	<b>St. Dev.</b>	<b>St. Dev.</b>	<b>St. Dev.</b>	<b>St. Dev.</b>	<b>St. Dev.</b>	<b>St. Dev.</b>	<b>St. Dev.</b>

Well A

Well B

shale sample		kerogen sample		shale sample		kerogen sample	
D band	G band	D band	G band	D band	G band	D band	G band
1,348.3	1,587.7	1,354.2	1,591.3	1,356.7	1,591.3	1,350	1,590.1
1,357.8	1,590.8	1,358.2	1,591.3	1,355.6	1,591.3	1,356.3	1,590.8
1,361	1,590.8	1,358.2	1,594.4	1,351.3	1,591.3	1,352	1,592.4
1,357.8	1,594	1,358.2	1,594.4	1,350.9	1,594.4	1,350	1,589.3
1,354.5	1,597.1	1,358.2	1,591.3	1,350.6	1,597.6	1,355	1,587.7
<b>Mean</b>	<b>Mean</b>	<b>Mean</b>	<b>Mean</b>	<b>Mean</b>	<b>Mean</b>	<b>Mean</b>	<b>Mean</b>
1,355.9	1,592.1	1,357.4	1,592.5	1,353	1,593.2	1,352.6	1,590
<b>St. Dev.</b>	<b>St. Dev.</b>	<b>St. Dev.</b>	<b>St. Dev.</b>	<b>St. Dev.</b>	<b>St. Dev.</b>	<b>St. Dev.</b>	<b>St. Dev.</b>
4.3	3.2	1.6	1.5	2.6	2.5	2.5	1.6

### 3-4.2 Raman spectroscopy for evaluating production potential of OM

Previous studies have documented that thermal maturity reflects a systematic change in the positions, separations and other important parameters of the bands in the Raman spectra for carbonaceous materials. As kerogen matures, it starts to make clusters of aromatic bands and also loses its heteroatoms (Tissot et al., 1984; Waples, 1981; Tyson, 1995; Kelemen and Fang, 2001). Such evolution is perceived by Raman spectroscopy at different levels of maturation, reflecting molecular structural transformations.

Figure 3-4-1 displays a non-linear correlation between band separation (G-D) versus maturity (%VRo) for samples that are taken from 12 different fields from (Spötl et al., 1998; Kelemen and Fang, 2001; Sauerer et al., 2017) and including samples from this study. Tmax which is also a major parameter representing the thermal maturity of the samples and is obtained from Rock-Eval analysis shows correlation with band separation, as in earlier studies (Beysac et al., 2002; Quirico

et al., 2005; Khatibi et al., 2017a,b; Schito et al., 2017; Ferrari and Robertson, 2000; Guedes et al., 2010; Ostadhassan et al., 2018).

It should be noted, band separation increases with a higher rate at lower maturities. This has been explained by the fact that organic matter cracks with different rate before and after the peak oil window which is now reflected in Raman signals as well (Kelemen and Fang, 2001; Gao et al., 2017; Ostadhassan et al., 2018; Khatibi et al., 2018b).

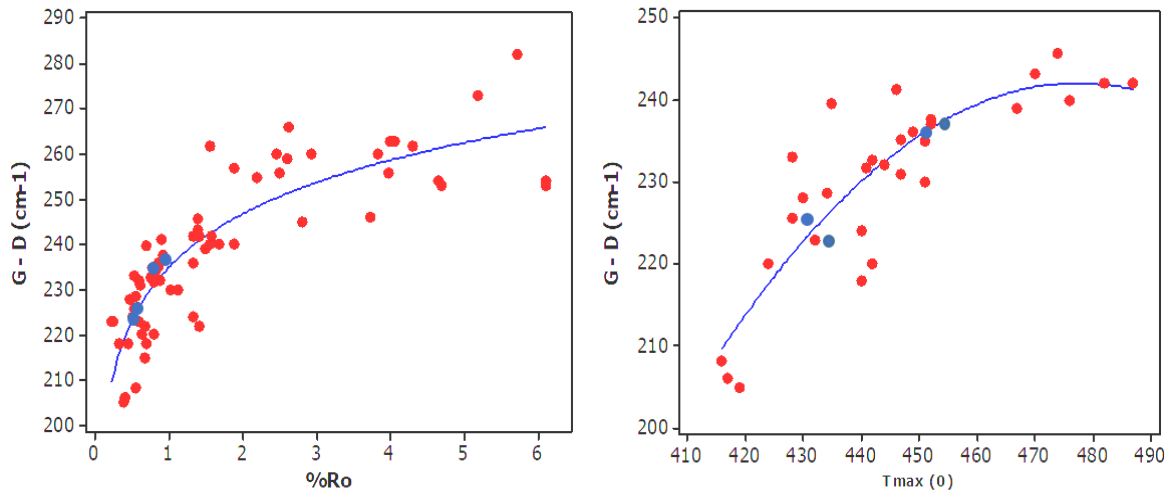


Figure 3-4-1 Band separation versus two common maturity indicators: (left) %Ro and (right) Tmax for different fields. Data are extracted from (Spötl et al., 1998; Kelemen and Fang, 2001; Sauerer et al., 2017). Blue circles are data from this study and red ones are from the literature.

In addition to understanding the thermal maturity of organic matter, its production potential regarding Rock-Eval parameters such as S1, S2 and production index (PI) is also important in evaluating productive intervals. As mentioned before, S1 is the amount of free hydrocarbons (gas and oil) already in the sample (in milligrams of hydrocarbon per gram of rock) which can be detected at 350°C (initial heating stage) (Behar et al., 2001; Baudin et al., 2015). S2 is the quantity of hydrocarbons that will be generated through pyrolysis (550°C). Production index is the ratio of generated hydrocarbons to potential hydrocarbons that can be produced, Equation 3 (Laughrey et al., 2013; Ma and Holditch, 2015), which can give an insight about the kerogen conversion level when is plotted vs. Tmax. Figure 3-4-2 shows that our samples are in a low level of conversion stage.

$$PI = S1 \left( \frac{mg\ HC}{g\ rock} \right) / \left( S1 \left( \frac{mg\ HC}{g\ rock} \right) + S2 \left( \frac{mg\ HC}{g\ rock} \right) \right) \quad (3)$$

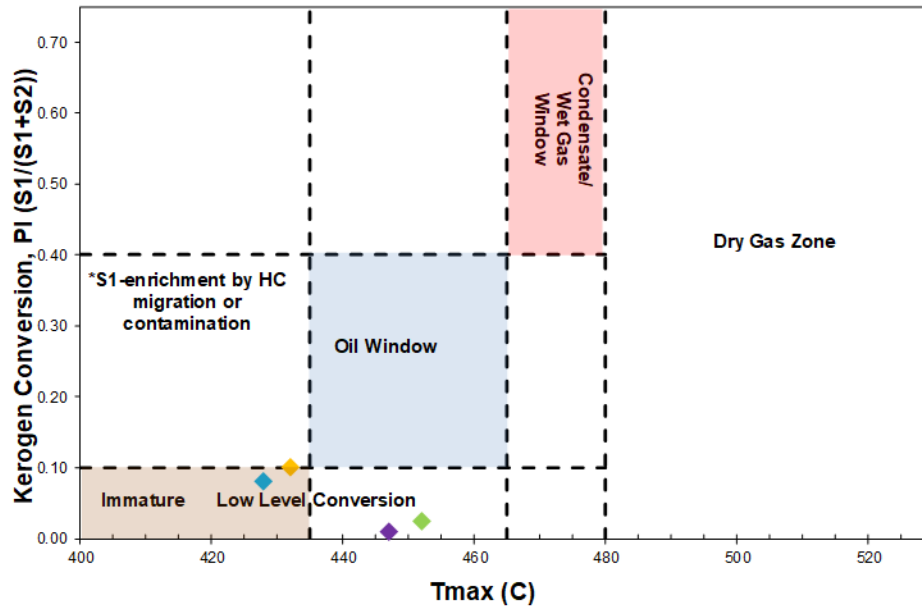


Figure 3-4-2 PI vs. Tmax for samples in the study. Such graph helps to understand conversion level of organic matter.

In the kerogen structure, aromatics linked by aliphatic and heteroatoms (Kelemen and Fang, 2001), in which solid bitumen can be trapped (Wopenka and Pasteris, 1993; Jehlicka et al., 2003). The increase in carbon aromaticity which takes place during maturation has been also detected during natural maturation caused by igneous intrusions (Dennis et al., 1982; Saxby and Stephenson, 1987; Kuangzong et al., 1991; Patience et al., 1992; Wei et al., 2005; Clough et al., 2015), or by the increase in depth of burial (Miknis, 1982; Barwise et al., 1984; Solli et al., 1984).

Fortunately, the complex structure of kerogen correlates strongly with its maturity. As hydrocarbon is being generated, aliphatic carbon linkages are lost (reduction in HI is a good indication of the reduction in aliphatic carbon). The main contributor in the process of hydrocarbon generation is aliphatic (Orr, 1981; Miknis and Smith, 1984; Hagaman et al., 1984; Schenk et al., 1986; Witte et al., 1988; Gao et al., 2017) which can be attributed to S2, since they are both representing kerogen potential hydrocarbon production. Such structural evolution can be monitored by different spectroscopy methods (Quirico et al., 2005; Marshall et al., 2007).

For instance, Infrared Spectroscopy (IR) showed the decrease in that aliphatic concentrations with maturity (Witte et al., 1998). In another study, quantitative  $^{13}\text{C}$  DP MAS NMR spectrum was used on samples exposed to the hydrous pyrolysis, results showed aliphatic groups are the important compound which is contributing to the hydrocarbon generation (Ostadhassan et al., 2018; Gao et al., 2017).

FTIR is an analytical technique to identify chemical compounds in organic materials as a complimentary tool to Raman spectroscopy by measuring the absorption of infrared (IR) light due to molecular vibrations of the sample. The spectrum of IR absorption is used as a fingerprint of a chemical substance and reports the existing functional groups. The peaks correspond to the frequencies of vibrations and the amplitude is a direct indication of the amount that is present in the material. In our study, FTIR was performed on pure kerogen (to avoid the influence of the inorganic mineral matter) from Well B and Well D which illustrated a qualitative and quantitative change in aromatic and aliphatic content with respect to the maturity. It is important to remember that these two samples have %VRo 0.59 and %VRo 0.92, respectively, reflecting lower and higher maturity levels, Figure 3-4-3. It can be found that sample with %VRo 0.59 has a higher peak for aliphatic groups, while a sample with %VRo 0.92 has higher peaks for aromatic carbons.

Using high-resolution transmission electronic microscope (TEM) also showed such change in kerogen molecular structure specifically clustering of aromatics (Quirico et al., 2005; Beyssac et al., 2002). Kerogen that was isolated from the sample of Well D, which has the highest maturity, was imaged in a novel approach under Hitachi HD-2300A Dual EDS Cryo STEM (scanning transmission electron microscope), Figure 3-4-4. The image revealed the imperfect stacked aromatic layers in the sample with higher maturity. We were not able to capture the same image for lower maturity samples.

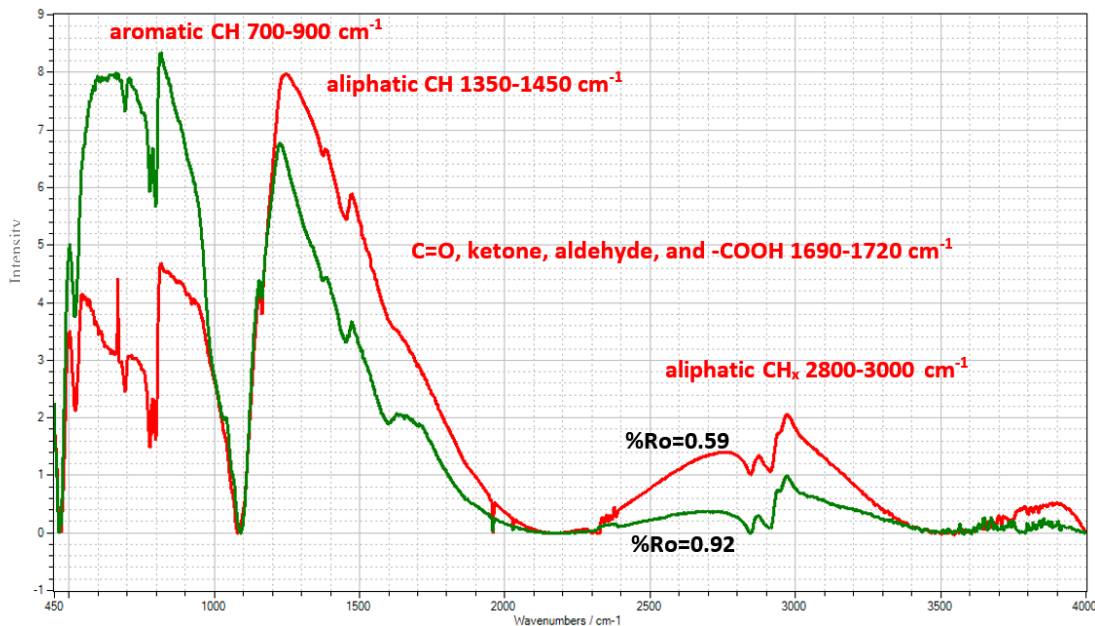
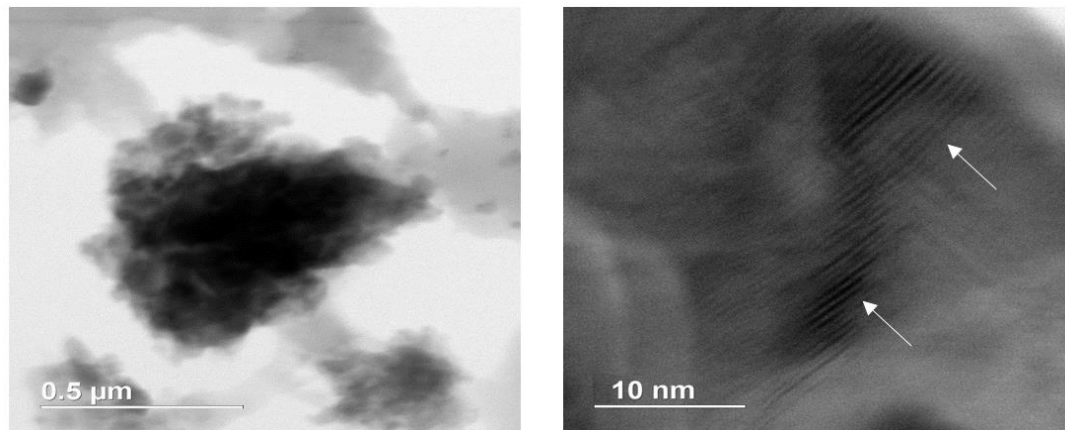


Figure 3-4-3 FTIR of Well A (red) and Well D (green) as lowest and highest mature samples in this study. Note Aliphatic C–H, C–H<sub>2</sub> and CH<sub>3</sub> decrease, Aromatic C=C and C–H (either 2 neighboring or 4 neighboring) increase. (Band assignments for the

*infrared spectra were based on literature (Painter et al., 1981; Solomon et al., 1988; Chen et al., 1998; Painter et al., 2012; Chen et al., 2015; Craddock et al., 2015).*



*Figure 3-4-4 Image of isolated kerogen for Well D with two different scales of: (left) 0.5 μm and (right) 10 nm captured by STEM. The image on the right shows imperfect stacked aromatic layer in the sample. By increasing maturity, aromatics stack and make larger clusters.*

Raman spectroscopy can detect such structural change as well which might have the potential to replace with conventional and bulk methods approaches which are usually exhaustive and time consuming for sample preparation and performing the measurement.

The origin of the G is due to the inplane  $E_{2g}$  vibrational modes of the carbon atoms in aromatic ring structures (Beysac et al., 2002; Beysac et al., 2003; Sauerer et al., 2018; Khatibi et al., 2018a,b). If the structure of organic matter has high aromatic content, it is corresponding to less potential of hydrocarbon production, thus, S2 can be correlated to the G band as aromatic indicator, Figure 3-4-5. As mentioned earlier, it has been shown G band shifts slightly towards higher shifts by increasing maturity concurrent with the increase in aromaticity (Kelemen and Fang, 2001). The negative correlation between S2 and the G band is a result of this matter.

Furthermore, Abundance of aromatic structures in conjunction with high maturity corresponds to lower hydrogen content (Van Krevelen, 1993), Figure 3-4-6. Therefore, HI (Hydrogen Index) could be correlated with G band position, Figure 3-4-6.

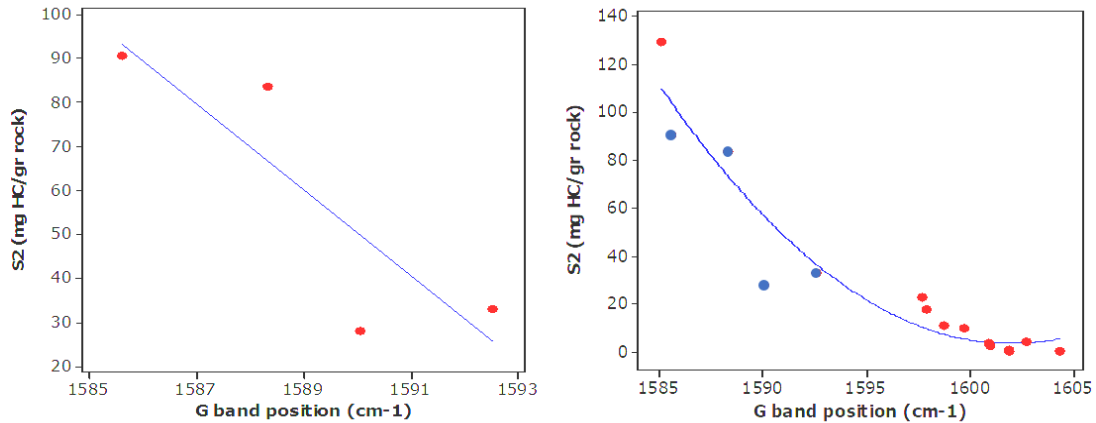


Figure 3-4-5 (left) Correlation of S2 with G band from Raman spectrum of four samples in this study. (right) The same plot using data from other sources (red circles) including samples in this study (blue circles) and (Cheshire et al., 2017; Sauerer et al., 2017) with 87% R2. Note the negative correlation which corresponds to less potential of production by increasing aromaticity.

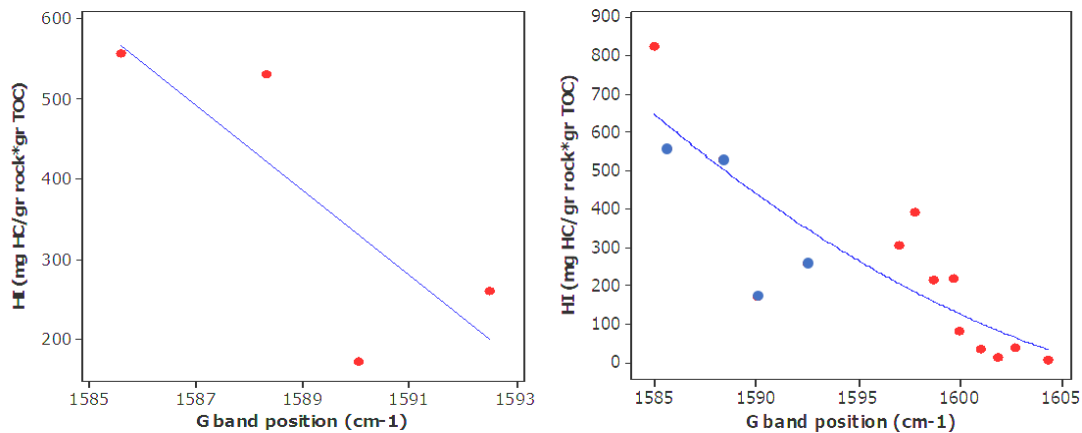


Figure 3-4-6 (left) Correlation of HI from Rock-Eval with G band position of four samples in this study. (right) The same plot using data from other sources (red circles) (Sauerer et al., 2017; Cheshire et al., 2017; Craddock et al., 2017) including samples in this study (blue circles) with R2 75%. HI for data from other sources were calculated based on the definition, as they did not report HI directly. Note the negative correlation which corresponds to less hydrogen content of organic matter by increasing aromaticity.

By increasing maturation and consequently hydrocarbon production, the heteroatom-rich OM lose their oxygenated/hydrogenated group (Oberlin et al., 1980; Oberlin, 1989; Rouzaud and Oberlin, 1989), as a consequence attachment that separate from aromatic carbons increase (Khatibi et al., 2017b; Kelemen et al., 2007). The D band signals ( $\sim 1350 \text{ cm}^{-1}$ ) refers to a disorder in the atoms representing discontinuities and defects of the  $\text{sp}^2$  carbon network, for instance as in heteroatoms (Khatibi et al., 2017b; Sauerer et al., 2017). Consequently, D band can be utilized as an indicator of attachments separated from OM which is happening while hydrocarbon generation. Thus, already generated hydrocarbon(S1) can be correlated with D band, Figure 3-4-7. According to previous studies (Guedes et al., 2010; Schito et al., 2017), when maturity increases, the D band shifts towards lower wavenumber ( $1370$  to  $1330 \text{ cm}^{-1}$ ) and displays lower intensities. This is

relatable to the increase of separating attachments from aromatic groups and transforming the organic matter from disordered state to more ordered molecule (Khatibi et al., 2018c). The disappearance of the D band in uppermost stage of maturity also verifies this phenomenon.

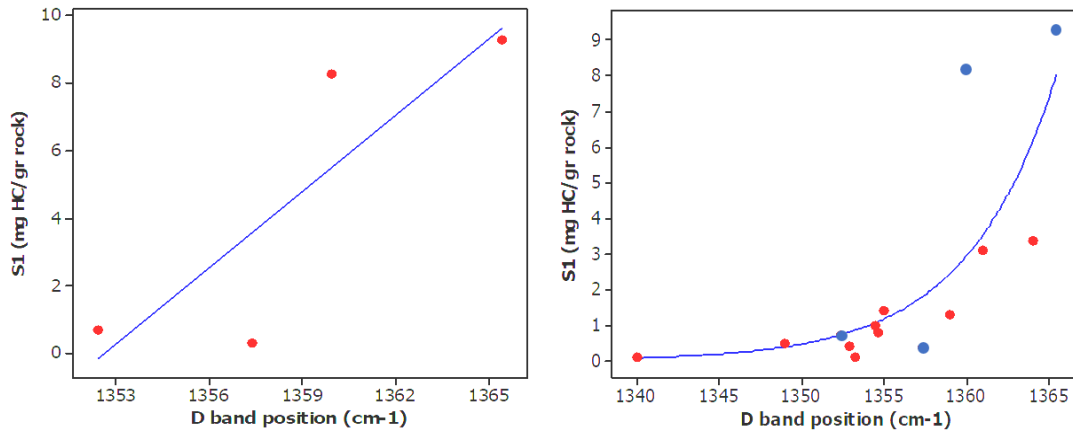


Figure 3-4-7 (left) Correlation of S1 with D band of four samples in this study. (right) The same plot using data from other sources (red circles) (Cheshire et al., 2017; Sauerer et al., 2017; Craddock et al., 2018) including samples in this study (blue circles) with 71% R<sup>2</sup>.

Correlating S1 and S2 with G and D band positions, provides us with a path to correlate the PI from Rock-Eval with PI derived from Raman signals based on the definition of PI (Equation 3), Figure 3-4-8.

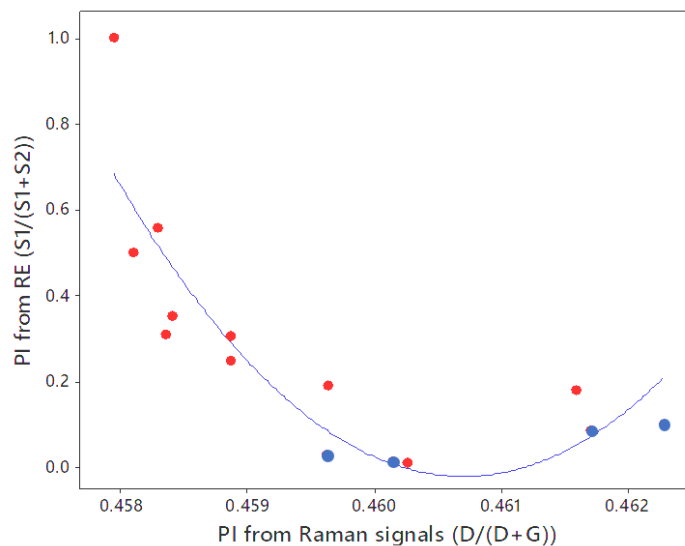


Figure 3-4-8 Correlation between PI from Rock-Eval and PI based on definition using Raman signals. Data from other sources (red circles) (Sauerer et al., 2017; Cheshire et al., 2017; Craddock et al., 2017) including samples in this study (blue circles) with 78% R<sup>2</sup>. PI data from other sources were calculated based on the definition, as they did not report PI directly.

Results from this study indicated that the maturation process of organic matter can be described as a nonlinear growth of aromatic clusters thus a disappearance of disordered molecules. Moreover,

Raman spectroscopy is directly dependent to the presence of various organic compounds with different structures in the organic matter. This makes it suitable and a good instrument that has the potential to yield significant information about the maturity levels of the organic matter. Having a good insight into the thermal maturity can lead to better realize the production potential of the organic matter. Additionally, integration of different analytical methods can assist researchers to study the molecular changes that kerogen will suffer during maturation process. The results from these studies will improve the efforts to build kerogen models considering fractions of various carbons at different maturities. Finally, it should be mentioned that Rock-Eval pyrolysis is usually suggested to be done on the samples approximately taken every 30 ft. (~10 m) in each well (Lafargue et al., 1998). Certainly, when it comes to the assessment of unconventional targets, closer sample spacing of 3 ft. (~1 m) is suggested to properly identify sweet spots. Considering the huge amount of analysis that is required to study these number of samples, Raman spectroscopy, can be replaced by pyrolysis. Raman spectroscopy is a fast and nondestructive equipment to create the profile of maturity, S1, S2 and PI and accelerate the analysis with good precision. Moreover, it has been shown that organic matter has a non-negligible effect on hydraulic fracturing of organic rich unconventional reservoirs (He et al., 2016; Wu et al., 2016; Zhao et al., 2016; Zhai et al., 2017; Khatibi et al., 2018c; Song et al., 2018; Zhu et al., 2018; He et al., 2018; ) [91-98], therefore such fast methods to characterize organic matter can be useful in geomechanical simulation of hydraulic fracturing operations.

This study was a preliminary effort and was done on a limited number of samples. Specifically, the STEM imaging was done based on a try an error operation since there is not any similar studies or known procedures to follow. We will continue this research by adding a greater number of samples for pyrolysis, Raman and FTIR. Creating a good database of Gas Chromatograph data is highly recommended and underway in next project.

### 3-5 Conclusions

Samples from four wells in the Bakken Formation were studied using a series of analytical techniques including Raman spectroscopy, RE pyrolysis, %VRO and FTIR. Then, we captured aromatic molecules under STEM to confirm our conclusions from these analytical tools. This was done in order to complete a set of information that can provide a precise and fast method to relate molecular structure of kerogen to its maturity and production potential.

Since this study was mainly focused on the applications of Raman spectroscopy to give a better insight into molecular structure of organic matter, thus, to avoid possible erroneous Raman signals and reduce the background noise, the study was performed on isolated kerogen material. This resulted in a better visible signal and more accurate results. Based on this study, we proposed that Raman spectroscopy has a good potential to predict the kerogen maturity, S1, S2, and Productivity index that is normally extracted from Rock-Eval pyrolysis and give us a better insight about molecular structure of organic matter. This method suggests a quick but precise approach to understand kerogen production potential, which is necessary to be evaluated for unconventional reservoirs. This study is underway on higher maturity samples with different kerogen types to support our methodology of integrating STEM imaging techniques and Raman spectroscopy.

### 3-6 References

Hutton, A., Bharati, S., Robl, T., 1994. Chemical and petrographic classification of kerogen/macerals. *Energy & Fuels* 8, 1478-1488.

McCarthy, K., Rojas, K., Niemann, M., Palmowski, D., Peters, K., Stankiewicz, A., 2011. Basic petroleum geochemistry for source rock evaluation. *Oilfield Review* 23, 32-43.

Wang, Zhouhua, Yun Li, Huang Liu, Fanhua Zeng, Ping Guo, and Wei Jiang. "Study on the Adsorption, Diffusion and Permeation Selectivity of Shale Gas in Organics." *Energies* 10, no. 1 (2017): 142.

Hackley, P.C., Araujo, C.V., Borrego, A.G., Bouzinos, A., Cardott, B.J., Cook, A.C., Eble, C., Flores, D., Gentzis, T., Gonçalves, P.A., 2015. Standardization of reflectance measurements in dispersed organic matter: Results of an exercise to improve interlaboratory agreement. *Marine and Petroleum Geology* 59, 22-34.

Sauerer, B., Craddock, P.R., AlJohani, M.D., Alsamadony, K.L., Abdallah, W., 2017. Fast and accurate shale maturity determination by Raman spectroscopy measurement with minimal sample preparation. *International Journal of Coal Geology* 173, 150-157.

Clementz, D.M., 1979. Effect of oil and bitumen saturation on source-rock pyrolysis: GEOLOGIC NOTES. *AAPG Bulletin* 63, 2227-2232.

Larter, S., Douglas, A., 1980. A pyrolysis-gas chromatographic method for kerogen typing. *Physics and Chemistry of the Earth* 12, 579-583.

Peters, K., 1986. Guidelines for evaluating petroleum source rock using programmed pyrolysis. *AAPG bulletin* 70, 318-329.

Lafargue, E., Marquis, F., Pillot, D., 1998. Rock-Eval 6 applications in hydrocarbon exploration, production, and soil contamination studies. *Revue de l'institut français du pétrole* 53, 421-437.

## Chapter 3

Behar, F., Beaumont, V., Penteadó, H.D.B., 2001. Rock-Eval 6 technology: performances and developments. *Oil & Gas Science and Technology* 56, 111-134.

Espitalie, J., Deroo, G., Marquis, F., 1985. Rock-Eval pyrolysis and its applications. *Revue De L Institut Francais Du Petrole* 40, 563-579.

Tissot, B.P., Welte, D.H., 1984. Diagenesis, catagenesis and metagenesis of organic matter, *Petroleum Formation and Occurrence*. Springer, pp. 69-73.

Waples, D.W., 1981. *Organic geochemistry for exploration geologists*. Burgess Pub. Co.

Tyson, R.V., 1995. Abundance of organic matter in sediments: TOC, hydrodynamic equivalence, dilution and flux effects, *Sedimentary organic matter*. Springer, pp. 81-118.

Kelemen, S., Fang, H., 2001. Maturity trends in Raman spectra from kerogen and coal. *Energy & fuels* 15, 653-658.

Beysac, O., Goffé, B., Chopin, C., Rouzaud, J., 2002. Raman spectra of carbonaceous material in metasediments: a new geothermometer. *Journal of metamorphic Geology* 20, 859-871.

Quirico, E., Rouzaud, J.-N., Bonal, L., Montagnac, G., 2005. Maturation grade of coals as revealed by Raman spectroscopy: Progress and problems. *Spectrochimica Acta Part A: Molecular and Biomolecular Spectroscopy* 61, 2368-2377.

Lahfid, A., Beysac, O., Deville, E., Negro, F., Chopin, C., Goffé, B., 2010. Evolution of the Raman spectrum of carbonaceous material in low-grade metasediments of the Glarus Alps (Switzerland). *Terra Nova* 22, 354-360.

Guedes, A., Valentim, B., Prieto, A., Noronha, F., 2012. Raman spectroscopy of coal macerals and fluidized bed char morphotypes. *Fuel* 97, 443-449.

Hinrichs, R., Brown, M.T., Vasconcellos, M.A., Abrashev, M.V., Kalkreuth, W., 2014. Simple procedure for an estimation of the coal rank using micro-Raman spectroscopy. *International Journal of Coal Geology* 136, 52-58.

Wilkins, R.W., Boudou, R., Sherwood, N., Xiao, X., 2014. Thermal maturity evaluation from inertinites by Raman spectroscopy: the 'RaMM' technique. *International Journal of Coal Geology* 128, 143-152.

Zhou, Q., Xiao, X., Pan, L., Tian, H., 2014. The relationship between micro-Raman spectral parameters and reflectance of solid bitumen. *International Journal of Coal Geology* 121, 19-25.

Lünsdorf, N.K., 2016. Raman spectroscopy of dispersed vitrinite—Methodical aspects and correlation with reflectance. *International Journal of Coal Geology* 153, 75-86.

Mumm, A.S., İnan, S., 2016. Microscale organic maturity determination of graptolites using Raman spectroscopy. *International Journal of Coal Geology* 162, 96-107.

Ferralis, N., Matys, E.D., Knoll, A.H., Hallmann, C., Summons, R.E., 2016. Rapid, direct and non-destructive assessment of fossil organic matter via microRaman spectroscopy. *Carbon* 108, 440-449.

## Chapter 3

Khatibi, Seyedalireza, Mehdi Ostadhassan, David Tuschel, Thomas Gentzis, Bailey Bubach, and Humberto Carvajal-Ortiz. "Raman spectroscopy to study thermal maturity and elastic modulus of kerogen." *International Journal of Coal Geology* 185 (2018): 103-118.

Khatibi, S., M. Ostadhassan, and A. Aghajanpour. "Raman spectroscopy: an analytical tool for evaluating organic matter." *J Oil Gas Petrochem Sci* 1, no. 1 (2018): 28-33.

Beysac, O., Goffé, B., Petitet, J.-P., Froigneux, E., Moreau, M., Rouzaud, J.-N., 2003. On the characterization of disordered and heterogeneous carbonaceous materials by Raman spectroscopy. *Spectrochimica Acta Part A: Molecular and Biomolecular Spectroscopy* 59, 2267-2276.

LeFever, J.A., 1991. History of oil production from the Bakken Formation, North Dakota.

Smith, M.G., Bustin, R.M., 2000. Late Devonian and Early Mississippian Bakken and Exshaw black shale source rocks, Western Canada Sedimentary Basin: a sequence stratigraphic interpretation. *AAPG bulletin* 84, 940-960.

Parapuram, George, Mehdi Mokhtari, and Jalel Ben Hmida. "An Artificially Intelligent Technique to Generate Synthetic Geomechanical Well Logs for the Bakken Formation." *Energies* 11, no. 3 (2018): 680.

Webster, R.L., 1984. Petroleum source rocks and stratigraphy of the Bakken Formation in North Dakota.

Smith, M.G., Bustin, R.M., 1995. Sedimentology of the Late Devonian and Early Mississippian Bakken Formation, Williston Basin. *Williston Basin Symposium*.

Liu, K., Ostadhassan, M., Gentzis, T., Carvajal-Ortiz, H., Bubach, B., 2017. Characterization of geochemical properties and microstructures of the Bakken Shale in North Dakota. *International Journal of Coal Geology*.

Sonnenberg, S.A., Pramudito, A., 2009. Petroleum geology of the giant Elm Coulee field, Williston Basin. *AAPG bulletin* 93, 1127-1153.

Jin, H., Sonnenberg, S.A., 2013. Characterization for source rock potential of the Bakken Shales in the Williston Basin, North Dakota and Montana. *Unconventional Resources Technology Conference (URTEC)*.

Gaswirth, S.B., Marra, K.R., Cook, T.A., Charpentier, R.R., Gautier, D.L., Higley, D.K., Klett, T.R., Lewan, M.D., Lillis, P.G., Schenk, C.J., 2013. Assessment of undiscovered oil resources in the bakken and three forks formations, Williston Basin Province, Montana, North Dakota, and South Dakota, 2013. *US Geological Survey*.

Jacob, H., 1989. Classification, structure, genesis and practical importance of natural solid oil bitumen ("migrabitumen"). *International Journal of Coal Geology* 11, 65-79.

Jarvie, D., Claxton, B., Henk, B., Breyer, J., 2001. Oil and shale gas from Barnett shale, Ft. Worth Basin, TX, Poster presented at the AAPG National Convention, Denver, CO.

Schito, A., Romano, C., Corrado, S., Grigo, D., Poe, B., 2017. Diagenetic thermal evolution of organic matter by Raman spectroscopy. *Organic Geochemistry* 106, 57-67.

## Chapter 3

Robl, T.L., Davis, B.H., 1993. Comparison of the HF-HCl and HF-BF<sub>3</sub> maceration techniques and the chemistry of resultant organic concentrates. *Organic Geochemistry* 20, 249-255.

Schimmelmann, A., Lewan, M.D., Wintsch, R.P., 1999. D/H isotope ratios of kerogen, bitumen, oil, and water in hydrous pyrolysis of source rocks containing kerogen types I, II, IIS, and III. *Geochimica et Cosmochimica Acta* 63, 3751-3766.

Amer, M., 2009. Raman spectroscopy for soft matter applications. John Wiley & Sons.

Tuinstra, F., Koenig, J.L., 1970. Raman spectrum of graphite. *The Journal of Chemical Physics* 53, 1126-1130.

Wang, Y., Alsmeyer, D.C., McCreery, R.L., 1990. Raman spectroscopy of carbon materials: structural basis of observed spectra. *Chemistry of Materials* 2, 557-563.

Reich, S., Thomsen, C., 2004. Raman spectroscopy of graphite. *Philosophical Transactions of the Royal Society of London A: Mathematical, Physical and Engineering Sciences* 362, 2271-2288.

Cesare, B., Maineri, C., 1999. Fluid-present anatexis of metapelites at El Joyazo (SE Spain): constraints from Raman spectroscopy of graphite. *Contributions to Mineralogy and Petrology* 135, 41-52.

Marshall, C.P., Edwards, H.G., Jehlicka, J., 2010. Understanding the application of Raman spectroscopy to the detection of traces of life. *Astrobiology* 10, 229-243.

Tuschel, D., 2013. Raman spectroscopy of oil shale. *Spectroscopy* 28, 5.

Huang, E.-P., Huang, E., Yu, S.-C., Chen, Y.-H., Lee, J.-S., Fang, J.-N., 2010. In situ Raman spectroscopy on kerogen at high temperatures and high pressures. *Physics and Chemistry of Minerals* 37, 593-600.

Marshall, C.P., Love, G.D., Snape, C.E., Hill, A.C., Allwood, A.C., Walter, M.R., Van Kranendonk, M.J., Bowden, S.A., Sylva, S.P., Summons, R.E., 2007. Structural characterization of kerogen in 3.4 Ga Archaean cherts from the Pilbara Craton, Western Australia. *Precambrian Research* 155, 1-23.

Lünsdorf, N.K., Dunkl, I., Schmidt, B.C., Rantitsch, G., Eynatten, H., 2014. Towards a higher comparability of geothermometric data obtained by Raman spectroscopy of carbonaceous material. Part I: evaluation of biasing factors. *Geostandards and Geoanalytical Research* 38, 73-94.

Spötl, C., Houseknecht, D.W., Jaques, R.C., 1998. Kerogen maturation and incipient graphitization of hydrocarbon source rocks in the Arkoma Basin, Oklahoma and Arkansas: a combined petrographic and Raman spectrometric study. *Organic Geochemistry* 28, 535-542.

Ferrari, A.C., Robertson, J., 2000. Interpretation of Raman spectra of disordered and amorphous carbon. *Physical review B* 61, 14095.

Guedes, A., Valentim, B., Prieto, A., Rodrigues, S., Noronha, F., 2010. Micro-Raman spectroscopy of collotelinite, fusinite and macrinite. *International Journal of Coal Geology* 83, 415-422.

Ostadhassan, Mehdi, Kouqi Liu, Chunxiao Li, and Seyedalireza Khatibi. *Fine Scale Characterization of Shale Reservoirs: Methods and Challenges*. Springer, 2018.

## Chapter 3

- Gao, Y., Zou, Y.-R., Liang, T., Peng, P.a., 2017. Jump in the structure of Type I kerogen revealed from pyrolysis and  $^{13}\text{C}$  DP MAS NMR. *Organic Geochemistry* 112, 105-118.
- Baudin, F., Disnar, J.-R., Aboussou, A., Savignac, F., 2015. Guidelines for Rock–Eval analysis of recent marine sediments. *Organic Geochemistry* 86, 71-80.
- Laughrey, C., Kostelnik, J., Harper, J., Carter, K., 2013. The Pennsylvania petroleum source rock geochemistry database.
- Ma, Y.Z., Holditch, S., 2015. *Unconventional Oil and Gas Resources Handbook: Evaluation and Development*. Gulf Professional Publishing.
- Wopenka, B., Pasteris, J.D., 1993. Structural characterization of kerogens to granulite-facies graphite: applicability of Raman microprobe spectroscopy. *The American Mineralogist* 78, 533-557.
- Jehlicka, J., Urban, O., Pokorný, J., 2003. Raman spectroscopy of carbon and solid bitumens in sedimentary and metamorphic rocks. *Spectrochimica Acta Part A: Molecular and Biomolecular Spectroscopy* 59, 2341-2352.
- Dennis, L.W., Maciel, G.E., Hatcher, P.G., Simoneit, B.R., 1982.  $^{13}\text{C}$  Nuclear magnetic resonance studies of kerogen from Cretaceous black shales thermally altered by basaltic intrusions and laboratory simulations. *Geochimica et Cosmochimica Acta* 46, 901-907.
- Saxby, J., Stephenson, L., 1987. Effect of an igneous intrusion on oil shale at Rundle (Australia). *Chemical Geology* 63, 1-16.
- Kuangzong, Q., Deyu, C., Zhanguang, L., 1991. A new method to estimate the oil and gas potentials of coals and kerogens by solid state  $^{13}\text{C}$  NMR spectroscopy. *Organic Geochemistry* 17, 865-872.
- Patience, R., Mann, A., Poplett, I., 1992. Determination of molecular structure of kerogens using  $^{13}\text{C}$  NMR spectroscopy: II. The effects of thermal maturation on kerogens from marine sediments. *Geochimica et Cosmochimica Acta* 56, 2725-2742.
- Wei, Z., Gao, X., Zhang, D., Da, J., 2005. Assessment of thermal evolution of kerogen geopolymers with their structural parameters measured by solid-state  $^{13}\text{C}$  NMR spectroscopy. *Energy & Fuels* 19, 240-250.
- Clough, A., Sigle, J.L., Jacobi, D., Sheremata, J., White, J.L., 2015. Characterization of Kerogen and Source Rock Maturation Using Solid-State NMR Spectroscopy. *Energy & Fuels* 29, 6370-6382.
- Miknis, F., 1982. NMR studies of solid fossil fuels. *Magnetic Resonance Review* 7, 87-121.
- Barwise, A., Mann, A., Eglinton, G., Gowar, A., Wardroper, A., Gutteridge, C., 1984. Kerogen characterisation by  $^{13}\text{C}$  NMR spectroscopy and pyrolysis-mass spectrometry. *Organic geochemistry* 6, 343-349.
- Solli, H., Van Graas, G., Leplat, P., Krane, J., 1984. Analysis of kerogens of miocene shales in a homogenous sedimentary column. A study of maturation using flash pyrolysis techniques and carbon- $^{13}$  CP-MAS NMR. *Organic geochemistry* 6, 351-358.

## Chapter 3

Witte, E., Schenk, H., Müller, P., Schwochau, K., 1988. Structural modifications of kerogen during natural evolution as derived from  $^{13}\text{C}$  CP/MAS NMR, IR spectroscopy and Rock-Eval pyrolysis of Toarcian shales. *Organic geochemistry* 13, 1039-1044.

Miknis, F.P., Smith, J.W., 1984. An NMR survey of United States oil shales. *Organic geochemistry* 5, 193-201.

Hagaman, E.W., Cronauer, D.C., Schell, F.M., 1984. Oil-shale analysis by CP/MAS- $^{13}\text{C}$  NMR spectroscopy. *Fuel* 63, 915-919.

Schenk, H., Witte, E., Müller, P., Schwochau, K., 1986. Infrared estimates of aliphatic kerogen carbon in sedimentary rocks. *Organic geochemistry* 10, 1099-1104.

Orr, W., 1981. Comments on pyrolytic hydrocarbon yields in source-rock evaluation. *Advances in organic geochemistry* 1981, 775-787.

Beysac, O., Rouzaud, J.-N., Goffé, B., Brunet, F., Chopin, C., 2002. Graphitization in a high-pressure, low-temperature metamorphic gradient: a Raman microspectroscopy and HRTEM study. *Contributions to Mineralogy and Petrology* 143, 19-31.

Painter, P.C., Snyder, R.W., Starsinic, M., Coleman, M.M., Kuehn, D.W., Davis, A., 1981. Concerning the application of FT-IR to the study of coal: a critical assessment of band assignments and the application of spectral analysis programs. *Applied Spectroscopy* 35, 475-485.

Solomon, P.R., Carangelo, R.M., 1988. FT-ir analysis of coal: 2. Aliphatic and aromatic hydrogen concentration. *Fuel* 67, 949-959.

Chen, J., Luo, P., Li, J., 1998. Using kerogen FTIR parameters for determination of organic facies. *Chinese science bulletin* 43, 681-684.

Painter, P., Starsinic, M., Coleman, M., 2012. Determination of functional groups in coal by Fourier transform interferometry. *Fourier Transform Infrared Spectroscopy* 4, 169-240.

Chen, Y., Zou, C., Mastalerz, M., Hu, S., Gasaway, C., Tao, X., 2015. Applications of micro-Fourier transform infrared spectroscopy (FTIR) in the geological sciences—A review. *International journal of molecular sciences* 16, 30223-30250.

Craddock, P.R., Le Doan, T.V., Bake, K., Polyakov, M., Charsky, A.M., Pomerantz, A.E., 2015. Evolution of kerogen and bitumen during thermal maturation via semi-open pyrolysis investigated by infrared spectroscopy. *Energy & Fuels* 29, 2197-2210.

Van Krevelen, D., 1993. *Coal: Typology-Physics-Chemistry-Composition*. Elsevier, Amsterdam.

Cheshire, S., Craddock, P. R., Xu, G., Sauerer, B., Pomerantz, A. E., McCormick, D., & Abdallah, W. (2017). Assessing thermal maturity beyond the reaches of vitrinite reflectance and Rock-Eval pyrolysis: A case study from the Silurian Qusaiba formation. *International Journal of Coal Geology*, 180, 29-45.

Craddock, P. R., Prange, M., & Pomerantz, A. E. (2017). Kerogen thermal maturity and content of organic-rich mudrocks determined using stochastic linear regression models applied to diffuse reflectance IR Fourier transform spectroscopy (DRIFTS). *Organic Geochemistry*.

## Chapter 3

Oberlin, A., Boulmier, J., Villey, M., 1980. Electron microscopic study of kerogen microtexture. Selected criteria for determining the evolution path and evolution stage of kerogen. *Kerogen: Insoluble organic matter from sedimentary rocks*: Paris, Editions Technip, 191-241.

Oberlin, A., 1989. High-resolution TEM studies of carbonization and graphitization. *Chemistry and physics of carbon* 22, 1-143.

Rouzaud, J., Oberlin, A., 1989. Structure, microtexture, and optical properties of anthracene and saccharose-based carbons. *Carbon* 27, 517-529.

Kelemen, S., Afeworki, M., Gorbaty, M., Sansone, M., Kwiatek, P., Walters, C., Freund, H., Siskin, M., Bence, A., Curry, D., 2007. Direct characterization of kerogen by X-ray and solid-state <sup>13</sup>C nuclear magnetic resonance methods. *Energy & Fuels* 21, 1548-1561.

Khatibi, Seyedalireza, Azadeh Aghajanzpour, Mehdi Ostadhassan, Ebrahim Ghanbari, Ehsan Amirian, and Rehanali Mohammed. "Evaluating the Impact of Mechanical Properties of Kerogen on Hydraulic Fracturing of Organic Rich Formations." In *SPE Canada Unconventional Resources Conference*. Society of Petroleum Engineers, 2018.

Zhu, Wei, Xu Chang, Yibo Wang, Hongyu Zhai, and Zhenxing Yao. "Reconstruction of Hydraulic Fractures Using Passive Ultrasonic Travel-Time Tomography." *Energies* 11, no. 5 (2018): 1-17.

He, Jianming, Chong Lin, Xiao Li, and Xiaole Wan. "Experimental investigation of crack extension patterns in hydraulic fracturing with shale, sandstone and granite cores." *Energies* 9, no. 12 (2016): 1018.

He, Jianming, Lekan Olatayo Afolagboye, Chong Lin, and Xiaole Wan. "An Experimental Investigation of Hydraulic Fracturing in Shale Considering Anisotropy and Using Freshwater and Supercritical CO<sub>2</sub>." *Energies* 11, no. 3 (2018): 557.

Wu, Yusong, Xiao Li, Jianming He, and Bo Zheng. "Mechanical properties of longmaxi black organic-rich shale samples from south china under uniaxial and triaxial compression states." *Energies* 9, no. 12 (2016): 1088.

Zhao, Zhiheng, Xiao Li, Yu Wang, Bo Zheng, and Bo Zhang. "A Laboratory Study of the Effects of Interbeds on Hydraulic Fracture Propagation in Shale Formation." *Energies* 9, no. 7 (2016): 556.

Zhai, Hongyu, Xu Chang, Yibo Wang, Ziqiu Xue, Xinglin Lei, and Yi Zhang. "Sensitivity Analysis of Seismic Velocity and Attenuation Variations for Longmaxi Shale during Hydraulic Fracturing Testing in Laboratory." *Energies* 10, no. 9 (2017): 1393.

Song, Jing, Yu-Shuang Yang, Zhi-Qing Liu, and Xue Li. "Macro and Micro Properties of Organic Matter in Hydraulic Mud Consolidation." *Journal of Marine Science and Engineering* 6, no. 1 (2018): 22.

## **Chapter 4 Understanding Organic Matter Heterogeneity and Maturation Rate by Raman Spectroscopy**

A paper published in the **International journal of Coal Geology**

Seyedalireza Khatibi, Mehdi Ostadhassan, Paul Hackley, David Tuschel, Arash

Abarghani, Bailey Bubach

### **Abstract**

Solid organic matter (OM) in sedimentary rocks produces petroleum and solid bitumen when it undergoes thermal maturation. The solid OM is a ‘geomacromolecule’, usually representing a mixture of various organisms with distinct biogenic origins, and can have high heterogeneity in composition. Programmed pyrolysis is a common method to reveal bulk geochemical characteristics of the dominant OM, while detailed organic petrography is required to reveal information about the biogenic origin of contributing macerals. Despite advantages of programmed pyrolysis, it cannot provide information about the heterogeneity of chemical compositions present in the individual OM types. Therefore, other analytical techniques such as Raman spectroscopy are necessary.

In this study, we compared geochemical characteristics and Raman spectra of two sets of naturally and artificially matured Bakken source rock samples. A continuous Raman spectral map on solid bitumen particles was created from the artificially matured hydrous pyrolysis residues, in particular, to show the systematic chemical modifications in microscale. Spectroscopic data was plotted for both sets against thermal maturity to compare maturation rate/path for these two separate groups. The outcome showed that artificial maturation through hydrous pyrolysis does not follow the same trend as naturally-matured samples although having similar solid bitumen reflectance values (%SBRo).

Furthermore, Raman spectroscopy of solid bitumen from artificially matured samples indicated the heterogeneity of OM decreases as maturity increases. This may represent an alteration in chemical structure towards more uniform compounds at higher maturity. This study may emphasize the necessity of using analytical methods such as Raman spectroscopy along with conventional geochemical methods to better reveal the underlying chemical structure of OM. Finally, observation by Raman spectroscopy of chemical alteration of OM during artificial maturation may assist in the proposal of improved pyrolysis protocols to better resemble natural geologic processes.

**Keywords: Organic matter, Heterogeneity, Raman spectroscopy, Maturation rate, Hydrous pyrolysis**

## 4-1 Introduction

Shale is the most abundant fine-grained sedimentary rock and is formed from compaction of silt and clay-sized minerals which also may contain a significant amount of solid organic matter (OM). Kerogen (the insoluble portion of OM) is a macromolecule and a mixture of OM types with different origins (Types I, II, III and IV) (Garcette-Lepecq et al., 2000). When kerogen experiences maturation, weight concentration and the composition of the individual macerals evolve (Yang et al., 2017). During this process, bigger molecules will break down and the outcome will be hydrocarbons and bitumen in addition to water, CO<sub>2</sub> etc. (Schito et al., 2017). The remainder of the organic matter acts as the storage reservoir by developing nanoscale pores which hold generated hydrocarbons (Curtis et al., 2012; Chen and Xiao, 2014). Furthermore, the process of thermal maturation will cause or enhance the development of local heterogeneities within the remaining organic matter (Kong et al., 2018). This is due to differences in the rate of maturation for the existing kerogen based on differences in type and origin (Yang et al., 2017). Additionally, heterogeneity may also be due to local variations in thermal alteration that is imposed on organic matter by catalysis from nearby mineral grains (Pan et al., 2009). Understanding these heterogeneous patterns will enable better characterization of geochemical, petrophysical and geomechanical properties of organic matter from a molecular point of view (Curtis et al., 2012). In addition, these studies will enhance our understanding about mechanisms related to generation and migration of hydrocarbons, especially in self-sourced unconventional reservoirs.

Despite the importance of assessing shale OM heterogeneity, common bulk-rock geochemical measurement methods that have been utilized for decades such as programmed pyrolysis and LECO total organic carbon (TOC) are incapable of providing information specific to individual OM types. SEM (scanning electron microscope) analysis combined with energy-dispersive X-ray spectroscopy (SEM-EDS) can detect local changes in the abundance of higher atomic weight elements. However, it cannot recognize variations in molecular chemical components which are the driving force behind OM heterogeneity (Schumacher et al., 2005; Piani et al., 2012). Organic petrography allows identification of various types of organic components but cannot detect molecular compositions (Hackley and Cardott, 2016). Moreover, geochemistry of organic matter which is controlled by molecular compounds is usually investigated by pyrolysis which is artificially maturing the samples. Yet, to obtain meaningful results, many parameters (pyrogram) that are involved in the experiments should be set accurately to resemble a natural maturation path (Carvajal-Ortiz and Gentzis, 2015). This process can be done in the absence or presence of water, anhydrous pyrolysis (AHP) and hydrous pyrolysis (HP), respectively.

Lewan (1979) discussed and performed several experiments on the role of water in petroleum formation. He showed that AHP will result in higher organic maturation rate compared to HP at the same temperature conditions. Michels et al. (1995) discussed the effects of effluents and water pressure on oil generation during confined pyrolysis. Lewan and Ruble (2002) showed that there is no correlation between OM kinetic parameters derived from open-system pyrolysis and HP. Pan et al. (2009, 2010) illustrated the impact of water on the organic carbon ratio and mineral acidity during the conversion process of OM to hydrocarbons. They concluded that organic matter maturation rate slows down when a large amount of water is present. Further, Lewan and Roy (2011) explained significant differences in the types of products when water is involved at higher thermal maturity, noting that water promotes thermal cracking of bigger molecules over cross-linking. Other researchers have investigated the role of clay minerals in maturation, crude oil formation, migration and accumulation (Curtis et al., 2012; Chen and Xiao, 2014; Wu et al., 2012; Zhu et al., 2013; Hu et al., 2014; Kadoura et al., 2016). Such studies illustrated that the composition of petroleum is modified by interaction of clay minerals, and also the presence of water affects the role of minerals in acid-catalyzed cracking of kerogen. Despite advances in our understanding of these interactions, mimicking the natural condition of kerogen conversion to hydrocarbon remains poorly understood.

In a molecule, atoms are connected by chemical bonds, and thus have periodic motions. These motions relative to each other are superpositions of normal mode vibrations with the same phase and normal frequency (Schrader, 2008). The most effective methods to observe vibrational spectra as a signature representing a specific chemical compound are infrared and Raman spectrometry.

Kelemen and Fang (2001) showed the application of Raman spectroscopy for studying thermal maturity of OM, particularly in Silurian and older rocks where vitrinite is absent. Other researchers also have used Raman spectroscopy to reveal structural changes in organic matter during maturation (Ferrari and Robertson, 2000; Jehlička et al., 2003; Quirico et al., 2005; Guedes et al., 2012, Liu et al., 2013). Khatibi et al. (2018a, b, c, d) showed the potential application of Raman spectroscopy in correlating Raman signals to geochemical and mechanical properties of organic matter. They explained that changes in Young's modulus are representative of molecular alterations happening through thermal maturation. The application of Raman spectroscopy in qualitatively predicting geochemical properties of organic matter in terms of Rock-Eval parameters has also been studied (Khatibi et al., 2018a, b). Although Raman spectroscopy suffers from strong fluorescence background noise for immature shale samples, Khatibi et al (2018d) showed that solvent extraction will reduce the fluorescence background if combined with specific signal processing techniques.

In this study, heterogeneity within the organic matter, solid bitumen, as a result of thermal advance (natural and artificial) has been studied in the Bakken Formation source rock samples. All samples were evaluated by OM reflectance, programmed pyrolysis and Raman spectroscopy. Then, maturation paths of two groups of naturally and artificially matured samples were compared. Raman spectroscopy results showed that HP did not follow the same natural geological conditions in maturation rate. This study also demonstrates the potential of Raman spectroscopy to analyze OM in terms of the spatial heterogeneity of solid bitumen. The results can enable us to build more accurate petroleum system models for shale plays, and also to develop protocols for pyrolysis to better resemble natural maturation conditions.

### **4-2 Samples and methods**

Six samples were retrieved from the Bakken Formation as one of the most important source rocks in the Williston Basin, and consists of upper and lower organic-rich shales and a middle member

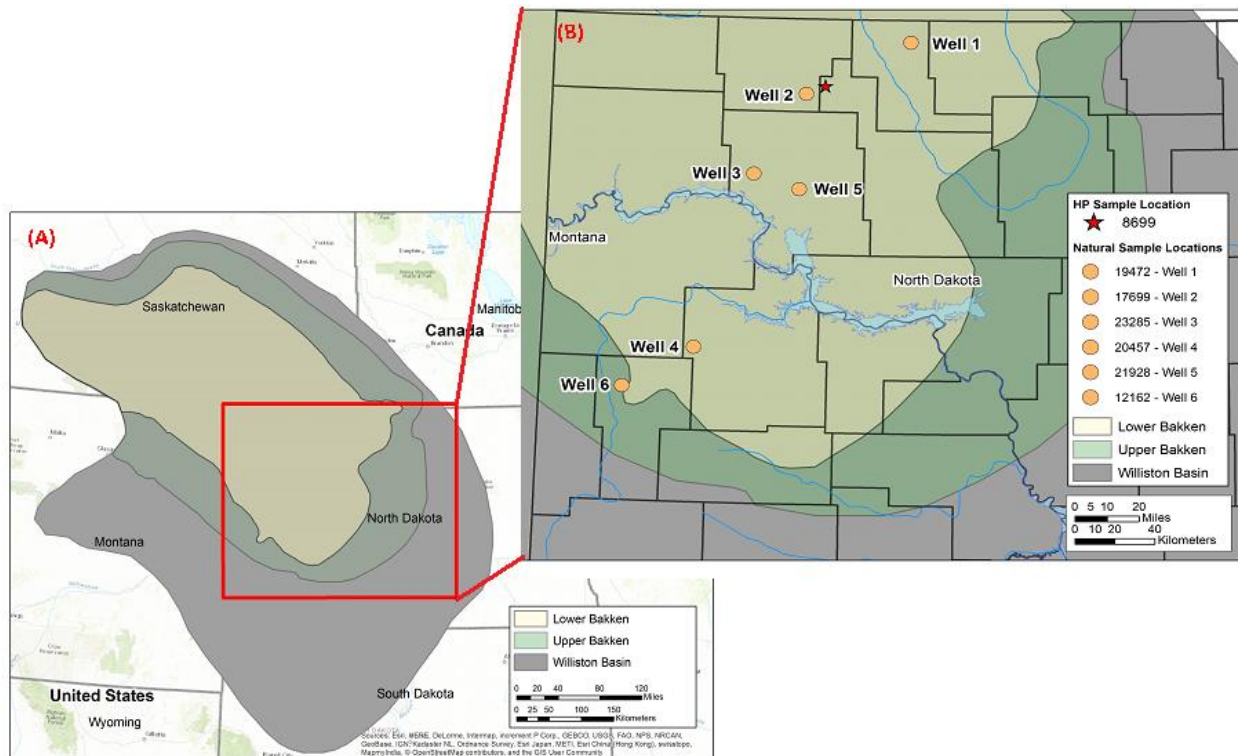
of very fine-grained dolomitic sandstone and siltstone that was deposited during the Late Devonian and Early Mississippian Periods (LeFever et al., 2011). Williston Basin is an elliptical shaped depression in the western portion of North Dakota, the northeastern region of Montana and extends into parts of Saskatchewan and Manitoba in Canada, Figure 4-2-1 (A). Upper and lower shales that are the source for the Middle Bakken which is the reservoir, have the same lithofacies type (E.g. Angulo and Buatois, 2012; Zhang and Buatois, 2014) and are considered to have been deposited under relatively deep marine (>200 meters depth) anoxic conditions (Steptoe, 2012). Six samples at different stages of thermal maturity varying from 0.38 to 0.98 %SBRo (Solid Bitumen reflectance) along with one immature sample (%SBRo of 0.32) that was artificially matured by HP to maximum maturity of 1.29 % SBRo were used in this study, Figure 4-2-1 (B). Geochemical analyses were performed by Rock-Eval 6, on both naturally and artificially matured samples, as summarized in Table 4-2-1.

Samples were prepared for petrographic analyses according to ASTM D2797 (ASTM, 2015a) wherein the rock particles were mounted in a thermoset plastic briquette, then ground and polished with successively finer abrasives until a 0.05-micrometer ( $\mu\text{m}$ ) finishing stage. Solid bitumen reflectance analyses followed ASTM D7708 (ASTM, 2015b). In this technique, incident white light 546  $\pm$  10 nm is reflected from solid bitumen positioned under the microscope crosshairs at 500x magnification, measured at a detector and compared to measured light reflected from a calibration standard. At least 20 measurements of solid bitumen reflectance were collected for each sample, with only 1 measurement per individual rock fragment. Since there was no reliable identification of primary vitrinite in the samples, mean random solid bitumen reflectance (%SBRo) is here reported in place of vitrinite reflectance, as practiced by many other workers (Jacob, 1989; Riediger, 1993; Jarvie et al., 2001; Hackley, 2012; Petersen et al., 2013; Valentine et al., 2014). Moreover, all analyses in the following sections were made on solid bitumen for better comparison purposes and consistency. Solid bitumen and vitrinite in shale are generally characterized as structureless gray substances in reflected white light, Figure 4-2-1 (C, D and E).

## Chapter 4

Table 4-2-1 Geochemical properties of two sets of Bakken samples: artificially matured by HP and naturally matured. Note the systematic changes in  $T_{max}$ , TOC, S2, HI, and PI with increasing maturity in both naturally and artificially matured samples.

	Sample No.	Depth (ft)	TOC (wt%)	S1 (mg HC/g)	S2 (mg HC/g)	$T_{max}$ (°)	HI ( $S2 \times 100 / TOC$ )	OI ( $S3 \times 100 / TOC$ )	PI ( $S1 / (S1 + S2)$ )	SBRo (%)	HP time (hrs.)	HP temp. (°C)
Artificially matured sample by HP	HP1		14.59	8.28	80.83	428	554	8	0.09	0.32	72	original
	HP2		13.3	4.5	72.02	429	542	10	0.06	0.35	72	280
	HP3		15.15	8	87.1	434	575	7	0.08	0.38	72	300
	HP4	7652	11.55	7.85	72.68	436	629	12	0.1	0.49	72	310
	HP5		10.66	6.78	53.47	431	502	9	0.11	0.54	72	320
	HP6		7.39	4.18	18.47	442	250	11	0.18	0.95	72	340
	HP7		8.12	3.19	11.16	451	137	12	0.22	1.19	72	350
	HP8		7.95	3.97	8.07	462	102	6	0.33	1.29	72	360
In situ matured samples	Well 1	5438	24.71	7.97	128.71	419	520	8	0.06	0.38	-	-
	Well 2	8326	16.27	8.27	90.69	428	557	2	0.08	0.54	-	-
	Well 3	9886	15.76	9.27	83.7	432	531	1	0.1	0.59	-	-
	Well 4	10555	13.26	0.31	33.01	449	260	1	0.013	0.86	-	-
	Well 5	10725.5	9.04	6.13	13.94	450	154	1	0.31	0.94	-	-
	Well 6	11199	16.36	0.71	28.05	452	171	1	0.024	0.92	-	-



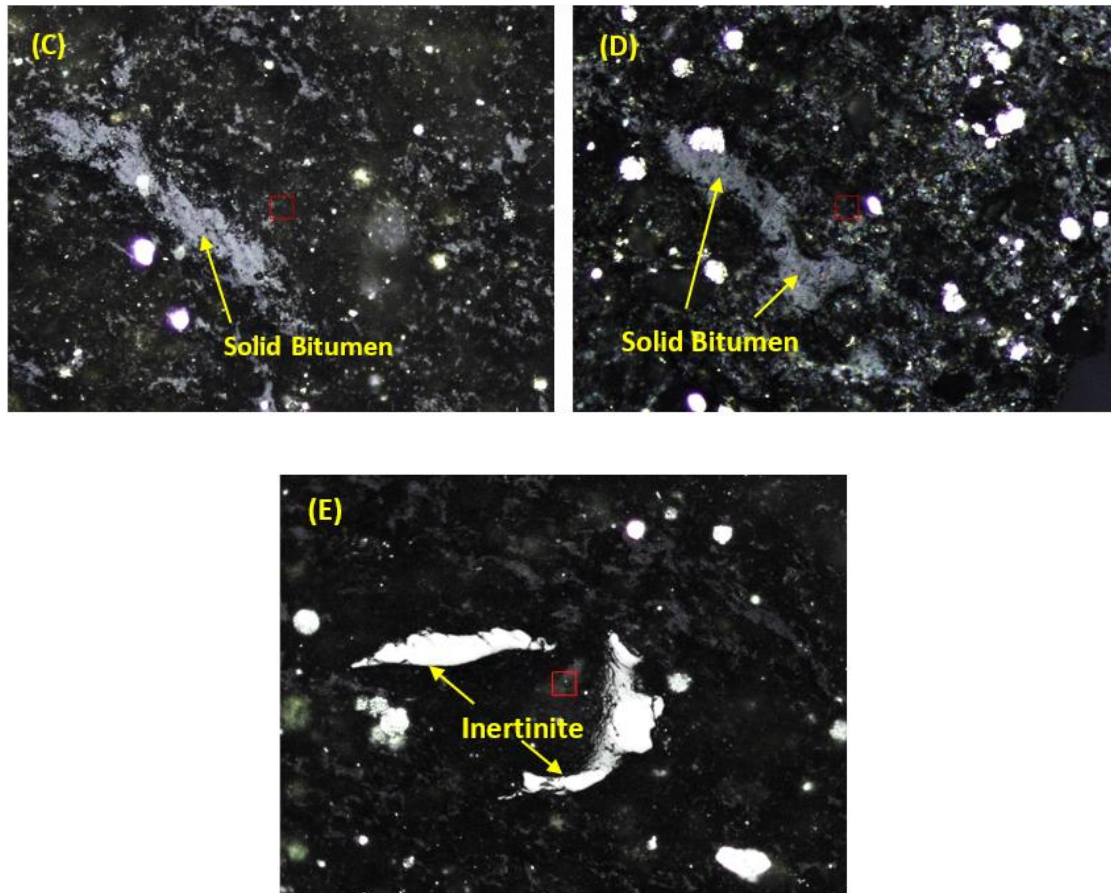


Figure 4-2-1 (A) and (B) location of the Bakken formation and the wells used in this study for sampling; (C) and (D) Solid bitumen in samples of Well 1 and Well 5, respectively, (E) occurrence of dispersed organic matter in the form of inertinite in Well 4. The red square in the middle of each image is a scale of 5  $\mu\text{m}$  of each side.

#### 4-2.1 Hydrous pyrolysis

In order to perform hydrous pyrolysis on the immature sample and generate results comparable to the natural maturation sequence, the sample was first homogenized (broken to smaller pieces and thoroughly mixed). Homogenization was performed to make sure every portion is representative of the same original sample. Then, each part was taken through the HP process at elevated temperatures (300–360 °C) based on the method of Lewan (1993, 1997) in which crushed rock samples (2-4 g) were loaded into reactors and covered with de-ionized water. The amount of water should cover the sample and also be in contact with it constantly at the maximum temperature for each step of the experiment. The amount of rock and water added to each experiment were calculated from rock densities, reactor internal volumes, and steam tables as described by Lewan (1993). The stainless steel (SS-316) SwageLok™ mini-reactor vessels [25-35 milliliter (mL) internal volume] were assembled from 1.5-inch tubing caps and plugs, sealing with ~270 foot-

pounds torque using Fel-Pro C5-A copper-based anti-seize thread lubricant. Once the reactor was sealed, it was placed into a gas chromatograph oven, and isothermally heated for 72 hrs. at 300-320-340-350-360 °C. It may take around 5-10 minutes for the oven to reach the experimental temperature which was not included in the main course of experiment durations. Pyrolyzed rock residues were removed and rinsed with acetone and then vacuum-dried overnight prior to preparations for further analyses.

#### **4-2.2 Raman Spectroscopy**

To generate the Raman spectrum, we illuminated the sample surface with monochromatic laser light. Raman mapping mode was acquired on the region of interest (ROI) where organic matter (solid bitumen) was detected. As the probe scanned the area, 1000 points were collected (2 spectra per  $1 \mu\text{m}^2$ ), Figure 4-2-2. The power of laser that was used for the acquisition of Raman data was 1 mW (1% of total laser power), with 1 second acquisition time, 3 seconds of accumulation which led to 3 mW.s of the energy dumped onto the surface of the sample. In terms of spectral precision, the grating (1200 grating/mm) was not moved from one spot to another; therefore, there was not any change in the spectral calibration. Moreover, the Raman spectrometer was calibrated before each data acquisition session using the  $520 \text{ cm}^{-1}$  Raman band of a silicon reference sample. The Si Raman band is an adjustment to an overall calibration of the spectrometer made with atomic emission lamps over the entire working spectral range of the spectrometer.

The benefit of using mapping mode is that statistical analysis can be used to estimate the shift of the major Raman bands of organic matter more accurately in microscale instead of acquiring a single Raman spectrum to represent the whole ROI. Furthermore, heterogeneity of OM composition can also be evaluated since a larger area is surveyed with a high spatial resolution. Moreover, one of the most important challenges regarding Raman spectroscopy is the fluorescence background which masks the Raman signal (Zhou et al., 2014; Myers et al., 2017). This issue is more critical while evaluating lower maturity samples due to the presence of high fluorescence intensity in OM, which is reduced at higher maturity (Lünsdorf, 2016; Sauerer et al., 2017). An appropriate processing technique can notably reduce the fluorescence background levels. For this purpose, a same polynomial baseline curve was fitted to the whole spectrum (from  $50 \text{ cm}^{-1}$  to  $2750 \text{ cm}^{-1}$ ) (Figure 4-2-3-left), which was the long wavelength function of the fluorescence, and then was subtracted from the spectrum (Figure 4-2-3-right). Lower order polynomial functions are less

flexible to adapt with the data and may not be able to include highly fluctuating backgrounds. Using this mathematical approach provides a flat zero baseline spectrum in order to pick Raman band positions in a more straightforward manner.

To improve signal to noise ratio (S/N) during Raman acquisition a binning procedure was used. In this process a number of adjacent spectra (binning factor) in the ROI were co-added to increase the signal to noise ratio as displayed in Figure 4-2-4. However, while using the binning factor, one should be cautious to avoid losing spectral features because of large binning. All spectra were collected with a frequency-doubled Nd:YAG 532 nm laser and the data were processed with the same background noise subtraction method explained earlier. Using 532 nm excitation with the MPlan 50X objective results in the beam diameter of 860 nm or 0.86 micrometers. The instrument was equipped with a 50X long working distance objective to easily locate the spot for Raman signal acquisition. Scan range of the instrument in mapping mode was  $120\ \mu\text{m} \times 120\ \mu\text{m}$  with step size of  $1.5\ \mu\text{m}$ .

It should be mentioned the sample for thermal alteration were checked by viewing spectra in 1-second real-time display and setting the laser power such that no changes in the spectra occurred over at least 20 seconds of laser illumination prior to acquisition of a spectrum. The stable spectrum throughout illumination indicated that no burning was occurring over that time period. Furthermore, the samples were viewed by white reflected light microscopy after the measurement looking for any visible signs of sample burning. The absence of any change in the appearance of the sample after laser illumination indicated that no burning had occurred.

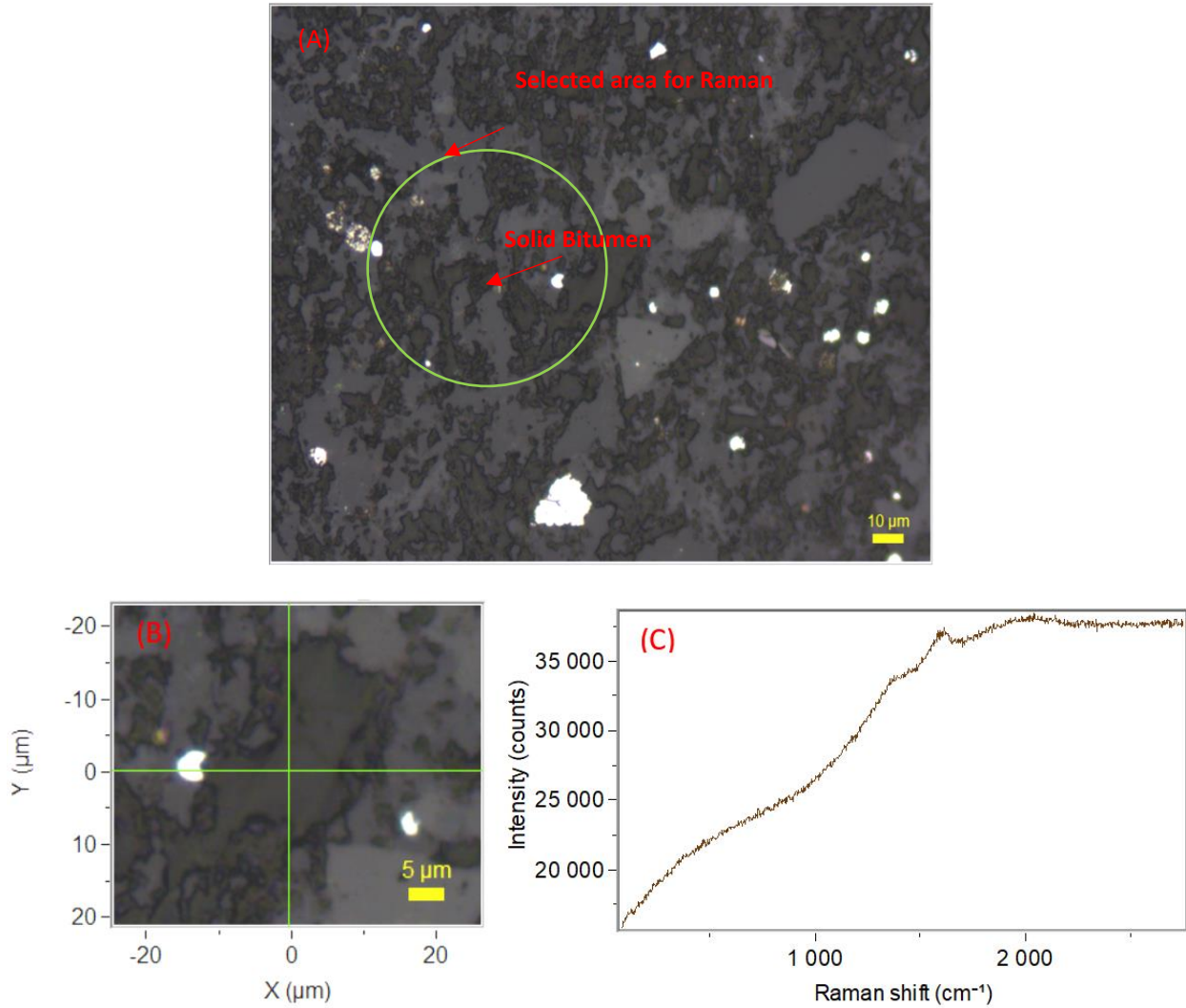


Figure 4-2-2 (A) area selected for Raman spectroscopy, a complete spectrum is acquired at every pixel of the area of interest (1000 spectra are acquired which can all be processed with the same processing steps), (B) a point selected on solid bitumen, (C) and its corresponding Raman spectrum.

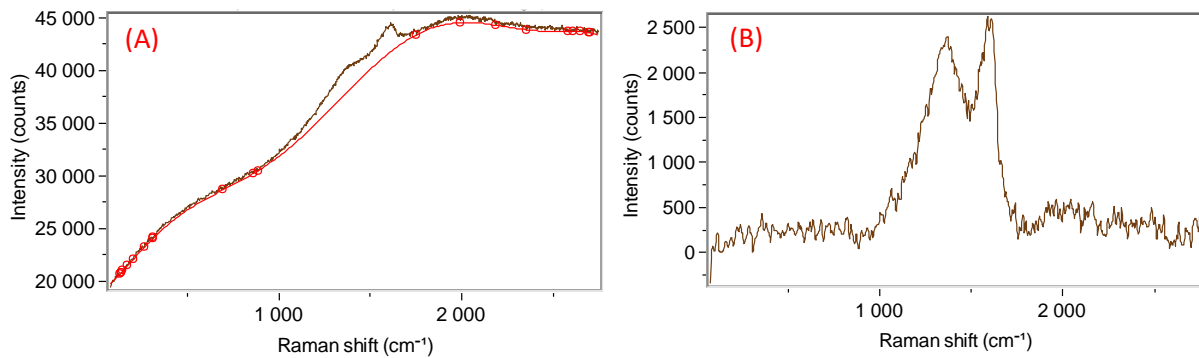


Figure 4-2-3 Raman signals before (A) and after (B) baseline correction for Well 2 as a naturally matured sample.

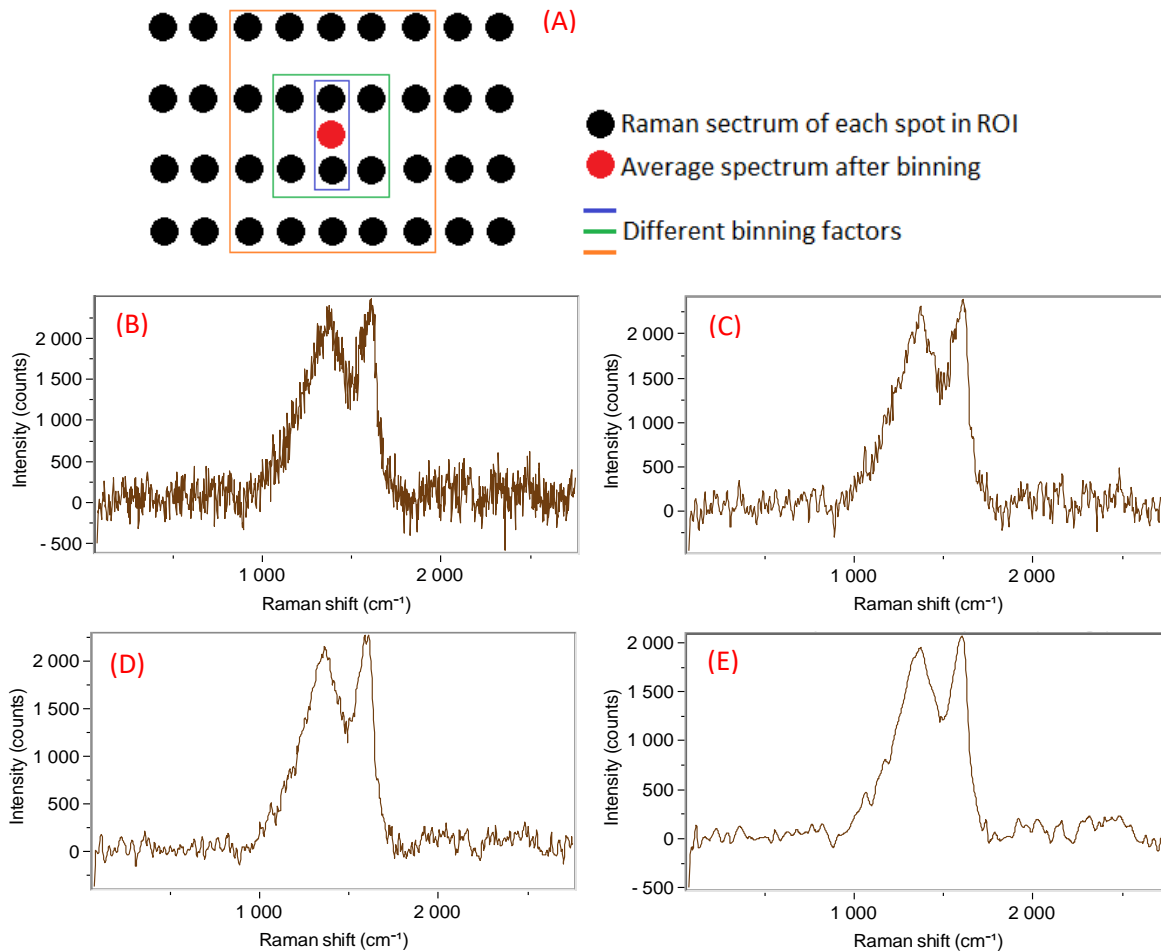


Figure 4-2-4 (A) schematic of binning; (B) single spectrum; (C) binning factor of 4; (D) binning factor of 8; (E) binning factor of 20. Note the increase in signal to noise ratio and correspondingly losing spectral features by increasing binning factor.

To characterize Raman spectral parameters such as peak position, intensity and area, a curve-fitting step should be performed. In this method, the experimental Raman spectrum was reconstructed by deconvolving overlapping peaks such that the summed spectrum of individual peaks matches the experimental data. A mixed Gaussian-Lorentzian peak morphology was used with 150 iterations until the best fit was achieved. The quality of fit was evaluated visually from the residual spectrum and numerically by the standard error ( $\chi^2$ ), where smaller  $\chi^2$  corresponds to a better reconstruction as outlined by previous researchers (Quirico et al., 2005; Sadezky et al., 2005; Bonoldi et al., 2016; Lupoi et al., 2017). Researchers often fit 5 peaks for OM evaluation in shale plays (Schito et al., 2017; Sauerer et al., 2017; Schmidt et al., 2017; Cheshire et al., 2017; Lupoi et al., 2017), known as D, G, D2, D3 and D4 as shown in Figure 4-2-5. In this study, 5 fits were fitted as well, but major bands (D and G) were only considered in the results (Table 4-2-2) as the molecular significance

and appearance of the minor bands (D2, D3 and D4) are not well understood (Beysac et al., 2003). Please note that the bands in Table 4-2-2 were derived from the average spectrum across the ROI.

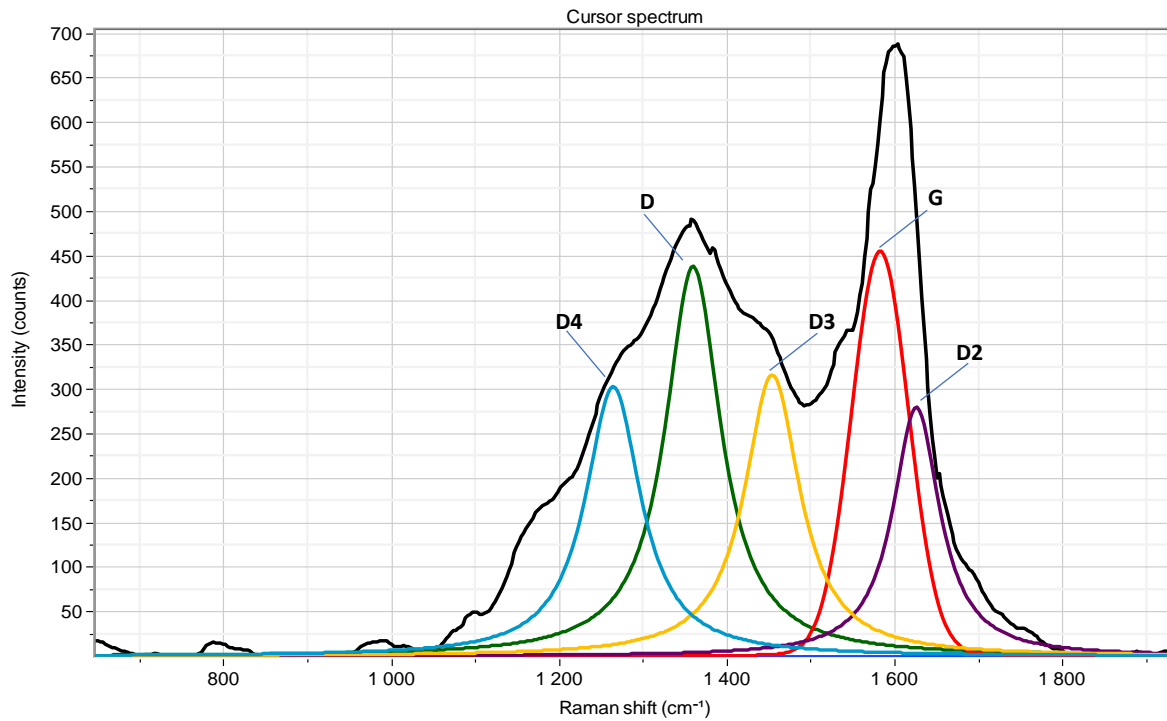


Figure 4-2-5 Schematic of band peaking procedure using 5 peaks (D, G, D2, D3 and D4) and the experimental Raman spectrum (black). By adding more peaks, the reconstructed spectrum is more similar to experimental results and the  $\chi^2$  value is reduced.

Table 4-2-2 Major D and G bands shifts for both artificially and naturally matured samples in this study derived from the average spectrum across the ROI.

	Sample No.	D band	G band	G-D band
Artificially matured sample by HP	HP1	1362	1600	238
	HP2	1363	1598	235
	HP3	1362	1601.5	239.5
	HP4	1358	1603	245
	HP5	1359	1602	243
	HP7	1363	1607	244
	HP8	1357	1604	247
	Naturally	Well 1	1367	1585
Well 2		1367	1587	220

Well 3	1360	1591	231
Well 4	1354	1591	237
Well 5	1359	1594	235
Well 6	1357	1601	244

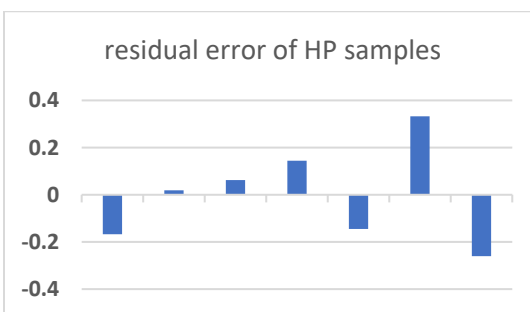
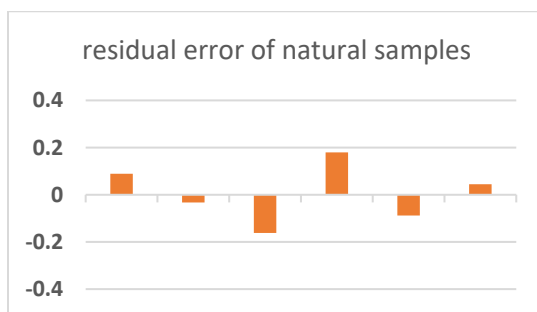
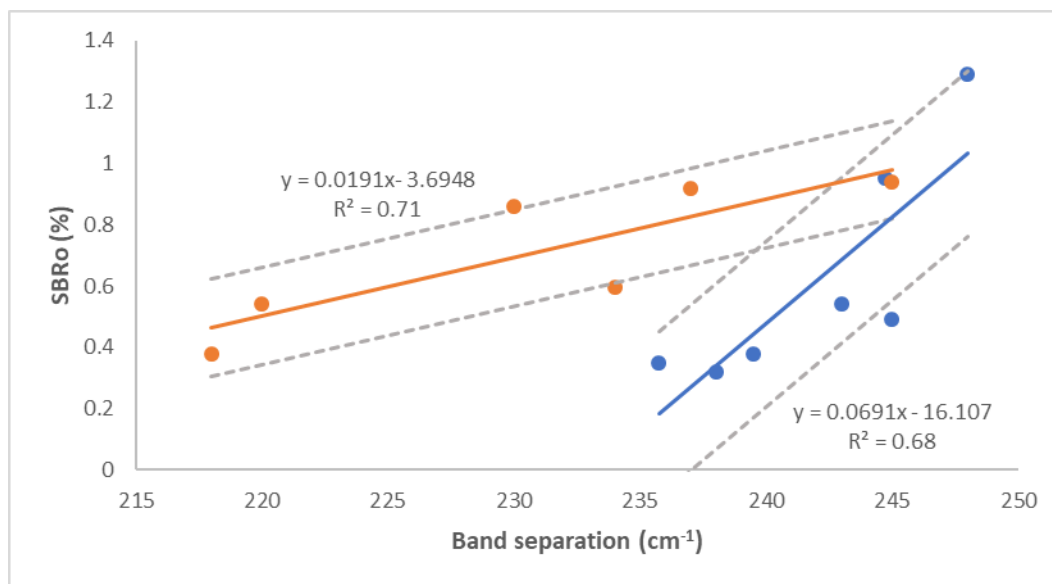
### 4-3 Results and discussion

LECO total organic carbon (TOC) values for the samples vary from 7.39 wt% to 24.71 wt%. The higher S1 values in the lower maturity samples could be the result of a) in-situ hydrocarbon generation, b) contamination by oil-based mud (in the naturally matured samples), or c) a combination of both (in the naturally matured samples). Some of the samples exhibit higher S2 values (33.01-128.71 mg HC/g rock), indicating excellent remaining hydrocarbon generating potential. The high Hydrogen Index (HI) values for the immature samples represents oil-prone organic matter. TOC and S2 (as well as HI) show decrease with increasing thermal maturity. The Production Index (PI) values are also low, which is common for samples that are immature to marginally mature.

Previous studies have reported that thermal maturity causes a logical variation in the positions, separations and other important parameters of Raman spectral bands for organic matter (Spötl et al., 1998; Ferrari and Robertson, 2000; Kelemen and Fang, 2001; Sauerer et al., 2017; Khatibi et al., 2018a, b). Moreover, similar studies have been conducted on solid bitumen in particular and the results found to be in agreement with the trend that was observed on the organic matter (Jehlička et al., 2003; Court et al., 2007; Zhou et al., 2014).

It is well known that with increasing kerogen maturity, aromaticity increases with concurrent loss of H, O, N and S content (Tissot and Welte, 1984; Tyson, 1995). Such compositional evolution can be reflected in both bulk geochemical analysis (programmed pyrolysis) and molecular scale as measured by Raman spectral character (Kelemen and Fang, 2001; Quirico et al., 2005; Sauerer et al., 2017). In Raman spectra, the major bands of D and G represent the aromaticity level of organic matter and the level of disorder in molecular structure of organic atoms. Therefore, Raman spectroscopy can detect different levels of thermal advance based on the response from these molecular signals. A well-known increase in the G-D band separation with maturity (up to dry gas window) is due to the shift in the D band position towards lower wavenumbers and the G band

towards higher wavenumbers (Kelemen and Fang, 2001). These shifts are attributed to the increase of larger aromatic clusters and better ordered-structure kerogen in terms of the existing organic compounds (Schito et al., 2017). Figure 4-3-1 shows a cross-plot of SBRO vs. band separation and Tmax vs. band separation along with 95% confidence interval (CI) of the regression line and corresponding error profile (residuals) for both naturally (orange) and HP samples (blue). Confidence interval represents the range that the mean response is likely to fall, given the specified settings of the predictors (Hicks and Irizarry, 2018). Residual error is the difference between the observed value and the estimated value by the regression. If the points in a residual plot are randomly dispersed around the horizontal axis, a linear regression model is appropriate for the data (Lawson and Erjavec, 2000) which is the case in the results from this study and observed errors. A similar plot was also shown by Zhou et al., (2014) which showed natural and artificially matured samples do not show the same trend when plotting full width at half maximum (FWHM) of D band vs. SBRO.



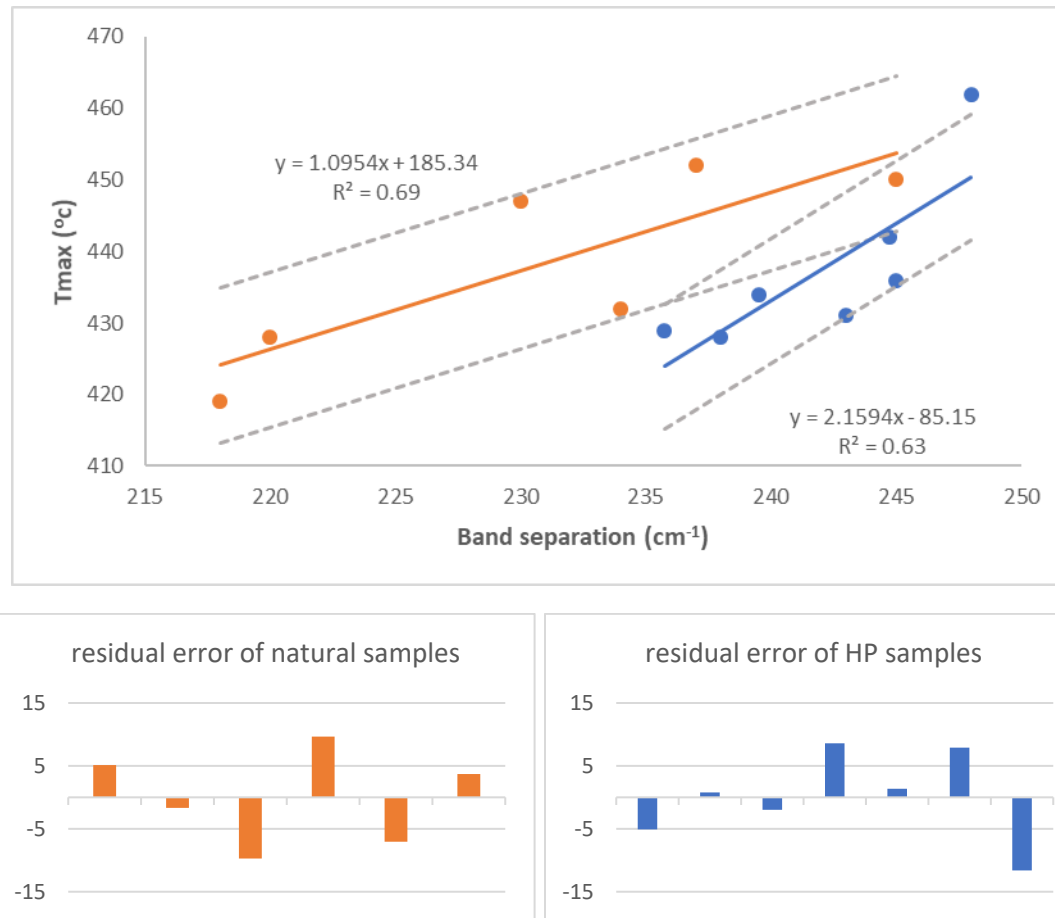


Figure 4-3-1 SBRO and  $T_{max}$  (as maturity indicators) vs. band separation along with 95% confidence interval of regression and residual error profile for each sample set. The 95% confidence interval defines a range of values that the population mean is covered with 95% of certainty. Note the consistent increase of band separation with increasing thermal maturity. Trendlines for HP and naturally matured samples along with their corresponding correlation coefficients are shown on each plot. Orange represents naturally matured samples and blue represents HP samples.

Functions fitted to the two separate datasets (naturally and artificially matured samples) show visibly distinct slopes. It is known that different organic matters mature at various rates due to the presence of specific functional groups (Yang et al., 2017) with different kinetic parameters. To remove this effect, as mentioned earlier, solid bitumen was used exclusively in our study. Lewan and Ruble (2002) concluded kinetic parameters derived from HP would determine geologically significant differences between source rocks bearing different kerogen types, conversely to open-system pyrolysis. This difference in maturation trend is also observed for changes in bulk measurements such as TOC, S<sub>2</sub> and HI, as shown in Figure 4-3-2. Relationships between measured % V<sub>Ro</sub> and programmed pyrolysis values have been introduced in previous studies (Olson, 2008; Klentzman, 2009; Hackley et al., 2015). For example, Epistalié et al. (1985), Dembicki (2016) and Abarghani et al. (2018) investigated different geochemistry datasets from the Bakken and

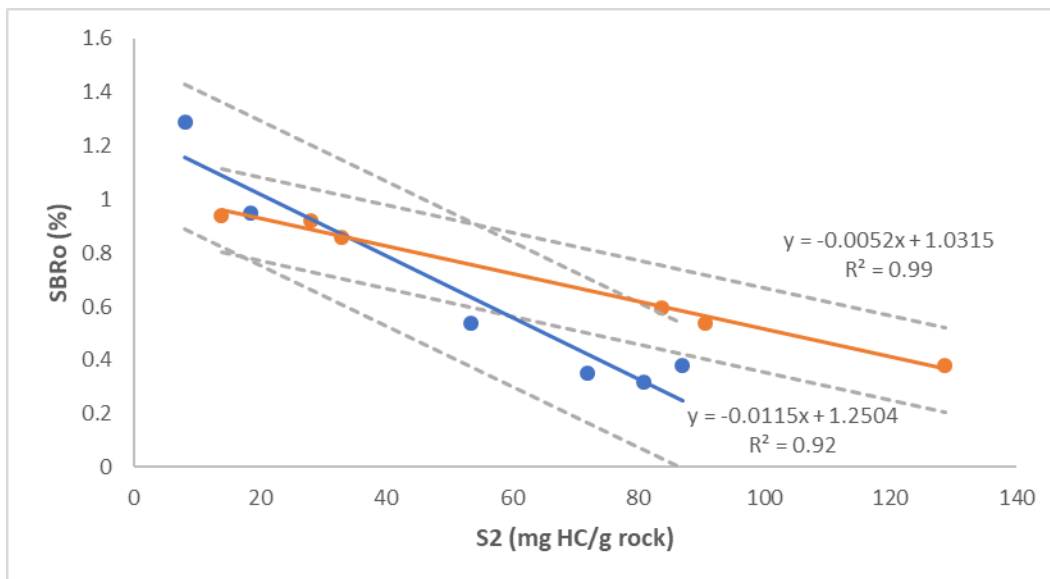
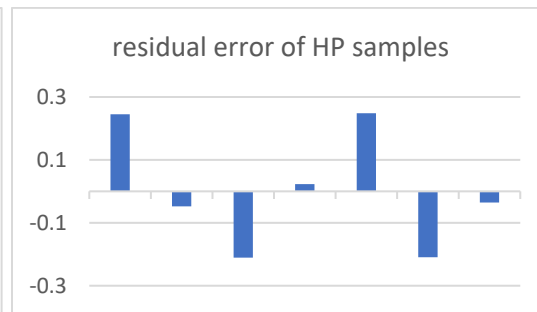
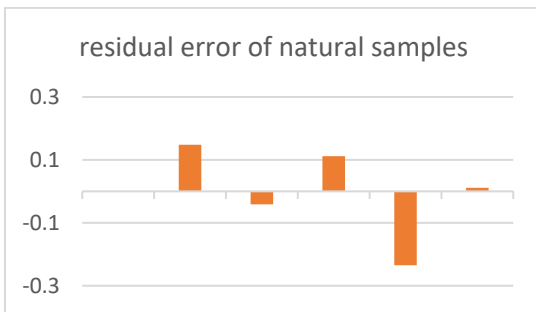
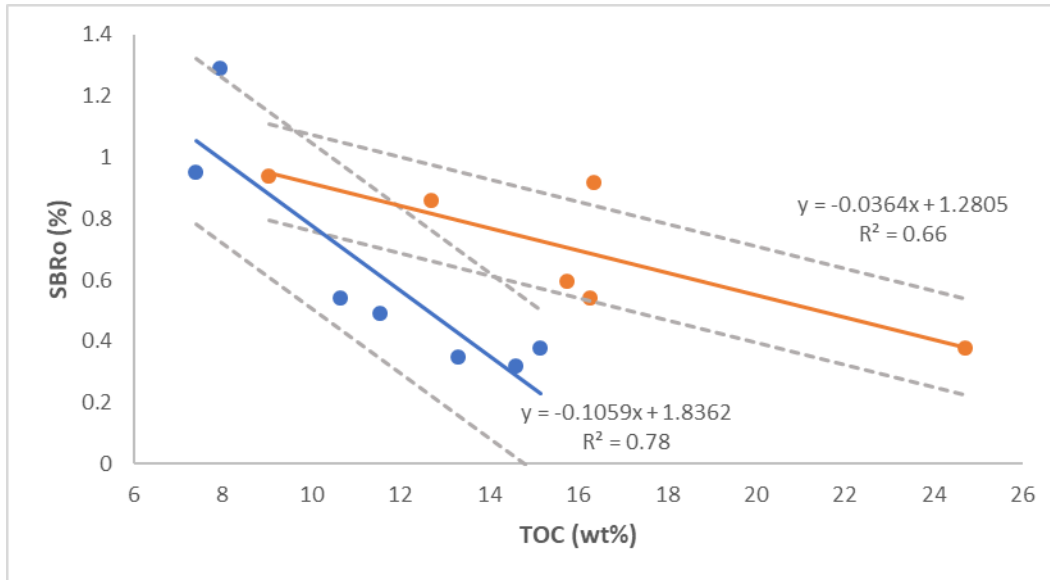
presented a 'normal' kerogen maturation pathway for  $T_{max}$  as a function of %VRo as shown in Figure 4-3-3. Figure 4-3-3 also depicts artificially matured samples of this study do not follow the trend of natural ones in  $T_{max}$ -VRo space which is also reflected in the Raman spectra (Figure 4-3-1). This difference is mainly inferred to the fact that HP residues are still reactive. Therefore, although the SBRo of HP samples are the same as the natural sequence, their compositions are not. Mumm and Inan (2016) presented different trends of maturity vs. band separation for different OM including Type II, III, coal and bitumen samples. They also observed, for the same reflectance range, the results for different types of organic matter could vary. They assumed such discrepancy might originate from the experimental setup, while part can be attributed to dissimilarities in structural composition of these samples which has been reflected in Raman signals. Ferralis et al., (2016) also used Raman spectroscopy in a novel quantitative method to correlate Raman signals to the microchemistry of carbonaceous materials through the elemental H:C ratio. Thus, they detected different trends for HP and naturally matured samples reflecting differences in structural characteristics of each set of samples.

This discrepancy in the rate and path of maturation for naturally and artificially matured samples can be referred to a separate reaction medium between HP and natural geologic processes of maturation. The importance of reaction medium (defined as the effect of water, minerals, heating rates, and pressure on organic maturation in HP) has been discussed extensively (Monthioux, 1987, 1988; Michels and Landais, 1994; Mansuy et al., 1995; Dieckmann et al. 2000; Bajc et al., 2001; Pan et al., 2009, 2010; Liang et al., 2015). Water as the exogenous source of hydrogen seems to have an important role in oil generation and simulation of the natural reaction medium (Lewan, 1997), whereas the dominant reaction pathway in the absence of water is formation of pyrobitumen due to C-C bond cross linking. Additionally, in the presence of water, the primary reaction pathway is formation of saturate-enriched oil due to thermal cracking of C-C bonds (Monthioux et al., 1985). Mineral acidity also increases maturation rate as well as affecting the byproducts from maturation (Pan et al., 2009), while impermeability of fine-grained sediments prevents forward reaction progress (McTavish, 1998; Li et al., 2004; Hao et al., 2007). Several researchers have investigated the effects of reaction medium in formation rates of hydrocarbon (Cramer et al., 1998, 2001; Tian et al., 2007). Definitely based on the extent of kerogen conversion, the amount of trapped bitumen in the pyrolyzed and naturally matured samples might be also different. Monthioux et al. (1985) showed natural maturation is best simulated when pyrolysis is performed

under confined conditions in which free volume or diluting inert gas is not present. Kinetic constants of geochemical reactions derived from HP has shown that reaction mechanisms in nature and in the laboratory are distinctly different (Mackenzie and McKenzie, 1983; Rullkotter and Marzi, 1988).

Therefore, it can be concluded that the presence of water, minerals, heating rates, and pressure are all affecting the maturation paths of organic matter in addition to the variability of the macerals present. Kinetics of hydrocarbon generation and maturation all are dependent upon molecular structure of kerogen (Tegelaar and Noble, 1994; Behar et al., 1997; Killips and Killips, 2013). This dependency can also be extended to nanomechanical and nanoporosity evolution of organic matter (Chen and Xiao, 2014; Liu et al., 2017; Liu et al., 2017). In this regard, bulk chemical measurements suffer notably from representing molecular structure of kerogen, a property which is not known fully. For instance, although Rock-Eval data and (Pseudo) Van Krevelen diagram as seen in Figure 4-3-4, exhibits very similar organic matter type/origin, detailed molecular analyses of the samples are proving otherwise.

To date, HP/AHP are known to be the most suitable simulation methods for thermal maturity progression. However, as it was discussed there exist several parameters that should be known prior to experiments to make them mimic natural maturity pathway. For example, a better understanding of molecular structure of OM that can be detected by Raman spectroscopy in a fast and accurate way using methods provided by Ferralis et al. (2016) and Khatibi et al. (2018d) can provide a better insight into the samples variability to set HP/AHP parameters. In order to achieve this goal, it is suggested first, different HP/AHP experiments to be performed on immature samples from the same source rock, then compare the cross-plot of Raman bands vs. maturity for both naturally and artificially matured samples as shown in Figure 4-3-1. If the fitted curves on both datasets exhibit the same slope, it can be concluded that HP/AHP has followed natural geologic processes for thermal maturation, which was not the case in this study. In conjunction with Raman spectroscopy, variations in the extent and timing of petroleum generation in pyrolysis can also be compared using gas chromatography–mass spectrometry (GC-MS) at the bulk scale to find the optimum method in which natural maturation is better followed.



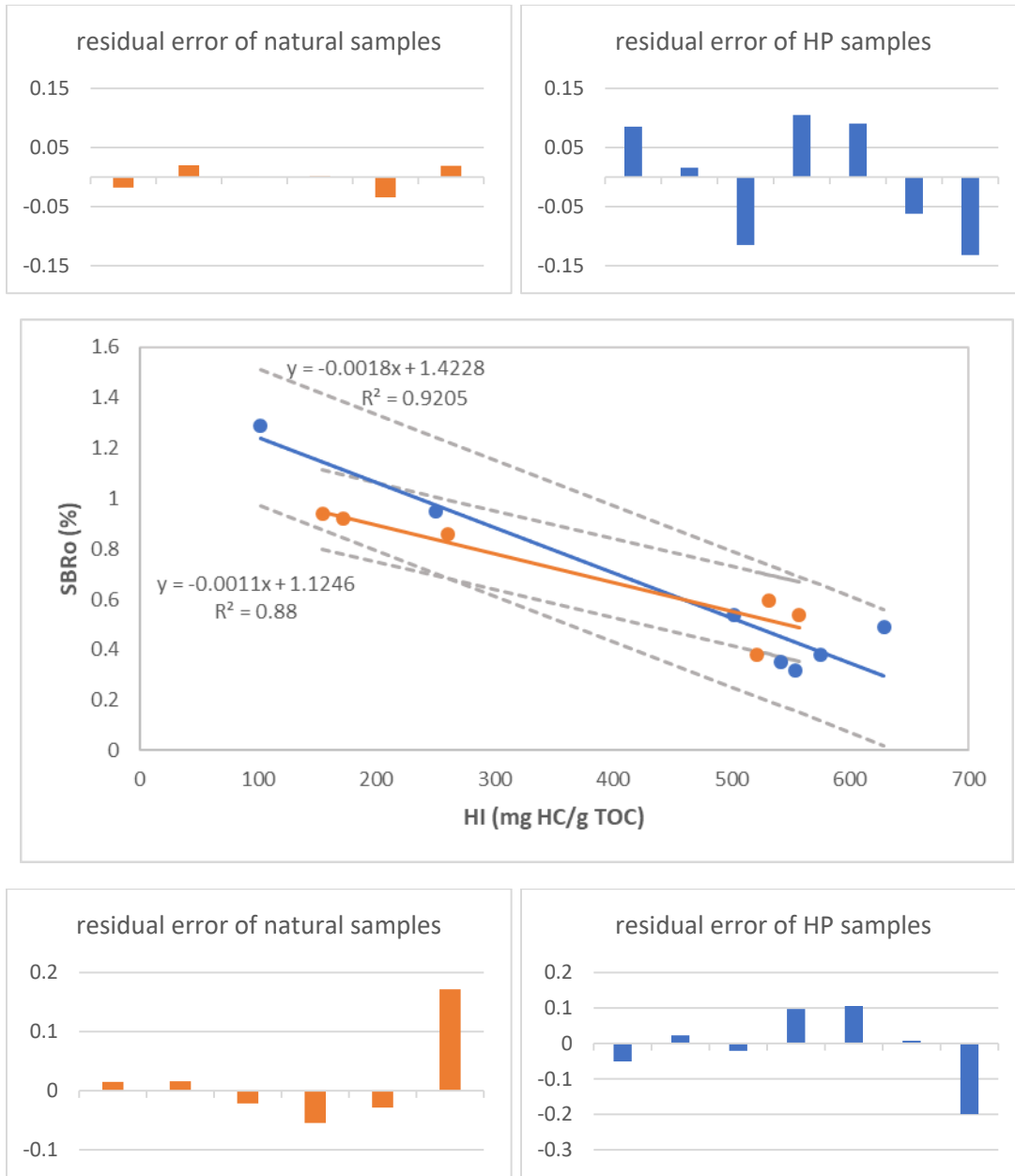


Figure 4-3-2 (top) %SBRo vs. TOC; (middle) %SBRo vs. S2; (bottom) %SBRo vs. HI along with 95% confidence interval of regression and residual error profile. For each parameter plotted vs. %SBRo, trends are different for artificially and naturally matured samples. Orange represents naturally matured and blue represents HP samples.

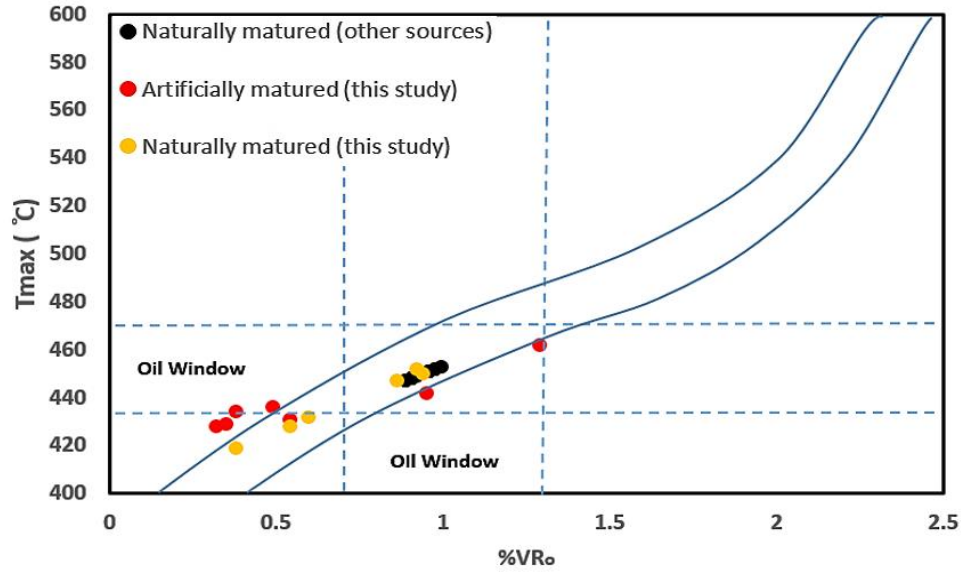


Figure 4-3-3 Observed relationship between VRo% and Tmax for natural samples (modified after Epistalié et al., 1985; Dembicki, 2016; Abarghani et al., 2018). It should be noted that measurements were based on %SBRo and were converted to vitrinite reflectance %VRo using the Jacob (1989) equation. Hydrous pyrolysis results (red circles) do not exactly follow the natural trend limits with dark blue curves. Light orange circles are naturally matured samples in this study, and black circles are naturally matured Bakken data extracted from Abarghani et al. (2018).

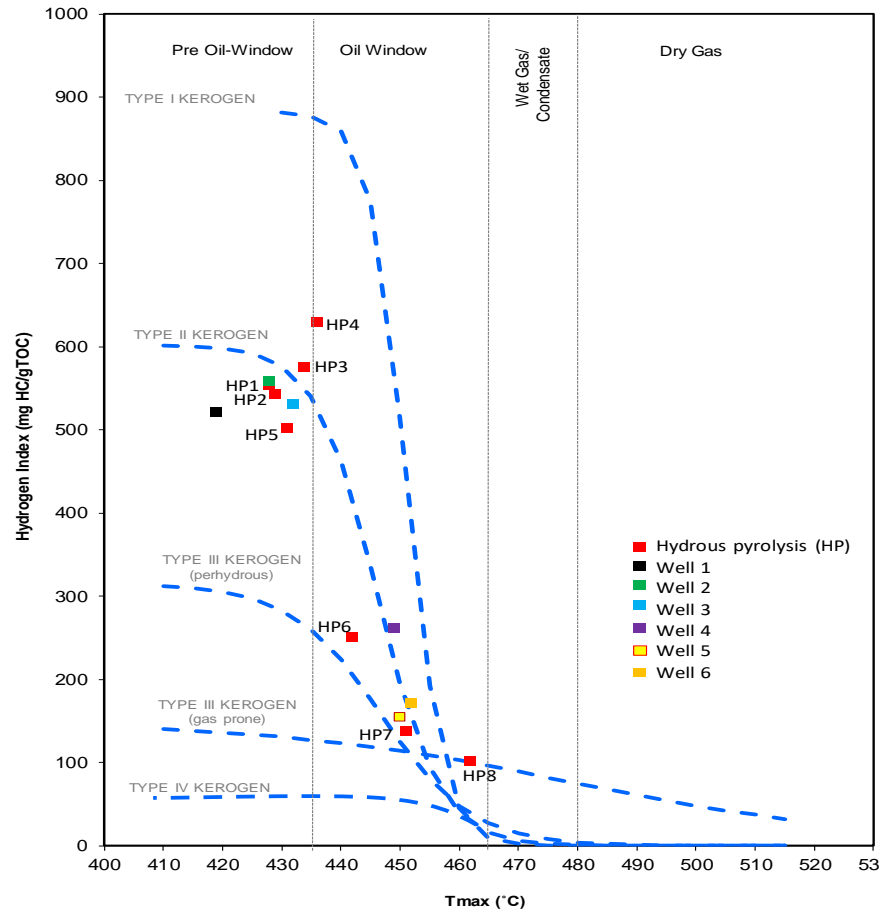


Figure 4-3-4 Hydrogen index vs. Tmax for kerogen typing. As seen all samples including naturally an artificially matured are approximately in type II kerogen (modified after Tyson, 1995).

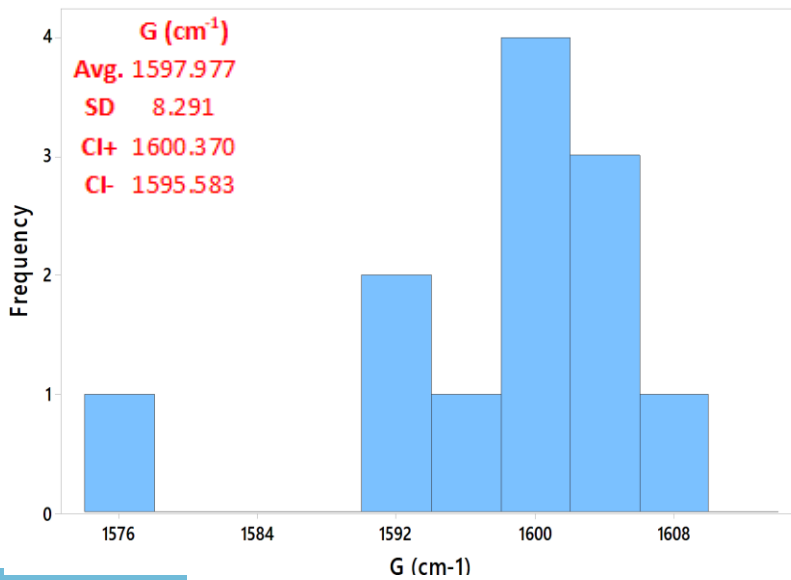
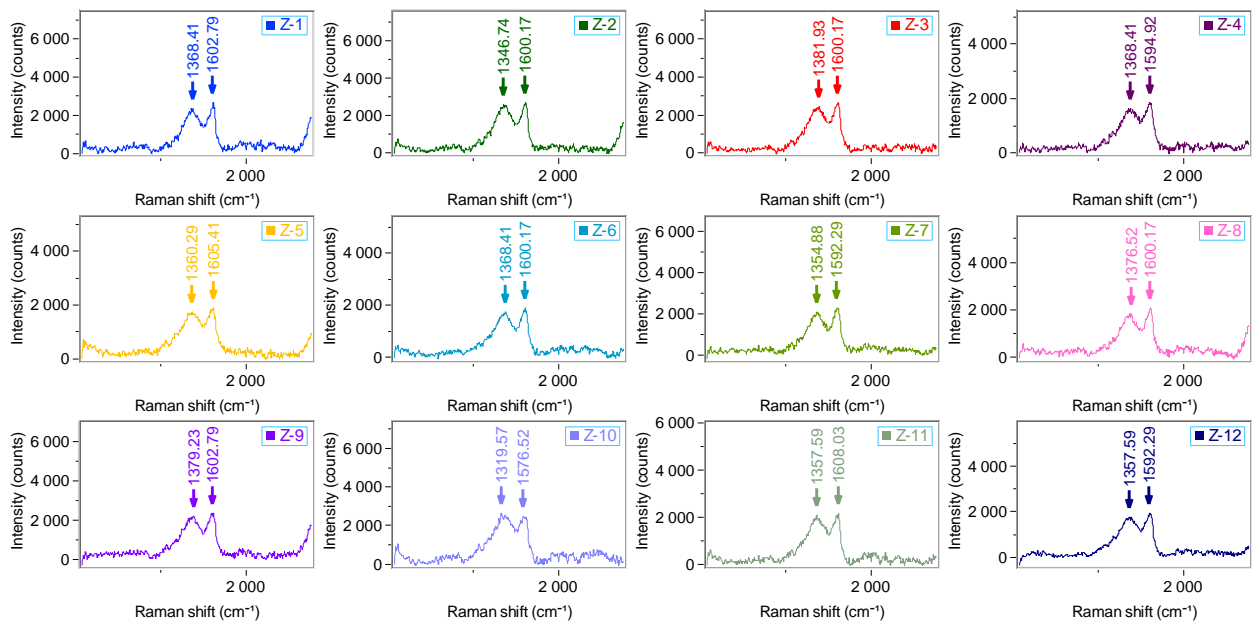
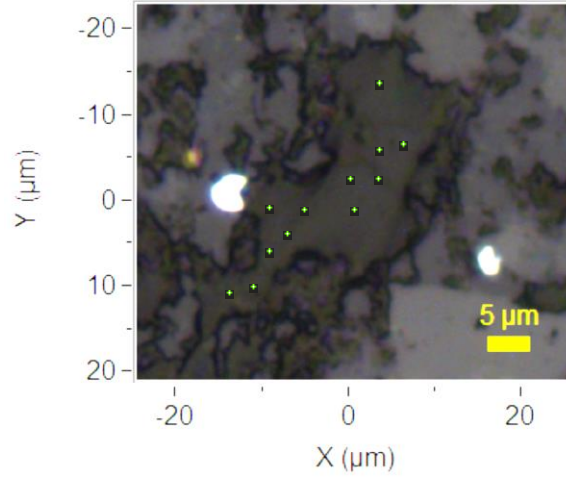
### 4-3.1 Heterogeneity

Spatial variability in chemical structures and other properties of organic matter can be distinguished using Raman spectral mapping mode. In this method, regions on the surface of solid bitumen were selected and their corresponding spectra were analyzed, as presented in Figure 4-3-5 to Figure 4-3-7. To avoid the inconsistency of different biogenic sources and natural variability, the following results are based on HP samples and Raman spectra were obtained only from solid bitumen particles. In order to minimize the effects of technical detail (excitation laser energy, processing steps, sample preparation etc.) the same procedures were used for all samples.

It has been shown that carbonaceous matters are sensitive to the polishing process, and the effect is significant (Lünsdorf, 2016). The excitation wavelength might also affect the Raman results, so in order to avoid such bias, the same wavelength for each and all sample surfaces was used to

acquire Raman spectra. Moreover, short laser excitation wavelengths (488 nm and less) are usually used for Raman acquisition of organic matter to invoke far less fluorescence background noise (Lünsdorf, 2016), which is also the case in this study. Raman spectral mapping mode showed that different locations within the same solid bitumen particle did not necessarily present the same Raman spectral characteristics. This variation in the spectra is represented herein by G-D band separation as well as the corresponding statistical details in the tables representing the histograms (Figure 4-3-5 to Figure 4-3-7). Please note bin size and the number of the bins in Figure 4-3-5 to Figure 4-3-7 were decided based on the discussion by Deviant (2011). If it is assumed that polishing and laser wavelength had negligible effects on collected data, it can be concluded that the variability in Raman spectral results might be due to the heterogeneity of organic matter in terms of chemical composition. Results are also in agreement with recent research that was performed by Jubb et al., (2018) who detected high variability in the Raman response across a less than 5  $\mu\text{m}$  spatial distances of single OM in shale samples.

Moreover, as thermal maturity advances, observed variation in G and D band parameters reduce for different locations within the same solid bitumen particle. This observation suggests that heterogeneity of organic matter decreases with increasing thermal maturity; note the decrease in standard deviation values or confidence interval range (upper and lower bounds of confidence interval define a range of values that we can be 95% certain contains the population mean) for different samples in Figure 4-3-5 to Figure 4-3-7. Similar results are also reported by Jubb et al., (2018) for Niobrara shale sample that OM chemical heterogeneity is lost for samples with higher thermal maturity. This can be explained by increase in aromaticity, and heteroatoms expulsion; therefore, no matter its origin or type, OM tends to become graphite-like at higher maturity (Tuinstra and Koenig, 1970; Waples, 1981; Tissot and Welte, 1984; Tyson, 1995; Ferrari and Robertson, 2000; Quirico et al., 2005; Potgieter-Vermaak et al., 2011; Zhou et al., 2014; Lünsdorf, 2016; Mumm and Inan, 2016; Schito et al., 2017). This is also in accordance with the original Van Krevelen diagram in which all kerogen types converge to the origin as their composition and structure become similar when thermal maturity is increased (Killops and Killops, 2013).



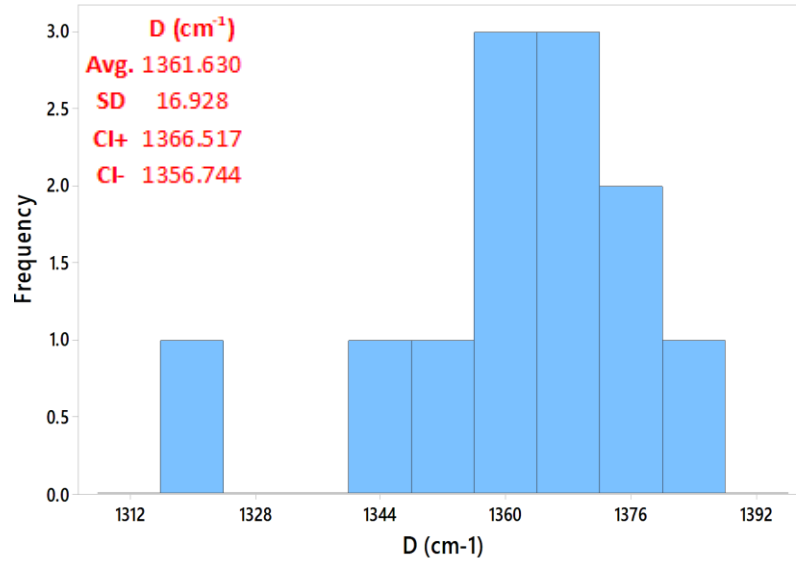
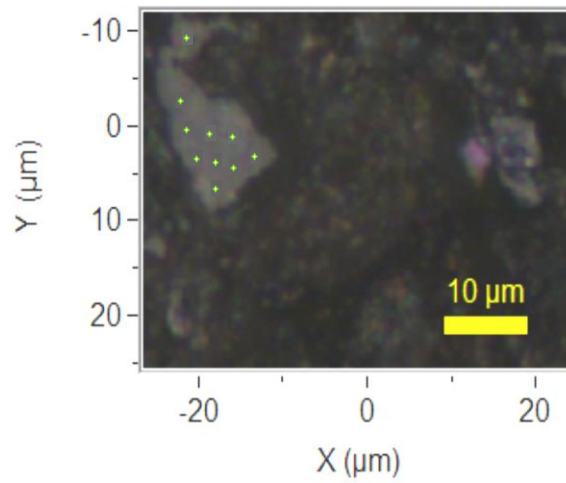
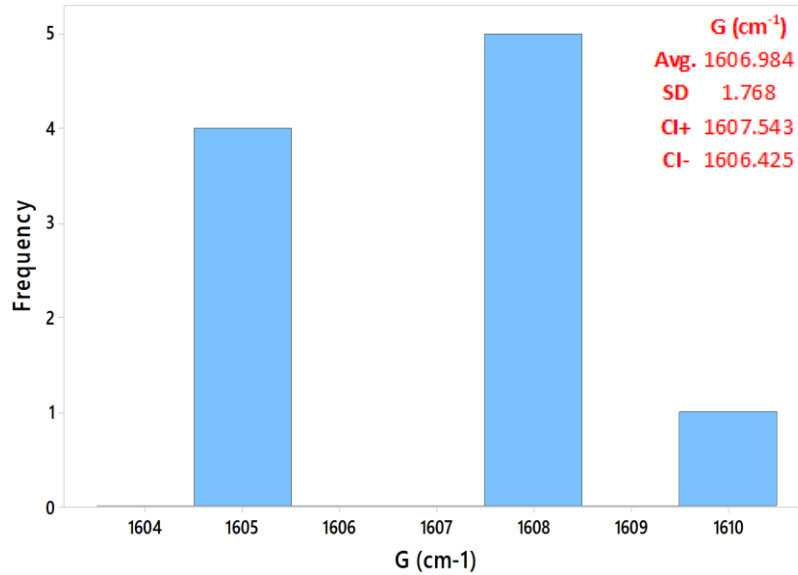
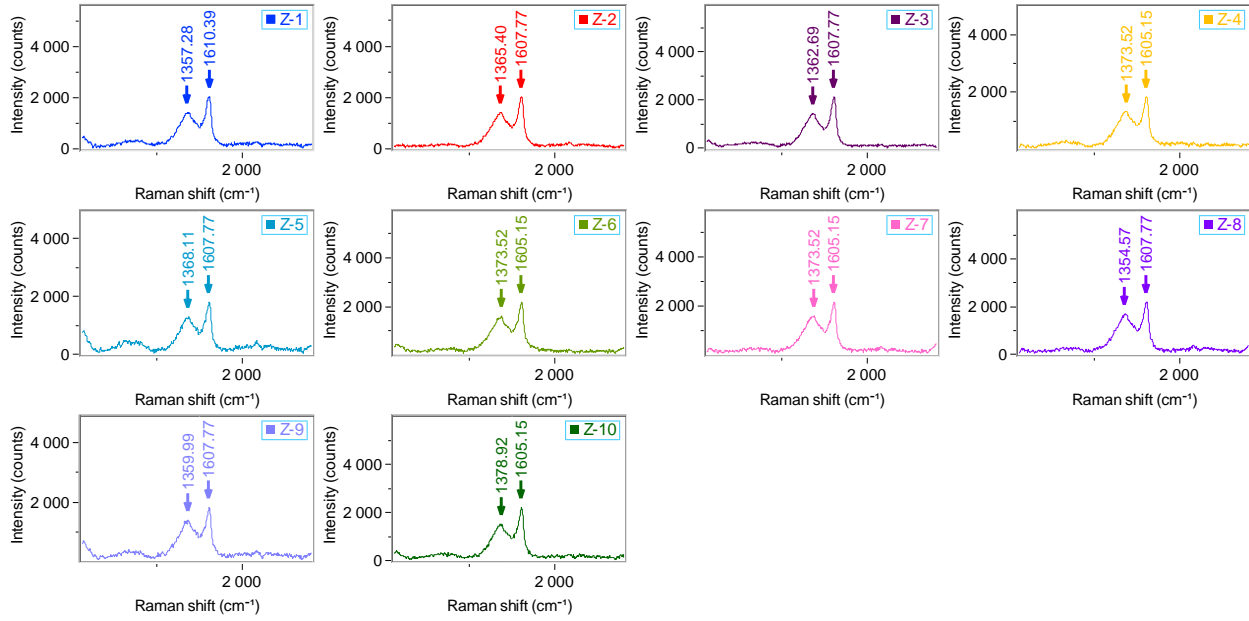


Figure 4-3-5 sample HP1 with 0.32 %SBRo: (top) Showing spots selected for averaging Raman signals (each green circle has about 3.36  $\mu\text{m}^2$  area); (middle) Raman spectra of corresponding spots; (bottom) Histogram of D and G bands position along with the statistical information of Avg.: average, SD: standard deviation, CI+: upper bound of confidence interval and CI-: lower bound of confidence interval. Bin sizes were defined based on Deviant (2011), range of data divided by number of bins.



# Chapter 4



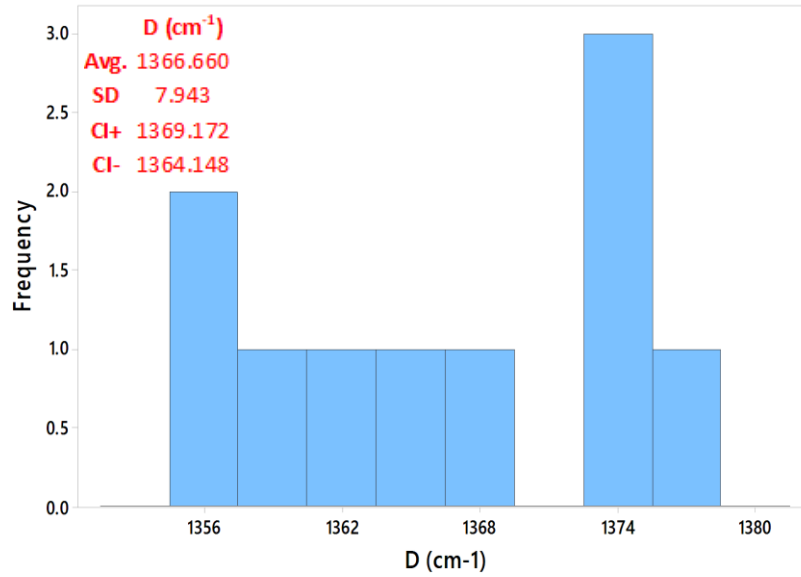
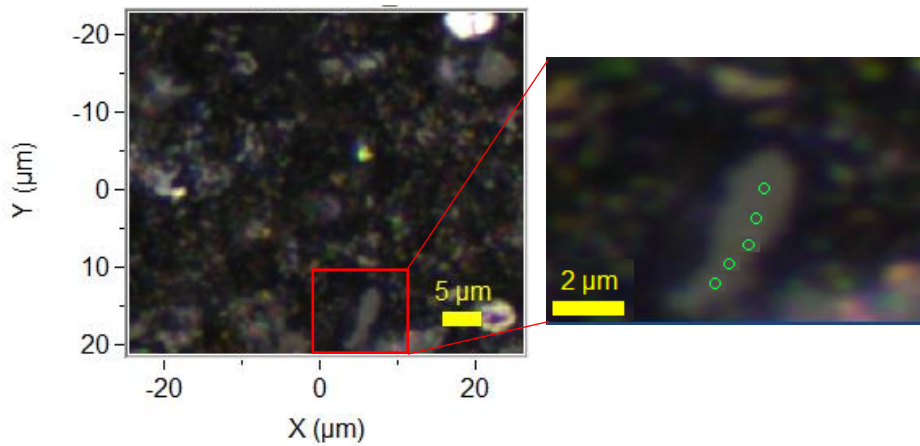
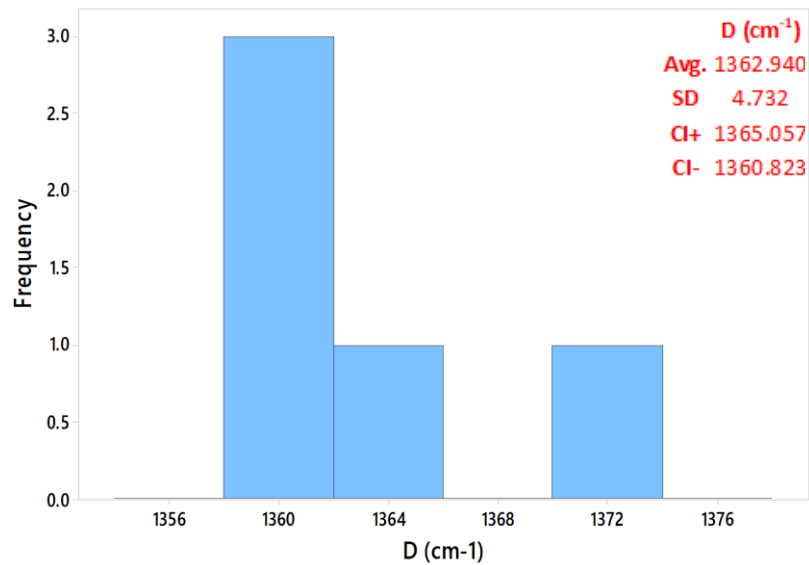
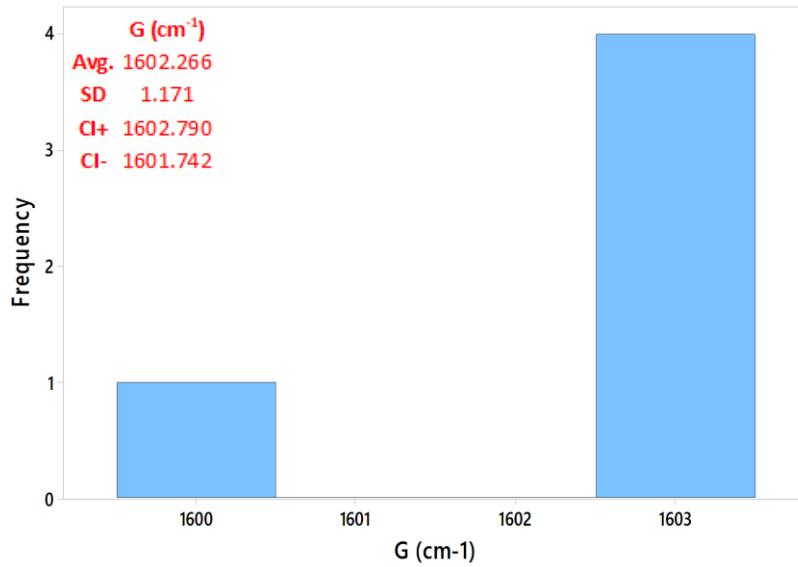
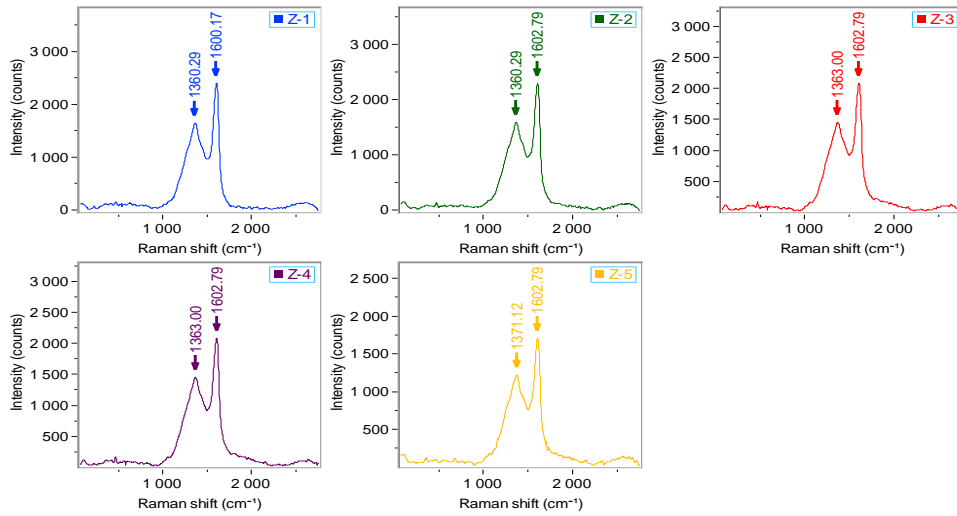


Figure 4-3-6 Sample HP6 with 0.95 %SBRo: (top) Showing spots selected for averaging Raman signals; (middle) Raman spectra of corresponding spots; (bottom) Histogram of D and G bands position along with the statistical information of Avg.: average, SD: standard deviation, CI+: upper bound of confidence interval and CI-: lower bound of confidence interval. Bin sizes were defined based on what is discussed by Deviant (2011), range of data divided by number of bins.



# Chapter 4

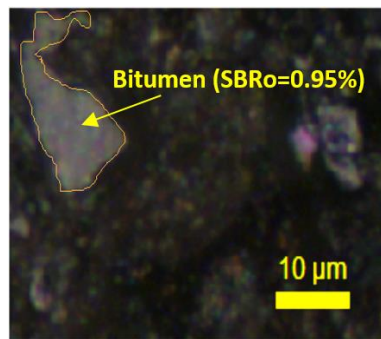
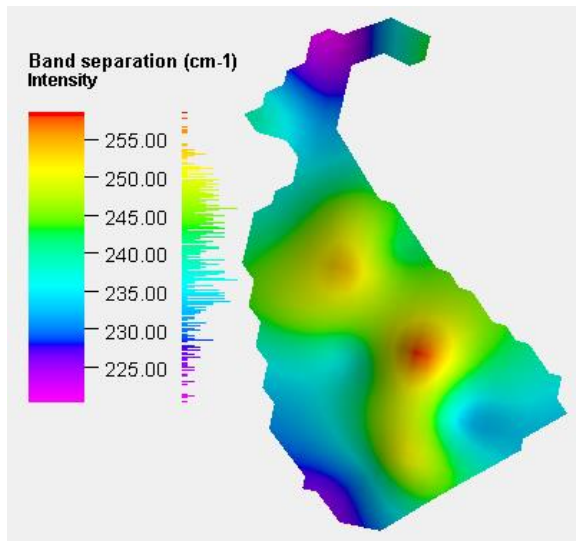
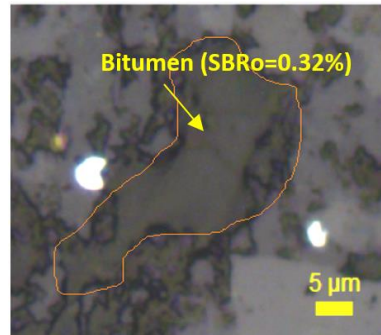
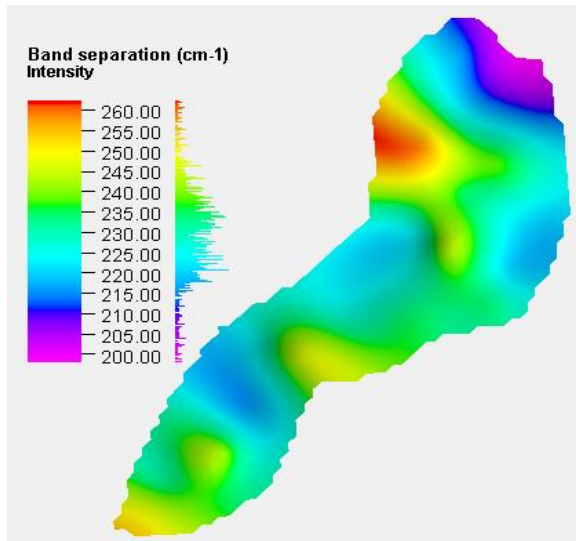


*Figure 4-3-7 Sample HP8 with 1.29 %SBRo: (top) Showing spots selected for averaging Raman signals; (middle) Raman spectra of corresponding spots; (bottom) Histogram of D and G bands position along with the statistical information of Avg.: average, SD: standard deviation, CI+: upper bound of confidence interval and CI-: lower bound of confidence interval. Bin sizes were defined based on what is discussed by Deviant (2011), range of data divided by number of bins.*

Raman band separation maps for solid bitumen particles in Figure 4-3-5 to Figure 4-3-7 are displayed in Figure 4-3-8. Table 4-3-1 also shows the corresponding standard deviation (SD) and coefficient of variation (CV) of spectra for each sample. Results are showing decreasing of band separation variability with increasing maturity. Interpolation method for surface data generation is performed using the minimum curvature method which uses an operator that keeps the surface data smooth with a minimum amount of bending, while attempting to honor the data as closely as possible (Yang et al., 2004; Amorin, 2009). It can be seen, across the surveyed solid bitumen particles, band separation (G-D) exhibits variations which might represent changes in chemical composition, matrix effects (specifically near the edge of the grain) and/or surface quality. In order to demonstrate these variations in Raman signals across each surveyed particle more clearly, CLS (classical least square) fitting was used as a multivariate decomposition technique. This procedure was used to calculate the contribution of the reference spectra in the same size area to create a profile based on the similarity of each spectrum to the reference spectrum. The reference spectrum was selected in the middle of each sample to be far from edges, Figure 4-3-9. From the figures it can be concluded: by increasing maturity the magnitude of fluctuations in band separation is decreasing, and distribution of band separation will become more uniform throughout the solid bitumen particle which might denote advancement towards compositional homogeneity. Similar results were observed by Lünsdorf (2016) and Jubb et al., (2018).

This representation of heterogeneity within a solid bitumen phase may explain other heterogeneous behaviors such as mechanical properties of OM. It has been shown in the literature, as thermal maturity increases, mechanical properties (e.g., elastic modulus) of organic matter alter (Eliyahu et al., 2014; Li et al., 2017). It can be described as in immature source rocks the OM appears to surround other minerals, becoming a load-bearing part of the rock framework (Liu et al., 2016; Zargari et al., 2011). Conversely, by increasing the maturity, kerogen becomes more isolated between the other grains and results in an increase in its Young's modulus (Zargari et al., 2011; Dietrich, 2015). In terms of molecular structural evolution, organic matter transforms gradually from chaotic and mixed-layered to a better-ordered aromatic molecular structure (Beysac et al.,

2003; Quirico et al., 2005; Khatibi et al., 2018d). This reasoning is also consistent with the previous paragraph regarding decreasing of heterogeneity of molecular structure by increasing maturity.



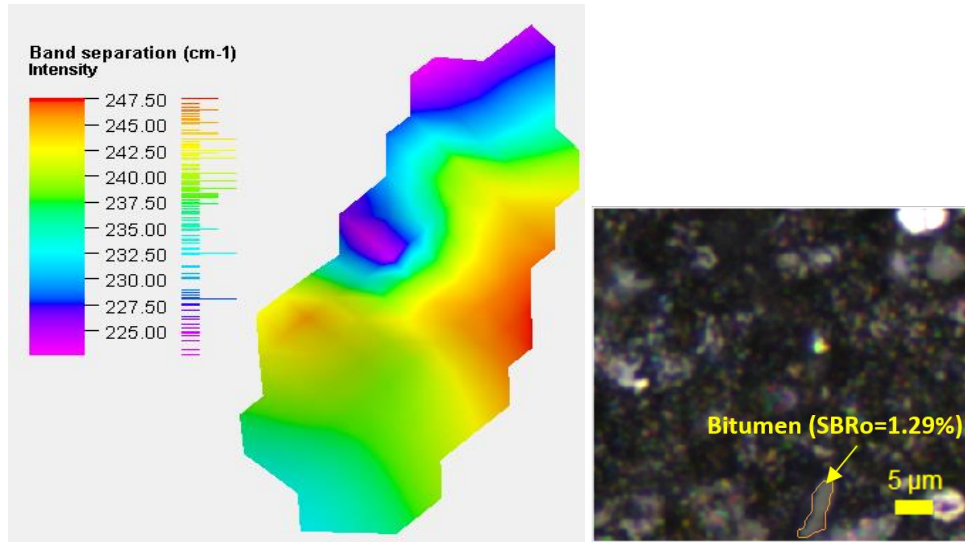


Figure 4-3-8 Raman map of a bitumen corresponding to Figure 4-3-5 to Figure 4-3-7 (HP 1, HP6 and HP8, respectively). Note the changes of band separation indicating changes of chemical composition of the solid bitumen. As seen, variation of band separation is reducing by increasing maturity. Please note bar graphs next to color scales shows the frequency of each band separation.

Table 4-3-1 Standard deviation (SD) and Coefficient of variation (CV) of band separations for HP 1, HP6 and HP8 for the entire area of interest. As see, by increasing maturity, the measures of variability are decreasing. CV is useful for calculating the relative magnitude of the standard deviation when few data are available for different datasets.

MATURITY OF THE SAMPLE	SD	CV
<b>0.32</b>	11.725	0.050
<b>0.95</b>	8.621	0.036
<b>1.29</b>	6.036	0.026

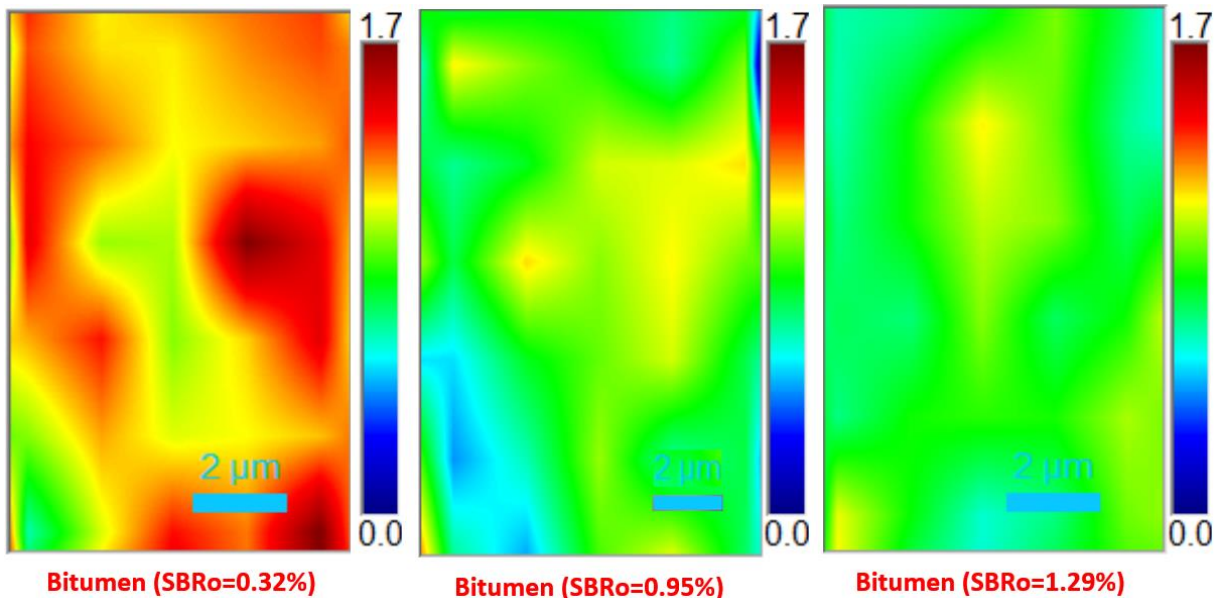


Figure 4-3-9 Results of classical least square fitting procedure for three samples of HP 1, HP6 and HP8. A reference spectrum in the middle of the window is selected and similarity of each spectrum to the reference spectrum is shown. Higher values in the legend show higher dissimilarity.

The continuous chemistry information obtained from solid bitumen particles by Raman spectroscopy may have the potential to enhance conventional petrographic or bulk geochemistry analytical approaches. For example, Raman spectroscopy has the benefit of minimal sample preparation (It can be done on sample chips as well) in a non-destructive manner and fast acquisition by pinpointing the organic matter and illuminating by proper laser wavelength. Additionally, the cross-plot of SBRo with Raman data, can enable us to adjust the condition of pyrolysis to make it resemble natural maturation pathways more accurately at the small scale and confirm it with bulk measurements in programmed pyrolysis. To do so, several HP and AHP setups can be performed and the cross-plot of Raman bands vs. maturity should be compared to naturally matured samples. Moreover, detecting heterogeneity and providing maturity maps can also be a tool for further understanding of kerogen characteristics. The latest requires extensive sample collection (sample number/ft) and spectroscopy study both laterally and vertically from source to reservoir. To accomplish more extensive results, this study will be continued by analyzing samples with a wider range of maturities, including different type of macerals, and complement our Raman data with Nano-IR measurements to give a better insight to heterogeneity of organic matters.

## 4-4 Conclusion

In this study, samples from the source rock of the Bakken Formation varying in depth and maturity were retrieved. One of the samples was then artificially matured through various stages of hydrous pyrolysis. Solid bitumen reflectance programmed pyrolysis and Raman spectroscopy were performed on all samples to obtain general maturity, bulk geochemistry and chemical fingerprinting. In the next step, Raman signals were acquired on solid bitumen particles on HP samples (at each stage) to show the heterogeneity of organic matter more possibly due to chemical composition. In addition, Raman data revealed different maturation rates between natural and artificially matured samples. We understand that various parameters are affecting the path that leads OM towards higher maturity levels, however, the overall impact of all of them would be on the chemical structure of the remaining OM. This structural evolution can be detected by Raman spectroscopy as a whole at different maturity levels no matter the dominant underlying reason. Previous studies evaluated these governing factors separately whereas here, we were able to see a combined effect of them via Raman spectra. Based on the results the following conclusions are made:

- Raman spectroscopy was able to detect molecular alterations in the organic matter as it undergoes thermal maturity.
- Raman mapping mode provided a way to compare different OM solid bitumen particles in microscale in a continuous format at varying maturity levels.
- We found, HP although known as the best thermal maturity simulation method, did not necessarily follow natural maturation conditions. This was revealed by the cross-plot of Raman spectroscopy data vs. conventional geochemistry results. The result can help to propose protocols and adjust experimental parameters for HP based on those cross-plots for more accurate thermal maturity progression steps in the lab.
- Raman spectroscopy can reflect heterogeneity of organic matter at microscale which can also represent expected heterogeneity in geochemical and geomechanical properties of the OM.
- It was found as maturity increases, heterogeneity of organic matter decreases and Raman map of solid bitumen particle shows more uniform distribution of G-D band characteristics.

## 4-5 Acknowledgment

The authors wish to thank Dr. Thomas Gentzis and Dr. Humberto Carvajal-Ortiz from Core Laboratories in Houston, TX, for providing us with geochemistry data and fruitful discussions. We would like to also thank, North Dakota Geological Survey, Core Library, for giving us access to the Bakken core samples, particularly Jeffrey Bader, state geologist and director as well as Kent Hollands, lab technician. Finally, we would also like to thank Dr. Aaron Jubb at the USGS Eastern Energy Resources Science Center in Reston, Virginia for providing his constructive comments and reviewing this manuscript.

## 4-6 Reference

Abarghani, A., Ostadhassan, M., Gentzis, T., Carvajal-Ortiz, H., Bubach, B., 2018. Organofacies study of the Bakken source rock in North Dakota, USA, based on organic petrology and geochemistry. *International Journal of Coal Geology* 188, 79-93.

Amorin, Richard. "Application of Minimum Curvature method to Well-path Calculations." PhD diss., 2009.

Angulo, Solange, and Luis A. Buatois. "Integrating depositional models, ichnology, and sequence stratigraphy in reservoir characterization: The middle member of the Devonian–Carboniferous Bakken Formation of subsurface southeastern Saskatchewan revisited Bakken Formation Reservoirs, Saskatchewan, Canada." *AAPG bulletin* 96, no. 6 (2012): 1017-1043.

Bajc, S., Ambles, A., Largeau, C., Derenne, S., Vitorović, D., 2001. Precursor biostructures in kerogen matrix revealed by oxidative degradation: oxidation of kerogen from Estonian kukersite. *Organic geochemistry* 32, 773-784.

Behar, F., Vandenbroucke, M., Tang, Y., Marquis, F., Espitalié, J., 1997. Thermal cracking of kerogen in open and closed systems: determination of kinetic parameters and stoichiometric coefficients for oil and gas generation. *Organic Geochemistry* 26, 321-339.

Beysac, Olivier, Bruno Goffé, Jean-Pierre Petitet, Emmanuel Froigneux, Myriam Moreau, and Jean-Noël Rouzaud. "On the characterization of disordered and heterogeneous carbonaceous materials by Raman spectroscopy." *Spectrochimica Acta Part A: Molecular and Biomolecular Spectroscopy* 59, no. 10 (2003): 2267-2276.

Bonoldi, Lucia, Lea Di Paolo, and Cristina Flego. "Vibrational spectroscopy assessment of kerogen maturity in organic-rich source rocks." *Vibrational Spectroscopy* 87 (2016): 14-19.

Carvajal-Ortiz, H., Gentzis, T., 2015. Critical considerations when assessing hydrocarbon plays using Rock-Eval pyrolysis and organic petrology data: Data quality revisited. *International Journal of Coal Geology* 152, 113-122.

Chen, J., Xiao, X., 2014. Evolution of nanoporosity in organic-rich shales during thermal maturation. *Fuel* 129, 173-181.

Cheshire, Stephen, Paul R. Craddock, Guangping Xu, Bastian Sauerer, Andrew E. Pomerantz, David McCormick, and Wael Abdallah. "Assessing thermal maturity beyond the reaches of vitrinite reflectance and Rock-Eval pyrolysis: A case study from the Silurian Qusaiba formation." *International Journal of Coal Geology* 180 (2017): 29-45.

Court, Richard W., Mark A. Sephton, John Parnell, and Iain Gilmour. "Raman spectroscopy of irradiated organic matter." *Geochimica et Cosmochimica Acta* 71, no. 10 (2007): 2547-2568.

Cramer, B., Krooss, B.M., Littke, R., 1998. Modelling isotope fractionation during primary cracking of natural gas: a reaction kinetic approach. *Chemical Geology* 149, 235-250.

Curtis, M.E., Cardott, B.J., Sondergeld, C.H., Rai, C.S., 2012. Development of organic porosity in the Woodford Shale with increasing thermal maturity. *International Journal of Coal Geology* 103, 26-31.

Dembicki, H., 2016. *Practical Petroleum Geochemistry for Exploration and Production*. Elsevier.

Deviant, S. *The practically cheating statistics handbook--*. Lulu. com, 2011.

Dieckmann, V., Horsfield, B., Schenk, H., 2000. Heating rate dependency of petroleum-forming reactions: implications for compositional kinetic predictions. *Organic Geochemistry* 31, 1333-1348.

Dietrich, Andrew B. "The impact of organic matter on geomechanical properties and elastic anisotropy in the Vaca Muerta shale." PhD diss., Colorado School of Mines. Arthur Lakes Library, 2015.

Eliyahu, Moshe, Simon Emmanuel, Ruarri J. Day-Stirrat, and Calum I. Macaulay. "Mechanical properties of organic matter in shales mapped at the nanometer scale." *Marine and Petroleum Geology* 59 (2015): 294-304.

Espitalie, J., Deroo, G., Marquis, F., 1985. La pyrolyse Rock-Eval et ses applications. Deuxième partie. *Revue de l'Institut français du Pétrole* 40, 755-784.

Ferrari, A.C., Robertson, J., 2000. Interpretation of Raman spectra of disordered and amorphous carbon. *Physical review B* 61, 14095.

Ferralis, Nicola, Emily D. Matys, Andrew H. Knoll, Christian Hallmann, and Roger E. Summons. "Rapid, direct and non-destructive assessment of fossil organic matter via microRaman spectroscopy." *Carbon* 108 (2016): 440-449.

Garcette-Lepecq, A., Derenne, S., Largeau, C., Bouloubassi, I., Saliot, A., 2000. Origin and formation pathways of kerogen-like organic matter in recent sediments off the Danube delta (northwestern Black Sea). *Organic Geochemistry* 31, 1663-1683.

Guedes, A., Valentim, B., Prieto, A., Noronha, F., 2012. Raman spectroscopy of coal macerals and fluidized bed char morphotypes. *Fuel* 97, 443-449.

Hackley, P.C., 2012. Geological and geochemical characterization of the Lower Cretaceous Pearsall Formation, Maverick Basin, south Texas: A future shale gas resource? *AAPG bulletin* 96, 1449-1482.

## Chapter 4

Hackley, P.C., Araujo, C.V., Borrego, A.G., Bouzinos, A., Cardott, B.J., Cook, A.C., Eble, C., Flores, D., Gentzis, T., Gonçalves, P.A., 2015. Standardization of reflectance measurements in dispersed organic matter: Results of an exercise to improve interlaboratory agreement. *Marine and Petroleum Geology* 59, 22-34.

Hackley, P.C., Cardott, B.J., 2016. Application of organic petrography in North American shale petroleum systems: A review. *International Journal of Coal Geology* 163, 8-51.

Hao, F., Zou, H., Gong, Z., Yang, S., Zeng, Z., 2007. Hierarchies of overpressure retardation of organic matter maturation: Case studies from petroleum basins in China. *AAPG bulletin* 91, 1467-1498.

Hicks, Stephanie C., and Rafael A. Irizarry. "A guide to teaching data science." *The American Statistician* 72, no. 4 (2018): 382-391.

Hu, M., Cheng, Z., Zhang, M., Liu, M., Song, L., Zhang, Y., Li, J., 2014. Effect of calcite, kaolinite, gypsum, and montmorillonite on Huadian oil shale kerogen pyrolysis. *Energy & Fuels* 28, 1860-1867.

Lawson, John, and John Erjavec. *Modern statistics for engineering and quality improvement*. Duxbury Press, 2000.

Huijun, L., Tairan, W., Zongjin, M., Wencai, Z., 2004. Pressure retardation of organic maturation in clastic reservoirs: a case study from the Banqiao Sag, Eastern China. *Marine and Petroleum Geology* 21, 1083-1093.

Jacob, H., 1989. Classification, structure, genesis and practical importance of natural solid oil bitumen ("migrabitumen"). *International Journal of Coal Geology* 11, 65-79.

Jarvie, D.M., Claxton, B.L., Henk, F., Breyer, J.T., 2001. Oil and shale gas from the Barnett Shale, Ft. Worth Basin, Texas (abs.): AAPG Annual Meeting Program, p. A100.

Jehlička, Jan, Ondřej Urban, and Jan Pokorný. "Raman spectroscopy of carbon and solid bitumens in sedimentary and metamorphic rocks." *Spectrochimica Acta Part A: Molecular and Biomolecular Spectroscopy* 59, no. 10 (2003): 2341-2352.

Jubb, Aaron M., Palma J. Botterell, Justin E. Birdwell, Robert C. Burruss, Paul C. Hackley, Brett J. Valentine, Javin J. Hatcherian, and Stephen A. Wilson. "High microscale variability in Raman thermal maturity estimates from shale organic matter." *International Journal of Coal Geology* 199 (2018): 1-9.

Kadoura, A., Nair, A.K.N., Sun, S., 2016. Adsorption of carbon dioxide, methane, and their mixture by montmorillonite in the presence of water. *Microporous and Mesoporous Materials* 225, 331-341.

Kelemen, S., Fang, H., 2001. Maturity trends in Raman spectra from kerogen and coal. *Energy & fuels* 15, 653-658.

Khatibi, S., Aghajanpour, A., Ostadhassan, M., Ghanbari, E., Amirian, E., Mohammed, R., 2018. Evaluating the Impact of Mechanical Properties of Kerogen on Hydraulic Fracturing of Organic Rich Formations, SPE Canada Unconventional Resources Conference. Society of Petroleum Engineers.

Khatibi, S., Ostadhassan, M., Aghajanpour, A., 2018. Raman spectroscopy: an analytical tool for evaluating organic matter. *J Oil Gas Petrochem Sci* 2, 00007.

## Chapter 4

Khatibi, S., Ostadhassan, M., Tuschel, D., Gentzis, T., Bubach, B., Carvajal-Ortiz, H., 2018. Raman spectroscopy to study thermal maturity and elastic modulus of kerogen. *International Journal of Coal Geology* 185, 103-118.

Khatibi, Seyedalireza, Mehdi Ostadhassan, David Tuschel, Thomas Gentzis, and Humberto Carvajal-Ortiz. "Evaluating Molecular Evolution of Kerogen by Raman Spectroscopy: Correlation with Optical Microscopy and Rock-Eval Pyrolysis." *Energies* 11, no. 6 (2018): 1-19.

Killops, S.D., Killops, V.J., 2013. *Introduction to organic geochemistry*. John Wiley & Sons.

Klontzman, J.L., 2009. Geochemical controls on production in the Barnett Shale, Fort Worth Basin.

Kong, L., M. O. Ostadhassan, J. Sarout, K. Ling, C. Li, and H. Wang. "Impact of Thermal Maturation on Wave Velocity in the Bakken Shale." In *SPE Western Regional Meeting*. Society of Petroleum Engineers, 2018.

LeFever, Julie A., Richard D. Le Fever, and Stephan H. Nordeng. "Revised nomenclature for the Bakken Formation (Mississippian-Devonian), North Dakota." (2011): 11-26.

Lewan, M., 1993. Laboratory simulation of petroleum formation, *Organic geochemistry*. Springer, pp. 419-442.

Lewan, M., 1997. Experiments on the role of water in petroleum formation. *Geochimica et Cosmochimica Acta* 61, 3691-3723.

Lewan, M., Ruble, T., 2002. Comparison of petroleum generation kinetics by isothermal hydrous and nonisothermal open-system pyrolysis. *Organic Geochemistry* 33, 1457-1475.

Lewan, M., Winters, J., McDonald, J., 1979. Generation of oil-like pyrolyzates from organic-rich shales. *Science* 203, 897-899.

Lewan, M., Winters, J., McDonald, J., 1979. Generation of oil-like pyrolyzates from organic-rich shales. *Science* 203, 897-899.

Lewan, M.D., Roy, S., 2011. Role of water in hydrocarbon generation from Type-I kerogen in Mahogany oil shale of the Green River Formation. *Organic Geochemistry* 42, 31-41.

Li, Chunxiao, Mehdi Ostadhassan, Thomas Gentzis, Lingyun Kong, Humberto Carvajal-Ortiz, and Bailey Bubach. "Nanomechanical characterization of organic matter in the Bakken formation by microscopy-based method." *Marine and Petroleum Geology* 96 (2018): 128-138.

Li, Chunxiao, Mehdi Ostadhassan, Senli Guo, Thomas Gentzis, and Lingyun Kong. "Application of PeakForce tapping mode of atomic force microscope to characterize nanomechanical properties of organic matter of the Bakken Shale." *Fuel* 233 (2018): 894-910.

Liang, M., Wang, Z., Zheng, J., Li, X., Wang, X., Gao, Z., Luo, H., Li, Z., Qian, Y., 2015. Hydrous pyrolysis of different kerogen types of source rock at high temperature-bulk results and biomarkers. *Journal of Petroleum Science and Engineering* 125, 209-217.

Liu, DeHan, XianMing Xiao, Hui Tian, YuShun Min, Qin Zhou, Peng Cheng, and JiaGui Shen. "Sample maturation calculated using Raman spectroscopic parameters for solid organics: Methodology and geological applications." *Chinese Science Bulletin* 58, no. 11 (2013): 1285-1298.

Liu, Y., Xiong, Y., Li, Y., Peng, P.a., 2017. Effect of thermal maturation on chemical structure and nanomechanical properties of solid bitumen. *Marine and Petroleum Geology*.

Liu, Kouqi, Mehdi Ostadhassan, and Lingyun Kong. "Pore structure heterogeneity in middle Bakken formation." In *51st US Rock Mechanics/Geomechanics Symposium*. American Rock Mechanics Association, 2017.

Lünsdorf, N.K., 2016. Raman spectroscopy of dispersed vitrinite—Methodical aspects and correlation with reflectance. *International Journal of Coal Geology* 153, 75-86.

Lupoi, Jason S., Luke P. Fritz, Thomas M. Parris, Paul C. Hackley, Logan Solotky, Cortland F. Eble, and Steve Schlaegle. "assessment of Thermal Maturity Trends in Devonian–Mississippian source rocks Using raman spectroscopy: limitations of Peak-Fitting Method." *Frontiers in Energy Research* 5 (2017): 24.

Mackenzie, A., McKenzie, D., 1983. Isomerization and aromatization of hydrocarbons in sedimentary basins formed by extension. *Geological Magazine* 120, 417-470.

Mansuy, L., Landais, P., Ruau, O., 1995. Importance of the reacting medium in artificial maturation of a coal by confined pyrolysis. 1. Hydrocarbons and polar compounds. *Energy & Fuels* 9, 691-703.

McTavish, R., 1998. The role of overpressure in the retardation of organic matter maturation. *Journal of Petroleum Geology* 21, 153-186.

Michels, R., Landais, P., 1994. Artificial coalification: comparison of confined pyrolysis and hydrous pyrolysis. *Fuel* 73, 1691-1696.

Michels, R., Landais, P., Torkelson, B., Philp, R., 1995. Effects of effluents and water pressure on oil generation during confined pyrolysis and high-pressure hydrous pyrolysis. *Geochimica et Cosmochimica Acta* 59, 1589-1604.

Monthioux, M., 1988. Expected mechanisms in nature and in confined-system pyrolysis. *Fuel* 67, 843-847.

Monthioux, M., Landais, P., 1987. Evidence of free but trapped hydrocarbons in coals. *Fuel* 66, 1703-1708.

Monthioux, M., Landais, P., Monin, J.-C., 1985. Comparison between natural and artificial maturation series of humic coals from the Mahakam delta, Indonesia. *Organic Geochemistry* 8, 275-292.

Mumm, Andreas Schmidt, and Sedat İnan. "Microscale organic maturity determination of graptolites using Raman spectroscopy." *International Journal of Coal Geology* 162 (2016): 96-107.

Myers, G.A., Kehoe, K., Hackley, P., 2017. Analysis of Artificially Matured Shales With Confocal Laser Scanning Raman Microscopy: Applications to Organic Matter Characterization. *Unconventional Resources Technology Conference (URTEC)*.

Olson, R. K., 2008, Cutting analyses, in coalbed methane and shale gas exploration strategies: Workshop for sorbed gas reservoir systems: AAPG Course 15, AAPG Annual Convention, San Antonio, Texas, April 24–25, 2008, 35 p

Ostadhassan, M., Liu, K., Li, C., Khatibi, S., 2018. Geochemical Properties, Fine Scale Characterization of Shale Reservoirs. Springer, pp. 57-70.

Pan, C., Geng, A., Zhong, N., Liu, J., Yu, L., 2009. Kerogen pyrolysis in the presence and absence of water and minerals: amounts and compositions of bitumen and liquid hydrocarbons. *Fuel* 88, 909-919.

Pan, C., Jiang, L., Liu, J., Zhang, S., Zhu, G., 2010. The effects of calcite and montmorillonite on oil cracking in confined pyrolysis experiments. *Organic Geochemistry* 41, 611-626.

Petersen, H.I., Schovsbo, N.H., Nielsen, A.T., 2013. Reflectance measurements of zooclasts and solid bitumen in Lower Paleozoic shales, southern Scandinavia: correlation to vitrinite reflectance. *International Journal of Coal Geology* 114, 1-18.

Piani, L., Robert, F., Beyssac, O., Binet, L., BOUROT-DENISE, M., Derenne, S., Le Guillou, C., Marrocchi, Y., Mostefaoui, S., ROUZAUD, J.N., 2012. Structure, composition, and location of organic matter in the enstatite chondrite Sahara 97096 (EH3). *Meteoritics & Planetary Science* 47, 8-29.

Potgieter-Vermaak, S., N. Maledi, N. Wagner, J. H. P. Van Heerden, R. Van Grieken, and J. H. Potgieter. "Raman spectroscopy for the analysis of coal: a review." *Journal of Raman Spectroscopy* 42, no. 2 (2011): 123-129.

Quirico, E., Rouzaud, J.-N., Bonal, L., Montagnac, G., 2005. Maturation grade of coals as revealed by Raman spectroscopy: Progress and problems. *Spectrochimica Acta Part A: Molecular and Biomolecular Spectroscopy* 61, 2368-2377.

Riediger, C., 1993. Solid bitumen reflectance and Rock-Eval Tmax as maturation indices: an example from the "Nordeg Member", Western Canada Sedimentary Basin. *International Journal of Coal Geology* 22, 295-315.

Rullkötter, J., Marzi, R., 1988. Natural and artificial maturation of biological markers in a Toarcian shale from northern Germany. *Organic Geochemistry* 13, 639-645.

Sadezky, Alexa, Harald Muckenhuber, Hinrich Grothe, R. Niessner, and Ulrich Pöschl. "Raman microspectroscopy of soot and related carbonaceous materials: spectral analysis and structural information." *Carbon* 43, no. 8 (2005): 1731-1742.

Sauerer, B., Craddock, P.R., AlJohani, M.D., Alsamadony, K.L., Abdallah, W., 2017. Fast and accurate shale maturity determination by Raman spectroscopy measurement with minimal sample preparation. *International Journal of Coal Geology* 173, 150-157.

Schito, A., Romano, C., Corrado, S., Grigo, D., Poe, B., 2017. Diagenetic thermal evolution of organic matter by Raman spectroscopy. *Organic Geochemistry* 106, 57-67.

Schmidt, J. S., R. Hinrichs, and C. V. Araujo. "Maturity estimation of phytoclasts in strew mounts by micro-Raman spectroscopy." *International Journal of Coal Geology* 173 (2017): 1-8.

Schrader, B., 2008. Infrared and Raman spectroscopy: methods and applications. John Wiley & Sons.

- Schumacher, M., Christl, I., Scheinost, A.C., Jacobsen, C., Kretzschmar, R., 2005. Chemical heterogeneity of organic soil colloids investigated by scanning transmission X-ray microscopy and C-1s NEXAFS microspectroscopy. *Environmental science & technology* 39, 9094-9100.
- Spötl, C., Houseknecht, D.W., Jaques, R.C., 1998. Kerogen maturation and incipient graphitization of hydrocarbon source rocks in the Arkoma Basin, Oklahoma and Arkansas: a combined petrographic and Raman spectrometric study. *Organic Geochemistry* 28, 535-542.
- Steptoe, Anne. "Petrofacies and depositional systems of the Bakken Formation in the Williston Basin, North Dakota." In *Masters Abstracts International*, vol. 51, no. 03. 2012.
- Tegelaar, E.W., Noble, R.A., 1994. Kinetics of hydrocarbon generation as a function of the molecular structure of kerogen as revealed by pyrolysis-gas chromatography. *Organic Geochemistry* 22, 543-574.
- Tian, H., Xiao, X., Wilkins, R., Li, X., Gan, H., 2007. Gas sources of the YN2 gas pool in the Tarim Basin—Evidence from gas generation and methane carbon isotope fractionation kinetics of source rocks and crude oils. *Marine and Petroleum Geology* 24, 29-41.
- Tissot, B.P., Welte, D.H., 1984. Diagenesis, catagenesis and metagenesis of organic matter, *Petroleum Formation and Occurrence*. Springer, pp. 69-73.
- Tuinstra, F., and J. Lo Koenig. "Raman spectrum of graphite." *The Journal of Chemical Physics* 53, no. 3 (1970): 1126-1130.
- Tyson, R.V., 1995. Abundance of organic matter in sediments: TOC, hydrodynamic equivalence, dilution and flux effects, *Sedimentary organic matter*. Springer, pp. 81-118.
- Valentine, B.J., Hackley, P.C., Enomoto, C.B., Bove, A.M., Dulong, F.T., Lohr, C.D., Scott, K.R., 2014. Organic petrology of the Aptian-age section in the downdip Mississippi Interior Salt Basin, Mississippi, USA: Observations and preliminary implications for thermal maturation history. *International Journal of Coal Geology* 131, 378-391.
- Van Krevelen, D.W., 1993. *Coal: typology, physics, chemistry, constitution*. Elsevier Amsterdam.
- Waples, Douglas Wendle. *Organic geochemistry for exploration geologists*. Burgess Pub. Co., 1981.
- Wu, L.M., Zhou, C.H., Keeling, J., Tong, D.S., Yu, W.H., 2012. Towards an understanding of the role of clay minerals in crude oil formation, migration and accumulation. *Earth-Science Reviews* 115, 373-386.
- Yang, Chin-Shung, Szu-Pyng Kao, Fen-Bin Lee, and Pen-Shan Hung. "Twelve different interpolation methods: A case study of Surfer 8.0." In *Proceedings of the XXth ISPRS Congress*, vol. 35, pp. 778-785. 2004.
- Yang, J., Hatcherian, J., Hackley, P.C., Pomerantz, A.E., 2017. Nanoscale geochemical and geomechanical characterization of organic matter in shale. *Nature communications* 8, 2179.
- Zargari, Saeed. "Effect of thermal maturity on nanomechanical properties and porosity in organic rich shales (a Bakken shale case study)." PhD diss., Colorado School of Mines. Arthur Lakes Library, 2015.

## Chapter 4

Zhang, Liya, and Luis A. Buatois. "Sedimentology, ichnology and sequence stratigraphy of the Upper Devonian–Lower Mississippian Bakken Formation in eastern Saskatchewan." *Bulletin of Canadian Petroleum Geology* 64, no. 3 (2016): 415-437.

Zhou, Q., Xiao, X., Pan, L., Tian, H., 2014. The relationship between micro-Raman spectral parameters and reflectance of solid bitumen. *International Journal of Coal Geology* 121, 19-25.

Zhu, G., Zhang, S., Su, J., Zhang, B., Yang, H., Zhu, Y., Gu, L., 2013. Alteration and multi-stage accumulation of oil and gas in the Ordovician of the Tabei Uplift, Tarim Basin, NW China: implications for genetic origin of the diverse hydrocarbons. *Marine and Petroleum Geology* 46, 234-250.

## Chapter 5 CNMR Relaxometry a New Approach to Detect Geochemical Properties of Organic Matter in Tight Shales

A paper published in the journal of **Fuels**

Seyedalireza Khatibi, Mehdi Ostadhassan, Z. Harry Xie, Thomas Gentzis, Bailey

Bubach, Zheng Gan, Humberto Carvajal-Ortiz

### Abstract

Understanding organic matter properties in terms of maturity and production potential are crucial for the initial assessment of unconventional plays. This is important since the amount of hydrocarbon that can be generated is a function of organic matter type and content in the formation and its thermal maturity. The complexity of shale plays in terms of constituent components has demonstrated that new analytical methods should be acquired to better understand hydrocarbon generation processes. In this study, a few samples from the upper and lower members of the Bakken Formation in the USA were selected from different depths and maturity levels. The samples were analyzed by a high frequency (22 MHz) nuclear magnetic resonance (NMR relaxometry) equipment, followed by Rock-Eval pyrolysis (using the Basic/Bulk-Rock method for all samples and a multi-heating rate method, MHR, for the two least mature samples) and bitumen reflectance evaluations. Results showed NMR can detect different hydrogen populations within the samples and distinguish among phases, such as solid organic matter, hydrocarbons (mobile oil), and water by T<sub>1</sub>-T<sub>2</sub> mapping. We were also able to relate different identified areas on NMR T<sub>1</sub>-T<sub>2</sub> maps to geochemical parameters of the organic matter obtained from Rock-Eval pyrolysis (such as S<sub>1</sub>, S<sub>2</sub>, and HI) and with thermal maturity (vitrinite reflectance-equivalent).

**Keywords:** Unconventional reservoirs, Bakken Formation, NMR relaxometry, NMR T<sub>1</sub>-T<sub>2</sub> map, Rock-Eval Pyrolysis

## 5-1 Introduction

The amount of hydrocarbons generated from organic matter in a source rock depends on different parameters, such as kerogen type, maturity levels, the total amount of organic carbon (McCarthy et al., 2011). The common methods for evaluating above parameters are programmed pyrolysis and organic petrography by microscopic methods. Open-system programmed pyrolysis or Rock-Eval pyrolysis (RE) is a widely accepted geochemical technique that measures four components related to the main major classes of organic constituents (S1-S4) (Lafargue et al., 1998; Behar et al., 2001; Carvajal-Ortiz and Gentzis, 2015).

The increase in exploration and production of unconventional reservoirs and their complexity has led to the employment of new methods for resource-play assessment, such as nuclear magnetic resonance (NMR). Solid state  $^{13}\text{C}$  nuclear magnetic resonance (NMR) spectroscopic methods have been used extensively to study the decomposition of organic matter in a wide range of media, such as sewage (Albrecht et al., 2008), co-composting and bio-wastes (Albrecht et al., 2009), kerogen degradation (Petsch et al. 2001), and recent sediments and soils (Carrie et al., 2012). NMR techniques contribute to the understanding of hydrocarbon resource-plays by studying the behavior and occurrence of petroleum accumulations. NMR techniques have the potential to characterize kerogen (Werner-Zwanziger et al., 2005; Kelemen et al., 2007; Mao, 2010; Washburn and Birdwell, 2013; Cao et al., 2013), bitumen (Feng et al., 2013; Solum et al., 2013), petroleum (Andrews et al., 2011; Korb et al., 2013), and asphaltenes (Lisitza et al., 2009; Andrews et al., 2011; Dutta Majumdar et al., 2013). Tinni et al. (2014) used NMR to characterize the mobility of fluids in both conventional and unconventional reservoirs. NMR has the advantage to determinate pore size distribution and liquid typing and saturation analysis (Kenyon, 1997; Coates et al., 1999; Rezaee et al., 2012; Al Hinai et al., 2014; Piedrahita and Aguilera, 2017). It can provide information to confidently infer pore sizes to the nano-meter scale, as well as distinguishing different hydrogen (proton) populations associated to the presence of water, oil, gas, and kerogen (Sondergeld et al., 2010; Sulucarnain et al., 2012; Behroozmand et al., 2015). Fleury and Romero-Sarmiento (2016) quantified the connectivity of the pore network system and provided a measure of tortuosity.

Recently, Birdwell and Washburn (2015) demonstrated, using multiple techniques to study hydrocarbons in shales, that their NMR data did not show any quantitative correlation with Rock-

Eval pyrolysis due to the low sensitivity of the NMR spectrometer (2 MHz) used and the poor resolution in the  $T_1$ - $T_2$  maps. Romero-Sarmiento et al. (2017) demonstrated that NMR  $T_1$ - $T_2$  maps, and particularly the  $T_1/T_2$  ratio, can be used to distinguish bitumen, oil, and organic matter as shown in the Jurassic-age Vaca Muerta Formation in Argentina. The above study correlated TOC obtained from Rock-Eval pyrolysis (using the IFPEN Shale Play® method) to ‘solid echo’ signal intensities calculated by the low field hydrogen NMR relaxometry technique. One of the main challenges still not solved is defining the margins of different components of organic rich shales in  $T_1$ - $T_2$  map that might overlap.

In the present study, the high frequency (22 MHz) NMR relaxometry technique was used as a new approach to identify hydrocarbon components and organic matter in tight shale samples and to establish a relationship between the NMR  $T_1$ - $T_2$  map and Rock-Eval pyrolysis parameters as well as thermal maturity. The proposed method provides a non-destructive complement to evaluate organic matter properties in relatively larger quantities, when compared to conventional methods that use only milligrams of sample. The method also combines geochemical and petrophysical data to better define the location of different components in the  $T_1$ - $T_2$  map.

## **5-2 Geological setting of the studied area**

The Bakken Formation is an organic-rich shale, mudstone and sandstone that was deposited during the Late Devonian and Early Mississippian periods. It is located in the Williston Basin, USA and extends into Canada (Smith and Bustin, 2000). Studies have shown that marine kerogen Type II is the most abundant organic matter in the Bakken (Sonnenberg and Pramudito, 2009; Jin and Sonnenberg, 2013; Liu et al., 2017; Khatibi et al., 2018a; Abarghani et al., 2018). Samples from the Bakken Formation were retrieved from six different wells (Wells 1-6) varying in depth and thermal maturity.

## **5-3 Analytical methods**

### **5-3.1 Reflectance measurements**

For petrographic analysis, six whole-rock samples were crushed to 20 mesh (850  $\mu$ m) particles, mixed with Epo Thin epoxy resin and hardener (ratio of 2:1) and left to harden under vacuum conditions for 24 hours (Hackley et al., 2015). The samples were polished using Buehler EcoMet/

AutoMet 250 automated polishing equipment. A Carl Zeiss Axio Imager A2m microscope, equipped with a white light source and a UV light was used to analyze the random reflectance and qualitative fluorescence, for reflectance measurements and visual kerogen analysis. Due to the absence of primary vitrinite, the equivalent vitrinite maturity %*VRo* – *eq* was calculated from the reflectance of solid bitumen (%*BRO*) present in the samples using the Jacob (1989) formula:

$$\%VRo \text{ (equivalent)} = \%BRO * 0.618 + 0.4 \quad (1)$$

### 5-3.2 Rock-Eval Pyrolysis

Crushed samples varying in weight from 15-60 mg were subjected to pyrolysis using a Rock-Eval 6 Turbo analyzer (Vinci Technologies, France) via the Basic/Bulk-Rock method (IFP methods). Each sample was placed in the pyrolysis oven and heated isothermally for 3 minutes at 300°C before the temperature was increased to 650°C at a rate of 25°C/min. In addition, the least mature and shallowest samples from Well 1 and Well 6 were analyzed using a modified IFP Shale Play® method, referred to therein as multi-heating rate (MHR) method. The initial heating temperature was 100°C and was increased to 200°C where it was kept isothermal for 3 minutes in order to complete the thermal extraction of the lightest hydrocarbon fraction (Sh0; C1-C15 hydrocarbons) (Romero-Sarmiento et al., 2014; 2015; Carvajal-Ortiz and Gentzis, 2018). From 200°C, the oven temperature was increased to 350°C at 25°C/min, staying isothermal for 3 minutes for the thermal extraction of the medium-heavy hydrocarbon fraction (Sh1; C15-C40 hydrocarbons; Sanei et al., 2015). The last temperature step consisted of ramping the temperature to 650°C at 25°C/min for the thermal cracking of the NSO and/or kerogen fraction (Sh2; Romero-Sarmiento et al., 2014; Sanei et al., 2015). For more details, the reader is referred to Romero-Sarmiento et al. (2014, 2015, 2016) and Carvajal-Ortiz and Gentzis (2018).

### 5-3.3 NMR relaxometry

When dealing with unconventional formations, such as shale oil or shale gas with the characteristics of low porosities, very small pores, co-existence of water, oil and other organic matter and ultra low permeability, the traditional low frequency NMR is insensitive and unable to detect fast decay signals from solid organic matter or distinguish between water and oil.

Since it was first launched commercially in 2013, high frequency (HF, at 22MHz) NMR techniques have quickly gained attention and acceptance in the unconventional rock core analysis

as a means to obtain quality petrophysical properties. HF NMR has the advantages of 30 to 50-fold more sensitivity than low frequency (usually 2 MHz or lower) NMR and much shorter inter-echo spacing time. These make the HF NMR an ideal tool to characterize unconventional mudstones because of its capability to detect hydrogen signals not only from water and oil but also from solid organic matter.

The two-dimensional NMR mapping techniques (Song et al., 2002), i.e.,  $T_1$ - $T_2$  correlation measurements, have gradually gained attention in the petroleum for advantages in plotting both relaxations time  $T_1$  and  $T_2$  simultaneously. Previous studies have shown the general location of different components in the  $T_1$ - $T_2$  map (Fleury et al., 2013; Fleury, 2014; Washburn and Birdwell, 2013; Fleury and Romero-Sarmiento, 2016). The summary of previous studies on the general location of different components in  $T_1$ - $T_2$  map is shown in Figure 5-3-1. The boundary of regions in the 2D map might overlap and cannot be defined clearly.  $T_1$  in organic solids is long because the frequency of fluctuations in solids are inefficient at transferring energy to the environment and cause overlapping of signals, while  $T_2$  relaxation times will be shorter due to the strong intramolecular dipolar coupling that quickly dephases the spins.

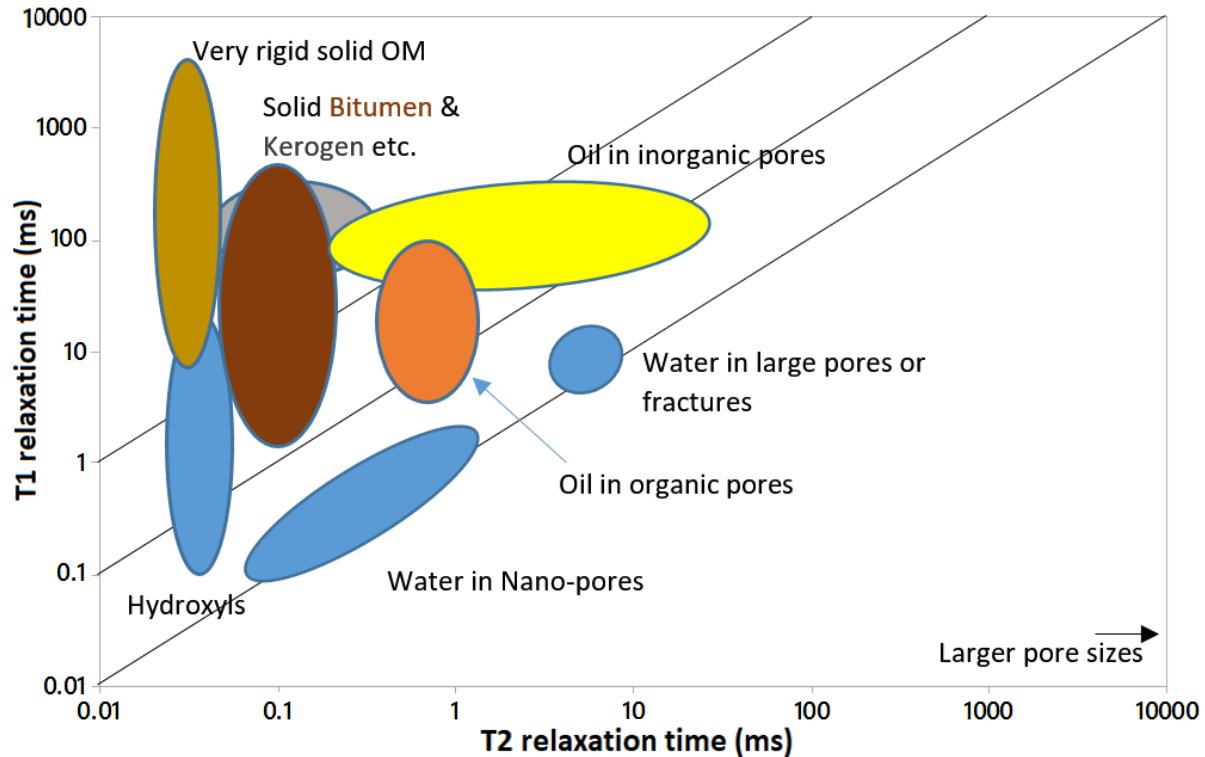


Figure 5-3-1 General map of T1-T2 map (modified after Fleury et al. (2016), Romero-Sarmiento et al. (2017), Washburn and Birdwell (2013), Mehana and El-monier (2016)).

Generally,  $T_2$  is the measure of molecular mobility. The longer is the  $T_2$ , the more mobile the molecules are. Therefore, signal regions on the right side of the map are from mobile components or from liquids in large pores, and on the left side are from more bound and more viscous liquids, from liquids in small pores, or from solid components. This leads to a direct result that  $T_2$  relaxation is inversely proportional to viscosity (Dunn et al., 2002). A decrease in viscosity is equivalent to an increase in  $T_2$  relaxation time if the liquids are present in similar size pores. Water, oil and solid organic matter can be identified with the ratios of  $T_1$  and  $T_2$  according to the Bloembergen-Purcell-Pound (BPP) theory and according to the molecule sizes relative to pore sizes. BPP theory is a theoretical model of NMR relaxation mechanism proposed by (Bloembergen et al., 1948). The theory explained the NMR relaxation constants (i.e. relaxation times,  $T_1$  and  $T_2$ ) of a pure substance in correspondence with its state, taking into account the effect of tumbling motion of molecules on the local magnetic field disturbance. The theory is in good agreement with numerous experiments on pure substances and complex compounds such as porous media with some exceptions.

In the present study, the NMR measurements were made at Core Laboratories with a customized 22MHz spectrometer from MR Cores, equipped with a 30 mm diameter probe, which is configured to have a very short ring down delay time (or “dead time”) of less than 15  $\mu$ s to allow for early time NMR data acquisition. This will enable us to capture signals from solid components with a very short T<sub>2</sub> in the sample. The NMR probe size allowed for measurements on samples of any shape or form that can be loaded into sample vials of 30 mm diameter. All samples in this study were shale fragments ranging from 12 g to 20 g in weight. The T<sub>2</sub> data were acquired using the CPMG sequence with an echo time spacing of TE = 0.07 ms. The T<sub>1</sub> data were acquired using an inversion-recovery sequence. The T<sub>1</sub>-T<sub>2</sub> correlation data were acquired using a pulse sequence of combining T<sub>1</sub> and T<sub>2</sub> data acquisitions, where 61 T<sub>1</sub> wait steps were used and 5000 echoes were recorded at each T<sub>1</sub> wait step, then processed using an Optimized Truncated Singular Value Decomposition (OTSVD) inversion method (Hansen, 1987; Hanson, 1971; Xu, 1998) to obtain the 2D T<sub>1</sub>-T<sub>2</sub> map. A standard sample of a known amount of water mixed with D<sub>2</sub>O sealed in a glass vial was used to calibrate the NMR instrument for quantitative data acquisition.

## 5-4 Results and discussion

### 5-4.1 Rock-Eval Pyrolysis and Organic Petrography

Pyrolysis results (Figure 5-4-1) and organic petrography study of the samples (Figure 5-4-2) show that organic matter type II is the main constituent of the organic facies. It should be noted, scale bar is 10 micrometers in Figure 5-4-2; excitation is at 465 nm; combined dichroic and barrier filter have a cut at 515 nm. Total magnification of photos A-C is 500X and the total magnification of photos D-F is 250X. Vitrinite reflectance-equivalent values (converted from bitumen Ro using the Jacob (1989) Formula) show that the organic matter in the six wells ranges from immature to approximately the middle part of the oil window (Table 5-4-1).

Table 5-4-1 Rock-Eval data for the six samples using the Basic/Bulk-Rock method.

Well	Depth (ft)	TOC (wt%)	S1	S2	S3	S3	T <sub>max</sub> (°C)	HI (S2x100/TOC)	BRO% (%)	VRo-eq (%)
			(mg HC/g)	(mg HC/g)	(mg CO <sub>2</sub> /g)	(mg CO/g)				
1	5438	24.71	7.97	128.71	2.08	1.66	419	520.88	0.16	0.38
2	8325	16.27	8.27	90.69	0.35	4.5	428	557.41	0.22	0.54
3	9886	15.76	9.27	83.7	0.08	0.25	423	531.09	0.30	0.59
4	10437	13.39	7.64	46.79	0.04	0.2	448	349.44	0.74	0.86

5	10725.5	9.04	6.13	13.94	0.11	0.2	450	154.2	0.87	0.94
6	3785	14.64	3.4	76	0.41	0.71	412	519.5	0.10	0.25

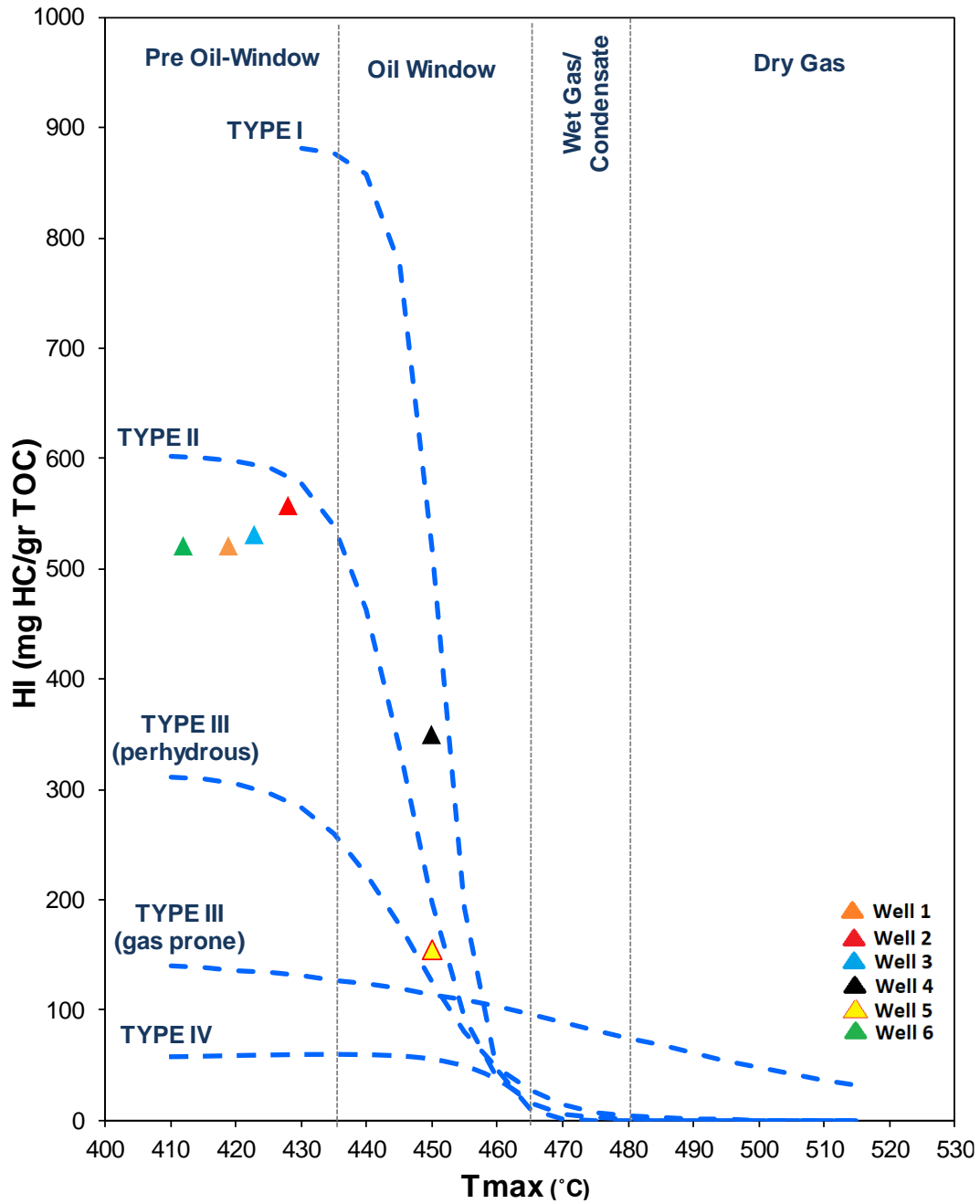


Figure 5-4-1 HI vs. Tmax is showing the type of kerogen in the six samples of this study.

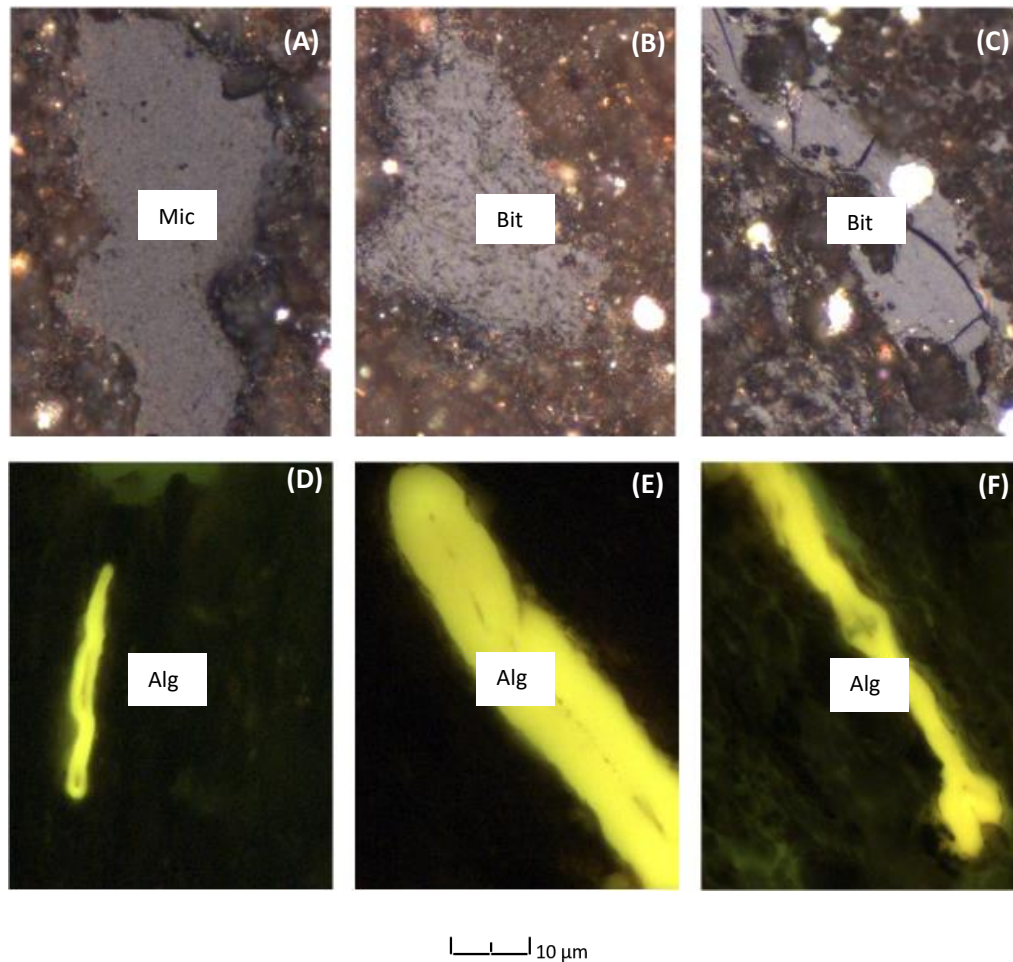
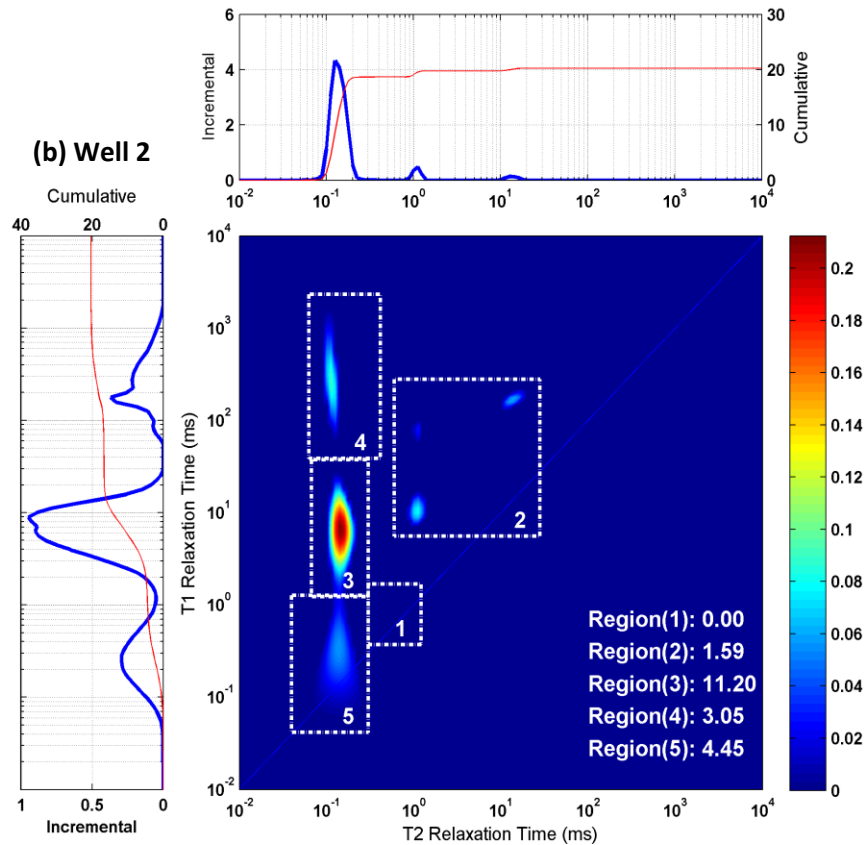
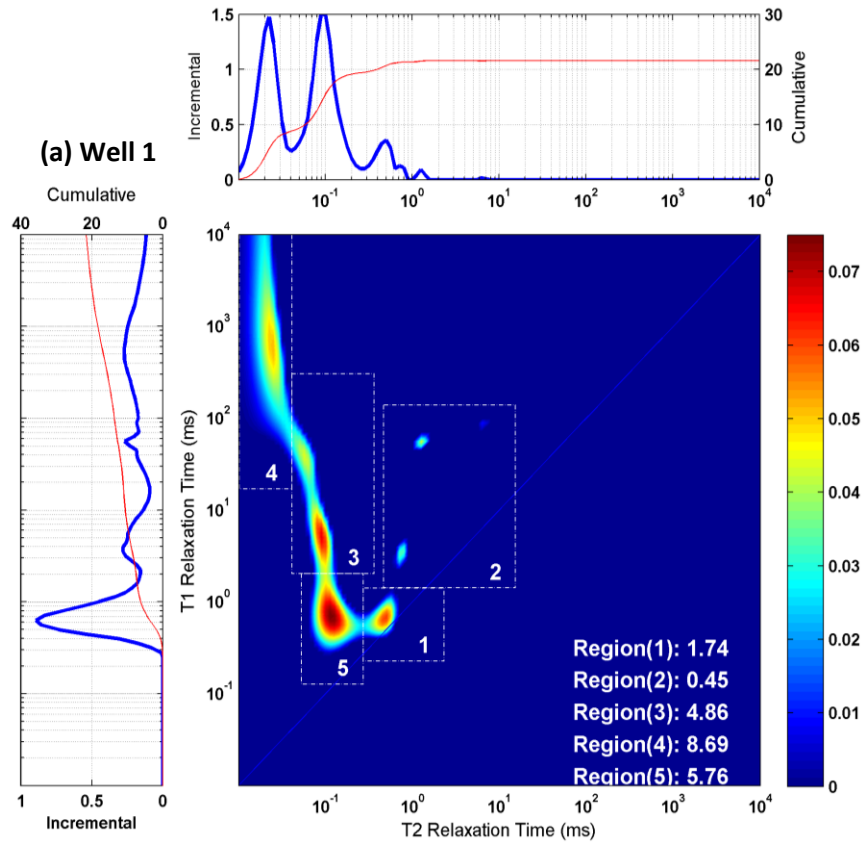
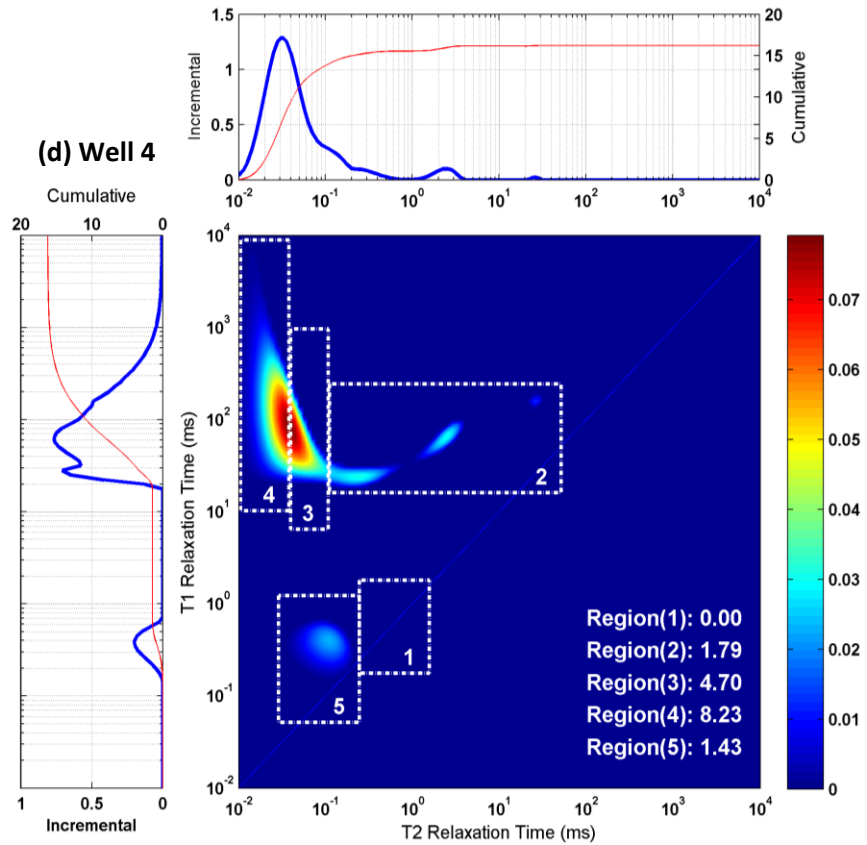
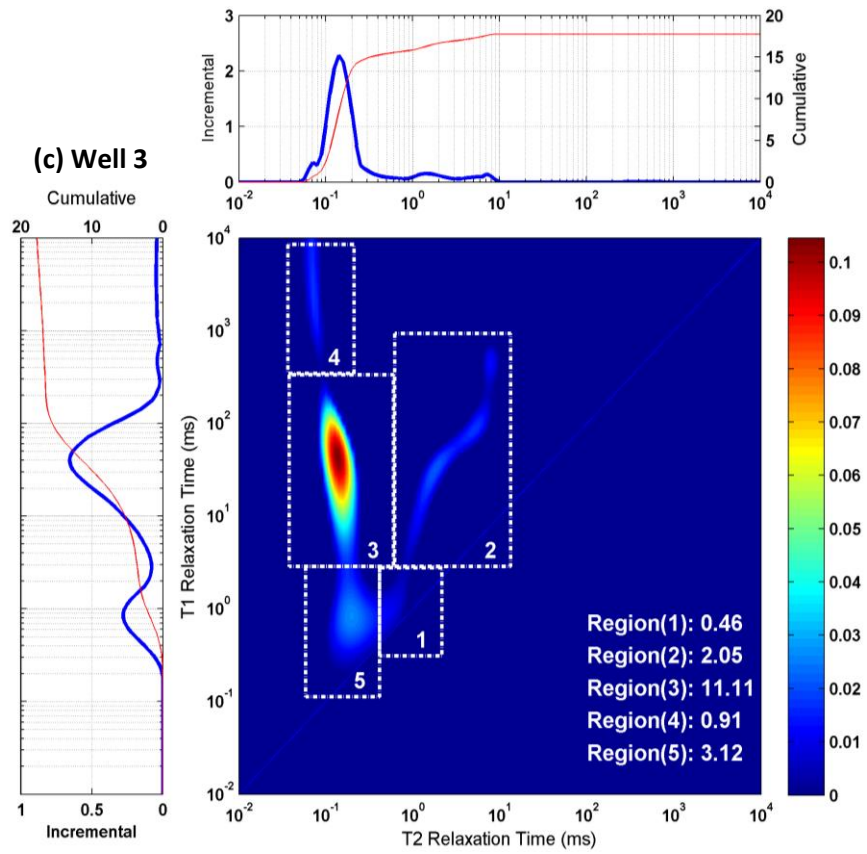


Figure 5-4-2 (A) Micrinite (Mic) showing granular texture ( $R_o=0.54\%$ ), 5438 ft; (B) Bitumen (Bit) with  $R_o$  of 0.50%, 8325 ft; (C) Bitumen (Bit) with  $R_o$  of 0.80%, 10437 ft; (D) Alginite (Alg) having greenish-yellow fluorescence, 5438 ft; (E) A large oil-prone Tasmanites alginite (Alg) exhibiting golden-yellow fluorescence color, 8325 ft; (F) Alginite (Alg) showing golden-yellow fluorescence, 8325 ft. Scale bar is 10 micrometers. Excitation is at 465 nm; combined dichroic and barrier filter have a cut at 515 nm. Total magnification of photos A-C is 500X and the total magnification of photos D-F is 250X.

### 5-4.2 NMR 2-D mapping

$T_1$ - $T_2$  maps for the six samples (Well 1 to Well 6) were generated. The samples were in their native form. The maps are shown in Figure 5-4-3 (a-f). In order to obtain quantitative information in each component on a  $T_1$ - $T_2$  map,  $T_1$  and  $T_2$  values as borders of the boxes are needed to be selected which are culled cut-offs. In normal cases, these borders (cut-offs) are clearly defined on a  $T_1$ - $T_2$  map, e.g. regions (1) and (2). But exceptions are quite often, e.g. regions (3) and (4) for the well 4, where knowledge of physical properties, such as  $T_1$  and  $T_2$ , of heavy hydrocarbons will be applied. It is also one of our goals to use Rock-Eval data to help us to define cut-offs for each region on a  $T_1$ - $T_2$  map.





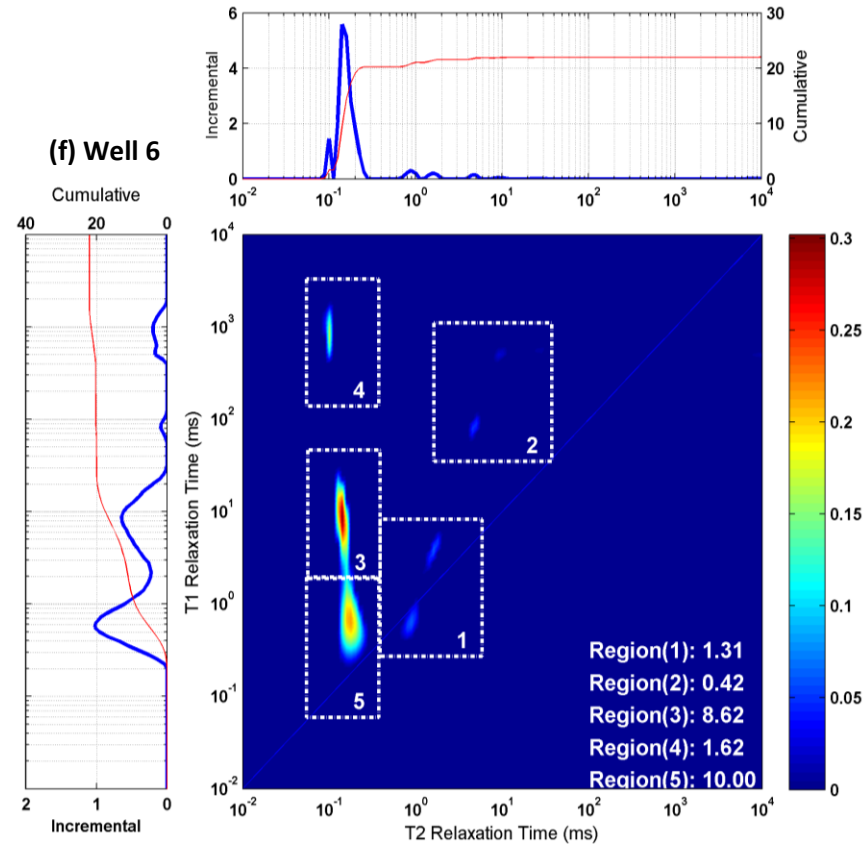
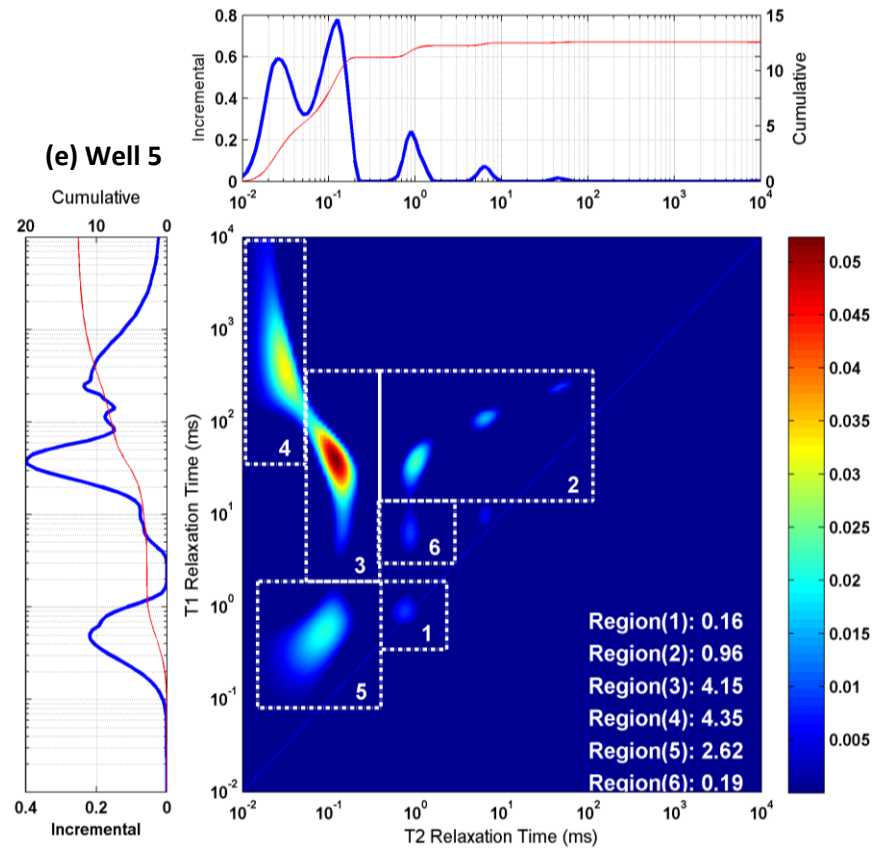


Figure 5-4-3 (a-f) T<sub>1</sub>-T<sub>2</sub> maps for Well 1 to Well 6. Regions (1) to (5) and their corresponding amplitudes (NMR Hydrogen fraction (mg/g)) are shown on each map. A cut-off of T<sub>2</sub>=0.05 ms derived from Well 1 and Well 5, was applied to Well 4 to separate Regions (3) and (4). 1-D distributions of relaxation times for each map are also shown at the top and left side (blue is incremental, and red is cumulative), which represent the intensity projection of the map on each axis. Signal amplitudes are expressed in a unit of milligram hydrogen per gram rock sample (mg H/g rock). It should be mentioned that the blue curve is incremental, and the red curve is cumulative.

In order to compare the NMR measurements with Rock-Eval pyrolysis and thermal maturity analysis, five regions on the map were identified, as shown in Figure 5-4-3. In reference to Section 3.3 and also Figure 5-3-1 as a general guide, Region (1) in Figure 5-4-3 shows a T<sub>1</sub>/T<sub>2</sub> ratio close to 1, so it represents water in nano-pores. Region (2) is in the oil position indicating moveable oils. Region (3) has a higher T<sub>1</sub>/T<sub>2</sub> ratio, T<sub>2</sub> is very short, and represents heavy oil or solid organic matter. Region (4) has the highest T<sub>1</sub>/T<sub>2</sub> ratio and shortest T<sub>2</sub>; it comes from very rigid solids that contain hydrogen. Region (5) has a small T<sub>1</sub>/T<sub>2</sub> ratio with a very short T<sub>2</sub>, it most likely comes from water in nano-pores, hydroxyl, or organic matter. This may be identified in combination with pyrolysis data. Region (6) in Figure 5-4-3 (e) is from oil in organic pores and can be part of Region (2). The amplitudes and values of T<sub>1</sub> and T<sub>2</sub> from each region are summarized in Table 5-4-2.

It should be noted that Region (4) on the T<sub>1</sub>-T<sub>2</sub> maps for Wells 1, 4, and 5 has very short T<sub>2</sub>s. This is thought to be caused by the existence of strong paramagnetic impurities in the samples. The Bakken Formation is known to contain pyrite and other iron-bearing minerals, such as ilmenite (Fe<sub>3</sub>O<sub>4</sub>) and chlorite, as well as halite which reduce the relaxation time T<sub>2</sub> (Rueslåtten et al., 1998).

Table 5-4-2 Amplitude of the NMR signal of regions 1 to 5 and T<sub>1</sub>/T<sub>2</sub> ratios.

Well No.	NMR Signal Amplitude (mg H/g)						Region (3) on the Maps		
	Region (1)	Region (2)	Region (3)	Region (4)	Region (5)	Region (6)	T <sub>1</sub> (ms)	T <sub>2</sub> (ms)	T <sub>1</sub> /T <sub>2</sub>
1	1.74	0.45	4.86	8.69	5.76	0	5.5	0.09	61.11
2	0.00	1.59	11.20	3.05	4.45	0	9.4	0.11	85.45
3	0.46	2.05	11.11	0.91	3.12	0	21.4	0.16	133.75
4	0.00	1.79	4.70	8.23	1.43	0	48.6	0.15	324.00
5	0.21	1.15	4.15	4.35	2.62	0.19	44.7	0.11	406.36
6	1.31	0.42	8.62	1.62	10.00	0	8.5	0.14	60.71

### 5-4.3 Correlations between NMR and Pyrolysis

We believe NMR can reveal the maturity stage of organic matter indirectly. As organic matter matures, it loses aliphatic chains (the portion with high hydrogen content) and becomes more aromatic (Khatibi et al., 2018b). Aromatic rings form clusters, which makes the solid organic

matter more rigid. Thus, the  $T_1$  relaxation times of organic matter are expected to be longer when it becomes more thermally mature (Bryan et al., 2003; Washburn and Birdwell, 2013). On the other hand, the solid organic matter shows  $T_2$  at almost constant value. Thus, the  $T_1/T_2$  ratio in Region (3) is expected to increase when maturity (as reflected by VRo-equivalent) increases, as shown in Figure 5-4-4. The correlation between  $T_1/T_2$  ratio vs. VRo (equivalent) using the second order polynomial fit is almost perfect for all samples including the two immature ones.

Another way to correlate NMR data to VRo (equivalent) is by using the amplitude of Region (3) representing solid organic matter, Figure 5-4-5. As seen, as maturity increases, the amplitude of Region (3) - representing hydrogen content - decreases, which in accordance to the general trend of maturation of organic matter. However, the two immature samples (Well 1 and Well 6) are shown as outliers, a behavior that will be discussed in the following paragraphs. It should be emphasized that the hollow triangle or square symbols in the following figures represent the wells that have not been used in the regression process.

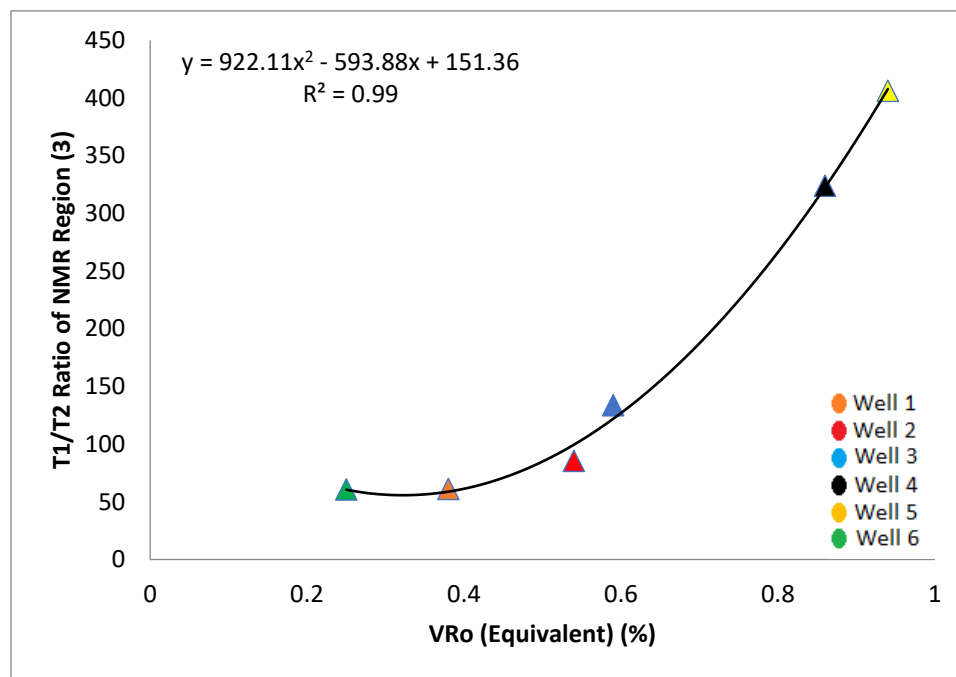


Figure 5-4-4  $T_1/T_2$  ratio of Region 3 from the NMR  $T_1$ - $T_2$  map vs. VRo (equivalent). The trend shows the  $T_1/T_2$  ratio increases with thermal maturity. The power function relationship has a correlation coefficient ( $R^2$ ) value of 0.99 including all samples.

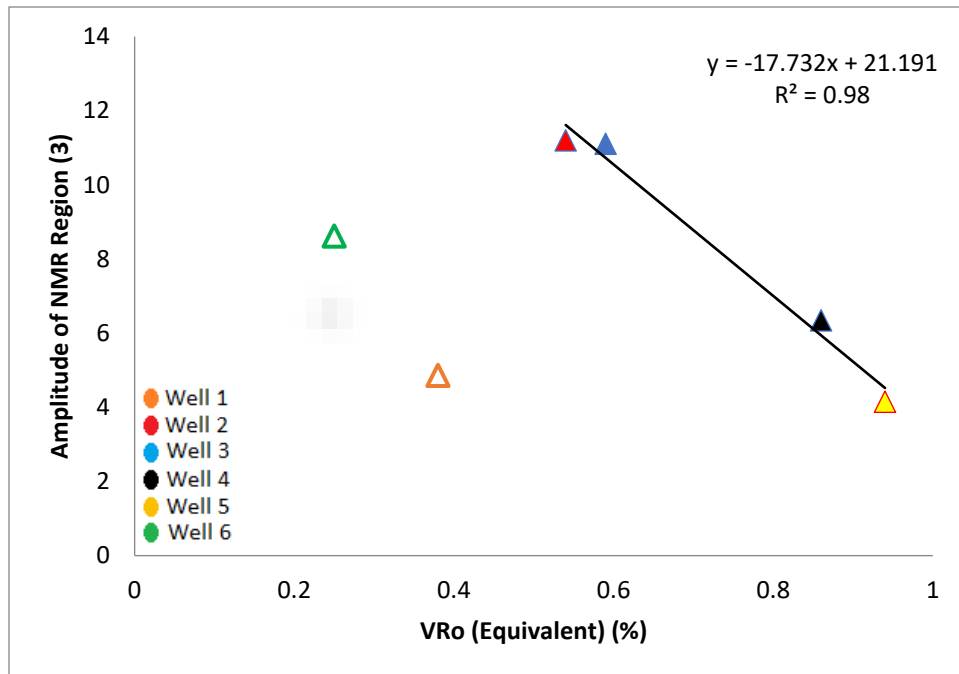


Figure 5-4-5 Hydrogen volume of Region 3 in the NMR T<sub>1</sub>-T<sub>2</sub> map vs. VRo (equivalent) from Petrography. The correlation coefficient of samples excluding two immature ones is 0.98.

It was stated earlier that NMR can present data from different sources of hydrogen population in the samples. Therefore, the hydrogen population that represents the organic matter zones in the T<sub>1</sub>-T<sub>2</sub> map could be correlated to the Hydrogen Index (HI) from Rock-Eval pyrolysis, as seen in Figure 5-4-6, which is also in accordance with Figure 5-4-5. Since, as maturity increases, hydrogen content of organic matter decreases, thus the amplitude of Region (3) decreases. So, maturity has a reverse and HI has a direct trend with the amplitude of Region (3).

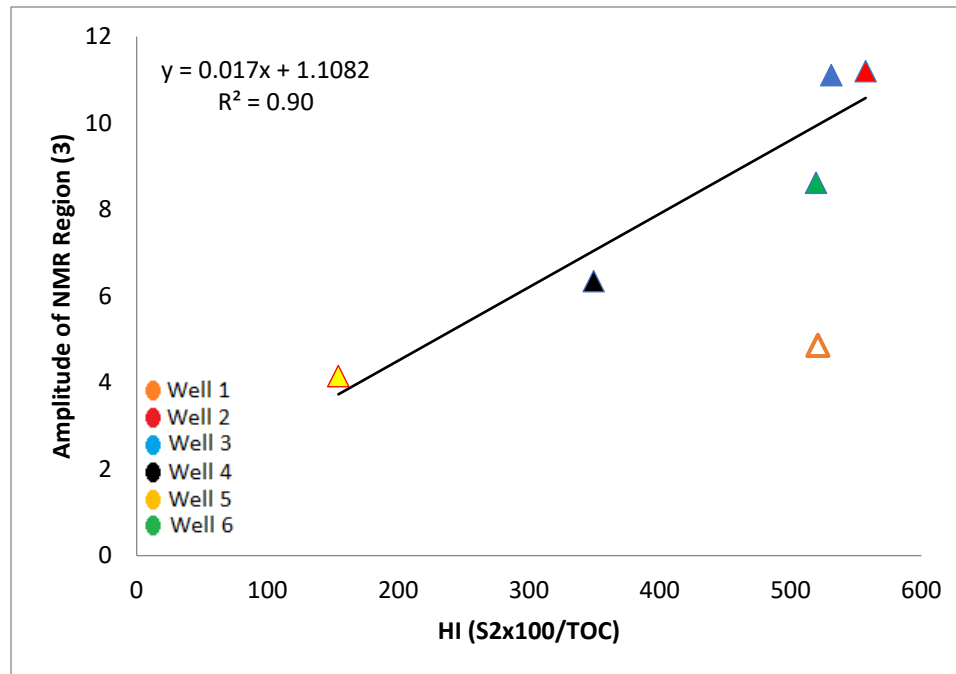


Figure 5-4-6 Hydrogen volume (mg H/g rock) of Region 3 in the NMR T<sub>1</sub>-T<sub>2</sub> map vs. HI from Rock-Eval. The linear relationship with correlation coefficient 0.90 excluding Well 1.

NMR can provide an improved understanding of S1 and S2 peaks in Rock-Eval pyrolysis. Since S1 is defined as the free hydrocarbons present in pores, it can be correlated to the hydrogen fraction (population) measured by NMR from the oil region (Region 2) in T<sub>1</sub>-T<sub>2</sub> maps, as seen in Figure 5-4-7. The immature sample in Well 1 is clearly an outlier. On the other hand, S2 in Rock-Eval is the potential of source rock to generate hydrocarbons upon heating. Molecular structures with higher hydrogen content, such as aliphatic ones, contribute the most to the conversion of organic matter to hydrocarbons (Witte et al., 1988; Gao et al., 2017). Accordingly, the hydrogen content in organic matter can be directly correlated to the S2 from Rock-Eval. Figure 5-4-8 shows the relationship between the amplitude of Region (3) vs. S2. The immature sample in Well 1 is still an outlier.

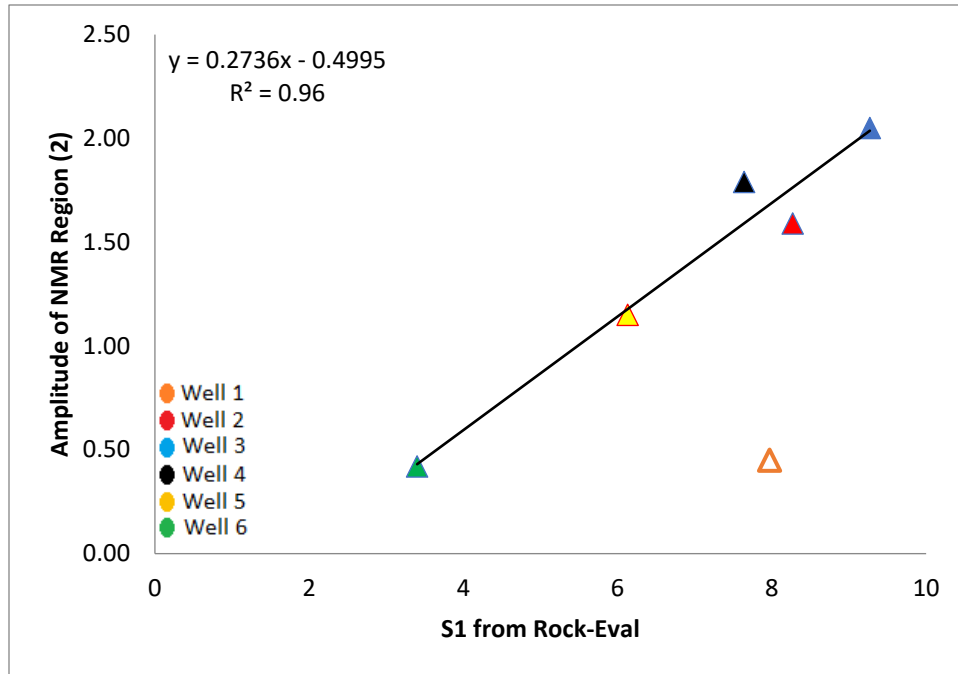


Figure 5-4-7 Hydrogen volume (mg H/g rock) of Region 3 in the NMR T1-T2 map vs. S1 from Rock-Eval. The linear relationship with correlation coefficient 0.96 excluding Well 1.

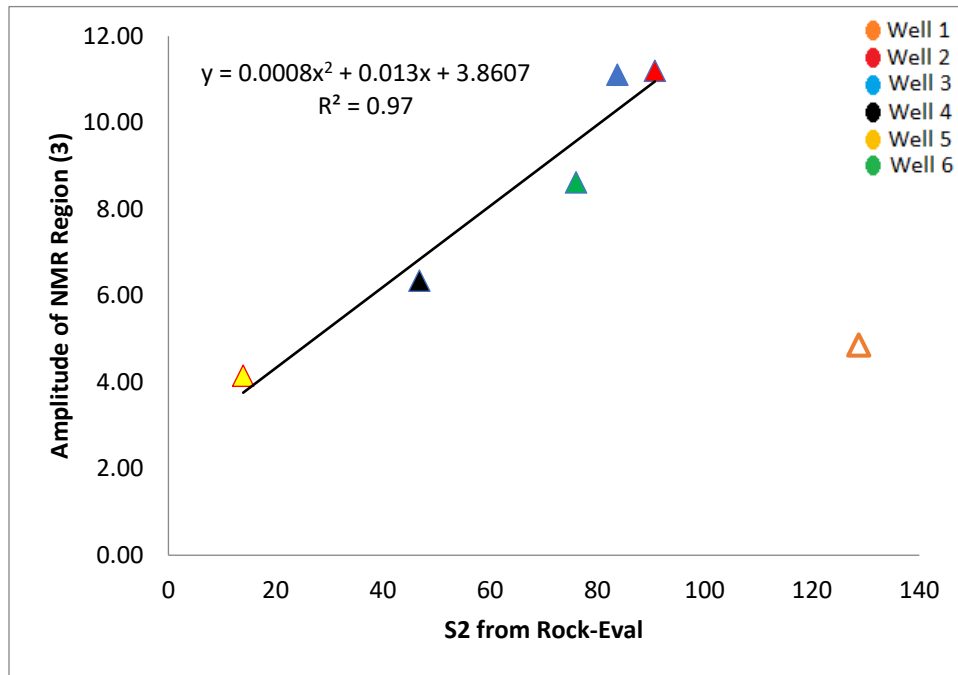


Figure 5-4-8 Hydrogen Volume of Region 3 in the NMR T1-T2 map vs. S2 HC volume from Rock-Eval, with correlation coefficient 0.97 excluding Well 1.

As seen, NMR spectroscopy shows high potential in correlating different regions on the T<sub>1</sub>-T<sub>2</sub> map to thermal properties of organic matter, except for two immature samples. In order to reason out this challenge, different causes were considered.

Firstly, we substituted S1 from the Basic/Bulk-Rock method for Sh0 from the MHR method for the immature samples in Well 1 and Well 6. The MHR method captures those light hydrocarbons that otherwise would be volatilized and not measured by the Basic/Bulk-Rock method in immature samples containing the highest amount of thermovaporizable light hydrocarbons. Using the MHR pyrolysis method (Table 5-4-3) resulted in the data points of the immature samples shifting to the left in the correlation with Region 2 from NMR. Well 1 moved closer to the trend line of the other five samples while this was not the case for Well 6 (Figure 5-4-9). Following the same idea, S2 and HI from the Basic/Bulk-Rock method can also be replaced with corresponding values in the MHR method. However, no major changes occurred in the values (compare Table 5-4-1 and Table 5-4-3).

Table 5-4-3 Data for the two immature samples processed using the MHR method.

Multi-heating method	Well	TOC (wt%)	Sh0 (mg HC/g)	Sh1 (mg HC/g)	OIL (mg HC/g)	Sh2 (mg HC/g)	S3 (mg CO <sub>2</sub> /g)	HI (Sh <sub>2</sub> x100/TOC)	OI (S <sub>3</sub> x100/TOC)
	1	25.79	5.51	9.1	14.61	126.17	0.16	489.22	0.62
6	14.64	1.72	5.74	7.46	75.55	0.19	516	2.97	

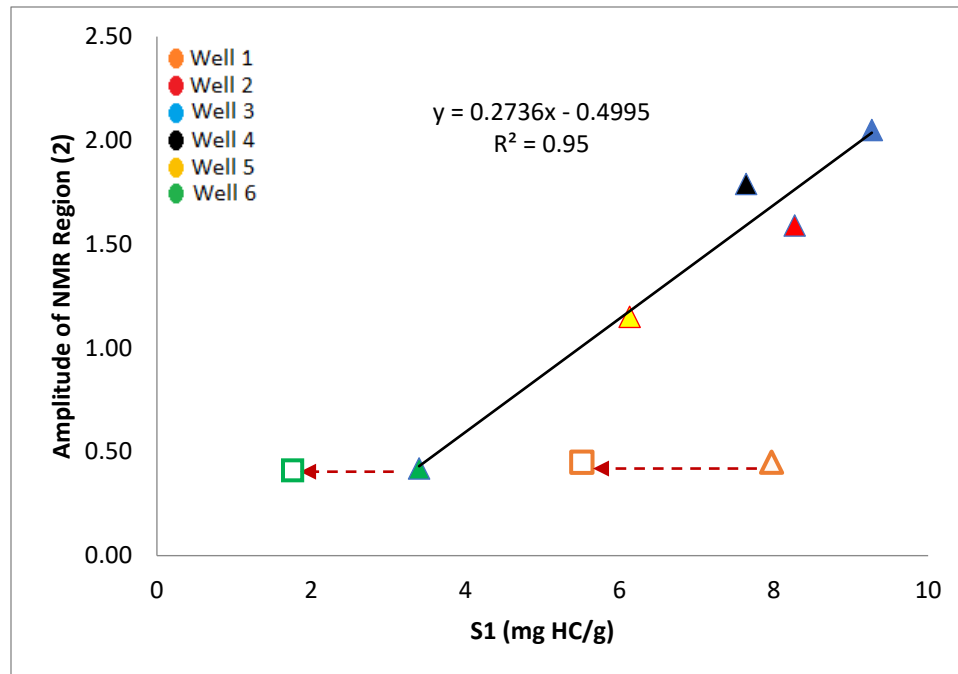


Figure 5-4-9 Hydrogen volume (mg H/g rock) of Region 3 in the NMR T<sub>1</sub>-T<sub>2</sub> map vs. S<sub>1</sub> from Rock-Eval. Squares are the corresponding Sh<sub>0</sub> from MHR method.

Another explanation which seems to be the dominant reason for such a behavior of Well 1 and Well 6 would be the overlapping boundaries of regions. Boundaries can be affected by the maturity level of organic matter, mineralogy, and the presence of magnetic minerals.

On the NMR maps of the two immature samples (Well 1 and Well 6), Region (5) has much more hydrogen signals than the other samples. As shown before, T<sub>1</sub>/T<sub>2</sub> ratios of immature samples are low, while T<sub>1</sub> relaxation times of hydroxyl signals are very long, so at low maturity levels organic matter signal might overlap with the signal from hydroxyl, i.e., some organic signals shift to Region (5) in the T<sub>1</sub>-T<sub>2</sub> map. Some minerals have hydroxyl groups (OH) in their structure, for example, ripidolite with a formula of (Mg, Fe, Al)<sub>6</sub>(Si, Al)<sub>4</sub>O<sub>10</sub>(OH)<sub>8</sub> or illite having a formula of K(Al<sub>2</sub>)(Si<sub>3</sub>Al)O<sub>10</sub>(OH)<sub>2</sub>. Kerogen has also OH group in its structure (Vandenbroucke and Largeau, 2007; Raja et al., 2017). This could explain the reason for the outlier behavior of Well 1 and 6 in Figure 5-4-5. Finally, it is seen that both Well 1 and Well 6 did not follow the overall observed trend in the cross-plot of %VR<sub>o</sub> and the amplitude of region 3 of NMR maps. As explained earlier, this is inferred possibly due to the overlapping of signals between region 3 with the OH signals that should appear in Region 5. However, Well 6 started to follow the trend of other

samples in the S1 and S2 peaks vs. Region 3 amplitude which made us to believe mineral content of the samples could possibly play an important role on the results.

To understand the chemical and mineralogical composition of the Bakken shale in high-resolution scale, the newly developed EDS (energy dispersive spectrometry) and backscattered electron (BSE) analysis were carried out on the samples. By a combination of the EDS and BSE results, a 2-D high-resolution mineralogical map of every single layer of the sample (Saif et al., 2017b) could be created. Chemical mapping provides the ability of better differentiation between various types of any individual mineral with a high degree of accuracy such as Na-Ca plagioclases and especially clay minerals. MAPS Mineralogy (Modular Automated Processing System; Saif et al., 2017a; Saif et al., 2017b) indicated that quartz, alkali feldspars, plagioclase, illite, pyrite, biotite, and muscovite are the most abundant minerals of the Bakken shales. As seen in Table 5-4-4, Well 1 has high Illite content. Moreover, ilmenite is also a magnetic mineral, which is only present in the Well 1 sample. Thus, it can be concluded that Well 1, due to having the lowest maturity and high content of magnetic minerals and minerals with OH group in their structure, shows a different trend.

*Table 5-4-4 XRD data of Wells 1-5 showing wt% of different minerals.*

<b>MINERAL (WT%)</b>	<b>WELL 1</b>	<b>WELL 2</b>	<b>WELL 3</b>	<b>WELL 4</b>	<b>WELL 5</b>	<b>WELL 6</b>
<b>QUARTZ</b>	6.08	44.66	43.28	77.59	26.57	39.1
<b>ALKALI FELDSPAR</b>	32.41	43.23	42.23	14.22	36.18	12.6
<b>PLAGIOCLASE</b>	2.27	0.7	0.52	0.38	1.19	4.2
<b>BIOTITE</b>	10.35	0.31	0.19	0.16	0.7	0
<b>MUSCOVITE</b>	3.91	0.43	0.58	0.2	0.82	15.5
<b>ILLITE</b>	36.67	5.67	6.37	1.13	12.62	10.3
<b>CHLORITE</b>	0.35	0.11	0.09	0	0.16	1.31
<b>ZIRCON</b>	0.01	0.01	0.01	0	0.01	0
<b>CALCITE</b>	0	0.39	0.21	0.58	0.81	1.5
<b>SIDERITE</b>	0	0	0.03	0.05	0.04	0
<b>DOLOMITE</b>	1.05	0.85	0.69	1.76	12.62	2.2
<b>ANKERITE</b>	0.41	0.34	0.22	0.7	3.34	0
<b>APATITE</b>	0.21	0.08	0.19	0.05	0.08	1.2
<b>MONAZITE</b>	0.31	0	0	0	0.01	0
<b>PYRITE</b>	5.71	3.05	5.23	3.07	4.62	3.84
<b>RUTILE</b>	0.2	0.15	0.17	0.1	0.2	0
<b>ILMENITE</b>	0.05	0	0	0	0	0
<b>HALITE</b>	0	0	0	0	0	1.79
<b>MARCASITE</b>	0	0	0	0	0	6

The proposed method is a fast and non-destructive way to understand kerogen thermal properties in terms of programmed pyrolysis. Furthermore, the minimal and rapid sample preparation for high frequency NMR enables us to evaluate such properties in a quick method even at the well site. In future studies, different samples from different formations and higher maturity levels would be evaluated to assess the potential of such a method.

## 5-5 Conclusions

The following conclusions can be drawn from this limited-in-scope study:

- The  $T_1/T_2$  ratio in Region (3) on NMR  $T_1$ - $T_2$  maps shows a positive trend with increasing thermal maturity, as expressed by vitrinite reflectance (equivalent) which is also robust in low mature samples.
- The amplitude of the Region (3) on NMR  $T_1$ - $T_2$  maps (related to organic matter) shows a strong correlation with  $V_{Ro}$  (equivalent), which is not applicable in low mature samples.
- Positive correlations between NMR and Rock-Eval pyrolysis  $S_1$  values for samples in the oil window were obtained. This means that NMR can be used to identify and correlate hydrocarbons (mobile oil) in Region (2) of the  $T_1$ - $T_2$  map against the  $S_1$  parameter.
- NMR 'solids' (viscous solids containing NSO compounds) in Region (3) of the  $T_1$ - $T_2$  map can be correlated to the  $S_2$  parameter from programmed pyrolysis.
- Region (3) volume shows a positive correlation with Hydrogen Index from Rock-Eval pyrolysis.
- The NMR method used in this study is promising and complementary to the traditional analytical methods, such as Rock-Eval pyrolysis and vitrinite reflectance. It shows a great potential and the ability to differentiate between hydrocarbons (mobile oil) versus moveable and non-moveable (solids) components in unconventional shale/mudrock samples. However, low mature samples and those with magnetic minerals might show different trends.
- The Complexity of unconventional shale plays has led to the employment of new analytical techniques. HF NMR can reveal porosity, permeability, and other petrophysical properties of the

sample, by adding geochemical parameters to this set of important characteristics using the proposed method, unconventional reservoirs will be better characterized.

## 5-6 References

Abarghani, A., Ostadhassan, M., Gentzis, T., Carvajal-Ortiz, H., Bubach, B., 2018. Organofacies study of the Bakken source rock in North Dakota, USA, based on organic petrology and geochemistry. *International Journal of Coal Geology* 188, 79-93.

Albrecht, R., Joffre, R., Le Petit, J., Terrom, G., Perissol, C., 2009. Calibration of chemical and biological changes in cocomposting of biowastes using near-infrared spectroscopy. *Environmental Science and Technology* 43, 804–811.

Albrecht, R., Ziarelli, F., Alarcon-Gutierrez, E., Le Petit, J., Terrom, G., Perissol, C., 2008. <sup>13</sup>C solid-state NMR assessment of decomposition pattern during co-composting of sewage sludge and green wastes. *European Journal of Soil Science* 59, 445–452.

Al Hinai, A., Rezaee, R., Esteban, L., & Labani, M. (2014). Comparisons of pore size distribution: A case from the Western Australian gas shale formations. *Journal of Unconventional Oil and Gas Resources*, 8, 1-13.

Andrews, A.B., Edwards, J.C., Pomerantz, A.E., Mullins, O.C., Nordlund, D., Norinaga, K., 2011. Comparison of coal-derived and petroleum asphaltene by <sup>13</sup>C nuclear magnetic resonance, DEPT, and XRS. *Energy & Fuels* 25, 3068-3076.

Behar, F., Beaumont, Y., De, B., Pentead, H.I. 2001. Rock-Eval 6 technology: performances and developments. *Oil and Gas Science and Technology. Review Institut Français du Pétrole Energ. Nouv.* 56, 111-134.

Behroozmand, A.A., Keating, K., Auken, E., 2015. A review of the principles and applications of the NMR technique for near-surface characterization. *Surveys in Geophysics* 36, 27-85.

## Chapter 5

Birdwell, J.E., Washburn, K.E., 2015. Multivariate Analysis Relating Oil Shale Geochemical Properties to NMR Relaxometry. *Energy Fuels* 29, 2234–2243.

Bloembergen, N., Purcell, E.M., and Pound, R.V., 1948, Relaxation Effects in Nuclear Magnetic Resonance Absorption, *Physical Review*, 73(7), 679-712.

Bryan, J., Kantzas, A., Moon, D., 2003. In situ viscosity of oil sands using low field NMR, Canadian International Petroleum Conference. Petroleum Society of Canada.

Cao, X., Birdwell, J.E., Chappell, M.A., Li, Y., Pignatello, J.J., Mao, J., 2013. Characterization of oil shale, isolated kerogen, and postpyrolysis residues using advanced <sup>13</sup>C solid-state nuclear magnetic resonance spectroscopy. *AAPG bulletin* 97, 421-436.

Carrie, J., Sanei, H., Stern, G., 2012. Standardisation of Rock-Eval pyrolysis for the analysis of recent sediments and soils. *Organic Geochemistry* 46, 38–53.

Carvajal-Ortiz, H., and Gentzis, T., 2018, Geochemical screening of source rocks and reservoirs: The importance of using the proper analytical program, *International Journal of Coal Geology*, 190, 56-69.

Carvajal-Ortiz, H., Gentzis, T., 2015. Critical considerations when assessing hydrocarbon plays using Rock-Eval pyrolysis and organic petrology data: Data quality revisited. *International Journal of Coal Geology* 152, 113-122.

Coates, G.R., Xiao, L., Prammer, M.G., 1999. NMR logging: principles and applications. Gulf Professional Publishing.

Dunn, K.-J., Bergman, D.J., Latorraca, G.A., 2002. Nuclear magnetic resonance: Petrophysical and logging applications. In: *Seismic Exploration*. 32, Pergamon, Amsterdam, New York, 93 pp.

Dutta Majumdar, R., Gerken, M., Mikula, R., Hazendonk, P., 2013. Validation of the Yen–Mullins model of Athabasca oil-sands asphaltenes using solution-state <sup>1</sup>H NMR relaxation and 2D HSQC spectroscopy. *Energy & Fuels* 27, 6528-6537.

## Chapter 5

Feng, Y., Le Doan, T.V., Pomerantz, A.E., 2013. The chemical composition of bitumen in pyrolyzed Green River oil shale: characterization by  $^{13}\text{C}$  NMR spectroscopy. *Energy & Fuels* 27, 7314-7323.

Fleury, M. "Characterization of shales with low field NMR." In *The International Symposium of Core Analysts*, Avignon, France, 8e11 September, SCA2014-014. 2014.

Fleury, M., Romero-Sarmiento, M., 2016. Characterization of shales using T 1–T 2 NMR maps. *Journal of Petroleum Science and Engineering* 137, 55-62.

Fleury, M., Kohler, E., Norrant, F., Gautier, S., M'Hamdi, J., Barré, L., 2013. Characterization and quantification of water in smectites with low-field NMR. *The Journal of Physical Chemistry C* 117, 4551-4560.

Gao, Y., Zou, Y.-R., Liang, T., Peng, P.a., 2017. Jump in the structure of Type I kerogen revealed from pyrolysis and  $^{13}\text{C}$  DP MAS NMR. *Organic Geochemistry* 112, 105-118.

Hackley, P.C., Araujo, C.V., Borrego, A.G., Bouzinos, A., Cardott, B.J., Cook, A.C., Eble, C., Flores, D., Gentzis, T., Gonçalves, P.A., 2015. Standardization of reflectance measurements in dispersed organic matter: Results of an exercise to improve interlaboratory agreement. *Marine and Petroleum Geology* 59, 22-34.

Hansen, P.H., 1987. The truncated SVD as a method for regularization. *BIT*, vol. 27, pp. 534–553.

Hanson, R.J., 1971. A numerical method for solving Fredholm integral equations of the first kind using singular values. *SIAM J. Numer. Anal.*, vol. 8, no. 3, pp. 616–622.

Jacob, H., 1989. Classification, structure, genesis and practical importance of natural solid oil bitumen ("migrabitumen"). *International Journal of Coal Geology* 11, 65-79.

Jin, H., Sonnenberg, S.A., 2013. Characterization for source rock potential of the Bakken Shales in the Williston Basin, North Dakota and Montana. *Unconventional Resources Technology Conference (URTEC)*.

## Chapter 5

Kelemen, S., Afeworki, M., Gorbaty, M., Sansone, M., Kwiatek, P., Walters, C., Freund, H., Siskin, M., Bence, A., Curry, D., 2007. Direct characterization of kerogen by X-ray and solid-state  $^{13}\text{C}$  nuclear magnetic resonance methods. *Energy & Fuels* 21, 1548-1561.

Kenyon, W., 1997. Petrophysical principles of applications of NMR logging. *The Log Analyst* 38.

Khatibi, Seyedalireza, Mehdi Ostadhassan, David Tuschel, Thomas Gentzis, Bailey Bubach, and Humberto Carvajal-Ortiz. "Raman spectroscopy to study thermal maturity and elastic modulus of kerogen." *International Journal of Coal Geology* 185 (2018): 103-118.

Khatibi, Seyedalireza, Mehdi Ostadhassan, David Tuschel, Thomas Gentzis, and Humberto Carvajal-Ortiz. "Evaluating Molecular Evolution of Kerogen by Raman Spectroscopy: Correlation with Optical Microscopy and Rock-Eval Pyrolysis." *Energies* 11, no. 6 (2018): 1-19.

Korb, J.-P., Louis-Joseph, A., Benamsili, L.s., 2013. Probing structure and dynamics of bulk and confined crude oils by multiscale NMR spectroscopy, diffusometry, and relaxometry. *The Journal of Physical Chemistry B* 117, 7002-7014.

Lafargue, E., Marquis, F., Pillot, D., 1998. Rock-Eval 6 applications in hydrocarbon exploration, production and soil contamination studies. *Review Institut Français du Pétrole* 63, 421-437.

Lisitz, N.V., Freed, D.E., Sen, P.N., Song, Y.-Q., 2009. Study of asphaltene nanoaggregation by nuclear magnetic resonance (NMR). *Energy & Fuels* 23, 1189-1193.

Liu, K., Ostadhassan, M., Gentzis, T., Carvajal-Ortiz, H., Bubach, B., 2017. Characterization of geochemical properties and microstructures of the Bakken Shale in North Dakota. *International Journal of Coal Geology*.

Mao, J., Fang, X., Lan, Y., Schimmelmann, A., Mastalerz, M., Xu, L., Schmidt-Rohr, K., 2010. Chemical and nanometer-scale structure of kerogen and its change during thermal maturation investigated by advanced solid-state  $^{13}\text{C}$  NMR spectroscopy. *Geochimica et Cosmochimica Acta* 74, 2110-2127.

## Chapter 5

Mehana, Mohamed, and Ilham El-monier. "Shale characteristics impact on Nuclear Magnetic Resonance (NMR) fluid typing methods and correlations." *Petroleum* 2, no. 2 (2016): 138-147.

McCarthy, K., Rojas, K., Niemann, M., Palmowski, D., Peters, K., Stankiewicz, A., 2011. Basic petroleum geochemistry for source rock evaluation. *Oilfield Review* 23, 32-43.

Petsch, S.T., Smernik, R.J., Eglinton, T.I., Oades, J.M., 2001. A solid state <sup>13</sup>C-NMR study of kerogen degradation during black shale weathering. *Geochimica et Cosmochimica Acta* 65, 1867–1882.

Piedrahita, J., Aguilera, R., 2017. Estimating Oil Saturation Index OSI from NMR Logging and Comparison with Rock-Eval Pyrolysis Measurements in a Shale Oil Reservoir, SPE Unconventional Resources Conference. Society of Petroleum Engineers.

Raja, M. A., Zhao, Y., Zhang, X., Li, C., Zhang, S., 2017. Practices for modeling oil shale pyrolysis and kinetics. *Reviews in Chemical Engineering* 34, 21-42.

Romero-Sarmiento, M.F., Ramiro-Martinez, S., Berthe, G., Fleury, M. Littke, R., 2017. Geochemical and petrophysical source rock characterization of the Vaca Muerta Formation: implications for unconventional resource estimations. *International Journal of Coal Geology* 184, 27-41.

Romero-Sarmiento, M.F., Euzen, T., Rolais, S., Juang, C., Littke R., 2016. Artificial thermal maturation of source rocks at different thermal maturity levels: applications to the Triassic and Doig formations in the western Canada sedimentary basin. *Organic Geochemistry* 97, 148-162.

Romero-Sarmiento, M.F., Pillot, D., Letort, G., Lamoureaux-Var, V., Beaumont, V., Huc, A.Y., Garcia, B., 2015. New Rock-Eval method of unconventional shale reservoir systems. *Review Institut Français du Pétrole Energ. Nouv.* 71, 1-9.

Romero-Sarmiento, M.F., Pillot, D., Letort, G., Lamoureaux-Var, V., Beaumont, V., Huc, A.Y., Garcia, B., 2014. New Rock-Eval method for characterization of shale plays. In: 14th Latin America Congress on Organic Geochemistry (ALAGO). Buzios, Rio de Janeiro-Brazil.

## Chapter 5

Rezaee, R., Saeedi, A., Clennell, B., 2012. Tight gas sands permeability estimation from mercury injection capillary pressure and nuclear magnetic resonance data. *Journal of Petroleum Science and Engineering* 88, 92-99.

Rueslåtten, Håkon, T. Eidsemo, and Carsten Slot-Petersen. "NMR studies of an iron-rich sandstone oil reservoir." In *Proceeding of the 1998 International Symposium of Society of Core Analysts, papers*, vol. 9821. 1998.

Saif, Tarik, Qingyang Lin, Branko Bijeljic, and Martin J. Blunt. "Microstructural imaging and characterization of oil shale before and after pyrolysis." *Fuel* 197 (2017): 562-574.

Saif, Tarik, Qingyang Lin, Alan R. Butcher, Branko Bijeljic, and Martin J. Blunt. "Multi-scale multi-dimensional microstructure imaging of oil shale pyrolysis using X-ray micro-tomography, automated ultra-high-resolution SEM, MAPS Mineralogy and FIB-SEM." *Applied energy* 202 (2017): 628-647.

Sanei, Hamed, James M. Wood, Omid H. Ardakani, Christopher R. Clarkson, and Chunqing Jiang. "Characterization of organic matter fractions in an unconventional tight gas siltstone reservoir." *International Journal of Coal Geology* 150 (2015): 296-305.

Smith, M.G., Bustin, R.M., 2000. Late Devonian and Early Mississippian Bakken and Exshaw black shale source rocks, Western Canada Sedimentary Basin: a sequence stratigraphic interpretation. *AAPG bulletin* 84, 940-960.

Solum, M.S., Mayne, C.L., Orendt, A.M., Pugmire, R.J., Adams, J., Fletcher, T.H., 2013. Characterization of macromolecular structure elements from a Green River oil shale, I. Extracts. *Energy & Fuels* 28, 453-465.

Sondergeld, C.H., Newsham, K.E., Comisky, J.T., Rice, M.C., Rai, C.S., 2010. Petrophysical considerations in evaluating and producing shale gas resources, *SPE Unconventional Gas Conference*. Society of Petroleum Engineers.

## Chapter 5

Song, Y-Q, Venkataramanan, L., Hürlimann, M.D., Flaum, M., Frulla, P, Straley, C., 2002. T1–T2 correlation spectra obtained using a fast two-dimensional Laplace inversion, *J. Magn. Reson.* 154, p. 261–268.

Sonnenberg, S.A., Pramudito, A., 2009. Petroleum geology of the giant Elm Coulee field, Williston Basin. *AAPG bulletin* 93, 1127-1153.

Sulucarnain, I.D., Sondergeld, C.H., Rai, C.S., 2012. An NMR study of shale wettability and effective surface relaxivity, *SPE Canadian Unconventional Resources Conference*. Society of Petroleum Engineers.

Tinni, A., Sondergeld, C., Rai, C., 2014. NMR T 1-T 2 response of moveable and nonmoveable fluids in conventional and unconventional rocks, *International Symposium of Core Analysts*, Avignon, France, pp. 8-11.

Vandenbroucke, M., and Largeau, C., 2007. Kerogen origin, evolution and structure. *Organic Geochemistry* 38, 719-833.

Washburn, K.E., Birdwell, J.E., 2013. Updated methodology for nuclear magnetic resonance characterization of shales. *Journal of Magnetic Resonance* 233, 17-28.

Werner-Zwanziger, U., Lis, G., Mastalerz, M., Schimmelmann, A., 2005. Thermal maturity of type II kerogen from the New Albany Shale assessed by  $^{13}\text{C}$  CP/MAS NMR. *Solid State Nuclear Magnetic Resonance* 27, 140-148.

Witte, E., Schenk, H., Müller, P., Schwochau, K., 1988. Structural modifications of kerogen during natural evolution as derived from  $^{13}\text{C}$  CP/MAS NMR, IR spectroscopy and Rock-Eval pyrolysis of Toarcian shales. *Organic geochemistry* 13, 1039-1044.

Xu, P, 1998. Truncated SVD methods for discrete ill-posed problems. *Geophy. J. Int.*, 135, 505–514.

## Chapter 6 Conclusions and recommendations

Based on the results from this research, the following conclusions were made:

- Raman spectroscopy, which is based on molecular vibrations, was able to detect molecular alterations in the organic matter as it undergoes changes in thermal maturity. Therefore, thermal maturity of the samples can be related to their Raman spectra.
- As maturity increases, major Raman signals start to separate from one another. This separation occurs between the G and D bands. The G band does not move significantly while the D band shifts towards lower wavelengths. From this observation, it is concluded that this specific Raman response directly correlates not only to the geochemical characteristics of the organic matter but also to the maturity of each sample.
- As thermal maturity increases, mechanical properties (e.g., elastic modulus) of organic matter alter. This alteration in elastic properties is due to macromolecular arrangements, transforming gradually from chaotic and mixed-layered to a better-ordered molecular structure.
- Comparing samples of different maturity levels to their corresponding predicted Young's moduli from Raman spectroscopy, it was observed that Young's modulus increases as maturity increases.
- Raman spectroscopy was able to estimate the Young's modulus of organic matter. It showed 0.32 GPa in the initial stages of maturation to 40 GPa in the late dry gas window.
- Organic matter is the least stiff constitute of mud rock
- Due to strengthening effect of kerogen, higher bottomhole pressure is required to open the fracture in kerogen rich shales.
- The strain-softening response of kerogen under loading condition implies that in the kerogen rich shale the tensile strength along the fracture does not decrease as much as in the kerogen free shale.
- In the case with kerogen, bottomhole pressure starts decreasing over time due to continuous decay of tensile strength of the minerals placed in sides of the fracture.
- In order to induce the same size of fracture in organic rich shale, more fluid is required to be injected compared to organic free case. Accordingly, total mechanical work is also more in case with kerogen.
- Raman spectroscopy has a good potential to predict the kerogen maturity, S1, S2, and Productivity index that is normally extracted from Rock-Eval pyrolysis and give us a better insight about the molecular structure of organic matter.

- Raman mapping mode provided a way to compare different OM and solid bitumen particles in microscale in a continuous format at varying maturity levels.
- We found, HP although known as the best thermal maturity simulation method, did not necessarily follow natural maturation conditions. This was revealed by the cross-plot of Raman spectroscopy data vs. conventional geochemistry results. The result can help to propose protocols and adjust experimental parameters for HP based on those cross-plots for more accurate thermal maturity progression steps in the lab.
- Raman spectroscopy can reflect heterogeneity of organic matter at microscale which can also represent expected heterogeneity in geochemical and geomechanical properties of the OM.
- It was found as maturity increases, heterogeneity of organic matter decreases and Raman map of solid bitumen particle shows more uniform distribution of G-D band characteristics.
- The T1/T2 ratio in Region (3) on NMR T1-T2 maps shows a positive trend with increasing thermal maturity, as expressed by vitrinite reflectance (equivalent) which is also robust in low mature samples.
- The amplitude of the Region (3) on NMR T1-T2 maps (related to organic matter) shows a strong correlation with VRo (equivalent), which is not applicable in low mature samples.
- Positive correlations between NMR and Rock-Eval pyrolysis S1 values for samples in the oil window were obtained. This means that NMR can be used to identify and correlate hydrocarbons (mobile oil) in Region (2) of the T1-T2 map against the S1 parameter.
- NMR 'solids' (viscous solids containing NSO compounds) in Region (3) of the T1-T2 map can be correlated to the S2 parameter from programmed pyrolysis.
- Region (3) volume shows a positive correlation with Hydrogen Index from Rock-Eval pyrolysis.
- The NMR method used in this study is promising and complementary to the traditional analytical methods, such as Rock-Eval pyrolysis and vitrinite reflectance. It shows a great potential and the ability to differentiate between hydrocarbons (mobile oil) versus moveable and non-moveable (solids) components in unconventional shale/mudrock samples. However, low mature samples and those with magnetic minerals might show different trends.

For future studies, the following points can be raised:

- More samples from different fields are necessary for more robust and elaborate study.
- While we were using Raman spectroscopy to predict the Young's modulus of OM, we used different samples with varying maturity. In future studies, the same sample which has undergone

artificially maturation can be used to eliminate the effect of different sampling in terms of minerals, maceral etc.

- In terms of comparing maturation rate for naturally and artificially matured samples, different protocols for HP and AHP methods should be applied to see which one mimics the same trend compared to naturally samples.
- The same methodologies might be applied in coal samples to examine the potential of Raman spectroscopy in different disciplines.
- In some Raman signals, the effect of minerals can be seen. In future studies, Raman at different spots of OM can be performed to correlate the effect of minerals to maturity.